



**HAL**  
open science

# Study of MHD instabilities in high flowrate induction electromagnetic pumps of annular linear design

Elena Martin Lopez

► **To cite this version:**

Elena Martin Lopez. Study of MHD instabilities in high flowrate induction electromagnetic pumps of annular linear design. Mechanics of materials [physics.class-ph]. Université Grenoble Alpes, 2018. English. NNT : 2018GREAI090 . tel-02055466

**HAL Id: tel-02055466**

**<https://theses.hal.science/tel-02055466>**

Submitted on 4 Mar 2019

**HAL** is a multi-disciplinary open access archive for the deposit and dissemination of scientific research documents, whether they are published or not. The documents may come from teaching and research institutions in France or abroad, or from public or private research centers.

L'archive ouverte pluridisciplinaire **HAL**, est destinée au dépôt et à la diffusion de documents scientifiques de niveau recherche, publiés ou non, émanant des établissements d'enseignement et de recherche français ou étrangers, des laboratoires publics ou privés.

## THÈSE

Pour obtenir le grade de

### **DOCTEUR DE LA COMMUNAUTE UNIVERSITE GRENOBLE ALPES**

Spécialité : **IMEP2 / MECANIQUE DES FLUIDES, PROCEDES,  
ENERGETIQUE**

Arrêté ministériel : 25 mai 2016

Présentée par

**« Elena MARTIN LOPEZ »**

Thèse dirigée par **Yves DELANNOY**  
codirigée par **Fabrice BENOIT**

préparée au sein du **SIMAP/EPM**  
dans **IMEP2 / MECANIQUE DES FLUIDES, PROCEDES,  
ENERGETIQUE**

## **Etude des instabilités Magnétohydrodynamiques dans les Pompes Electromagnétiques à induction annulaire à fort débit**

Thèse soutenue publiquement le « **29/11/2018** »,  
devant le jury composé de :

**Mr. Alain JARDY**

Professeur, Ecole des Mines de Nancy, Président du jury et Rapporteur

**Mr. Thierry ALBOUSIERE**

Directeur de Recherche, CNRS à Lyon, Rapporteur

**Mr. Christophe GISSINGER**

Maître de Conférence, Ecole Normale Supérieure de Paris, Membre

**Mr. Yves FAUTRELLE**

Professeur Emérite, Université Grenoble Alpes, Membre

**Mr. Yves DELANNOY**

Professeur, Université Grenoble Alpes, Membre

**Mr. Fabrice BENOIT**

Ingénieur de Recherche, CEA Cadarache, Membre





*“Success consists of going  
from failure to failure  
without loss of enthusiasm.”*

*Winston Churchill*



## ABSTRACT

Electromagnetic Linear Induction Pumps (EMPs) are an important research subject in the development of Gen IV sodium-cooled fast reactors. Especially, in the framework of the French Alternative Energies and Atomic Energy Commission's (CEA) R&D numerical simulation program, the prediction of the behavior of Annular Linear Induction Pumps (ALIPs) is being evaluated because of its safety advantages compared to mechanical pumps.

For nuclear safety reasons, it is needed to know the behavior of an ALIP at off-design conditions. Consequently, the present work is focused on the study of magnetohydrodynamic (MHD) phenomenology and instabilities, these last occurring at the transition from linear to non-linear branch of the performance curve at the maximum of pressure. This phenomenon is associated to a consequent decrease of the pump developed pressure and efficiency and takes place at large magnetic Reynolds number ( $Rm_B$ ), which quantifies the relation convection to diffusion of the magnetic field.

This research aims to develop different tools permitting to describe phenomena and predict behavior for different performance regimes. This reasoning has been constructed following three main axes based on bibliographic researches on the subject. They consist of i) the characterization of main effects triggered during the performance of ALIPs using theoretical approaches and obtaining of stability thresholds from which the MHD flow might become unstable, ii) the development of accurate numerical models able to reproduce physical behavior close to real facilities and iii) the observation and analysis of phenomena using different methods for the post-treatment of big data acquired through the exploitation of the experimental facility PEMDyn, located in CEA Cadarache, France.

In this work, the comparison of obtained results through these three different approaches has permitted to describe the MHD instabilities expected at operations with high values of slip magnetic Reynolds number ( $Rms$ ). They are characterized by low frequency (LF) pulsations, velocity and magnetic field inhomogeneities, vibrations, etc. Here it has been obtained that these phenomena might be due to an amplification of inlet perturbations, triggered by the value of the slip velocity. Such amplification may be quantified with theoretical or numerical models, and has been observed on experiments.

Furthermore, the current study puts the accent on the required level of detail in analytical and numerical models depending on their scope, and thus, an important number of models with different accuracies and assumptions has been developed. One of main conclusions extracted shows the importance of end effects due to the finite length of the inductor on the performance and stability of ALIPs.

**Keywords:** Magnetohydrodynamic, annular induction pump, stability threshold, performance curve, sodium-cooled fast reactor.

## RESUMÉ

Les pompes à induction linéaires électromagnétiques (PEMs) sont un sujet de recherche important dans le développement des réacteurs rapides refroidis au sodium de génération IV. En particulier, dans le cadre du programme de simulation numérique R&D du Commissariat à l'énergie atomique et aux énergies alternatives (CEA), la prédiction du comportement des pompes à induction linéaires annulaires (ALIP) a été évaluée en raison de ses avantages en termes de sécurité par rapport aux pompes mécaniques.

Pour des raisons de sûreté nucléaire, il est nécessaire de connaître le comportement d'une ALIP dans des conditions hors conception. En conséquence, le présent travail se concentre sur l'étude de la phénoménologie magnétohydrodynamique (MHD) et de ses instabilités, ces dernières se produisant lors du passage d'une branche linéaire à une branche non linéaire de la courbe de performance au maximum de pression. Ce phénomène est associé à une diminution conséquente de la pression et du rendement développés par la pompe et intervient dans des régimes de fonctionnement à grand nombre de Reynolds magnétiques ( $Rm_B$ ), lequel quantifie la relation convection-diffusion du champ magnétique.

Cette recherche vise à développer différents outils permettant de décrire des phénomènes et de prévoir des comportements pour différents régimes de performance. Ce raisonnement a été construit selon trois axes principaux basés sur les recherches bibliographiques plus notables sur le sujet. Ils consistent en i) la caractérisation des principaux effets déclenchés lors de l'opération de l'ALIP à l'aide d'approches théoriques et l'obtention de seuils de stabilité à partir desquels l'écoulement MHD pourrait devenir instable, ii) la mise au point de modèles numériques précis capables de reproduire les comportements physiques proches de ceux des installations réelles et iii) l'observation et l'analyse de phénomènes utilisant différentes méthodes pour le post-traitement de données volumineuses acquises par l'exploitation de l'installation expérimentale PEMDyn, située au centre du CEA Cadarache.

Dans ces travaux, la comparaison des résultats obtenus à travers ces trois approches différentes a permis de décrire les instabilités MHD attendues lors de l'opération à grand nombre de Reynolds magnétique de glissement ( $Rms$ ). Ils sont caractérisés par des pulsations à basse fréquence (LF), des inhomogénéités de vitesse et de champ magnétique, des vibrations, etc. On a obtenu ici que ces phénomènes pourraient être dus à une amplification des perturbations à l'entrée, déclenchée par une certaine valeur de la vitesse de glissement. Cette amplification peut être quantifiée avec des modèles théoriques ou numériques et a été observée lors d'expériences.

En outre, cette étude met l'accent sur le niveau de détail requis dans les modèles analytiques et numériques en fonction de leur portée. Un nombre important de modèles avec différentes exactitudes et hypothèses ont donc été développés. Une des conclusions principales extraites montre l'importance des effets de bouts dus à la longueur finie de l'inducteur sur les performances et la stabilité des ALIPs.

## REMERCIEMENTS

C'est en regardant en arrière qu'on se rend compte de la distance que l'on a parcourue.

Cette période de trois ans a constitué une véritable étape charnière entre la fin des études, avec ses dernières traces de naïveté, et le début de la vie adulte, moment où les idées commencent à s'éclaircir, enfin. Pour cette métamorphose, je tiens à remercier le grand nombre de personnes qui m'ont apporté l'élan et le recul nécessaires pour aboutir cette course de longue haleine.

En première lieu, je voudrais exprimer ma gratitude à mon directeur de thèse Monsieur Yves Delannoy, pour sa patience, son humilité et son savoir-faire. Il a été mon référent de compétence technique et d'éthique du travail. Je le remercierai toujours pour toute la formation scientifique qu'il m'a apporté. Je me suis sentie capable grâce à ton implication et ta confiance.

Je tiens à remercier aussi à mon encadrant au sein du CEA, Monsieur Fabrice Benoit de son approche pragmatique et sa compréhension. Avec toi j'ai appris des véritables leçons de vie qui m'ont fait évoluer, tant sur le plan professionnel comme humain. Merci de me faire devenir un peu plus forte.

Merci à Christine Biscarrat, ma tutrice spirituelle. Tu as été un de plus forts appuis pendant ces trois ans. Je te remercie pour tous tes bons conseils et pour l'amitié qui est restée après cette belle période.

Merci à Emmanuel Sanseigne, chef du Laboratoire LCIT qui m'a accueilli pendant ces trois ans, pour rester toujours à l'écoute et de ses qualités humaines. Merci Florence de ta bonne humeur et ta tendresse, pour tous les moments de panique où tu m'as aidé et encouragé.

Je voudrais aussi dédier un mot spécial à l'équipe du laboratoire LETS. Estelle, Denis, Mathilde, Pascal et Serge, vous vous êtes toujours rendus disponibles pour une question de plus sur les bruits de machine à laver sur PEMDyn, merci de votre bienveillance et soutien. Ça a été un vrai plaisir de travailler avec vous.

Merci Linards d'avoir été la voix de l'expérience au final du tunnel. Ton support m'a guidé vers la bonne direction tout le long de la thèse. Je voudrais profiter pour remercier aussi tout l'équipe de chercheurs de l'Institut de Physique de Riga de leur implication dans le projet, merci pour cette collaboration satisfaisante.

Je pourrais écrire des pages et des pages sur tous les bons moments que j'ai passé avec tous les intégrants du LCIT. Grace à votre bonne humeur, respect et affection je me suis sentie un peu moins étrangère parmi vous (sans compter quelques l'accent bien sur).

Merci Rémi pour ton charisme et ton calme, de m'avoir encouragé dans les moments de frustration (typiquement quand on a cherché désespérément le fameux signe moins dans le code). Tu m'as aidé à concevoir ce projet de thèse dans sa globalité, et ainsi tu es devenu une

des personnes qui m'a fait apprécier le plus toute l'expérience scientifique grâce à ta motivation, patience et amitié.

Merci à Alvaro et Alexandre, qui se sont chargés de plusieurs parties importants de ce travail. Je suis très satisfaite de l'expérience d'encadrement partagé avec chacun de vous. J'espère aussi d'avoir été à l'hauteur pour vous.

Je n'oublierai jamais tous les moments partagés avec toi Chiara, ma binôme italienne expatriée comme moi. On a évolué ensemble et finalement on est arrivées au but toutes les deux. Merci vraiment d'avoir été présente toujours que j'en ai eu besoin, tu es devenue quelqu'un d'important pour moi.

Merci Xavier et Christophe, les irréfutables gardiens de la salle de calcul (ainsi que Lucas pendant une période), d'avoir été toujours ouverts à la discussion et de votre intérêt et bienveillance. Merci pour toutes les conversations musicales, spécialement à propos de la guitare jazz.

Merci Sylvain, Emmanuel, Thomas, Julien(s) et Xavier pour être toujours à l'écoute et de m'avoir fait autant rigoler pendant mon séjour parmi vous. Merci pour cette formation intensive de français avec des petits passages sudistes (mais, c'est qui dégün ?).

Merci à tous mes amis espagnols et français, pour tous les moments précieux, appels sans fin, sorties et discussions riches. Irene, Marta, Carlos, Theo (Tyllo), Manon, JB et Frédéric, je vous remercie de m'avoir enrichi autant avec vos atouts.

Merci aux personnes retrouvées en cours de route, spécialement à ce genre qu'on ne s'attend pas à rencontrer et qui nous donne le dernier bout d'énergie dont on a besoin pour conclure la tâche. Merci Tristan. Tu m'as transmis ta sérénité et ta joie et tu continues à le faire à mon côté sans hésitation.

Merci à Laura, mi Superhermana, avec qui j'ai grandi ces 20 dernières années. J'ai vraiment de la chance d'avoir une amie si charmante, honnête et douée que toi. Je ne te le remercierai jamais assez.

Je ne pourrais pas finir ces remerciements sans penser à toute ma famille, qui a toujours été présente et qui m'a permis d'aboutir ce grand projet dans ma vie. Malgré la distance je vous ai senti près de moi tout le long.

Merci à mon frère et sœurs Pati, Adri y Sari. Merci à mis Abuelitas Antonia y Nené.

Merci Papá d'être mon exemple d'audace et d'avoir fait le chemin plus riche avec ton originalité et créativité irréfutables. Merci pour tes paroles caches et essentielles au bon moment.

Merci Mamá, d'être la plus tendre, gentille, intelligente et courageuse, de ne m'avoir jamais laissé lâcher, de ta confiance et de tes conseils sensibles, adéquats et exacts. Une grande partie de cela est grâce à toi. Tu es le genre de femme que j'aspire à devenir un jour.

## TABLE OF CONTENTS

ABSTRACT .....	5
RESUMÉ .....	6
REMERCIEMENTS .....	7
LIST OF MOST CITED ACRONYMS.....	11
1. CONTEXT AND SCOPE OF THE WORK.....	12
1.1. Context of the research.....	12
1.1.1. French nuclear program, CEA and SIMaP .....	12
1.1.2. Development of new concepts of reactor: SFR reactors .....	14
1.1.3. MHD and working principle of an EMP .....	16
1.1.4. PEMDyn experimental loop .....	17
1.2. Scope of the work.....	18
2. PHENOMENOLOGY AND BIBLIOGRAPHIC STUDY .....	20
2.1. Bases on MHD system of equations .....	20
2.1.1. Electromagnetic equations .....	20
2.1.2. Hydrodynamic equations.....	21
2.1.3. Non-dimensional numbers .....	22
2.1.4. Performance of an EMIP .....	25
2.1.5. Simplified model of an EMIP .....	26
2.1.6. Efficiency of an EMIP.....	30
2.2. State-of-art of present physical phenomena in ALIPs .....	32
2.2.1. Velocity profile under travelling magnetic field .....	32
2.2.2. End effects .....	33
2.2.3. Pump-circuit coupling .....	35
2.2.4. Studies on stability .....	37
2.3. Numerical studies on MHD instability.....	44
2.4. Experimental studies on MHD instability .....	51
3. ANALYTICAL DEVELOPMENTS .....	56
3.1. Theoretical investigations in ALIP phenomenology.....	56
3.1.1. Void magnetic field in the case of an ALIP .....	56
3.1.2. Basic flow solution .....	60
3.1.3. End effects impact on performance .....	69
3.2. Stability analysis .....	77

3.2.1.	Linear stability for the case of azimuthal perturbations .....	77
3.2.2.	Linear stability for the case of radial perturbations.....	84
3.2.3.	Energetic stability analysis .....	94
4.	NUMERICAL DEVELOPMENTS .....	102
4.1.	Methodology of MHD simulation of ALIPs .....	102
4.1.1.	Presentation of the EPM-INDUC code .....	102
4.1.2.	Description of the pump in the model .....	106
4.1.3.	Validation of EPM-INDUC code .....	110
4.2.	2D axisymmetric models.....	112
4.2.1.	MHD coupling with the discrete-coils model .....	112
4.2.2.	Axisymmetric sheet-of-current inductor model .....	116
4.2.3.	Axisymmetric periodic model .....	119
4.2.4.	Comparison of 2D models.....	122
4.3.	3D models .....	125
4.3.1.	Development and first results.....	125
4.3.2.	Stationary analysis of perturbations .....	130
4.3.3.	Transient analysis of perturbations.....	142
5.	EXPERIMENTAL DEVELOPMENTS .....	146
5.1.	PEMDyn experimental loop setup and equipment.....	146
5.2.	Experimental campaigns .....	155
5.2.1.	Magnetic field measurement without sodium .....	155
5.2.2.	Experimental performance curves and comparison to numerical simulations .....	157
5.2.3.	ENS Sensor calibration .....	159
5.2.4.	MHD instability characterization .....	164
6.	CONCLUSIONS AND PERSPECTIVES.....	172
	BIBLIOGRAPHY .....	177
	Annex I: Study of stability and available analytical methods.....	182
	Linear Stability method.....	182
	Weakly non-linear method.....	184
	Energetic method .....	187
	Annex II: EPM-INDUC code structure .....	189
	Module equations .....	189
	Boundary conditions .....	192

## **LIST OF MOST CITED ACRONYMS**

- ALIP: Annular Linear Induction Pump
- ASTRID: Advanced Sodium Technological Reactor for Industrial Demonstration
- CEA : Commissariat à l'énergie atomique et aux énergies alternatives
- CFD: Computational Fluid Dynamics
- DSP: Double Supply Pulsations
- EMIP: ElectroMagnetic Induction Pump
- ENS: Ecole Normale Supérieure
- FFT: Fast Fourier Transform
- FLIP: Flat Linear Induction Pump
- GIF: Generation IV International Forum
- HF: High Frequency
- LF: Low Frequency
- MHD: MagnetoHydroDynamics
- PIV: Particle Image Velocimetry
- PSD: Power Spectral Density
- RANS: Reynolds Average Stress Model
- RMS: Root Mean Square
- SFR: Sodium-cooled Fast Reactor
- TMF: Travelling Magnetic Field

## 1. CONTEXT AND SCOPE OF THE WORK

### 1.1.Context of the research

#### 1.1.1. French nuclear program, CEA and SIMaP

The birth of French nuclear program shares some analogies with the Manhattan Project, since both were triggered by the outbreak of the Second World War when Nazi Germany occupied Poland on first September of 1939. Nevertheless, French efforts were not focused on constructing weapons but on France's dire need for energy, since war has consumed much of its coal existences. Thereby, French scientists were more willing to use nuclear to provide answers to energy needs rather than to create a massive atomic bomb [1].

At that time, physicist and chemist Frederic Joliot-Curie was one of the greatest exponents in nuclear research with the Russian-born French physicist Lew Kowarski. Together they achieved their first fission reaction on January 26, 1939, permitting the observation of radioactive fragments that confirmed the occurrence of a sustained chain reaction. This experience motivated Joliot-Curie to ask for government investment in order to develop a model of a self-sustaining chain reaction with uranium and heavy water. However, the challenge at that time was to gather both components.

Despite their successes in obtaining experimental materials, the German invasion of France in May 1940 put a hold on further research as the French were forced to hide their supplies of heavy water and uranium.

It wasn't until the liberation of France in 1944 and the return of prominent scientists including Kowarski, Halban, Jules Guéron, and Bertrand Goldschmidt that Frédéric Joliot-Curie was able to restart atomic research. He was determined to pursue with the project.

Avid defensor for the civil applications of atomic energy, the day after the bombing of Nagasaki he published an article in *L'Humanité* proclaiming: *"It is true that the immense reserves of energy contained in the uranium devices can be liberated slowly enough to be used practically for the benefit of mankind. I am personally convinced that it [atomic energy] will be of inestimable service to mankind in peacetime."*

After the war, the Nation was once again in desperate need of energy with its coal and oil reserves brutally devoured, so Joliot-Curie's petitions for investment were heard by Charles de Gaulle, who was at that time in charge of provisional France's government. On October of 1945, only 2 months after the end of the war with the surrender of Japan, the Atomic Energy Commission (CEA - *Commissariat à l'énergie atomique*) was officially established. Its formal mission was to pursue scientific and technical research for the use of atomic energy in the domains of science, industry, and national defence. Joliot-Curie was named as the high commissioner in charge of all scientific and technical work and Raoul Dautry as general administrator, managing the administrative and financial side.

## CHAPTER 1

From the beginning, the CEA had significant political influence with relative autonomy, with its headquarters based five kilometres south of Paris at the Fort of Châtillon. Three main goals had been identified by the recently established CEA: to construct a heavy water and uranium reactor which could create radioactive isotopes, to then use them to create a larger pile and a nuclear centre, and finally to build a nuclear power plant.



Unlike the Manhattan Project, the success of the CEA did not remain a secret. French press called it “*a great achievement, French and peaceful, which strengthens our role in the defence of civilization.*”

Nowadays, the CEA employs near 16000 permanent workers, divided into 5 directions established in nine centres spread throughout France working in partnership with other research bodies, local authorities and universities. Its areas of skills are based in 4 main domains: defence and security, development of low-carbon energies (nuclear and renewable), technology research for industry and fundamental research.

The French nuclear program also involves a number of universities for fundamental research and education. Grenoble-INP is a key player in this domain with its engineer's diploma in nuclear engineering, and the associated research laboratories. Among them, SIMaP is in charge of the research in material science, with a number of specific projects on materials for the nuclear domain, and also a group dedicated to electromagnetic processing of materials, where fundamental research on Magneto-Hydro-Dynamics takes place.



Grenoble-INP is one of the largest engineering schools in France, with good ranks for material science. SIMaP has a permanent staff of 100 persons, 70 PhD students plus invited researchers and post-doctorants. Its five groups work on the design and elaboration of metallic materials and ceramics, the design and operation of processes, structural and multiphysic characterization, and multi-scale modelling. The applications are in the domains of energy, transport and metallurgy.

### 1.1.2. Development of new concepts of reactor: SFR reactors

At the present time, *Electricité de France* (EDF) continues to operate 58 nuclear reactors in France, producing approximately the 75% of total electricity supply in the country. This strategy makes France the largest net exporter of electricity in the world and gains over 3 billion of euros in revenue per year. Nevertheless, rising costs and aging facilities will probably force the shutdown of several plants in the coming years and radioactive waste storage and transmutation remain still as middle-open questions.

In this sense, an international cooperation project named *Generation IV International Forum* (GIF) was created, where France is one of the original nine members. The aim was to identify the new generation of nuclear fission reactors capable to meet the challenge of major energy production with minor nuclear waste improving safety, sustainability and economic competitiveness and with vows of non-proliferation. The GIF identified six new concepts of reactors as candidates able to tackle the challenge, which are listed on *Figure 1*.

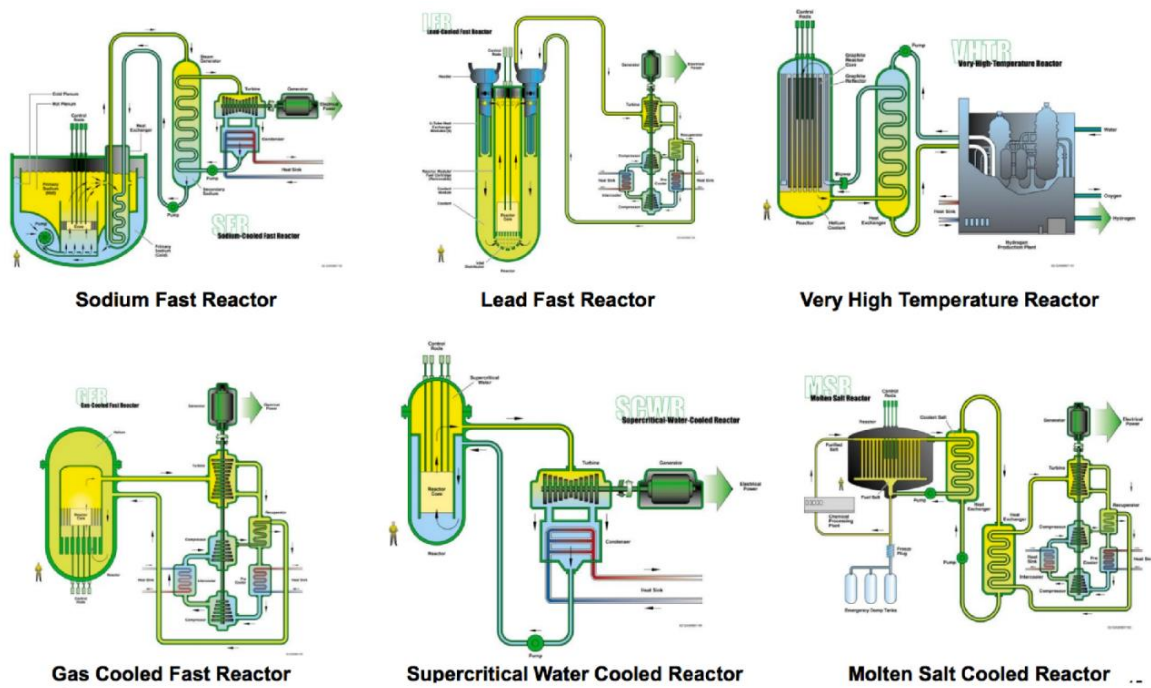


*Figure 1: Six concepts of 4<sup>th</sup> Generation reactors presented by GIF*

Among the technologies proposed, the *Sodium Fast Reactor* (SFR) concept is the one with higher accumulated experience, since there are several past and present examples of prototypes and commercial SFRs worldwide, since it uses a fast spectrum of neutrons which makes possible to use available fissile and fertile materials (including depleted uranium), considerably more efficiently than thermal spectrum reactors with once-through fuel cycles. Furthermore, thanks to the fast spectrum, a close-fuel cycle is foreseen producing energy and more fuel while destroying the Plutonium and long-lived elements created by precedent generations of nuclear power plants.

In France, the first prototype of SFR *Rapsodie* achieved criticality in 1967 in CEA Cadarache centre in the south of France with a nominal capacity of 20 MWth. Afterwards, power was increased to 40 MWth for 10 years and was operated until April 1983 when it was shut down permanently. Other two commercial SFRs followed this prototype, *Phénix* and *Super-Phénix*, started-up in France in 1973 and 1986 respectively. The CEA acquired an important experience and *savoir-faire* on sodium fast reactor technology through *Phénix* reactor, built in Marcoule centre, which still remains.

In June 2006, the French government signed for an industrial demonstrator, capable of transmutation and separation of long-life isotopes. ASTRID project, which stands for *Advanced Sodium Technological Reactor for Industrial Demonstration*, was conducted by CEA for the operational management, core design and R&D work since 2010, with its industrial partners (French ones: EDF, AREVA etc. and international ones: JAEA, GE, etc.).

It is in this framework that the CEA aims to develop innovative technology adapted to the standards of safety and performance requirements for the design of Generation IV reactors.

One of the challenges to face comes directly from the nature of sodium. Sodium is a fitting candidate as heat transfer fluid because of its high thermal conductivity and high boiling temperature and suitable for fast reactors because of its neutronics behaviour. However, it is chemically reactive, which requires special precautions to prevent contact with water and air, since those provoke respectively abrupt reactions and fires.

ElectroMagnetic Pumps (EMPs) are an interesting alternative to mechanical pumps for the transportation of sodium in secondary cooling systems of SFRs (*Figure 2*). This is due to their better safety features such as the absence of moving parts and leaktight construction. CEA's R&D program evaluates the interest of implementing a high discharge EMP on the secondary loop of SFRs due to its safety advantages.

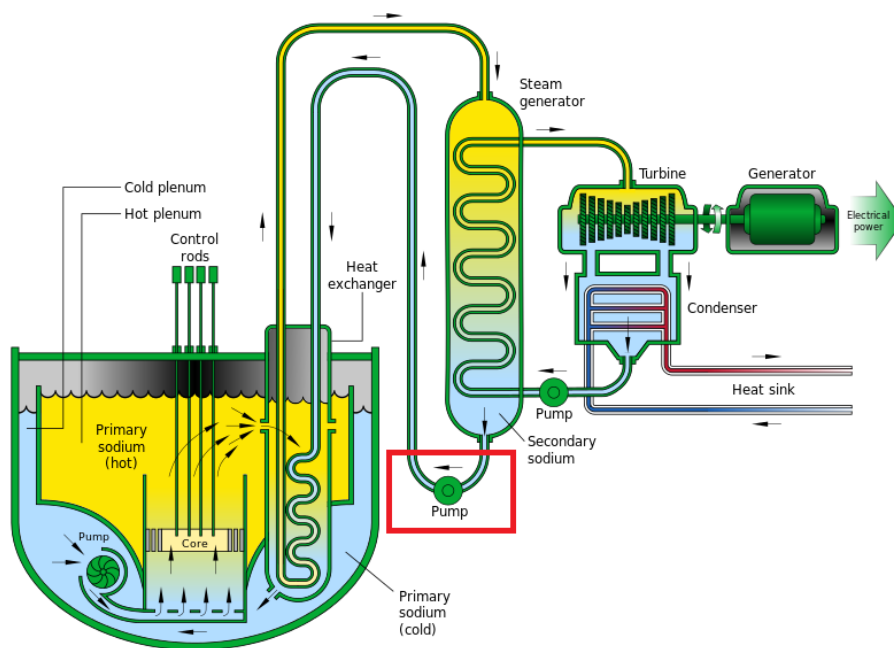


Figure 2: SFR pool-type reactor scheme

### 1.1.3. MHD and working principle of an EMP

Motion of liquid metals can be achieved using magnetic fields through contactless pumping and having immobile parts, therefore hermetic construction. This makes EMPs an interesting alternative to mechanical pumps with significant safety improvements, since the sodium would be confined in the pumping channel and in case of device failure reparations could be done without direct manipulation of the fluid.

There exist three different concepts of EMPs, *Flat Linear Induction Pumps* or FLIPs, *helical induction pumps* or HIPs and *Annular Linear Induction Pumps* or ALIPs. In industry ALIPs are widely used for transportation of liquid metals since they present fewer difficulties of feasibility and manufacturing than the rest of EMP types.

ALIP electromagnetic pump (EMP) architecture is composed by a cylindrical annular channel where the fluid is driven by the application of an external travelling magnetic field along the device. Phenomena responsible for its operation involve the combination of electromagnetism and hydrodynamics laws under the field of studies named *Magnetohydrodynamics* (MHD).

The study of MHD as a distinct subject gained its broader recognition in the late 1930s. First studies focused on the interaction of electroconductive but non-magnetic (relative magnetic permeability  $\mu = 1$ ) fluids (liquid metals, electrolytes and ionized gases) with magnetic fields. First of all, the relevance of the subject is connected to geophysical phenomena and magnetic field self-excitation [2]. In the 1960s development of MHD in engineering became increasingly important mostly due to the issues of power generation in thermonuclear reactors (the problem of plasma containment) and sodium cooled fast breeder reactors (SFR) for transport of liquid metal using electromagnetic (EM) pumps. The latter is still an actual topic of engineering and physical studies up to date.

The design of an ALIP (*Figure 3*) comprises one external inductor where three phase coils are embedded in laminated ferromagnetic core, the annular channel where liquid metal flows in the direction of traveling magnetic field and an inner ferromagnetic core or a second inductor.

The aim of this construction is to generate by electric supply coils a magnetic field perpendicular to flow (radial component). From cross product of induced currents in sodium (azimuthal) and radial component of magnetic field, axial electromagnetic (EM) force in the direction of travelling

field is induced in the liquid metal. This force is the responsible for the fluid motion.

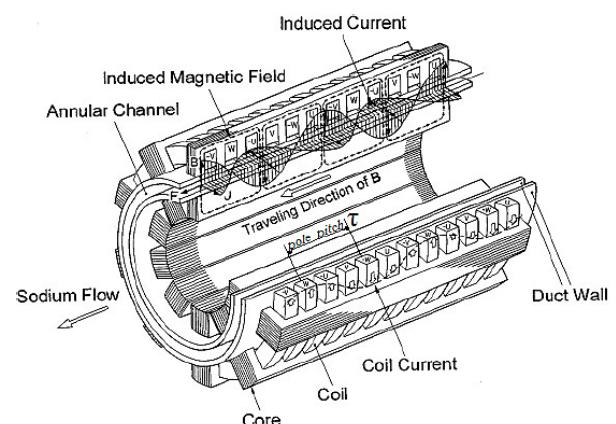


*Figure 3: ALIP configuration*

However, high discharge EMPs can face stability problems according to the working regime. Similarly to the case of an induction motor, they can suffer stalling problems and also can develop inhomogeneity of the flow, low frequency fluctuations, vibrations and additional loss of developed pressure and a consequent decrease of efficiency. Bibliography suggests that these phenomena are due to non-linear effects depending on working parameters. That is the reason why it is imperative to study the performance EMPs in order to choose the safety admissible regime and avoid undesirable instabilities.

### 1.1.4. PEMDyn experimental loop

PEMDyn facility (*Figure 4*) is an experimental loop of sodium with an EMP which has been designed and put in operation in 2015 at CEA Cadarache research center. The project is in charge of testing the experimental high flowrate EMP designed for a maximum flowrate of 1500 m<sup>3</sup>/h and maximum power of 325 kW.

Its principle target is to obtain relevant information from experimental measurements about nominal performance and instable regimes behavior to characterize phenomena through comparison to analytical and numerical models. In this framework, the CEA aims to develop a sufficiently realistic numerical model able to predict the performance of high discharge ALIPs for the secondary loop EMP of a SFR.

For this reason, the experimental loop is equipped with specific instrumentation for sodium that permits to examine different parameters, such as the developed pressure, mass flow rate, local velocity, magnetic field components, temperatures, etc. Experimental campaigns purpose to monitor and record several sets of data and signals for different working regimes of the ALIP.



*Figure 4: Experimental high discharge ALIP in PEMDyn loop*

## 1.2. Scope of the work

The aim of the PhD is that of building consistent analytical and numerical tools permitting to predict the performance of an ALIP at off-design conditions and validate them through the PEMDyn loop experimental measurements. This document contains the latest analytical and numerical researches with experimental qualitative comparison.

The current work is constructed following three main axes:

1. **Elaborate analytical predictions for physical behavior at different regimes:**

For this aim, the entire problem has been analyzed and splitted into different complementary effects. Finally, the impact of each one of them was studied using non-dimensional numbers.

2. **Construct different precision-level numerical fully coupled MHD models**

We seeked to develop models coherent with theory forecasts in order to better evaluate the different phenomena studied theoretically. Different working conditions had to be analyzed as a function of several input parameters (electric supply, inlet disturbance, inlet velocity, etc.).

3. **Exploitation of experimental PEMDyn loop**

An action plan for measurement acquisition at different working regimes was required. We needed to fix working conditions and sensor recording parameters for the post-treatment of measurements in PEMDyn loop depending on the effects we wanted to observe. Afterwards, measurements had to be interpreted using different indicators giving valuable information of a phenomenon.

These three points must be concluded with an exhaustive comparison results extracted from the different approaches presented.

For this aim, this PhD work was carried out with the help of different teams and employing several tools. First of all, a bibliographic study gave the reference point about investigations already done and expectations. It should be said that Linards Goldsteins previous works [3] on the subject gave some hints about the continuity of the research. The first year of PhD was the moment when questions started to appear, and we looked for methods to answer them.

From an analytical point of view, two collaborations were essential: On the one hand, the IPUL Latvian team for the understanding of linear methods applied to ALIPs. On the other hand, CEA Saclay DRF team, for giving firsts hints about the MHD base flow problematic and for the explanations about energetic stability methods. The post-treatment of results was done mainly with Matlab and Python.

An electromagnetism module on Fluent (EPM-INDUC) developed by Yves Delannoy from SIMaP laboratory (Grenoble, France) was employed for all the numerical simulations carried out in this work. The fact of using different precision-level models with the own architecture of the code have permitted to launch fully coupled MHD simulations with reasonable calculation times. Results have been analyzed using several Matlab post-treatments.

## CHAPTER 1

PEMDyn loop was piloted by LETS laboratory in CEA Cadarache, who are specialist in sodium technology. Experimental procedure was set with the help of LCIT engineers' team and advice from Latvian experts. Finally, results were sorted and analyzed using Matlab post-treatments. For this last, several indicators were defined to help correlation among the enormous amount of brut measurements registered.

Ultimately, the advice and contributions given by the two main supervisors of this research, Yves Delannoy as PhD director and professor of fluid mechanics and electromagnetic processes at Grenoble INP University and Fabrice Benoit as CEA supervisor and engineer responsible for EMP R&D coordination, were essential for the culmination of the current work.

## 2. PHENOMENOLOGY AND BIBLIOGRAPHIC STUDY

This chapter starts with a synthesis of phenomenology found in annular electromagnetic pumps. For this aim, a general theoretical study of the performance of an ALIP is presented with an overview of main phenomena documented in the literature and hints about available methods to deal with the study of MHD stability.

In a second place, we introduce a specific bibliographic study about numerical and experimental approaches on the subject.

In addition, personal remarks are given all along the chapter in order to establish approaches considered in following developments.

### 2.1. Bases on MHD system of equations

#### 2.1.1. Electromagnetic equations

The system of Maxwell equations controlling the electromagnetic field can be written in a continuous material without magnetisation nor electric polarisation, neglecting the density of electric charge and the displacement currents (quasi-steady approximation) [4]:

$$\nabla \cdot \mathbf{E} = \frac{\rho_q}{\varepsilon_0} \quad (1)$$

$$\nabla \times \mathbf{E} = -\frac{\partial \mathbf{B}}{\partial t} \quad (2)$$

$$\nabla \cdot \mathbf{B} = 0 \quad (3)$$

$$\nabla \times \mathbf{B} = \mu_0(\mathbf{j} + \mathbf{j}_e) \quad (4)$$

The total magnetic field in (4) is generated by the external supply currents  $\mathbf{j}_e$  which are assumed to be known, and the induced currents  $\mathbf{j}$  which come from the Ohm's law in differential form:

$$\mathbf{j} = \sigma(\mathbf{E} + \mathbf{u} \times \mathbf{B}) \quad (5)$$

By inserting (5) into (4) and applying curl (rotor) operator, it follows:

$$\nabla \times \nabla \times \mathbf{B} = \mu_0\sigma[\nabla \times \mathbf{E} + \nabla \times (\mathbf{u} \times \mathbf{B})] + \mu_0\nabla \times \mathbf{j}_e \quad (6)$$

Using (2) and (3), the induction equation for magnetic flux density  $\mathbf{B}$  is obtained:

$$\Delta \mathbf{B} = \mu_0\sigma \left[ \frac{\partial \mathbf{B}}{\partial t} - \nabla \times (\mathbf{u} \times \mathbf{B}) \right] - \mu_0\nabla \times \mathbf{j}_e \quad (7)$$

To fulfill also the Gauss equation for  $\mathbf{B}$  in (3), it is useful to introduce magnetic vector potential, since it reduces the problem to only one EM variable to solve:

$$\nabla \times \mathbf{A} = \mathbf{B} \quad (8)$$

$$\nabla \cdot \mathbf{A} = 0 \quad (9)$$

An induction equation can be written for the vector potential  $\mathbf{A}$  by substituting (8) into (2), integrating to  $\mathbf{E} = -\frac{\partial \mathbf{A}}{\partial t} - \nabla V$  and using it and (4) to eliminate  $\mathbf{E}$  and  $\mathbf{j}$  from (5). Substituting (8) and using (9) to transform the double curl of  $\mathbf{A}$  into a Laplacian, we get an equation involving the electric scalar potential  $V$ , (which is identically 0 in our cylindrical channel for axisymmetric conditions, but not in general):

$$\Delta \mathbf{A} = \mu_0 \sigma \left[ \nabla V + \frac{\partial \mathbf{A}}{\partial t} - (\mathbf{u} \times \nabla \times \mathbf{A}) \right] - \mu_0 \mathbf{j}_e \quad (10)$$

Since  $\mathbf{B}$  and  $\mathbf{u}$  are solenoidal fields, (7) can be transformed, to show a convection operator ( $\mathbf{u} \cdot \nabla$ ):

$$\Delta \mathbf{B} - \mu_0 \sigma \left[ \frac{\partial \mathbf{B}}{\partial t} - (\mathbf{B} \cdot \nabla) \mathbf{u} + (\mathbf{u} \cdot \nabla) \mathbf{B} \right] = -\mu_0 \nabla \times \mathbf{j}_e \quad (11)$$

When magnetic field is found using ((11), or (10) and (8), the electromagnetic force can be calculated as:

$$\mathbf{f}_{EM} = \mathbf{j} \times \mathbf{B} = \left( \frac{\nabla \times \mathbf{B}}{\mu_0} - \mathbf{j}_e \right) \times \mathbf{B} = \frac{(\mathbf{B} \cdot \nabla) \mathbf{B}}{\mu_0} - \nabla \left( \frac{\mathbf{B}^2}{2\mu_0} \right) - \mathbf{j}_e \times \mathbf{B} \quad (12)$$

Force calculated from (12) is used as source term in Navier-Stokes equation.

### 2.1.2. Hydrodynamic equations

As for other fluid mechanics cases, the liquid metal flow in an EMIP is ruled by the Navier-Stokes equations. This system is formed by the momentum conservation with the addition of the electromagnetic force as source term (13), and the continuity equation for incompressible fluids (14).

$$\rho \left[ \frac{\partial \mathbf{u}}{\partial t} + (\mathbf{u} \cdot \nabla) \mathbf{u} \right] = -\nabla p + \eta \Delta \mathbf{u} + \mathbf{f}_{EM} \quad (13)$$

$$\nabla \cdot \mathbf{u} = 0 \quad (14)$$

Or expressing (13) and (14) in terms of vorticity:

$$\boldsymbol{\omega} = \nabla \times \mathbf{u} \quad (15)$$

$$\rho \left( \frac{\partial \boldsymbol{\omega}}{\partial t} + (\mathbf{u} \nabla) \boldsymbol{\omega} - (\boldsymbol{\omega} \nabla) \mathbf{u} \right) = \eta \Delta \boldsymbol{\omega} + \nabla \times \mathbf{f}_{EM} \quad (16)$$

The introduction of Navier-Stokes equations inevitably leads to a system of nonlinear differential equations. For this reason, obtaining an analytical expression is not always assured. One of the exceptions is the case of a Hartmann flow [5], characterized by a low magnetic Reynolds number and a laminar regime ( $100 < \text{Re} < 2000$ ), which is possible to solve analytically. Unfortunately, none of these conditions are met in sodium EMIPs.

As in most real cases, the flow in an EMIP is in turbulent regime ( $\text{Re} > 2000 \dots 3000$ ), that means that there are indeterminate velocity fluctuations. These flows may be studied with RANS macroscopic models (Reynolds Averaged Navier-Stokes) where the components of the velocity are averaged on a volume. Among the most common, we find the two equations models  $k$ - $\omega$  and  $k$ - $\varepsilon$ , where the assumption of turbulence isotropy is considered to solve the closure problem in N-S equations. However, since MHD turbulence is itself a research subject, being rigorous this also might affect to validity of RANS turbulence model chosen.

### 2.1.3. Non-dimensional numbers

In dimensionless form, the equations involve a set of characteristic parameters of the system that depend on the characteristic scales of the problem. In the case of EMIPs, there are several spatial and velocity scales that can be considered. This leads to very different values for some dimensionless numbers, so it is important to define the evaluated phenomenon qualitatively to avoid confusion. From the previous description of the MHD coupled system, a list of dimensionless numbers characterizing the operating modes of the EMIPs is introduced.

#### 1. Reynolds number

This shows the ratio between the inertia force  $\rho(\mathbf{u} \cdot \nabla) \mathbf{u}$  and the viscous force  $\eta \Delta \mathbf{u}$  in Navier-Stokes equation.

$$Re = \frac{\rho_{Na} U_z L}{\mu}$$

With the sodium density  $\rho_{Na}$ , axial sodium velocity averaged over the channel  $U_z$ , characteristic spatial scale  $L$  and hydraulic viscosity  $\mu$ . The characteristic spatial scale is the thickness of the channel  $d_h$ .

The Reynolds number characterizes transition of a flow to turbulence. In a tube of hydraulic diameter  $D_h$  ( $= d_h/2$  in our pump channel), turbulence occurs normally above a critical Reynolds number of roughly 2000, which is largely exceeded in our applications. However, the magnetic field may postpone this transition and even transform the type of turbulence found in the channel (from 3D turbulence to 2D turbulence) in a way that is still not well known for non-uniform magnetic fields.

## 2. Magnetic Reynolds number

It is built as the ratio between the convective term of the induction equation (or induction term due to the flow)  $\nabla \times (\mathbf{u} \times \mathbf{B})$  and its diffusion term (ohmic dissipation)  $\eta \Delta \mathbf{B}$ .

$$R_m = \frac{U_z L}{\eta}$$

With the characteristic velocity  $U_z$ , the characteristic spatial scale  $L$  and magnetic diffusivity  $\eta = 1/\mu_0 \sigma_{Na}$ .

The choice left for velocity and space scales leads to consider several magnetic Reynolds numbers.

- **Magnetic Reynolds number at synchronism:** Here, the characteristic velocity scale is the synchronism velocity or progressive field velocity ( $U_B = \omega/k$ ), the spatial scale is the inverse of the wavenumber of the magnetic field, i.e.  $L = 1/k = 2\tau/2\pi$  where  $2\tau$  is the wavelength of the magnetic field. A correction factor is considered in order to take into account the difference of electrical conductivities between the hydraulic gap  $d_h$  and the magnetic gap  $d_m$ .

$$R_{mB} = \frac{\mu_0 \sigma_{Na} \omega d_h}{k^2 d_m}$$

This number largely exceed 1 for our pumps, which means that in normal operating conditions ( $U_z \sim \omega/k$ ), the magnetic field will be strongly convected by the flow, which leads to large inlet and outlet zones were the pump does not work as a segment of an infinite pump.

- **Global Slip Magnetic Reynolds number:** In this case we consider as characteristic velocity scale the slip velocity, i.e. the difference between the travelling field velocity and the average sodium velocity over the channel  $U_z$ . From this, the global slip ratio is defined as the averaged slip velocity divided by the field velocity,  $S = (U_B - U_z)/U_B$ .

This non-dimensional number shows the distortion of magnetic field lines generated by the liquid sodium flow in the core part of the pump (far from inlet and outlet effect).

$$Rms = S \cdot R_{mB}$$

## 3. Hartmann number

This is the square root of the ratio between the velocity induced Laplace force  $\sigma \mathbf{v} \times \mathbf{B} \times \mathbf{B}$  and viscous forces  $\rho \nu \Delta \mathbf{v}$ . The characteristic spatial scale is the thickness of the channel  $d_h$ , and if  $B_0$  is the scale of the radial magnetic field,

$$Ha = B_0 d_h \sqrt{\frac{\sigma}{\rho \nu}}$$

This parameter characterizes the thickness of Hartmann layers [5] as  $\delta_{Ha}/d_h = Ha^{-1}$ .

#### 4. Stuart number or interaction parameter

It is built as the ratio between Laplace force  $\mathbf{j} \times \mathbf{B}$  and inertia force  $\rho(\mathbf{u} \cdot \nabla)\mathbf{u}$ , using  $\mathbf{j} \sim \sigma \mathbf{u} \times \mathbf{B}$  which is the correct scale for the electric current if  $\mathbf{u}$  represents the slip velocity and  $\mathbf{B}$  the radial magnetic field. This number is also linked to the ratio between the square value of Hartmann number and Reynolds number:

$$N = \frac{\sigma B_0^2 (U_B - U_z)}{\rho U_z^2 / d_h} = \frac{S}{1 - S} \frac{Ha^2}{Re}$$

This number compares characteristic time scales linked to electromagnetic force and flow inertia. Strong values indicate a strong effect of the Laplace force, which drives the flow field instantaneously. In our applications  $N$  is of order unity, showing that the inertia effects cannot be neglected.

All these non-dimensional numbers are involved in the choice of design and operation parameters of an ALIP. From previous researches we can extract qualitative information about the phenomena occurring for each working regime of a device. As an example, the following tables show some reference values of the non-dimensional numbers mentioned above for the Japanese ALIP developed by Toshiba [6] and for PEMDYN experimental pump [7].

Table I. Design parameters of Toshiba and PEMDYN ALIPs

Parameters	Description	Toshiba	PEMDYN
$L_{inductor}$	Length of inductor	4.41 m	1.98 m
$d_h$	Hydraulic gap	0.077 m	0.04783 m
$d_m$	Magnetic gap	0.084 m	0.06015 m
$f$	Frequency	20 Hz	10 Hz
$2\tau$	Pole length	0.63 m	0.66 m
$N_{poles}$	Pole number	7	3
$U_B$	Synchronism velocity	12.4 m/s	6.6 m/s
$U_z$	Optimal sodium velocity	10.27 m/s	5.14 m/s

$S$	Slip ratio	0.172	0.22
$B_0$	Magnetic field in the channel (max.)	0.4 T	0.14 T

Table II. Sodium properties at  $T = 335^\circ\text{C}$  and  $T = 170^\circ\text{C}$

Parameters	Description	T = 335 °C	T= 170 °C
$\sigma_{Na}$	Electrical conductivity	5.1 e + 6 S/m	8.1e + 6 S/m
$\rho_{Na}$	Density	872,3 kg/m <sup>3</sup>	910.6 kg/m <sup>3</sup>
$\mu_{Na}$	Dynamic viscosity	3.16 e – 4 Pa · s	4.94 e – 4 Pa · s

Table III. Characteristic dimensionless numbers for Toshiba and PEMDyn ALIP

Dimensionless number	Description	Toshiba T = 335 °C	PEMDyn T= 170 °C
$Re$	Reynolds number	1.09 e+6	1.82 e+5
$R_{mB}$	Magnetic Reynolds number at synchronism	7.45	5.61
$R_{ms}$	Global magnetic slip Reynolds number	1.28	1.23
$Ha$	Hartmann number	3951.1	857.4
$N$	Stuart number	2.97	2.4

### 2.1.4. Performance of an EMIP

In this section simplified analytical cases [3] showing the performance of an annular EMIP are used to separate and recognize the different phenomena that may appear depending on the working regime. The chosen approach focuses on the methodology for evaluating the complex multi-physical nature of MHD systems from simplified cases making possible to describe specific phenomena related to the operation of the ALIPs and to understand the physics that govern them.

The following two models describe the same case of an ideal EMIP with an infinite linear current layer both in Cartesian and Cylindrical coordinates. In the case of an ALIP type pump it is more suitable to use the second case since the geometry is 2D-axisymmetric. On the other hand, the problem in partial equations with its corresponding boundary conditions is more complex to solve (the solution is expressed in the form of modified Bessel equations

because of the cylindrical geometry of the problem). Nevertheless, the Cartesian solution can be considered in the case of an ALIP when the magnetic gap is small compared to its radius. Moreover, the Cartesian solution may be further simplified when the magnetic gap is thin compared to the inductor wavelength, i.e. when the following conditions (17) are established:

$$H_R = \frac{R_2 - R_1}{R_1} \ll 1 \quad \text{and} \quad H_\lambda = k(R_2 - R_1) \ll 1 \quad (17)$$

Where  $R_2$  and  $R_1$  are respectively the upper and lower radius defining the magnetic gap  $d_m$ , and  $k$  the wavenumber of the magnetic field. From now on we will consider  $H_R$  and  $H_\lambda$  as the parameters that quantify if the thin channel approximation is acceptable.

In following analytical developments when conditions (17) would be applied we would say that the thin channel approximation has been considered.

### 2.1.5. Simplified model of an EMIP

An ideal ALIP is infinitely long and consists of a channel located between two perfect ferromagnetic irons without metallic walls where thin channel approximation (17) holds. The magnetic field is created by a thin layer of linear current and the solid-body approximation with constant velocity ( $U_z$ ) is considered for the liquid metal flow (*Figure 5*).

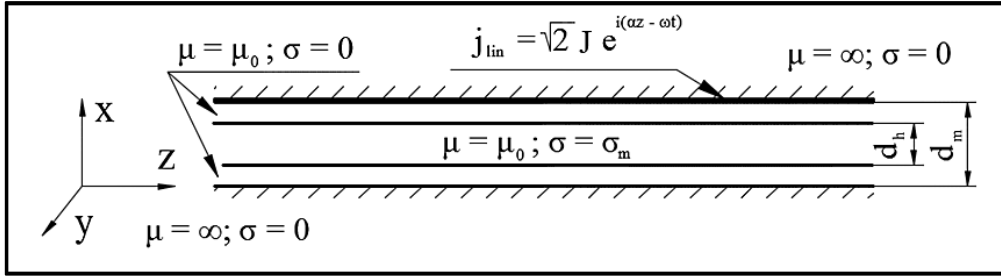


Figure 5: Scheme of an ideal ALIP in Cartesian Coordinates

The infinite current layer approximation is used to avoid the rather complex definition of phase distribution of the inductor.

An ideal EMIP is, by definition, powered by a travelling wave without extra harmonics:

$$\mathbf{j}_{lin} = \sqrt{2}J \cdot e^{i(kz - \omega_B t)} \mathbf{e}_y \text{ [A/m]} \quad (18)$$

The 2D induction equation for the  $y$  component of the vector potential in Cartesian coordinates gives:

$$\frac{\partial^2 A}{\partial x^2} + \frac{\partial^2 A}{\partial z^2} - \mu_0 \sigma \left[ \frac{\partial A}{\partial t} + \left( U_z \frac{\partial A}{\partial z} \right) \right] = 0 \quad (19)$$

## CHAPTER 2

With the boundary condition at the top of the channel:

$$\left. \frac{\partial A}{\partial x} \right|_{x=d_m} = \mu_0 j_{lin} \quad (20)$$

For the case without electrical currents imposed on the yoke, boundary condition at the bottom of the channel gives an axis of symmetry condition:

$$\left. \frac{\partial A}{\partial x} \right|_{x=0} = 0 \quad (21)$$

In order to further simplify the system, it is convenient to use the reference frame of the liquid metal (relative velocity). However, this is only possible for the consideration of uniform velocity profile. This result puts in evidence that the magnetic field that propagates along the pump will be "braked" due to the flow velocity, where the "slip" ratio characterizes the effect described:

$$S = 1 - \frac{U_z}{U_B} = 1 - \frac{U_z}{2\tau f} \quad (22)$$

Linear current density expression transforms into:

$$j_{lin} = \sqrt{2}J e^{ik(U_B St - z)} \quad (23)$$

So we look for solution of vector potential in complex harmonic form:

$$A = \text{Re}\{A_0(x) \cdot e^{ik(U_B St - z)}\} \quad (24)$$

In this frame we do not consider the liquid metal velocity in the channel and induction equation to solve becomes:

$$\Delta \mathbf{A} = \mu_0 \sigma \frac{\partial \mathbf{A}}{\partial t} \quad (25)$$

Where  $\sigma$  value varies depending on the zone, as shown in *Figure 5*.

Using boundary conditions, the form of solution for the vector potential is:

$$A(x, z) = \frac{\mu_0 \sqrt{2} J}{\lambda} \cdot \frac{ch(\lambda x)}{sh(\lambda d_m)} \cdot e^{ik(U_B St - z)} \quad (26)$$

Where  $\lambda$  is the complex coefficient for the magnetic field diffusion in the liquid metal, expressed as a function of the global slip magnetic Reynolds number ( $R_{ms}$ ).

$$\lambda^2 = k^2(1 + iR_{ms}) \quad (27)$$

## CHAPTER 2

The quasi-stationary developed pressure is found for the expression of the vector potential averaged in the gap between yokes  $d_m$  for a length of inductor  $L$ :

$$\Delta p = \frac{\sigma}{2} \cdot \left( \frac{\mu_0 \sqrt{2} J}{k d_m} \right)^2 \cdot L \cdot \frac{U_{BS}}{1 + Rms^2} = \mu_0 J^2 \cdot \frac{L \tau}{\pi d_m} \cdot \frac{Rms}{1 + Rms^2} \quad (28)$$

Last term in (28) shows that the electromagnetic pressure is a non-linear function on the global slip Reynolds number. Different behaviour is analysed for two cases:

- When  $Rms \ll 1$ , the quadratic term can be neglected, and it follows that for small values of  $Rms$  pressure grows linearly:

$$\Delta p \sim Rms \quad (29)$$

- When  $Rms \gg 1$ , the quadratic term is not negligible, so pressure decays proportionally to  $Rms$  :

$$\Delta p \sim \frac{1}{Rms} \quad (30)$$

The maximum value of the function is obtained between the two previous cases around  $Rms \sim 1$ . It can be found by relying on the analysis of functions, with the imposition:

$$\begin{aligned} \frac{d}{d(Rms)} \left( \frac{Rms}{1 + Rms^2} \right) = 0 &\quad \rightarrow \quad \frac{1 - Rms^2}{(1 + Rms^2)^2} = 0 \\ &\quad \rightarrow \quad \Delta p|_{Rms=1} = Max \end{aligned} \quad (31)$$

It is important to note that the maximum of pressure is the half of the linear approximation.

The graphical representation of (28) in *Figure 6* gives the performance curve of an ALIP in Cartesian Coordinates and its two limit cases (29) and (30) for high and low  $Rms$  respectively. The decreasing non-linear part of the curve ( $Rms \gg 1$ ) is characteristic of induction machines and is one of the key concepts for the analysis of instabilities.

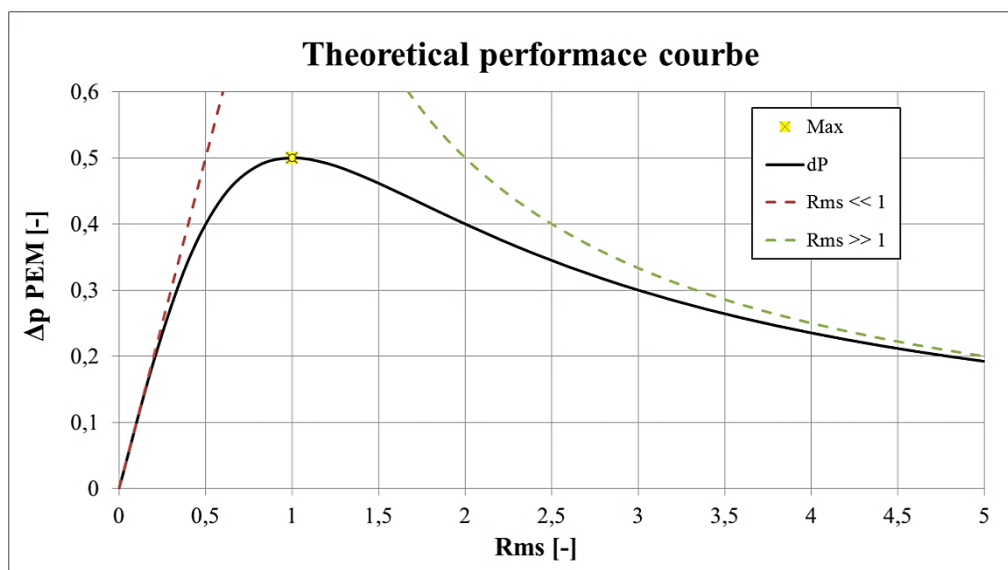


Figure 6 : Developed pressure of an ALIP in Cartesian Coordinates as a function of  $Rms$  [3].

Talking more practically about the different behaviours found, we find out that there are mainly two regimes of performance (Figure 7). First, a stable regime corresponding to linear trend where the input of an external perturbation of velocity or magnetic field will be damped by the system, and secondly, an unstable regime characterized by non-linear phenomena where inlet perturbations will be amplified. Figure 8 shows qualitatively this behaviour for the input of an azimuthal velocity perturbation at the inlet of the system and its development along the duct for both cases. This reflection highlights the importance of characterizing the inset threshold of undesirable instabilities in ALIPs and of fixing the optimal performance as the most efficient stable regime.

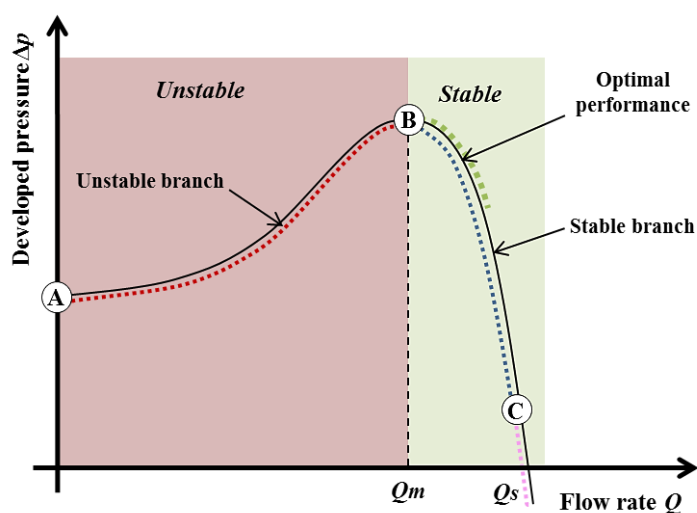


Figure 7: Developed pressure of an ALIP in Cartesian Coordinates as a function of  $Rms$  [3].

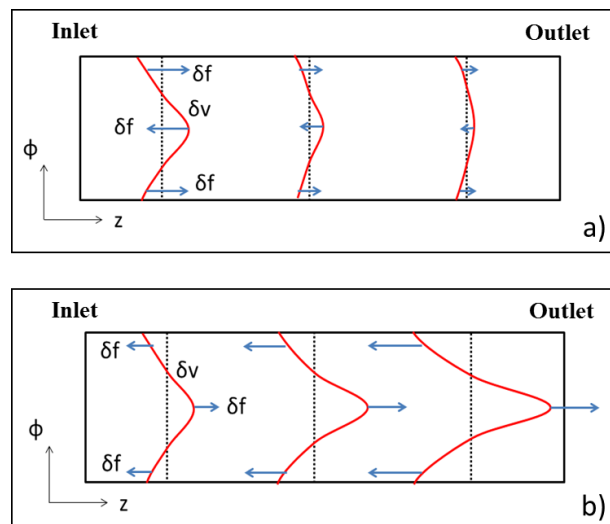


Figure 8: Development of an azimuthal velocity perturbation from inlet to outlet for a) a stable performance regime b) an unstable performance regime [3].

Nevertheless, in the case of a real ALIP the thin channel approximation (17) is questionable, and we should use a cylindrical solution at finite thickness to wavelength ratio. This time, the solution for amplitude of magnetic vector potential in cylindrical coordinates is found in form of Bessel functions of first and second time. In chapter 3, the analysis of the impact of curvature on the performance curve is developed.

### 2.1.6. Efficiency of an EMIP

The model of ALIP considered in previous case is only a simplification of the real device, which is constructed using three-phase alternating power furnished by discrete coils. If we consider real components, this configuration is characterized by winding resistance, magnetic resistance or hysteresis losses, leakage reactance, resistance of liquid metal and hydraulic losses (Figure 9).

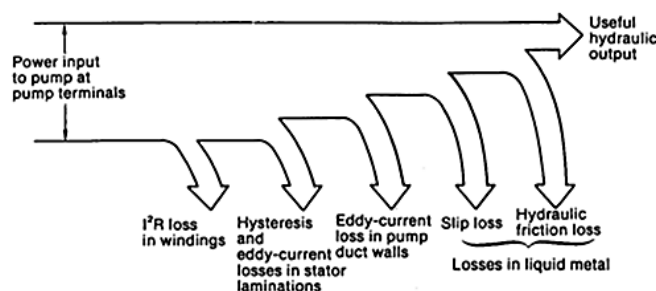


Figure 9: Balance of power in the ALIP [8].

Considering all these losses, the efficiency of the ALIP is determined the same manner as that for a mechanical pump as the ratio of the hydraulic output to the electrical input of the pump:

$$Efficiency = \frac{P_{ALIP}}{P_{input}} \times 100 = \frac{\Delta P_{ALIP} \cdot Q}{\sqrt{3}VI \cos\varphi} \times 100 \quad (32)$$

Where  $\cos\varphi$  is the power factor of the AC circuit.

For the case of PEMDyn, a SIMaP-CEA collaboration report [8] shows the balance of power and efficiency obtained via COMSOL simulation with solid body approximation. For this simulation with 312.5 A of RMS phase current in the 36 inductor slots with 16 windings turns per coil and 20 Hz of supply frequency is considered to evaluate the impact of different working regimes in terms of sodium velocity.

For these conditions losses due to winding resistance ( $P_{coils}$ ) and hysteresis in the magnetic yoke ( $P_{yoke}$ ) are estimated of 12.4 kW and 2.5 kW respectively. For these elements it is defined that:

$$P_{input} = P_{coils} + P_{yoke} + \Sigma P_{joule} + P_{ALIP} \quad (33)$$

$$\Delta P_{ALIP} = \Delta P_{hydraulic} - \Delta P_{loss}$$

Table IV sums up this balance showing for different velocities: in yellow the Joule losses in sodium and duct ( $\Sigma P_{joule}$ ), in blue the ALIP output values in terms of pressure ( $\Delta P_{ALIP}$ ) and hydraulic power ( $P_{ALIP}$ ), in green the input power ( $P_{input}$ ) and in red the efficiency of the ALIP.

The maximum efficiency is 42% and it is obtained at 10 m/s, corresponding to the maximum pressure developed by the pump.

Table IV: Calculation of efficiency for PEMDyn [8]

Velocity (m/s)	$P_{Na}$ (kW)	$P_{duct}$ (kW)	$\Delta P_{ALIP}$ (bars)	$P_{ALIP}$ (kW)	$P_{input}$ (kW)	Efficiency (%)
0	36,3	2,8	0,64	0,0	54,0	0,0
5	32,8	5,1	0,81	16,0	68,7	23,3
10	27,8	19,4	1,17	46,3	108,3	42,7
11	26,6	29,3	1,07	46,9	117,6	39,9
12	27,9	43,2	0,58	27,5	113,5	24,2

In literature we also find different parametric studies evaluating the impact on efficiency in order to obtain an optimal design of EMIP. This is the case of the study of the NRF of Korea [9] [10], where efficiency in ALIPs is calculated using an equivalent circuit method where equivalent resistances and reactances are estimated as function of the pump geometrical and electromagnetic variables using Laithewaite's standard design formula [11]. Thus, efficiency is obtained for different design parameters (pump core length, inner core diameter, inter core gap, number of pole pairs, etc.). An example of these design optimization studies is shown in Figure 10 for the number of pole pairs and the length of the outer core. Furthermore, there exist other studies based on the optimization of the winding distribution [12], which claim to

obtain an improvement in efficiency from 41% for the standard design against 48% for the slot optimized pump.

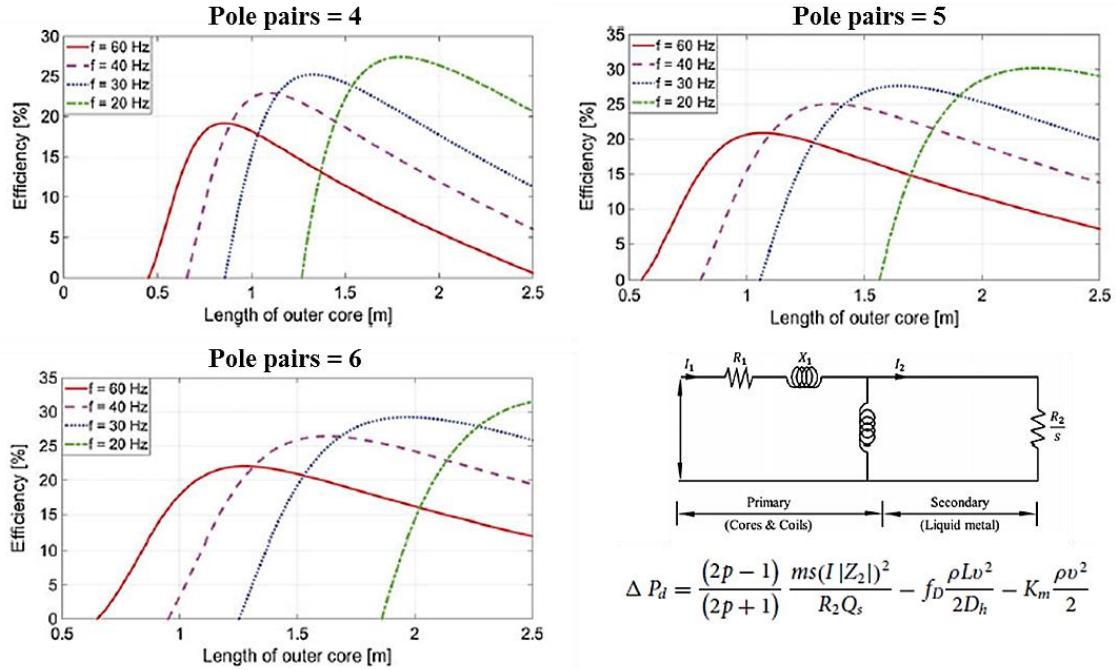


Figure 10: Efficiency curves for the change in the outer core length for different pole pairs and equivalent circuit method used [9]

## 2.2.State-of-art of present physical phenomena in ALIPs

This last simplified model opens the discussion on various research topics that characterize the operation of EMIPs. In this section different phenomena studied in literature are reviewed such as the velocity profile in the channel under travelling field, the impact of end effects in the performance of an ALIP and the bases of pump-circuit coupling. This last opens up the discussion to the study of azimuthal MHD instabilities.

### 2.2.1. Velocity profile under travelling magnetic field

Among basic examples from literature dealing with the analytical solving of a fully-coupled MHD flow we find the case of a of a Hartmann flow [5], which considers an electrical conductor fully developed flow through a rectangular section under the effect of a permanent transversal magnetic field. This flow is notably characterized by a fine boundary layer and a flat piston-like bulk flow.

Several similitudes are found with the physical behavior of an ALIP or a MHD generator [13] [14], since for regimes close to synchronism, the velocity profile is similar to that presented in the Hartmann case.

However, even if both flows share some characteristics, there are also several big differences. On the contrary to the Hartmann flow, where electric currents are confined in the boundary

layer, for the case of an ALIP these thin layers are not active, because the configuration of an annular pump permits the electric currents to close over the azimuth. In addition, the presence of a travelling magnetic field (TMF) is much more complex to be considered.

Authors Ueno et al. [14] had already performed a study to obtain the velocity profile of MHD flows under travelling sinusoidal magnetic field. They found that the interaction parameter  $N$  has a leading role in the velocity profile. Their study shows (*Figure 11*) that flows with enough inertia i.e. low values of  $N$ , would present a flatten profile (case C), while, conversely, flows with high interaction parameter would present a distribution over the channel varying between piston-like profile and a Poiseuille one.

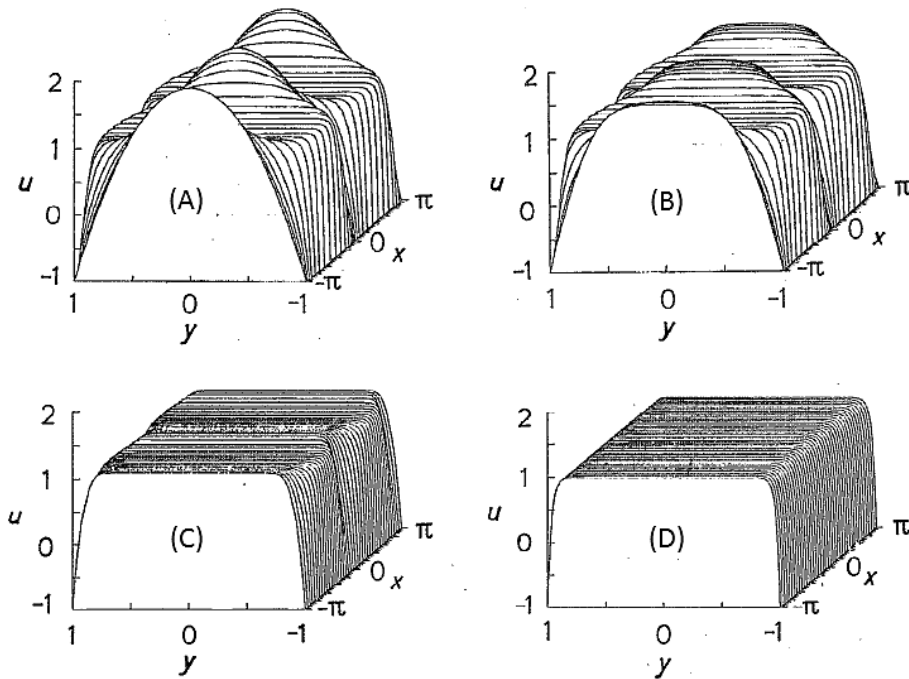


*Figure 11: Velocity profiles in various cross sections for a flow under TMF [14].*  
 (A)  $N = 5.03 \times 10^3$ ,  $Ha = 31.6$  (B)  $N = 1.59 \times 10^2$ ,  $Ha = 31.6$   
 (C)  $N = 1.59$ ,  $Ha = 31.6$  (D)  $N = 1.59 \times 10^{-2}$ ,  $Ha = 31.6$

Having a look at dimensionless numbers in subsection 2.1.3 we can still extract a last conclusion from the last study. Example C is the closest in value to PEMDyn case. Furthermore, it is also important to remark that Hartmann number is one order of magnitude greater in PEMDyn (857.4) than in the example C (31.6), so the flattening effect on the profile would be even more important. We will use this consideration in following developments.

### 2.2.2. End effects

The impact of a finite inductor in the performance of EMPs has been largely studied. Authors have noticed the appearance of an additional pulsative component of the magnetic field and negative influence in performance.

## CHAPTER 2

For the case where the fluid is at rest, [15] has considered a model close to that presented in subsection 2.1.5 but for a finite length configuration of the active part of the EMIP and only transverse component of the magnetic field averaged in the gap for an arbitrary number of poles ( $2p$ ) delimiting the length of the inductor ( $L=2\tau p$ ). As a result, they obtained that for odd numbers of  $2p$  pulsating component of the transverse magnetic field appeared in inlet and outlet sections of the pumping channel, but the wave remained travelling in the inductor zone. On the contrary, for an even number of  $2p$ , the magnetic field in inlet and outlet zones was zero, but in the inductor zone a pulsating component appeared in addition to the progressive wave.

The conclusion to be drawn from this analysis is that for a real EMIP of finite length a pulsative component of the transverse magnetic field appears, which in complex form can be expressed as:

$$B_p^2 = \cos^2(\pi p)(e^{i\omega t})^2 = \cos^2(\pi p)(e^{i2\omega t}) \quad (34)$$

Here, it is exposed as an exclusively electromagnetic effect and the direct cause of the occurrence of pressure pulsations at twice of the supply frequency or Double Supply Frequency (DSF) pulsations. This is rather significant since pressure pulsations in EMIP appear not only because of coupling effects, and thus, this effect has been classically considered as one of the most important to study and suppress. Some detailed and recent works on suppression of DSF pulsations can be found in literature [16].

However, in literature we also find several studies concerning the convection effect of the flow in end effects [17] [18]. Using a Fourier transform in the axial direction, [17] finds three poles interpreted as three kinds of travelling waves along the axial direction, one being the infinite solution, inlet-end-effect wave damping in the direction of the flow and an outlet-end-effect wave damping contrary to the flow. In [18] two different effects were defined: one due to the damped electromagnetic wave propagating to different sides of the boundaries without sharp magnetic field gradients, and the other due to the entry of the flow into the active domain, which supposes a considerable braking effect and important gradient of the magnetic field. It was also suggested that end effects have a non-negligible impact on the force distribution of finite length, and then, negatively affecting on their performance.

Furthermore, in article [19] it is performed a linear stability study of an EMP considering end effects. It concluded that depending on a constant function over the machine length the inlet wave could increase or decrease stability.

In bibliography we also find design proposals for the suppression of this effect, such as linear winding grading [17] [18].

In chapter 3, the impact of finite length effect on the performance curve of an ALIP is treated inspired by the study [17] using Fourier methods.

### 2.2.3. Pump-circuit coupling

From a hydraulic point of view, the stability of the pump-circuit coupling is as well a complex subject of study. Starting with a "bottom-up" approach considered in the internal report [20], for an elementary pump model with solid-body approximation (the flow in stable performance has similar profile to Hartmann flow), the steady-state operation occurs at the point of intersection of the characteristic pressure-flow rate curve of the pump  $P(Q)$ , and the external circuit load curve  $C(Q)$  :

$$P(Q) = C(Q) \quad (35)$$

This operating point is stable in the case where any deviation of the flow from its nominal value generates a pressure difference of opposite sign:

$$\frac{d}{dQ} [P(Q) - C(Q)] < 0 \quad (36)$$

If this condition is not fulfilled there will be possibility of stalling of the EMIP, which means that the stability pump-circuit coupling would depend on the response of the pump to the external load. This phenomenon is analogous to the case of the stalling of an induction motor [21].

From a dynamic systems analysis point of view [22], the mechanism of this type of instability is a saddle-node bifurcation which depends on the slopes of the performance curve of the ALIP  $P(Q)$  and external circuit load  $C(Q)$ . *Figure 12* describes two different scenarios according to the external pressure drop curve. The first case treated shows a quadratic load curve ( $C(Q) = \alpha Q^2$ ) with intersection at point 1 where criterion (36) is fulfilled and thus the system is considered globally stable, while for the second case ( $C(Q) = P_0 + \alpha Q^2$ ) the load curve presents two intersections, points 2 and 3, and the criterion is no longer valid. This last case is said globally unstable.

Even so, being more rigorous we should remark that the pressure drop of a closed hydraulic loop is quadratic with velocity (case 1) while that of a lift circuit between two reservoirs presents a constant (case 2). We can extract as conclusion that it would be rather unlikely to see this kind of instability in an experimental loop such as PEMDyn, or in the secondary loop of a nuclear reactor.

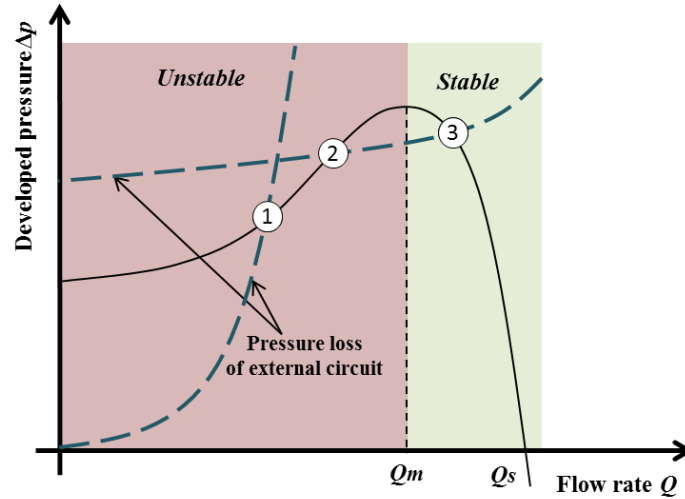


Figure 12 : Coupling a pump to an external circuit for two different characteristic curves [20].

On the other side, this model remains still quite hypothetical, since it does not consider the azimuthal dependence of the velocity profile but a homogenous flow with constant velocity. In the 1960s, Gailitis and Lielausis [23] had proposed a first model dealing with this problem. Their qualitative analysis treats azimuthal velocity distributions along the pumping channel using the analogy with two elementary pumps connected in parallel hydraulically and in series electrically, as it is shown in the diagram of *Figure 13a*. This comes to say that the reduced pressure and discharge of the combined pump verify:

$$\begin{aligned}
 p &= p_1 = p_2 \\
 q &= (q_1 + q_2)/2
 \end{aligned}
 \tag{37}$$

The stability of the distribution of the total flow between the two pumps is evaluated using the following expression:

$$\frac{d}{dq_1} [p_1(q_1) - p_2(q - q_1)] < 0
 \tag{38}$$

When the criterion (38) is not satisfied, each elementary pump will operate on a different branch of its characteristic (*Figure 13b*), where the intermediate point between the two characterizes the operation of the composite pump. Decreasing the discharge from point A in (*Figure 13b*), starting from point D criterion (38) is violated, and the flow rates of each channel become different. Each of the elementary pumps evolves towards B and L, keeping the same pressure, as is the case for the points E and C. In this case, the point F is the one defining the global operation of the composite pump.

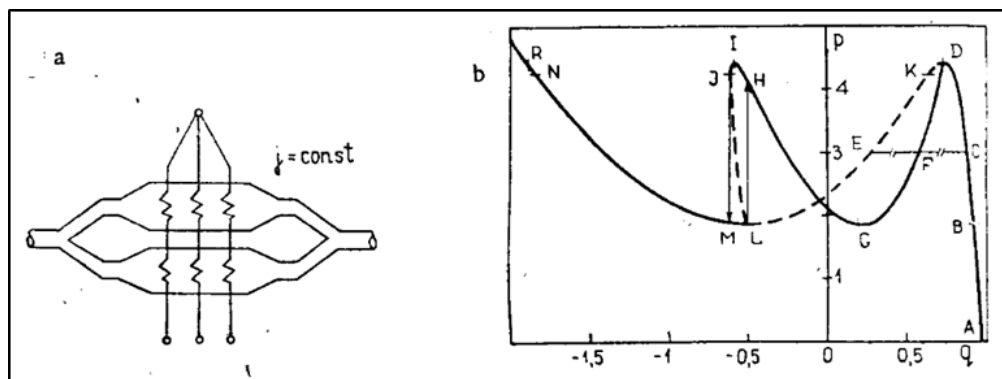


Figure 13 : a) Composed model of two elementary ALIPs connected in parallel to approximate the real velocity distribution b)  $P$ - $Q$  characteristics of single ALIP (ABCDKELMRN) and global result for composed system (ABCDFGHIJL) [23].

However, this approach is still rather simplistic compared to reality, where we have a continuous azimuthal distribution of the velocity that could be linked to a composite pump with infinite number of channels. Furthermore, the electric currents could be deviated from their ideal azimuthal circuit (because of electric potentials developed by the serial connection of different pumps), what could modify the characteristic of each elementary pump. Last but not least, the elementary pump model used in this paper is very simple (Cartesian, thin channel, no end effect) and can hardly be used for real applications.

#### 2.2.4. Studies on stability

In this section we deal with MHD instabilities inherent to the operation of an ALIP, and thus we seek to have a physical vision of the phenomenology related to the coupled system of equations. In particular, one of the questions to be clarified is based on the origin of low-frequency pulsations found experimentally for regimes with  $Rms$  greater than unity [24].

In the works of Linards Goldstein [3] it seems plausible that these pulsations are a direct consequence of the coupling terms of the system. Based on linear algebra, he has developed an analytical study which obtains the different excitation thresholds of unstable modes.

However, the problem of MHD instability is intrinsically non-linear. The previous approach can thus only be understood as an approximation of the real problem, since it is constrained by the exclusive consideration of infinitely small perturbations. Therefore, it seems necessary to evaluate the problem with other complementary methods which may consider the impact of non-linear terms in the equations.

In order to build a model able to integrate all the phenomena related to the loss of stability of the ALIP, we must begin by considering the bases of stability theory and nonlinear dynamics [22]. These physical theories will allow us to deduce, from the principles of the calculus of variations, the threshold values which separate the different regimes of the flow.

The logic used to deal with this problem would be clearer if we proceed from a historical outlook. In the middle of the 17th century, Newton invented differential calculus and discovered the laws of motion and universal gravitation. More specifically, he solved the

## CHAPTER 2

problem of two bodies, that is, the problem of the movement of the earth around the sun. Later generations tried to find the three-body extended solution, but the problem became much more complex. After decades of effort, it was considered impossible to obtain an explicit expression for the three-body movement. It was not until the end of the 19th century that Poincare introduced a new point of view. He decided to focus on obtaining a qualitative result rather than a quantitative one. For example, instead of questioning the exact position of the planets at each moment, the question was rather whether the solar system will always remain stable or evolve in such a way that, planets will escape to infinity. This question summarizes the main concept of modern dynamics and the emergence of a new vision of physical determinism.

In the case of the study of the phenomena occurring during the operation of an EMIP the concept remains the same. It is very complex, to obtain an expression that correctly defines the velocity field and the magnetic field at each instant for different initial conditions (i.e. disturbances at the inlet) and for different operating regimes (i.e. *slip ratio*). On the other hand, if one adopts a qualitative point of view, it is much simpler to evaluate if there is a critical value of a characteristic parameter of the non-linear system (i.e. *Rms*) above which all the solutions of the problem do not tend monotonously to a single solution or *basic flow solution*, or if the energy of any disturbance will be damped or not by the system.

This last paragraph summarizes the two main approaches on which the current analytical study is oriented. The first is focused on the importance of evaluating the system's dependence on initial conditions (chaotic systems). The second approach presents the need for defining different thresholds characterizing stability according to the operating regime and the size of the initial disturbance. This last objective must receive priority over the first approach because of its industrial utility. We should start showing different stability criteria for the evaluation of a dynamic system as proposed in [25].

For our MHD system we can define energy of the system as the sum of the kinetic and magnetic energy, we say that the base solution is stable for any perturbation of initial conditions if:

$$\lim_{t \rightarrow \infty} \varepsilon(t)/\varepsilon(0) \rightarrow 0 \quad (39)$$

Being  $\varepsilon(t)$  the temporal evolution of perturbation's energy.

This definition shows the asymptotic character of stability, for which a dynamic system is considered stable if all initial conditions or disturbances are damped out in time.

If there is a positive value  $\delta$  such that the base solution is stable when  $\varepsilon(0) < \delta$ , then it is said to be conditionally stable. That is, the number  $\delta$  defines a set of initial values that make the solution tend to a zero perturbation ( $\mathbf{u}'=0$  and  $\mathbf{b}'=0$ ), and thus, it constitutes the initial energy deviation radius where the system doesn't move towards an unstable regime. If  $\delta$  tends to infinity, then the solution is unconditionally or globally stable. In the case where  $d\varepsilon(t)/dt \leq 0$  for all times the solution is then monotonically stable.

Then, the stability limit is the region  $F(v_c, \delta) = 0$  of critical values  $(v_c, \delta)$  in the  $(v, \varepsilon(0))$  plane which marks the boundary separating the stable from unstable flows. There we can define two types of stability in Figure 14: (1) Non-conditionally stable and (2) conditionally stable but not unconditionally stable.

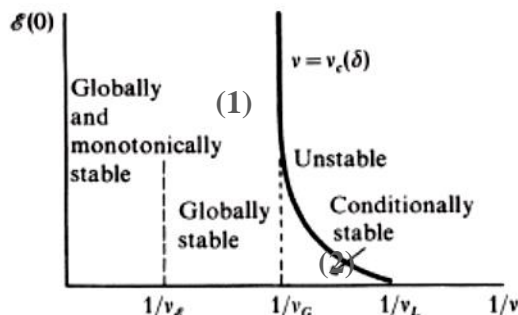


Figure 14 : Theoretical definition of stability thresholds [25].

Thus, unstable regimes can either be a function of the initial disturbance from a certain threshold of a characteristic parameter of the system (2), either be unconditionally unstable from a higher threshold of the same parameter (1).

The values of the characteristic parameter of Figure 14 ( $1/v$ ) are referred to hydrodynamic cases, where the parameter relates to kinematic viscosity, since it characterizes the ability of the system to dissipate energy. The different thresholds in Figure 14 show the structure of the stability theory:

- ❖  $\nu_\varepsilon$  : When  $\nu > \nu_\varepsilon$  the base solution is monotonically and globally stable. If  $\nu < \nu_\varepsilon$  a perturbation may exist for which  $d\varepsilon(t)/dt > 0$  at  $t = 0$ .  $\nu_\varepsilon$  is the energetic stability limit.
- ❖  $\nu_G$ : When  $\nu > \nu_G$  the base solution is globally stable, and if  $\nu \leq \nu_G$  base solution is unstable, but also could be conditionally stable depending on initial disturbance energy.  $\nu_G$  is the global stability limit.
- ❖  $\nu_L$ : When  $\nu > \nu_L$  the base solution is conditionally stable.  $\nu_L$  is the linear stability threshold

In conclusion, we use linear theory to seek the reaction of the system to infinitely small perturbations and estimate the threshold of a parameter defining the system when small disturbances start to grow in amplitude. However, it can say nothing about the threshold of loss of global stability for real size disturbances. It is in this framework that it appears the need for using methods able to analyse the impact of non-linear effects, inherent to the system of equations.

## CHAPTER 2

Unfortunately, it is not so simple to address the resolution of nonlinear differential equations. Compared to earlier approach, a solid and widely developed mathematical tool based on linear algebra, there is not a consolidated method for nonlinear analysis. For this reason, the current study presents the two methodologies found in bibliography to take up the challenge. They are respectively the weakly non-linear and the energetic approach.

In order to become familiar with the formulation of the stability problem, Annex I: Study of stability and available analytical methods presents the bases of the linear method of normal modes, weakly non-linear method and energetic method applied to the MHD system of equations.

The most relevant example of application of linear stability method is carried out in [23], which aims to derive the presence of arbitrary azimuth dependence of disturbances in an ALIP. The main hypotheses of this study are (i) axially infinite pump and perturbation (ii) purely radial magnetic field (valid if  $d_m \ll \lambda$ ), (iii) non-oscillating perturbations (neither in time nor along the axis), (iv) perfectly axial, inertia free and radially uniform fluid flow.

The perturbation modes are expressed in the form:

$$\begin{aligned} u_z(\theta) = U_0 + u'_z \cos(m\theta) \quad ; \quad B_r(\theta) = B_0 + b'_r \cos(m\theta) \\ m = 1, 2, 3 \dots \quad |u'_z| \ll U_0 \quad |b'_r| \ll |B_0| \end{aligned} \quad (40)$$

This study regards marginal stability for each mode  $m$ , since every small amplitude mode perturbation analyzed neither grow nor die out, only its existence is evaluated for different performance regimes ( $Rms$ ). From linearization of the system with boundary conditions the characteristic equation may be expressed as an equality between the pressure developed by the pump and expression (41) for each perturbation mode ( $m= 1, 2, 3 \dots$ ):

$$\tilde{p}_m = \frac{2|\tilde{u}_z|((1 + \kappa_m)^2 + Rms^2)(1 - \tilde{u}_z)}{Rm_s^2 - 1 - \kappa_m} - \tilde{u}_z|\tilde{u}_z| \quad (41)$$

Where  $\kappa_m = \left(\frac{\tau m}{R\pi}\right)^2$  and the pressure is scaled by the friction pressure loss along the channel

The instability threshold of every azimuthal mode is then derived in terms of dimensionless pressure  $\tilde{p}_m$  for a given flow velocity, since expressing directly the velocity where the pump becomes unstable presents some difficulties. We have drawn pressure limits for each mode  $m$  together with the PQ curve for PEMDyn parameters (Tables I-III) in *Figure 15* using equation (41) and (28) respectively. The instability threshold for mode  $m$  can be interpreted as the possibility of the system to develop stationary velocity disequilibrium of the azimuthal mode distribution as soon as the pressure  $\tilde{p}_m$  is reached or exceeded by the ALIP.

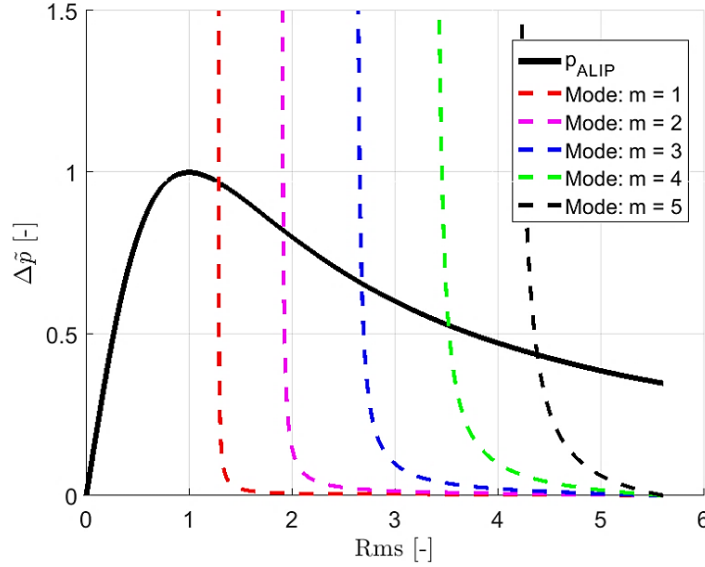


Figure 15: Azimuthal modes excitation thresholds for PEMDyn parameters.

In the case of practical significance, the friction pressure loss may be neglected and the stability criteria can also be expressed in terms of slip Magnetic Reynolds number (42). The result with  $m = 1$  is used as reference criterion for azimuthal instability in ALIPs in many other works [6] [24] [26], since it can be considered as the most unstable mode.

$$R_{ms} \geq \sqrt{1 + \kappa_m} = \sqrt{1 + \left(\frac{\tau m}{R\pi}\right)^2} \quad (42)$$

However, this analysis still remains quite crude, since strong hypothesis are considered. Among other suggestions, the conclusions of [23] highlight the importance of considering longitudinal end effects, which may appreciably delay the onset of instability. This effect is evaluated in latter sections.

Another example found in literature is Linards Goldsteins' convective instability analysis [3], in which the evolution of axial and azimuthal ( $m-k$ ) modes along the pump is regarded in the case the perturbation may grow exponentially while it propagates downstream. This means that, considering disturbances as a *white noise*, a convective unstable system behaves like a noise amplifier. The excitation frequencies obtained seem to be related to what it is referenced in literature as *Low Frequency (LF) pulsations*. These fluctuations of electrical parameters and pressure have been observed in large sodium ALIPs for relatively high values of  $Rms$  [27].

Nevertheless, when several  $m-k$  modes are excited, the spectrum obtained becomes quite complex because of the interferences between them. Conversely, a situation where we consider a reduced number of  $m$  modes remains feasible to build and provide a spectrum that is simpler to interpret.

## CHAPTER 2

The linear method of normal modes gives a first estimate of the modes that can make the pump unstable according to the working regime. However, the rather restrictive assumption of the infinitesimal sizes of the disturbances leaves open the question of the impact of a finite disturbance to the stable operation of the pump.

In bibliography we also find examples of non-linear energetic method applied to magnetohydrodynamic problems in order to consider the impact of non-linear effects. This is the case of the study on the stability of the Hartmann layer [28]. In this work both linear and energetic approaches are considered and compared for the case of an electrically conducting flow under a steady magnetic field at high Hartmann number.

On the one hand, it is suggested that it is the instability of the Hartmann layer that control the MHD flow, rather than the global flow that controls the transition. This is based on the fact that experiments [29] have shown that laminarization is controlled by the ratio Reynolds to Hartmann ( $Re/Ha$ ) number rather than the Reynolds alone.

On the other hand, it also highlights that it is fundamental to study the instability of finite perturbations, rather than infinitesimal, since the critical  $Re/Ha$  number using energetic stability analysis is approximately 26 (Figure 16) for a Hartmann layer with a magnetic field normal o the wall, and then, much closer to the experimental one ( $\sim 300$ ) than the linear method result, with approximate value of 48250.

However, even if the energetic threshold is closer to the experimental one, there is still an order of magnitude of difference. There, it is insisted that the energetic method provides a lower bound, due to the fact of the general character of the method to consider all possible perturbations.

Another relevant study found in literature is that of Carmi and L alas [30]. This time the analysis is applied to a more general Hydromagnetic case without steady consideration for the magnetic field. Nevertheless, the most important conclusion to extract from this analysis is about the form of posing the problem, due to the conservative character of the study since rather crude estimates are considered.

Anyway, this method must be seen as a complement to the linear theory of stability in the sense that, the linear theory may show that a given flow is unstable to some perturbations but not that the flow is stable to all, whereas the energy method may show that a flow is stable to

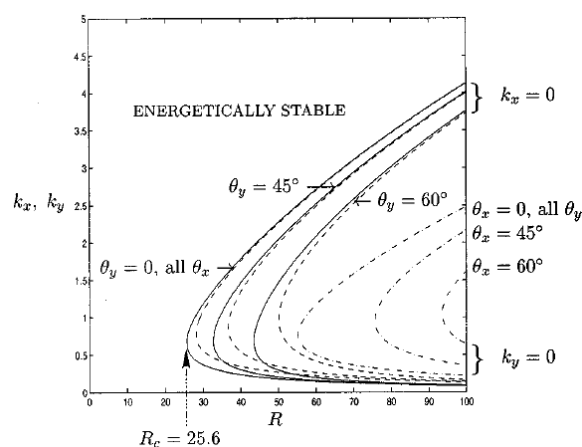


Figure 16: Marginal curves for energetic stability of the Hartmann layer [28]

## CHAPTER 2

all perturbations but not that the flow is unstable to some. It is also important to highlight that, since in energetic method the most general form must be chosen for validity of the approach, it does not give any information about disturbance itself, and neither can it say anything about its growth rate. In following developments, both approaches are considered and compared.

### 2.3. Numerical studies on MHD instability

In classical MHD research the only possibility to tackle with the problem of instability was by theoretical or basic experimental approach. However, during 1960s the development of modern numerical methods made emerge a powerful tool for physical analysis, and even if sometimes it was seen as a less accurate approach than analytical, numerical simulation became an essential step in the understanding of MHD phenomena. This allowed carrying out physical models without being forced to take many hypotheses to avoid complicated formulation of problems. Anyway, it would be too optimistic to believe that numerical approach is more valid than theoretical, since other problems are dealt with, and that is where the matter lies; every methodology must be treated as a complement to the other.

Doing some researches about numerical methods available, we find out that several CFD models more adapted to the coupled MHD case than conventional ones have been developed. For example, in [31] and [32] it is proposed a new Reynolds stress closure for modeling MHD turbulence. The scope of the work is to enable more accurate description of Joule dissipation and to capture the length-scale anisotropies and tendencies towards two-dimensionality characteristic of MHD turbulence [33] for conductive flows under permanent magnetic field and at low magnetic Reynolds numbers.

We also find in literature an alternative approach [34] which adapts a two equations model ( $k$ - $\varepsilon$  or  $k$ - $\omega$ ) when non-equilibrium effects are significant. In contrast to previous approaches, which formulate the closure adding a supplementary transport equation that modifies the eddy viscosity, this new closure implies that the nonequilibrium effects enter through the resulting history-dependent effective strain rate tensor.

However, for the current study case, friction forces can be considered negligible in a stable stationary operation of an EMIP compared to the gradient of pressure, which equilibrates the electromagnetic force [17]. It is thus possible to use a standard two equations model ( $k$ - $\omega$  SST) for the CFD simulation in numerical models, even if it gives a poor estimation of MHD turbulence, because of the weak role of turbulent stresses present in an EMIP compared to other terms.

About the development of models, we found in bibliography that for MHD analysis in ALIPs, most of developments are done using 2D models, because even if 3D simulation is more appropriate, usually it is more time consuming. This approach is possible thanks to symmetries of the problem and permits to analyze different phenomena separately. In this field two possibilities are found, the radial and the azimuthal symmetry approximations.

In the first instance, axisymmetry is considered. This is the case for studies [35] and [36], carried out by the CNRS using HERACLES code, originally developed for compressible flows in astrophysics. Therefore, simulations were carried out using an isothermal equation of state with small Mach number. The model was considered in fully-transient travelling magnetic field (TMF) formulation with sinusoidal surface current applied at the outer boundary.

## CHAPTER 2

The first of these articles [35] analyze the radial distribution of different variables (velocity, force, magnetic field, etc.) of an infinite ALIP for laminar cases with low Hartmann number (two orders of magnitude smaller than the case of an EMIP). Here, the transition of stable to stalled flows is regarded as an instability triggered by magnetic flux expulsions when operating far from synchronism and thus, at high slip. This phenomenon is illustrated in the two following figures:

- ❖ *Figure 17* shows the pump lying on a stable fixed point stabilized by the magnetic tension, where the balance of Lorentz forces and pressure gradient is ensured.
- ❖ *Figure 18* shows that when the velocity difference between the flow and the wave leads to a stronger shear of the magnetic field lines, the magnetic field is expelled away from the bulk flow where the magnetic tension cannot counteract the pressure gradient anymore. This leads to a saddle-node bifurcation of the flow.

Therefore, we can say that the skin depth for the penetration of the radial component of magnetic field is controlled by the slip between the velocity of the fluid and the wave speed.

However, the described conditions are not expected in ALIPs, and distribution in velocity boundary layer in *Figure 17*, presenting transition between Poiseuille and Hartmann profiles, remains quite hypothetical, as it was exposed at the end of section 2.1.3.

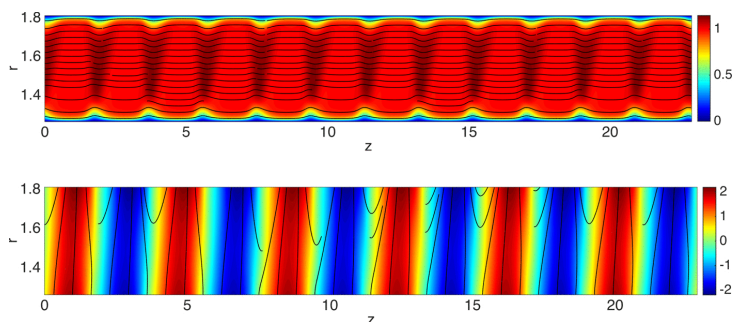


*Figure 17: Structure of the axial velocity (top) and the radial magnetic field (bottom) for  $Rm = 30$ ,  $Ha = 100$ , and  $Re = 100$ , close to synchronism [35].*

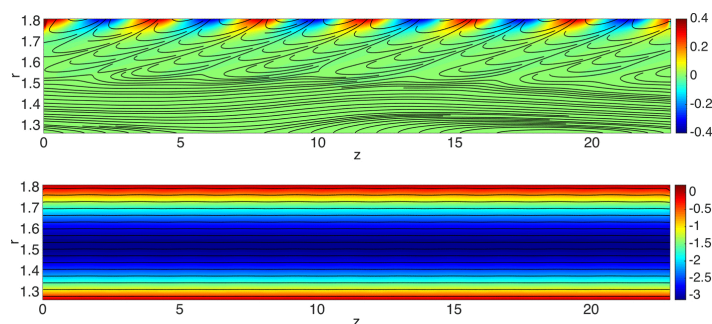


*Figure 18: Structure of the axial velocity (top) and the radial magnetic field (bottom) for  $Rm = 120$ ,  $Ha = 100$ , and  $Re = 100$ , after the transition [35].*

The second part of the study [36] treats the effect of a finite-length inductor on the onset of axisymmetric instability. This time the numerical analysis is extended for dimensionless numbers values closer to those of the performance of an ALIP and the presence of inlet and outlet boundary conditions is introduced.

The main conclusions of the article are sum up in *Figure 19*. This shows that the end-effects (at  $z = H/4$  and  $z = 3H/4$ ) have a non-negligible impact on the radial velocity distribution of the flow, and then on the appearance of unstable regimes. From this reasoning, we could also expect to obtain different performances between an ideal infinite ALIP and a finite inductor configuration. This problem will be discussed in the next chapters.

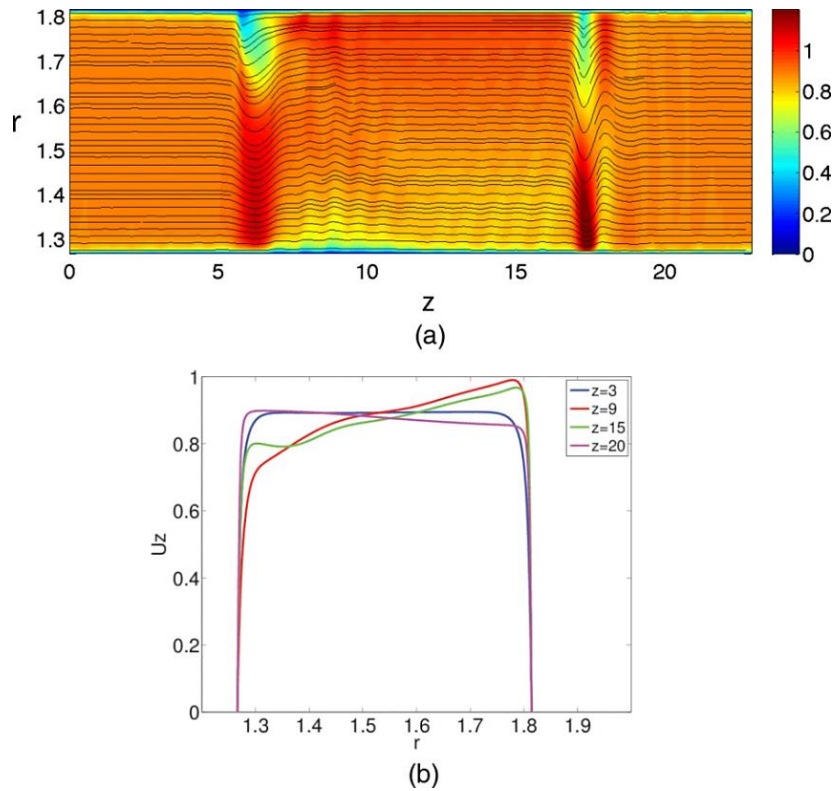


*Figure 19: (a) Colorplot of the time averaged axial velocity field for  $Rm = 60$ ,  $Ha = 1200$ , and  $Re = 5000$ . (b) Velocity profiles in the radial direction for different  $z$ . [37].*

In a second family of papers, the 2D numerical simulations capable of describing MHD instability [23] are those considering the plane  $\theta$ - $z$ . This is the case of the model developed by Araseki et al. [24] [38] in which physical quantities are averaged over the height of the channel to simplify investigation of azimuthal perturbations, and therefore only one component of the magnetic field is taken into account. Mesh with  $36 \times 200$  cells was used in transient calculation with time step  $10^{-4}$  s. This model is shown in *Figure 20*.

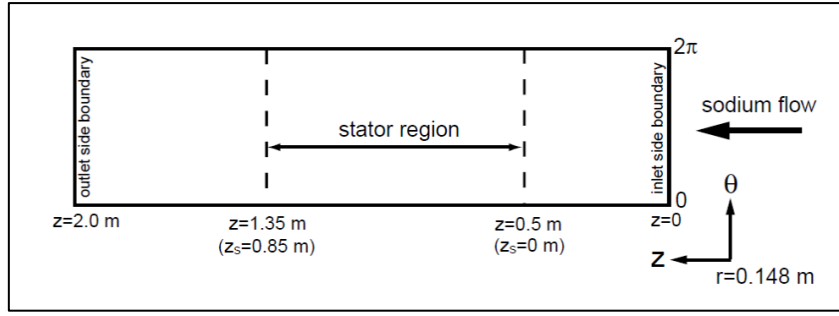


Figure 20: 2D model of an ALIP in  $z$ - $\theta$  plane for azimuthal MHD instability analysis [24].

The applied magnetic field in the stator is represented by equation (43), where input parameters  $\beta$ ,  $\gamma$  and  $\phi$  may describe the azimuthal non-uniformity of field and amplitude  $B_{a0}$  is obtained via analytical two-dimensional analysis in  $r$ - $z$  plane and averaging over the channel.

$$B_{ar} = B_{a0}(1 + \beta \cdot \sin(\gamma\theta + \phi)) \cdot \sin(\omega t - \alpha z) \quad (43)$$

Figure 21 exposes several cases of magnetic field distribution for different asymmetries of the ALIP structures, as a sum of modes  $\gamma$  (1-3). However, this might be seen as a simplification of the problematic, since the real non-uniform pattern of a pump may not be as simple as exposed. Following developments focus on the study of mode 1 with applied magnetic field non-uniformity of 10% ( $\beta = 0.1$ ,  $\gamma = 1.0$ ,  $\phi = \pi/2$ ).

Qualitatively, the flow starts to be inhomogeneous when  $Rms > 1$ , and velocity distribution becomes more complex presenting higher vorticity with  $Rms$  near the stator end (Figure 22).

Furthermore, simulations confirm that the increase of vorticity leads to the trigger of LF pulsations and decrease of the peak at the double of the supply frequency (DSF pulsations), as it can be seen in pressure spectrums of Figure 23.

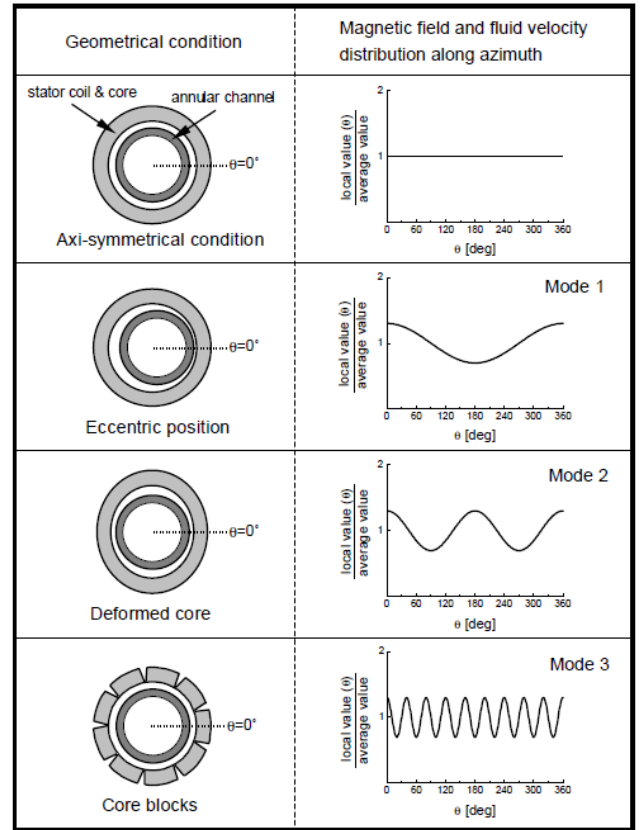


Figure 21: Several modes of magnetic field perturbations over the azimuth [24]

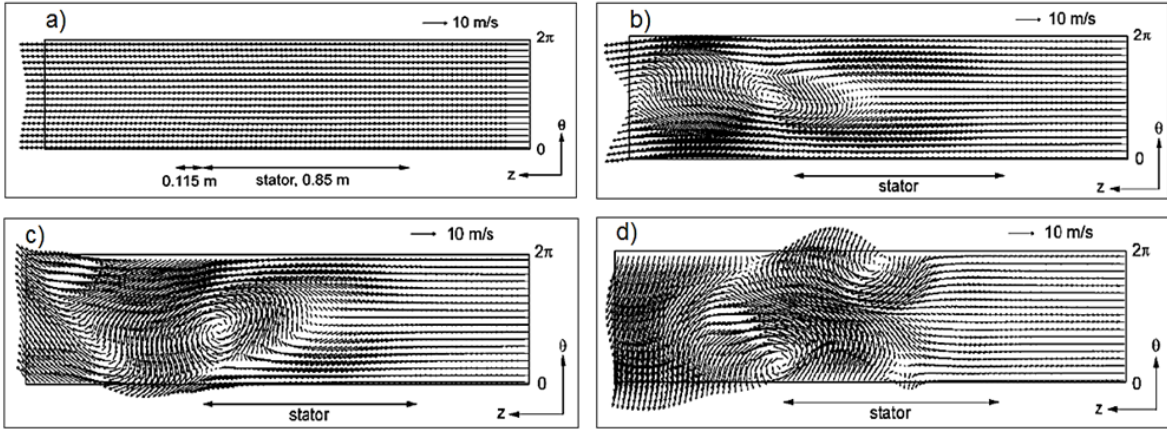


Figure 22: Sodium flowing from right to left in anon-uniform  $B_a$ , Mode 1,  $\pm 10\%$  at  
 a)  $Rms= 0.75$  b)  $Rms= 1.56$  c)  $Rms= 1.89$  d)  $Rms= 2.31$  [24]

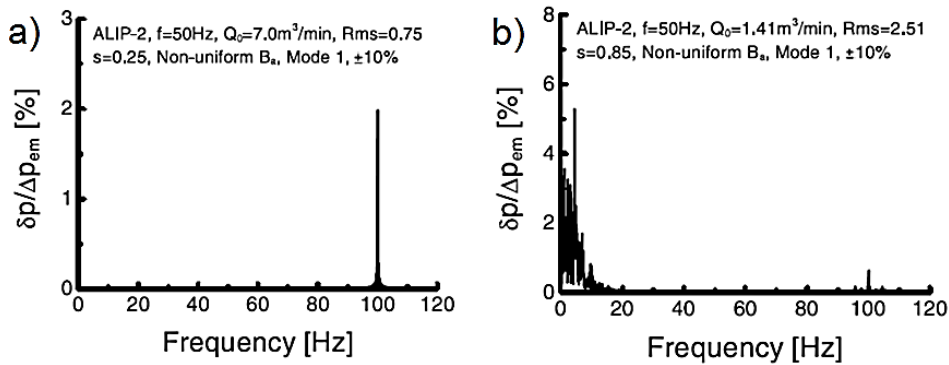


Figure 23: Pressure pulsation spectrum for a) An stable case at  $Rms= 0.75$  b) An unstable case at  $Rms= 2.51$  [24]

Nevertheless, the 2D approach is an uncomplete vision of the global problem and in the best of cases we should sought for the fully-coupled 3D solution. Unfortunately, simulations with complex geometry in TMF formulation are time-costing and generally aren't robust enough, so it isn't easy to deal with the posing of the 3D model. One of the available options to improve is to change the formulation of the problem. As it was exposed previously, we can choose between two magnetic formulations depending on convenience, either in terms of magnetic field (TMF formulation), either in terms of electric and vector potential ( $A-\phi$  formulation). This last is the case of 3D simulations carried out by Asada et al. [39] for Toshiba Corporation applications, which is in fact the only one found in literature facing the challenge.

There, they have developed a code for electromagnetism using edge-based finite element method which is coupled with another fluid dynamic simulation part, this time driven by the commercial software *Star-CD*, a code using the finite volume method for CFD simulations. The turbulence model chosen is a classical two-equation  $k-\epsilon$  model, without special consideration for MHD turbulence.

Simulations were carried out with a simplified 3D geometry and parameters were considered those of experiment [6] by Ota et al. for different coil currents and sodium flow rates with a supply frequency of 20.4 Hz. Furthermore, in order to test numerically the conclusions extracted from [23], one of simulations was carried out with an azimuthal non-uniform velocity distribution at inlet in the form of mode 1 with amplitude of 30%.

It is shown in *Figure 24* the comparison between two simulations at the same working regime ( $Rms=1.75$ ), one presenting averaged velocity (No.1), and another one with azimuthal distribution described above (No.7). The flow is highly excited with low frequencies for the last case compared to the simulation with homogenous velocity (*Figure 24.*).

The text suggests that these random fluctuations in simulation No.7 might be caused by vortices in liquid sodium flow. This is confirmed in contours of *Figure 25*, presenting axial velocity distribution at different times of simulation No.7, where reverse flow appears at the outlet at 0.4 s, and then changes its shape over time.

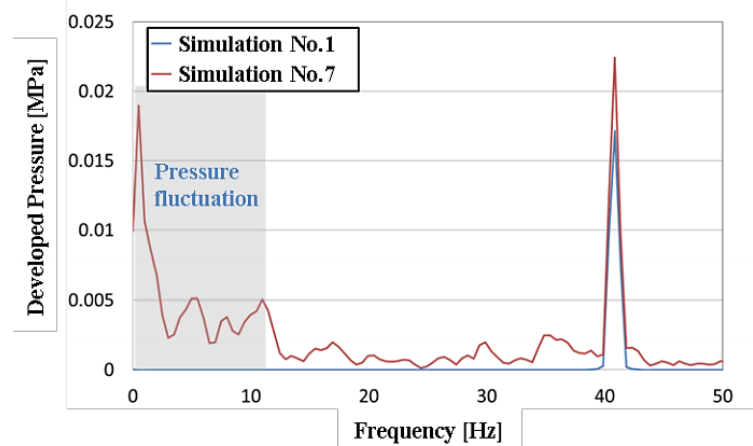


*Figure 24: Pressure spectrum for homogenous inlet condition (blue) and azimuthal velocity distribution (red) simulations [39].*

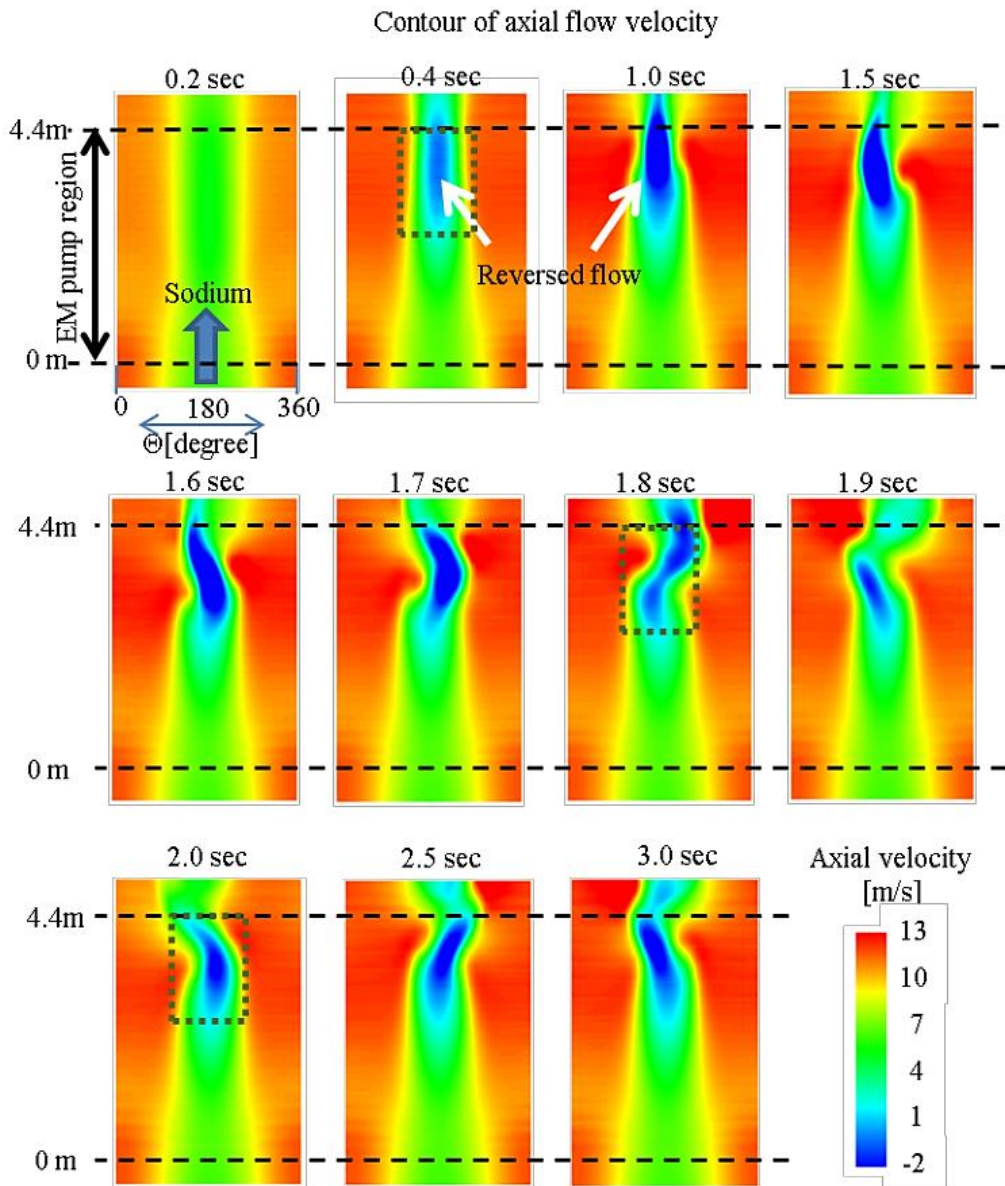


Figure 25: Contours of axial velocity at different instants for inhomogenous simulation [39].

## 2.4. Experimental studies on MHD instability

In this part some of outstanding experimental studies are evaluated. All of them have in common that they aim to provide data about the performance of EMIPs and to quantify instability phenomena. Authors observe respectively measurements of flow rate, static pressure and magnetic flux for performance account, and measurements of local velocity, dynamic pressure and magnetic field over the azimuth for instability characterization.

One of the most valuable examples of performance validation of ALIPs is referred in Japanese study by OTA et al. [6], where the purpose of experimental measurements is to validate P-Q curves obtained numerically with EAGLE code for different electric supplies. Here, a large sodium immersed self-cooled ALIP was used with a magnetic Reynolds number at synchronism of 6.42, a maximum flow rate of  $160 \text{ m}^3/\text{min}$  and a developed pressure of 2.8 bars (*Figure 26*).

At the beginning of this work, the external magnetic flux was measured over the azimuth and found nearly uniform (maximum deviation  $\sim 5\%$ ).

The developed pressure and flow rate have been measured for different openings of the control valve and supply frequencies with fixed ratio  $V/f$ . The performance curves are shown in *Figure 27A* in terms of  $R_{ms}$ . There, we notice that the highest head point was placed in the band of  $R_{ms}$  values between 1.4 and 1.5. It is also marked that during the experiment fluctuations of pressure and flow rate appeared when the  $R_{ms}$  value was higher than this value.

The highest efficiency is 46% in *Figure 27B* for a supply frequency of 16 Hz and at a  $R_{ms}$  value of 1.4, close to pressure maximum. In the figure it can also be appreciated that the pump efficiency decreases rapidly since it entered into the area of  $R_{ms} > 1.5$ .

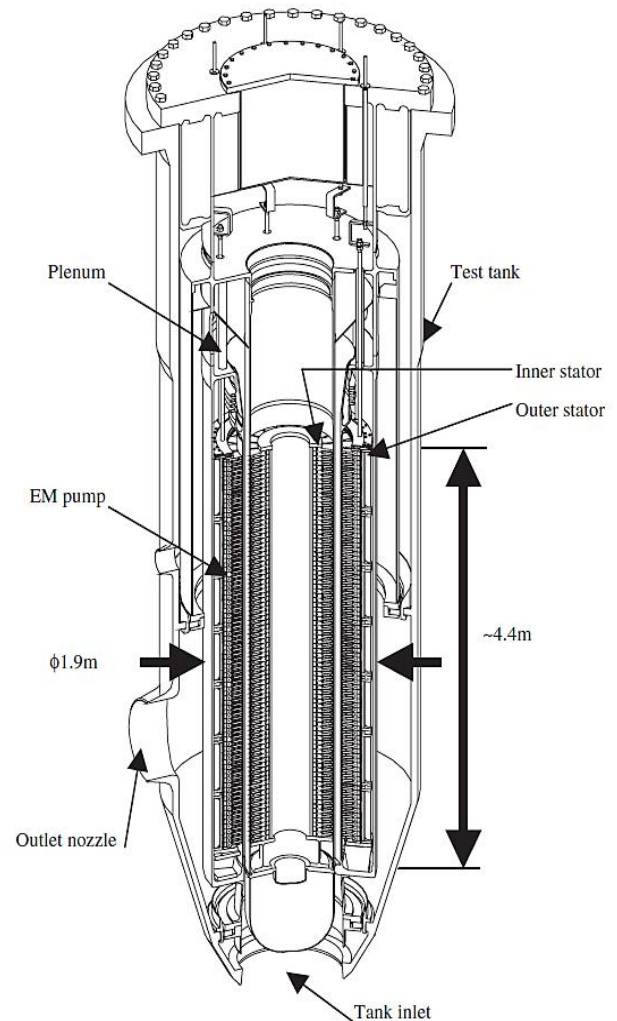


*Figure 26: Bird-view of immersed ALIP [6]*

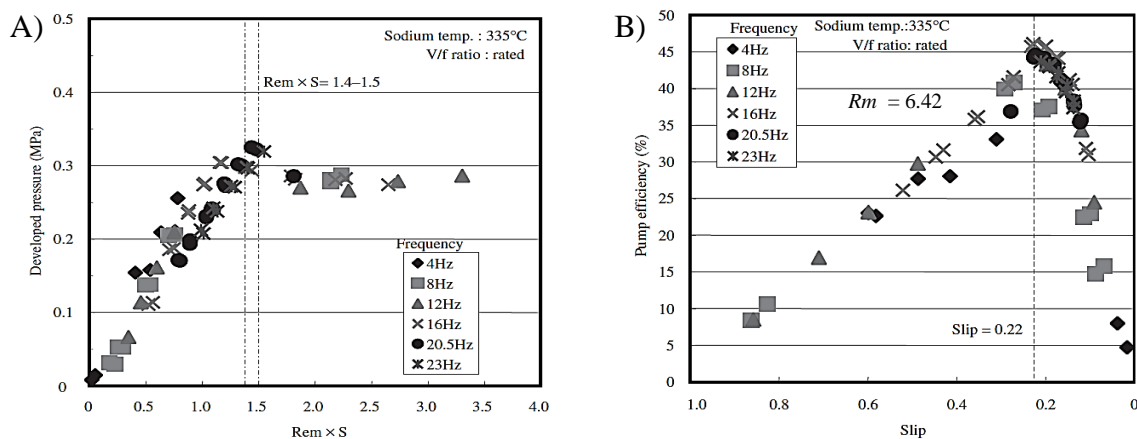


Figure 27: Experimental results for A) performances curves in terms of  $Rms$  B) Pump efficiency in terms of slip [6]

Using this information, they divide the performance of ALIPs into stable, transition and unstable zones of PQ curve, as it shows Figure 28. Authors conclude that each of these three areas has following behaviour:

- ❖ **Area I:** It represents the nominal operation of the EMIP, without significant fluctuation of measurements, and homogenous flow. It is considered as the stable operating regime.
- ❖ **Area II:** This zone constitutes the transition of flow. Close to the peak on the left-hand side of PQ curve, pressure and magnetic field start to oscillate considerably, and flow loses homogeneity. Furthermore, the article remarks that in this area the pump current, the flow rate and the head could not be controlled. This transition is represented in Figure 29.
- ❖ **Area III:** The left-hand side of the curve, with  $Rms$  higher than 1.4-1.5, is mainly characterized by the drastic loss of head and efficiency. Fluctuations of flow rate and pressure were important. It is considered as the unstable operating regime.

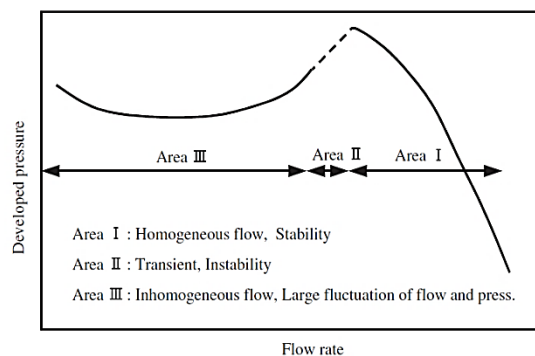


Figure 28: Classification of zones of PQ characteristic [6]

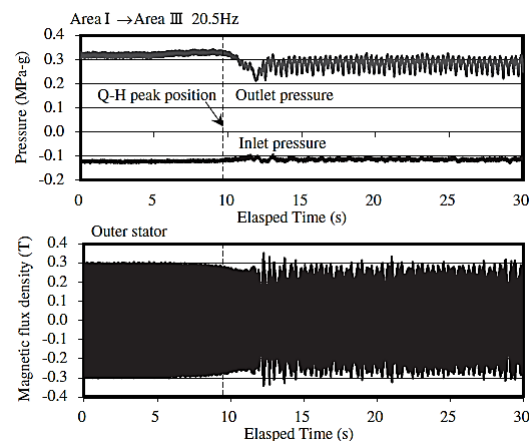
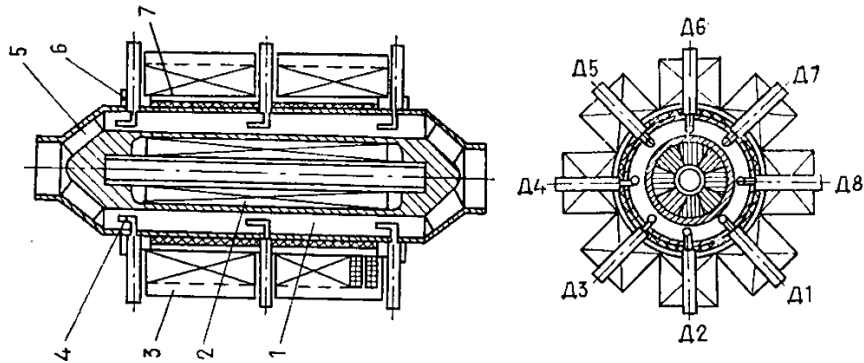


Figure 29: Trend of magnetic flux and pressure between Area I and Area III [6]

Other examples in literature have sought to characterize quantitatively what happens when passing from the right-hand side of the PQ curve peak to the left-hand side, or in other words, which are the phenomena involved during the transition to unstable operating of an ALIP. This is the case of article by Kirillov and Ostapenko [26], where local characteristics of ALIP are evaluated for different regimes. Their experiment consisted of magnetic field measurement using 8 radial inductive coils over azimuth in 7 cross sections and local axial velocity measurements using Pitot tubes in 8 different azimuths and 3 cross sections. *Figure 30* shows the sketch of inductive coils and Pitot tubes distribution in the ALIP.



*Figure 30: Sketch of experimental ALIP disposition of inductive coils and Pitot tubes in the channel [26].*

Results for velocity and magnetic field distribution over the length of the channel showed that amplification increases with the increment of slip (*Figure 31*). Nevertheless, when slip reaches a higher value ( $s = 0.67$ ) some sort of saturation effect happens. Amplification is lower than in the precedent case ( $s = 0.62$ ).

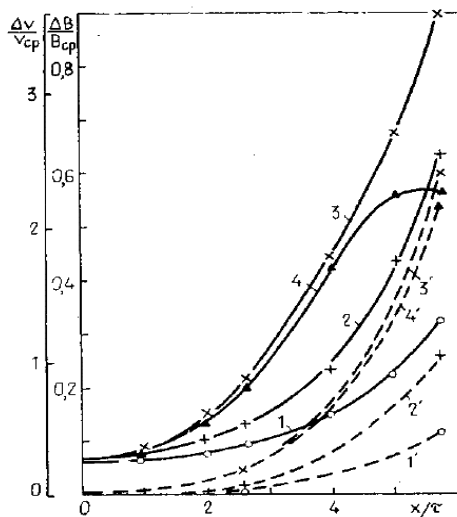


*Figure 31: Velocity (dotted lines) and magnetic field (continuous lines) perturbations over length of the pump [26].  $U = 150V$  and 6 poles. 1,1' -  $s = 0.32$ ; 2,2' -  $s = 0.48$ ; 3,3' -  $s = 0.62$ ; 4,4' -  $s = 0.67$ .*

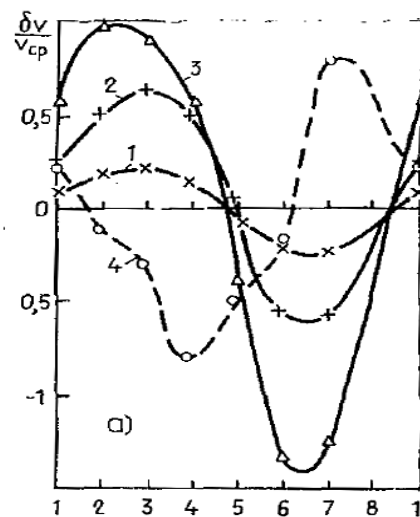


*Figure 32: Velocity perturbation over azimuth.  $U = 150V$ , 6 poles,  $13 \leq N_\lambda \leq 21$  [26] 1 -  $s = 0.32$ ; 2 -  $s = 0.48$ ; 3 -  $s = 0.62$ ; 4, -  $s = 0.72$ .*

It can be also noted that the saturation has also an effect on azimuthal distribution. *Figure 32* puts in evidence that velocity perturbations are similar to simple harmonic shape of mode 1, which is amplified with the increase of slip, and then demonstrating theory [23]. But, when  $s = 0.72$  amplitude is lower and the shape of perturbation becomes more complex than the rest of measurements. Again, a sort of saturation effect appears for a certain critical slip. Authors justify this effect in *Figure 33* as function of interaction parameter  $N$  for different ALIP configurations.

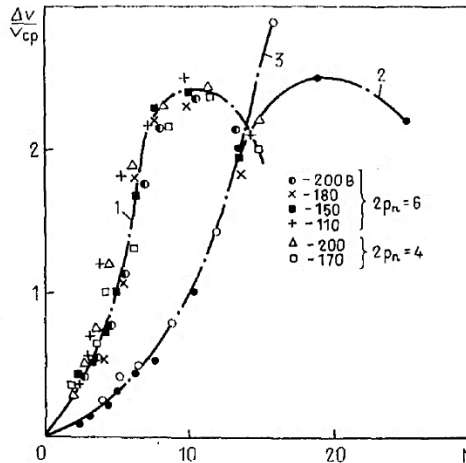


*Figure 33: Velocity perturbation as function of interaction parameter  $N$  ; 1- symmetric air gap 2- asymmetric air gap 3-with lateral side bars [26]*

Another critical issue in the research on MHD instabilities concerns the relation of Low Frequency (LF) and Double Supply Frequency (DSF) pulsations in ALIPs. This question has been largely studied by authors in [16] [40] [24] [38], where conclusions were extracted from the same experimental facility ALIP-2, mainly using measurements of vibrations and time evolution of magnetic field and dynamic pressure.

In these researches authors observed characteristic phenomena from both sides of the PQ curve with respect to pressure maximum. They agreed that regimes where  $Rms < 1$  DSF pulsation dominates, whereas with the increase of  $Rms$  this effect tends to disappear and LF start to acquire more importance (*Figure 34*).

*Figure 35* and *Figure 36* serve as example of pressure pulsations and its spectrums for both cases with  $Rms < 1$  and  $Rms > 1$  respectively. Here, DSF peak is strong in the first case, while in the second one it decreases in the detriment of a broad band of LF pulsations.

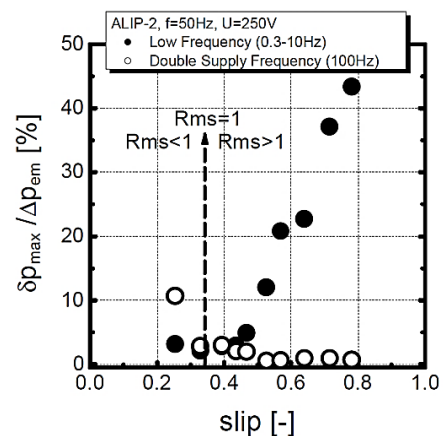


*Figure 34: Distribution of amplitude of pressure pulsations as a function of  $Rms$  ; in white - DSP pulsations ; in black - LF pulsations [24]*

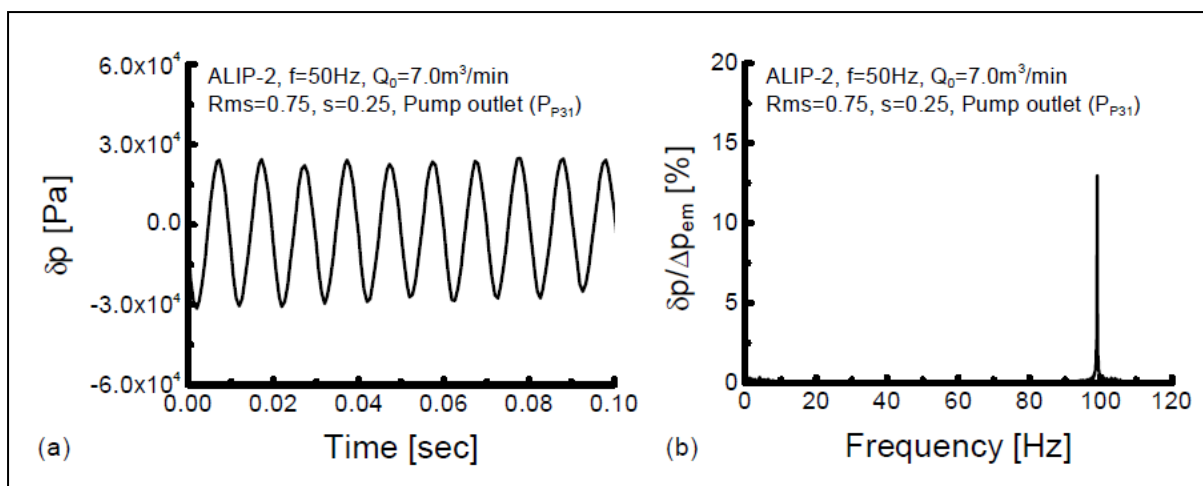


Figure 35: Pressure pulsations and its spectrum at  $Rms = 0.75$  [24]

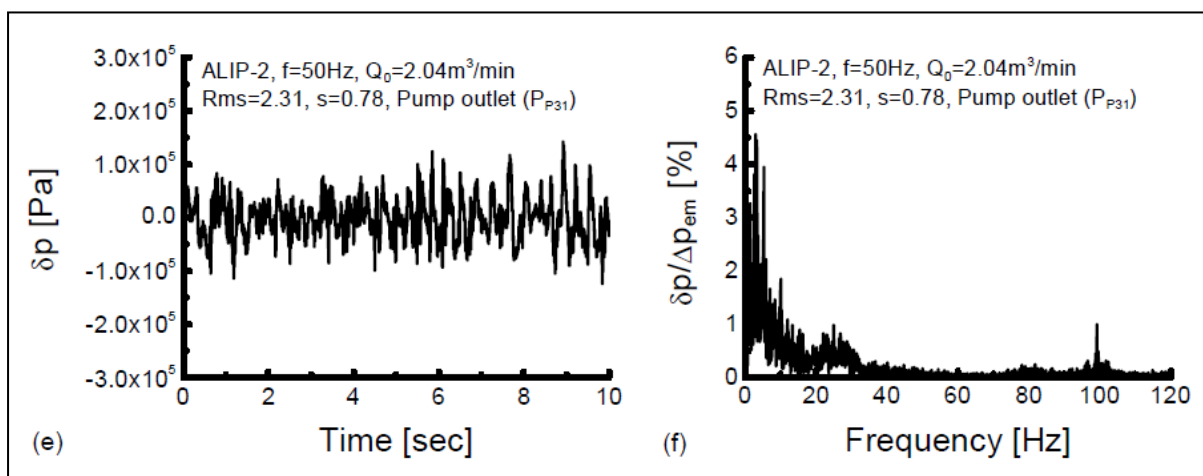


Figure 36: Pressure pulsations and its spectrum at  $Rms = 2.31$  [24]

From these results, authors suggest different ideas to suppress DSF and LF pulsations respectively [40]. Even if the stabilization methods in ALIPs are out of the scope of the current work, here principal alternatives are presented for both cases.

A suitable effect has been found with linear grading of magnetic field for the case of DSF pulsations. This method implies the improvement of end effects, since DSF pulsations are purely electromagnetic effect, directly linked to the finite length of the ALIP.

For the case of LF pulsations the problematic is different, and then options too. Since 1980s authors have explored the idea of changing the connections of coils in the inductor by applying a phase shift. The aim of this change of configuration is to alter the distribution of magnetic force to reduce instability. In [38] Araseki et al. have tested the idea, which has provided a satisfactory stabilization effect observed in pressure spectrums for ALIPs with phase shift of  $+60^\circ$ .

### 3. ANALYTICAL DEVELOPMENTS

The current theoretical study might be seen in two different parts. First, it focuses on the phenomenological study of three main concepts already explored in bibliography. They are:

1. The impact of a discontinuous multiphase inductor in the calculation of the void magnetic field without electric conductive flow.
2. The solving of the base flow solution for the coupled stationary MHD system and the description of the velocity profile.
3. The study of end effects and their influence on performance.

All of these points aim to put the accent into the importance of modelling some effects and the possibility of neglecting others because of its low impact in general behaviour of an ALIP, giving hints for numerical and experimental studies presented in latter chapters.

The second part will consist of a number of explored analytical methods in order to characterize the stability thresholds for different kinds of situations, which are indeed supported by the bibliographic researches presented in previous chapter.

#### 3.1. Theoretical investigations in ALIP phenomenology

##### 3.1.1. Void magnetic field in the case of an ALIP

In previous researches, Linards Goldsteins [3] had already estimated analytically the magnetic field in the void channel for the case of a flat linear induction pump (FLIP) and justified that the calculation was also valid for the case of ALIPs fulfilling the dimension relation (17), i.e. thin channel consideration. In fact, the result in cylindrical coordinates involves a development in Bessel functions with a complicated formulation of their coefficients, where numerical methods are needed for some steps of the calculation. However, the Cartesian assumption remains quite hypothetical, and validity of the formulation might be questioned for the case of an ALIP.

Here, we pose the cylindrical problem for one-phase inductor with axisymmetric, infinite and periodic configuration in the axial direction, where superposition of phases will be applied later. The duct is confined between two perfect magnetic yokes ( $\mu_r = \infty$ ), where the field is produced by coils with alternatively  $+I$  and  $-I$  with axial periodicity of  $2\tau$  (*Figure 37A*). The coils are placed on the top of the channel at  $r = R_2$ , and are supposed infinitely thin, with a perfect magnetic material out of them representing the magnetic yoke of a real inductor. The inner core is also modelled by a perfect magnetic material at  $r = R_1$ .

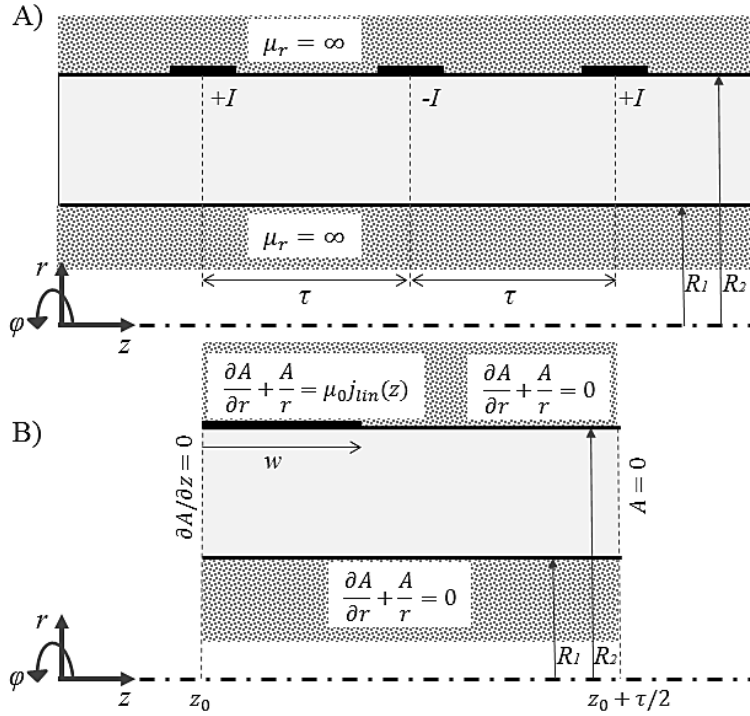


Figure 37 : A) Geometry of one-phase inductor B) Zoom on boundary conditions

The magnetic problem in the non-conducting gap is posed using the induction equation for the vector potential  $A$ . Due to axisymmetry, it corresponds to a Laplace equation in cylindrical coordinates for the azimuthal component  $A$  of the vector potential:

$$\frac{\partial^2 A}{\partial r^2} + \frac{1}{r} \frac{\partial A}{\partial r} + \frac{\partial^2 A}{\partial z^2} - \frac{A}{r^2} = 0 \quad (44)$$

The magnetic field is then given by:

$$B_z = \frac{\partial A}{\partial r} + \frac{A}{r} \quad \text{and} \quad B_r = -\frac{\partial A}{\partial z} \quad (45)$$

For our periodic problem, that also has symmetries, we can reduce the domain to half the distance between two consecutive (and opposite) coils, as shown in *Figure 37B*. The boundary conditions are also shown, and consist of two symmetry or antisymmetry conditions on the axial direction at  $z=z_0$  and  $z=z_0+\tau/2$  respectively, and two others on the radial direction representing the magnetic jump at the interface between two materials.

Using the Heaviside function  $H_0$  for the definition of linear current distribution  $j_{lim}$ , and the half width  $w$  of each coil, the problem to be solved is thus:

$$\frac{\partial^2 A}{\partial r^2} + \frac{1}{r} \frac{\partial A}{\partial r} + \frac{\partial^2 A}{\partial z^2} - \frac{A}{r^2} = 0 \quad \text{for } z_0 < z < z_0 + \frac{\tau}{2} \quad \text{and } R_1 < r < R_2 \quad (46)$$

$$\frac{\partial A}{\partial r} + \frac{A}{r} = \mu_0 j_{lin} = \mu_0 \frac{I_e}{2w} H_0(z_0 + w - z) \text{ at } r = R_2 \quad ; \quad \frac{\partial A}{\partial r} + \frac{A}{r} = 0 \text{ at } r = R_1 \quad (47)$$

$$A = 0 \text{ at } z = z_0 + \frac{\tau}{2} \quad ; \quad \frac{\partial A}{\partial z} = 0 \text{ at } z = z_0 \quad (48)$$

Equation (46) accepts the separation of variables in the form  $A = f_z(z) \cdot f_r(r)$ , which gives an equation where left-hand side depends only on  $r$  and the right-hand side only of  $z$ , and then both are equal to a constant  $c$ . This implies that solution for  $f_z(z)$  is in the form of sine and cosine if  $c > 0$  ; whereas  $c < 0$  would lead to a  $z$  dependence in the form of  $ch$  and  $sh$  that can only be null to fulfil the boundary conditions at  $z=0$  and  $z=z_0+\tau/2$ . Therefore we choose  $c = \alpha^2$ , and by applying boundary conditions we find that any linear combination of the Fourier modes in the form  $f_{zk} = \cos(\alpha_k(z - z_0))$  is acceptable for  $f_z$ . In fact, the superposition of elementary solutions of the linear potential equation implies that we can choose separate functions  $f_r$  for each mode, so that we'll look for a general solution under the following form, where  $f_{rk}$  are function of  $r$  only:

$$A(r, z) = \sum_{k=1}^{\infty} f_{rk} \cos(\alpha_k(z - z_0)), \text{ with } \alpha_k = (2k - 1)\pi/\tau \quad (49)$$

The functions  $f_{rk}$  have to verify the following equation and boundary conditions:

$$r^2 \frac{d^2 f_{rk}}{dr^2} + r \frac{df_{rk}}{dr} - (1 + \alpha_k^2 r^2) f_{rk} = 0 \text{ for } R_1 < r < R_2 \quad (50)$$

$$\left\{ \begin{array}{l} \sum_{k=1}^{\infty} \left( \frac{\partial f_{rk}}{\partial r} + \frac{f_{rk}}{r} \right) \cos(\alpha_k(z - z_0)) = 0 \text{ at } r = R_1 \\ \sum_{k=1}^{\infty} \left( \frac{\partial f_{rk}}{\partial r} + \frac{f_{rk}}{r} \right) \cos(\alpha_k(z - z_0)) = \mu_0 j_{lin} \text{ at } r = R_2 \end{array} \right. \quad (51)$$

The differential equation (50) is close to the modified Bessel equation. Using the new dependent variable  $x = \alpha_k r$ , we obtain that the general solution of equation is in the form:

$$f_{rk} = a_k I_1(x) + b_k K_1(x) \text{ with } x = \alpha_k r \quad (52)$$

Where coefficients  $a_k$  and  $b_k$  are fixed by boundary conditions (51), what is only possible if we write  $j_{lin}$  as a Fourier series:

$$j_{lin} = \frac{I_e}{2w} H_0(z_0 + w - z) = \sum_{k=1}^{\infty} C_k \cos(\alpha_k(z - z_0)) \quad (53)$$

## CHAPTER 3

In fact, supply current is AC, so  $I_e$  is a time dependent function:

$$I_e = \sqrt{2} n_w I_{rms0} \cos(\omega t + \phi_0) \quad (54)$$

With root mean square (RMS) amplitude  $I_{rms0}$ , pulsation  $\omega$ ,  $\phi_0$  its phase lag and  $n_w$  the number of windings.

Then, for the case of a multiphase infinite inductor, we can express solution as the superposition of one-coil solution centred at  $z = z_n$  formulated with phasors:

$$\bar{A}(r, z) = \sum_{k=1}^{k_{max}} \left\{ [A_k I_1(\alpha_k r) + B_k K_1(\alpha_k r)] \sum_{n=0}^{N-1} \bar{I}_e \cos(\alpha_k (z - z_n)) \right\} \quad (55)$$

Where  $k_{max}$  is the order of Fourier series used to represent each periodic coil, and  $N$  is the number of periodic coils.

For PEMDyn case, there are 6 periodic coils distributed over the 36 slots of the inductor, so if the three phases are equilibrated (same RMS current  $I_p$ ), we obtain:

$$\frac{\bar{A}(r, z)}{2\sqrt{2} n_w I_p} = \sum_{k=1}^{k_{max}} \left\{ [A_k I_1(\alpha_k r) + B_k K_1(\alpha_k r)] \cos\left(\frac{\alpha_k \tau}{12}\right) \sum_{m=0}^2 e^{-im\frac{\pi}{3}} \cos(\alpha_k (z - Z_m)) \right\} \quad (56)$$

With  $Z_m = \frac{m\tau}{3} + \frac{\tau}{12}$ , where  $m$  designates each one of the three equilibrated phases.

The results of equation (56) have been evaluated for parameters close to those of PEMDyn pump, where all data used for calculation is presented in *Table V* and *Table VI*. Then, magnetic field can be calculated using  $A$  and its derivatives along  $r$  and  $z$ . Using expressions (45), we have represented in *Figure 38* the RMS value of field for both radial and axial components in the magnetic gap, and in *Figure 39* the fields components in the middle of the gap at different moments in each period and RMS amplitude. One of main conclusions extracted from these results is that we can evaluate the order of magnitude of each component at given conditions. It can be appreciated that the maximum value of radial component at the middle of the gap (about 0.4 T) is larger than that of axial component (about 0.1 T) for the present void calculation.

Table V. Parameters for PEMDyn magnetic field solving

$R_1$	Internal radius of channel	0.10955 [m]
$R_2$	External radius of channel	0.15738 [m]
$2\tau$	Pole length	0.66 [m]
$L_{induct}$	Length of inductor	1.98 [m]
$w_{slot}$	Width of the slot	0.01492 [m]
$n_w$	Number of windings	36
$I_{rms0}$	Total current per slot	300 [A]

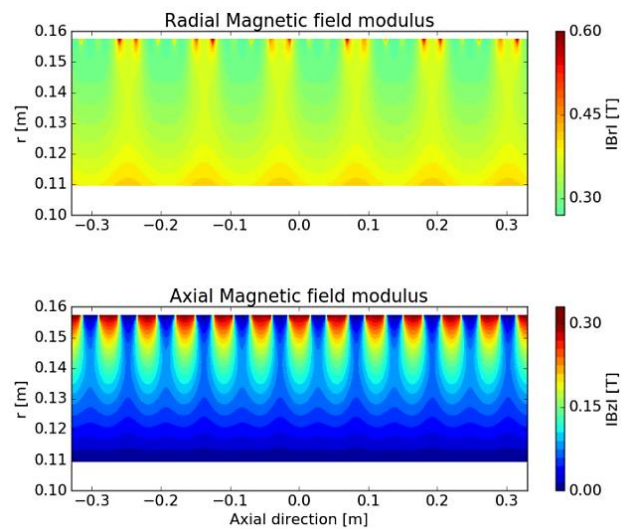


Figure 38 : Contours of radial and axial magnetic field modulus over the channel

Table VI. Parameters for spatial discretization and Fourier series

$n_z$	Number of points along a half wavelength	500
$n_r$	Number of points across the air gap	20
$k_{max}$	Order of Fourier series	100

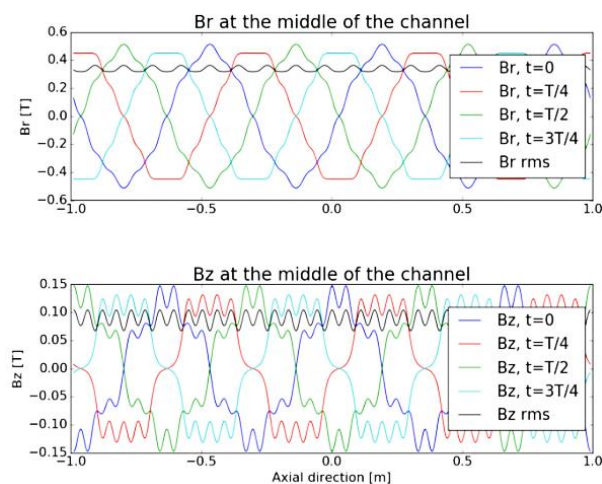


Figure 39 : Plots of radial and axial magnetic field at the middle of the channel

### 3.1.2. Basic flow solution

The solving of the flow under alternative magnetic field is a recurrently subjected to study in bibliography, as it is the case of the analysis by Turcotte et al. [41], who proposed to solve the periodic boundary layer problem using expansion techniques. Here, our contribution to the topic puts the accent on the bulk flow solution depending on the working regime and evaluates the impact of different hypothesis on obtained solution to propose a compromise

for the suitable description of governing physical phenomena of the non-perturbed fully developed stationary MHD flow.

In an ALIP, the magnetic field produced by a large number of discrete coils over the azimuth can be modelled using an equivalent thin sheet of current infinitely long on the  $z$  direction (Figure 40). The linear current density ( $j_{lin} = j_{peak} \cos(kz - \omega t)$ ) is applied on the  $\varphi$  direction, where  $k = 2\pi\tau$  is the axial wave number and  $\omega = U_B \cdot k$  the pulsation, with  $\tau$  the wavelength imposed by the coil connections and  $U_B$  the velocity of the traveling magnetic field. The geometry is also simplified using a perfect ferromagnetic boundary condition at the bottom, without magnetic permeability jump in our equations in order to consider the guiding and confining effects of the magnetic yoke. The full magnetic gap is filled by the conducting fluid (conductivity  $\sigma_{Na}$ ), so the effect of the metallic tubes present in the real pump is neglected in this case; as well as the effect of the air layers between the tubes and the magnetic yokes. Furthermore, the velocity of the base flow is supposed purely axial and its value  $U_0(r)$  would depend only on radius.

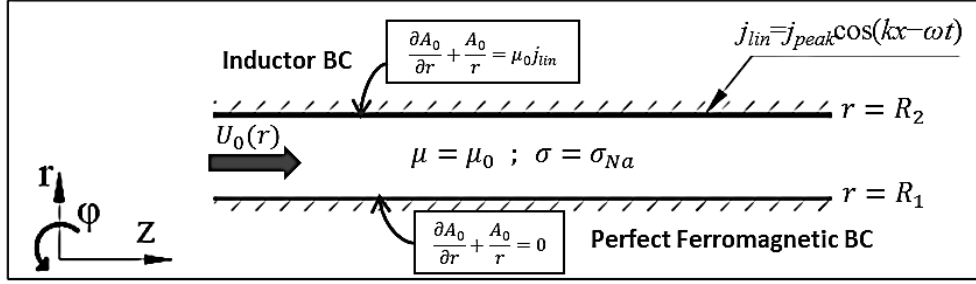


Figure 40 : Schema of an ALIP

### 3.1.2.1. Basic flow solution with solid body approximation

The MHD system of equations governing an ALIP is composed by coupled Navier-Stokes (NS) equation and induction equation written here in terms of vector potential. This last equation reads:

$$\Delta \mathbf{A} = \mu_0 \sigma \left[ \frac{\partial \mathbf{A}}{\partial t} - \mathbf{u} \times (\nabla \times \mathbf{A}) \right] \quad (57)$$

Where  $\mathbf{B} = \nabla \times \mathbf{A}$  and  $\nabla \cdot \mathbf{A} = 0$ .

Then, simplified induction equation for base solution of complex amplitude of vector potential  $\hat{A}_0$  with solid body approximation for  $U_0$  (axial velocity independent of  $r$ ) can be written:

$$\frac{d^2 \hat{A}_0}{dr^2} + \frac{1}{r} \frac{d\hat{A}_0}{dr} - \frac{\hat{A}_0}{r^2} = k^2 (1 - iRms) \hat{A}_0 \quad \text{for } R_1 < r < R_2 \quad (58)$$

## CHAPTER 3

The global slip magnetic Reynolds number is defined by  $Rms = \mu_0 \sigma (U_B - U_0)/k$ , where  $U_B$  is the magnetic field velocity and  $U_0$  is the base flow axial velocity.

Putting it into dimensional form together with boundary conditions:

$$\frac{d^2 \tilde{A}_0}{d(\lambda \tilde{r})^2} + \frac{1}{(\lambda \tilde{r})} \frac{d\tilde{A}_0}{d(\lambda \tilde{r})} - \left( \frac{1}{(\lambda \tilde{r})^2} + 1 \right) \tilde{A}_0 = 0 \quad \text{for } \tilde{R}_1 < \tilde{r} < \tilde{R}_2 \quad (59)$$

$$\begin{cases} \frac{d\tilde{A}_0}{d\tilde{r}} + \frac{\tilde{A}_0}{\tilde{r}} = 0 & \text{at } \tilde{r} = \tilde{R}_1 \\ \frac{d\tilde{A}_0}{d\tilde{r}} + \frac{\tilde{A}_0}{\tilde{r}} = 1 & \text{at } \tilde{r} = \tilde{R}_2 \end{cases} \quad (60)$$

Where  $\lambda^2 = 1 + iRms$  and non-dimensional form is built using  $\tilde{r} = r/L$  and  $\tilde{A}_0 = A_0/(B_{ref}L)$  with  $L = 1/k$  and  $B_{ref} = \frac{\mu_0 J_{peak}}{k(R_2 - R_1)} = \frac{\mu_0 J_{peak}}{kd_m}$

Solution will be in the form of modified Bessel functions:

$$\tilde{A}_0(\tilde{r}) = a_0 I_1(\lambda \tilde{r}) + b_0 K_1(\lambda \tilde{r}) \quad (61)$$

Here coefficients  $a_0$  and  $b_0$  are:

$$a_0 = \frac{K_0(\lambda \tilde{R}_1)}{\lambda [K_0(\lambda \tilde{R}_1) I_0(\lambda \tilde{R}_2) - K_0(\lambda \tilde{R}_2) I_0(\lambda \tilde{R}_1)]} \quad (62)$$

$$b_0 = \frac{1}{\lambda \left[ K_0(\lambda \tilde{R}_1) I_0\left(\frac{\tilde{R}_2}{\tilde{R}_1}\right) - K_0(\lambda \tilde{R}_2) \right]} \quad (63)$$

Using parameters adapted to PEMDYN pump (shown in *Table I*) dimensional results are plotted for a range of different slip velocities.

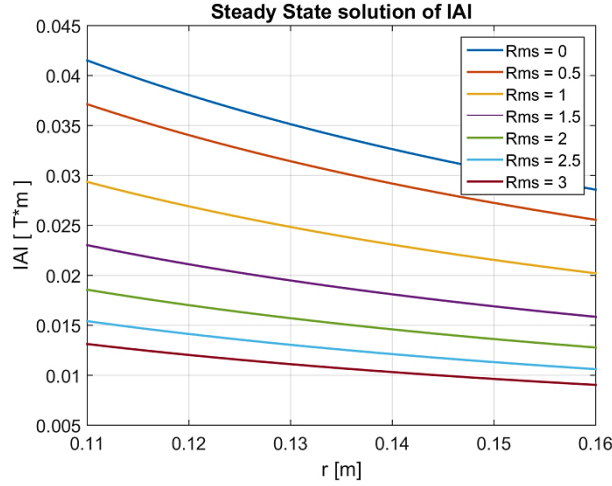


Figure 41 : Vector potential modulus over radius

Furthermore, radial and axial components of magnetic field can be obtained from expression (131):

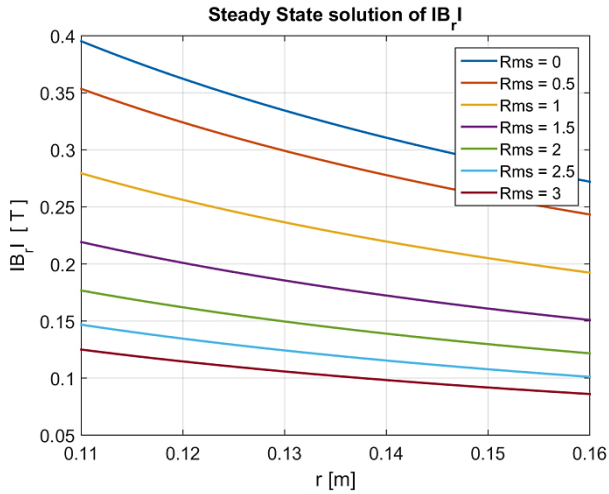


Figure 42 : Radial magnetic field module over radius

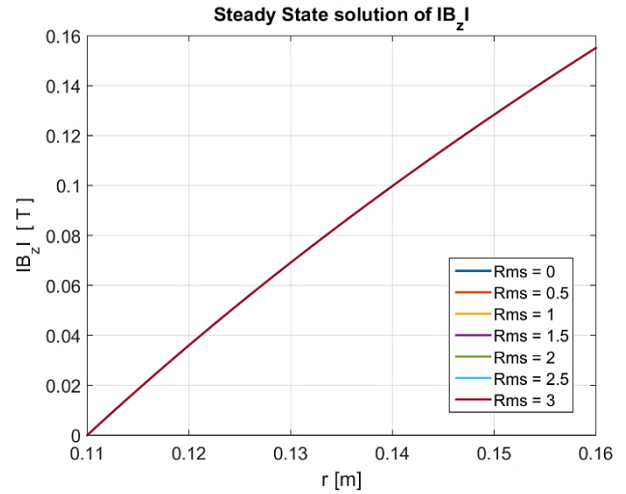


Figure 43 : Axial magnetic field module over radius

Now, it is interesting to analyse the problem using coherent approximations for the case being. In precedent *Figure 42* and *Figure 43* we can notice that radial component is greater than axial one for small enough values of *Rms*. In cases with thin magnetic gap compared to the mean radius, the curvature terms can be neglected and calculation of axial magnetic field component will be only necessary for the estimation of azimuthal currents, responsible for the pumping axial force. So, the steady problem in magnetic field formulation for the radial component becomes in non-dimensional form:

$$\frac{d^2 \tilde{B}_{r0}}{dr^2} = (1 - iRms) \tilde{B}_{r0} \quad \text{for } \tilde{R}_1 < \tilde{r} < \tilde{R}_2 \quad (64)$$

## CHAPTER 3

With perfect ferromagnetic and source of current boundary conditions at the bottom and top of the channel respectively:

$$\frac{\partial \tilde{B}_{r0}}{\partial \tilde{r}} = \begin{cases} 0 & \text{at } \tilde{r} = \tilde{R}_1 \\ -i & \text{at } \tilde{r} = \tilde{R}_2 \end{cases} \quad (65)$$

So, general solution is found in the form:

$$\tilde{B}_{r0}(\tilde{r}) = a \cdot \cosh\left(c \cdot (\tilde{r} - \tilde{R}_1)\right) + b \cdot \sinh\left(c \cdot (\tilde{r} - \tilde{R}_2)\right) \quad (66)$$

With  $c^2 = (1 - iRms)$

Regarding boundary conditions we find  $b = 0$  and solution for  $\tilde{B}_{r0}$  becomes:

$$\tilde{B}_{r0}(\tilde{r}) = -i \frac{\cosh\left(c \cdot (\tilde{r} - \tilde{R}_1)\right)}{c \cdot \sinh\left(c \cdot (\tilde{R}_2 - \tilde{R}_1)\right)} \quad (67)$$

Then, we can approximate  $\tilde{B}_{r0}$  with a Taylor expansion in  $\sinh$  and  $\cosh$  for small values of  $\tilde{R}_2 - \tilde{R}_1$ . This condition translates into a thin magnetic gap compared to the wavelength where we can suppose that variation along the width of the channel is negligible:

$$\tilde{B}_{r0} \cong \frac{-i}{1 - iRm_B(1 - \tilde{U}_0)} = \frac{1}{Rms + i} \quad (68)$$

Following the same procedure for  $\tilde{B}_{z0}(\tilde{r})$  we can estimate it using boundary conditions:

$$\frac{\partial \tilde{B}_{z0}}{\partial \tilde{r}} = \begin{cases} (\tilde{R}_2 - \tilde{R}_1) & \text{at } \tilde{r} = \tilde{R}_1 \\ 0 & \text{at } \tilde{r} = \tilde{R}_2 \end{cases} \quad (69)$$

And with thin magnetic gap assumption it yields:

$$\tilde{B}_{z0} \cong (\tilde{r} - \tilde{R}_1) \quad (70)$$

This last expression (70) has linear behaviour with radius and no dependency on the working regime ( $Rms$ ), similarly to the analytical solution shown in *Figure 43*. We can also note that in the case of extremely thin magnetic gap  $\tilde{B}_{z0} \ll \tilde{B}_{r0}$ .

With both components we can estimate currents for the basic steady state:

$$\tilde{\mathbf{j}}_0 = \mu_0 \nabla \times \tilde{\mathbf{B}}_0 = \begin{cases} 0 \\ \left(i\tilde{B}_{r0} - \frac{\partial \tilde{B}_{z0}}{\partial \tilde{r}}\right) e^{i(z-\tilde{t})} \\ 0 \end{cases} \quad (71)$$

Using approximations above azimuthal component can be expressed as:

$$\tilde{j}_{\varphi 0} = i\tilde{B}_{r0} - 1 = -\frac{Rms}{i+Rms} \quad (72)$$

These estimations for  $\tilde{B}_{r0}$ ,  $\tilde{B}_{z0}$  and  $\tilde{j}_{\varphi 0}$  will be useful for the consideration of basic solution in latter stability analyses.

### 3.1.2.2. Basic flow solution with radial dependency of profile

Some assumptions in last developments could result too conservative for a good estimation of basic flow solution, such as the solid body approximation for the velocity field. In order to obtain a better description of the MHD flow, and so on obtain a closer estimate of instability threshold we should consider the dependency on radius for velocity.

However, the system becomes non-linear and thus not easy to solve, so several hypotheses have to be considered. In this section, the theoretical approach based on [42] is explained.

Induction equation in terms of vector potential in our axisymmetric problem writes:

$$\frac{\partial^2 \mathbf{A}}{\partial r^2} + \frac{1}{r} \frac{\partial \mathbf{A}}{\partial r} + \frac{\partial^2 \mathbf{A}}{\partial z^2} - \frac{\mathbf{A}}{r^2} = \mu_0 \sigma \left( \frac{\partial \mathbf{A}}{\partial t} + U_0(r) \frac{\partial \mathbf{A}}{\partial z} \right) \quad (73)$$

The magnetic field  $\mathbf{B} = \nabla \times \mathbf{A}$  is then given by:

$$B_z = \frac{\partial A_\varphi}{\partial r} + \frac{A_\varphi}{r} \quad \text{and} \quad B_r = -\frac{\partial A_\varphi}{\partial z} \quad (74)$$

And with boundary conditions:

$$\begin{cases} \frac{\partial A_\varphi}{\partial r} + \frac{A_\varphi}{r} = 0 & \text{at } r = R_1 \\ \frac{\partial A_\varphi}{\partial r} + \frac{A_\varphi}{r} = \mu_0 j_{lin} & \text{at } r = R_2 \end{cases} \quad (75)$$

For this infinite ideal EMIP, all the electromagnetic variables will be travelling waves. Introducing the Reynolds magnetic number  $Rm_B = \mu_0 \sigma U_B / k$ , and the axial velocity profile  $U_0(r)$  which varies over the channel radius, equations (73) and (74) in terms of complex amplitudes become:

$$\frac{d^2 A_0}{dr^2} + \frac{1}{r} \frac{dA_0}{dr} - \frac{A_0}{r^2} = k^2 (1 - iRm[1 - u(r)]) A_0 \quad (76)$$

$$B_{z0} = \frac{dA_0}{dr} + \frac{A_0}{r} \quad \text{and} \quad B_{r0} = -ikA_0 \quad (77)$$

## CHAPTER 3

Where  $u(r) = U_0(r)/U_B$  and  $Rm_B(1-u)$  is the global slip magnetic Reynolds number if  $u$  is uniform. Once induction equation is condensed, we look at Navier-Stokes equation:

$$\rho \frac{\partial \mathbf{u}}{\partial t} + \rho(\mathbf{u} \cdot \nabla) \cdot \mathbf{u} = -\nabla p + \rho\nu \nabla^2 \mathbf{u} + \mathbf{j} \times \mathbf{B} \quad (78)$$

The electromagnetic force per unit volume,  $\mathbf{F} = \mathbf{j} \times \mathbf{B}$ , has a mean part and an oscillating part at  $2\omega$ , for each component  $F_z = -j_\theta B_r$  and  $F_r = j_\theta B_z$ . Furthermore, the fluid inertia is assumed sufficient to damp out the effect of alternating forces (at  $2\omega$ ), so that  $U_0(r)$  only depends on the mean forces which are invariant along  $z$ .

Using  $j_0 = i\sigma k A_0(U_B - U_0)$  and  $B_{r0} = ikA_0$ , the mean part of the axial force per unit volume is  $f_z = -Re\{i\sigma k A_0(U_B - U_0)ikA_0^*\}$ , so that:

$$f_z = \sigma k^2 (U_B - U_0(r)) |A_0|^2 / 2 \quad (79)$$

Where  $|A_0|$  is the complex module of  $A_0$ .

It is thus apparent that the electromagnetic force is opposed to  $U_0(r) - U_B$ , so it will always tend to reduce the slip velocity.

For a developed velocity profile ( $U_0$  function of  $r$  only), neglecting friction forces, the Navier-Stokes equation becomes a balance between electromagnetic force and the pressure gradient. It is obtained that the velocity profile  $U_0(r)$  follows the law:

$$U_0(r) = U_B - \frac{2}{\sigma k^2 |A_0(r)|^2} \frac{dp}{dz} \quad (80)$$

And the pressure gradient is related to the flowrate by the integral of this law:

$$Q = Q_B - \frac{4\pi}{\sigma k^2} \frac{dp}{dz} \int_{R_1}^{R_2} \frac{r dr}{|A_0(r)|^2} \quad (81)$$

Where the synchronous flowrate is  $Q_B = \pi(R_2^2 - R_1^2)U_B$ .

This latest formula gives the performance of the pump from the flowrate. It shows that the pressure-flowrate curve should be a straight descending curve crossing the  $Q$  axis at  $Q = Q_B$ , if the magnetic field was independent of  $Q$  ( $A_0$  independent of  $Q$ ). This is indeed the case if  $Rm_B(1-u(r)) \ll 1$ , a case where the induction equation (76) does not depend on the velocity. Such a situation occurs for low values of the global slip magnetic Reynolds number, which is the mean of  $Rm_B(1-u(r))$  over the hydraulic gap.

## CHAPTER 3

For high global  $Rms$ , equations (76) and (80) are coupled and form a non-linear problem. So, it is needed to recourse to numerical methods in order to solve the system.

For a given flowrate  $Q$ , the reduced velocity profile is initialized to the uniform value  $u = Q/Q_B$  and (76) is solved after discretization by finite differences on an equally spaced grid. The pressure gradient is then calculated with (81), the velocity profile with (80) and the process is repeated until convergence.

Equations are first solved for non-dimensional variables and then results are presented for PEMDyn with an electric supply of 300 A and 20 Hz. So, the applied peak linear current density is:

$$j_{peak} = \sqrt{2} \cdot 300A \cdot 36 \text{ coils} \cdot 16 \frac{\text{turns}}{\text{coil}} \cdot \frac{1}{1.98 \text{ m}} = 123422.275 \text{ A/m}$$

The rest of parameters used for solving are in the following *Table VII* and are chosen close to those of PEMDyn.

*Table VII. Parameters for analytic solving*

$R_1$	Internal radius of channel	0.10955 [m]
$R_2$	External radius of channel	0.15738 [m]
$R_m$	Mean radius of channel	0.13346 [m]
$d_h$	Hydraulic gap	0.04788 [m]
$d_m$	Magnetic gap	0.04788 [m]
$L_{inductor}$	Length of inductor	1.98 [m]
$\sigma_{Na}$	Electrical conductivity of sodium	5.1e + 6 [S/m]
$\rho_{Na}$	Density of sodium	868.8 [kg/m <sup>3</sup> ]
$2\tau$	Pole length	0.66 [m]
$U_B$	Synchronism velocity	13.2 [m/s]

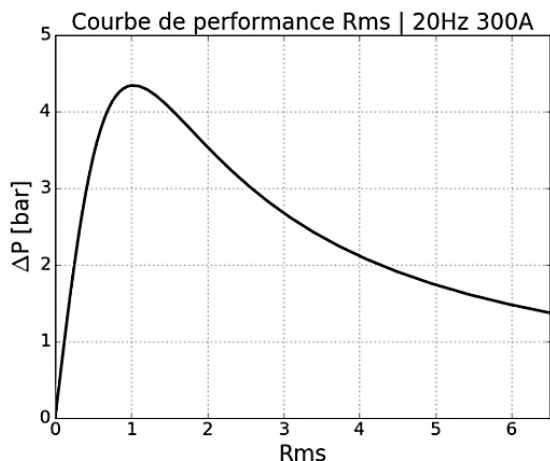


Figure 44 : Analytical Performance curve in terms of  $Rms$

Sweeping on values of global  $Rms$  (reducing the velocity from synchronism to smaller values), velocity profiles and axial and radial magnetic field components over the channel are analysed.

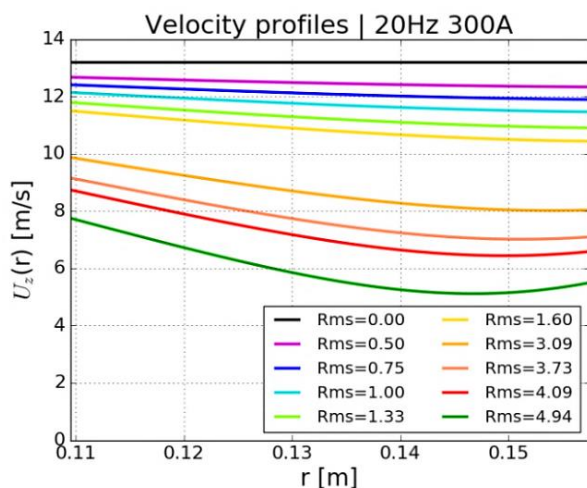


Figure 45: Velocity profile dependency on  $Rms$

This curve on *Figure 44* is the so-called PQ performance curve (for Pressure  $P$  and Flow rate  $Q$ ), expressed this time in terms of global  $Rms$  instead of flow rate. It is similar to the performance curve of an asynchronous motor that predicts stalling. So, the change of slope appearing from the maximum onwards can be interpreted as a MHD stalling phenomenon, since developed pressure by the pump drops and it is likely to lose stability of the EMIP. It can also be appreciated that *Figure 44* shows that the maximum of pressure is located at global  $Rms$  equal to 1, and in this case has a value of 4.34 bars.

First, it is seen on *Figure 45* that for low global  $Rms$  regimes (close to synchronism) the bulk velocity profile tends to be flat, as it happens for the case of Hartmann flow. However, with increasing  $Rms$ , the velocity tends to be higher at the bottom of the channel than close to the inductor. This occurs for configurations with significant curvature ( $d_h/R_{mean} \gg 1$ ). This phenomenon is also found later in numerical simulations.

On the other hand, the deviation from a uniform profile is also present in configurations presenting  $d_h/R_{mean} \ll 1$ , where velocity is more important at the top of the channel (close to the inductor). In these last cases, it is possible to simplify equations using Cartesian coordinates instead of cylindrical.

Nevertheless, we can conclude that this deviation remains small enough, and thus the use of “piston flow” solutions would be valid for many analytical studies.

Regarding modulus of axial and radial magnetic fields over the channel thickness (*Figure 46* and *Figure 47* respectively), two conclusions are extracted:

1. Axial component reaches its maximum at the top of the channel, and zero at the bottom because of perfect ferromagnetic boundary condition. Linear tendency is obtained over the channel with no significant variation with global  $Rms$ .
2. Radial component is expulsed out of the channel with the increment of slip. When global  $Rms$  is important enough we can appreciate that the order of magnitude of axial and radial components is similar.

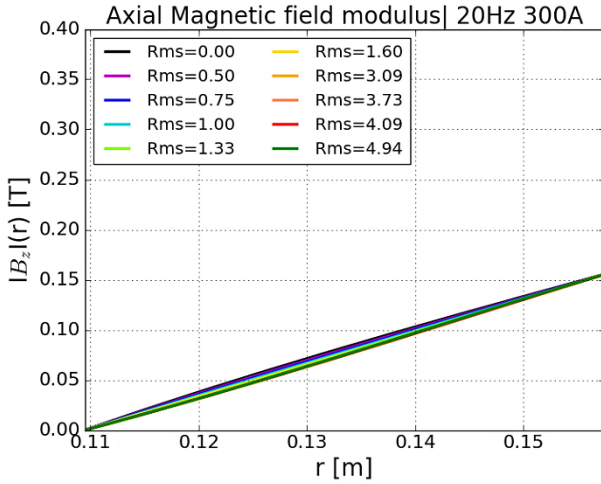


Figure 46 : Axial component dependency on  $Rms$

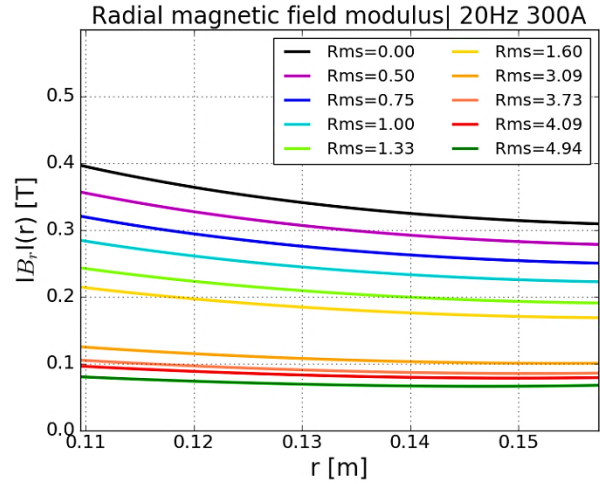


Figure 47: Radial component dependency on  $Rms$

The expulsion of the magnetic radial component translates into a loss of magnetic force in the channel, since the radial component is responsible for axial EM force. In fact, this phenomenon might be the responsible for the transition from stable flows to unstable regimes, characterized among others by the loss of developed pressure.

### 3.1.3. End effects impact on performance

Previous analyses have often considered infinitely-long sheet of current to simplify calculation. Conversely, it is important to highlight that end effects have a non-negligible impact on ALIPs performance. In fact, previous work in [17] point out that the magnetic field distortion by fringe effects may cause reduction of pump efficiency, especially due to forces opposite to motion in the inlet region, and Gailitis et al. had also mentioned in [23] that “*the finite length of the machine may appreciably delay the onset of the (azimuthal) instability*”. In this section, end effects caused by finite length are investigated analytically, and for this aim, we consider the equivalent current sheet model with finite axial length shown in *Figure 48*.

Here, we look for a valid solution able to take into account the perturbation caused by end effect near the inductor extremity. Due to convection of the magnetic field, this perturbation would have a small effect upstream and a large effect downstream. We assume here that our infinite pump solution is valid far from the borders of the inductor and that the inlet and outlet produce end effects superposed to the infinite pump solution, with an amplitude

decaying exponentially without forcing term  $j_{lin}$ . In other words, we look for a free decay solution after the inductor border.

This sub-section presents investigations about end-effect published in [43], which were carried out using a simpler approach than in [17], based on existing theories for linear motors [44].

The geometry considered is rotationally symmetric and axially infinite, except the inductor, simplified to a thin sheet of current at  $r=R_2$ , where the linear density follows a progressive sine wave with wavelength  $2\tau$ . The length of the inductor is  $L=2\tau p$ , where  $p$  is the number of pole pairs, and the wavenumber is defined as  $k=\pi/\tau$ . The yokes, represented in *Figure 48* with dashed zones, are supposed again magnetically perfect and in in contact with the liquid sodium or current sheet at  $r=R_1$  and  $r=R_2$ .

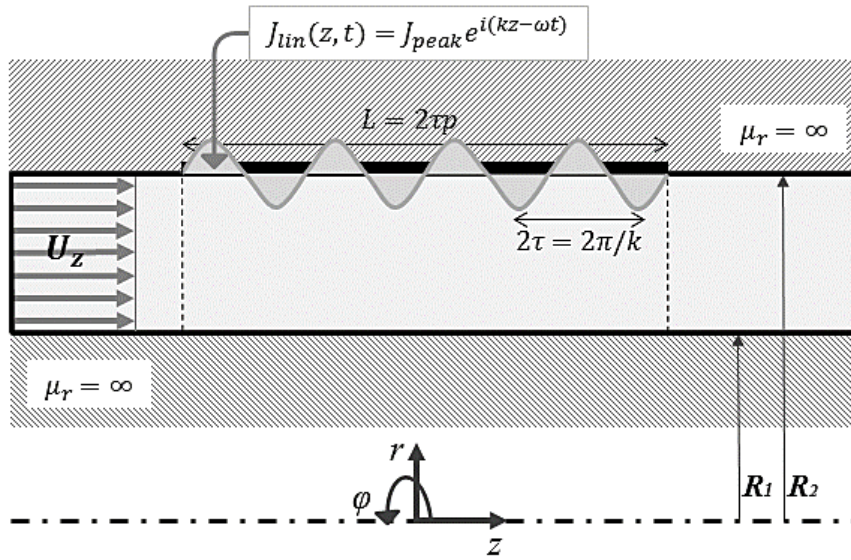


Figure 48: Finite length pump model

With these conditions, we can write the induction equation using the azimuthal component of the magnetic vector potential  $A_\varphi$  and the axial component of the velocity  $U_z$ , since other components of both vector fields are zero due to the rotational symmetry and the developed flow conditions along  $z$ . Furthermore, it is important to note that we assume solid-body approximation for the axial velocity. Then, induction equation and magnetic field components read:

$$\frac{\partial^2 A_\varphi}{\partial z^2} + \frac{\partial^2 A_\varphi}{\partial r^2} + \frac{1}{r} \frac{\partial A_\varphi}{\partial r} - \frac{A_\varphi}{r^2} = \mu_0 \sigma \left( \frac{\partial A_\varphi}{\partial t} + U_z \frac{\partial A_\varphi}{\partial z} \right) \quad (82)$$

$$B_z = \frac{\partial A_\varphi}{\partial r} + \frac{A_\varphi}{r} \quad \text{and} \quad B_r = -\frac{\partial A_\varphi}{\partial z} \quad (83)$$

## CHAPTER 3

The boundary conditions impose:

$$\begin{cases} B_z = 0 & \text{at } r = R_1 \\ B_z = \mu_0 \text{Re}\{J_{lin}(z)e^{-i\omega t}\} & \text{at } r = R_2 \end{cases} \quad (84)$$

Where  $J_{lin}(z) = J_{peak}e^{ikz}$  for  $-p\tau < z < p\tau$  and  $J_{lin}(z) = 0$  elsewhere.

Looking for an harmonic solution of the vector potential in the form  $A_\varphi(r, z, t) = \text{Re}\{A_0(r, z)e^{-i\omega t}\}$ , equation (82) and its boundary conditions (84) become a two dimensional value problem for the complex field  $A_0(r, z)$ . Using dimensionless variables  $\alpha = A_0/(\mu_0 J_{peak}/k)$ ,  $\eta = (r - R_1)/(R_2 - R_1)$ ,  $\xi = kz$  and  $q = U_z/U_B$ , the problem can be written:

$$\frac{\partial^2 \bar{\alpha}}{\partial \eta^2} + \left(\frac{H_R}{1 + H_R \eta}\right) \frac{\partial \bar{\alpha}}{\partial \eta} + \left(\frac{H_R}{1 + H_R \eta}\right)^2 \bar{\alpha} = H_\lambda^2 \left(-\frac{\partial^2 \bar{\alpha}}{\partial \xi^2} - Rm_B \left(i\bar{\alpha} - q \frac{\partial \bar{\alpha}}{\partial \xi}\right)\right) \quad (85)$$

$$\frac{\partial \bar{\alpha}}{\partial \eta} + \left(\frac{H_R}{1 + H_R \eta}\right) \bar{\alpha} = \begin{cases} 0 & \text{for } \eta = 0 \\ H_\lambda \bar{\phi}_{lin} & \text{for } \eta = 1 \end{cases} \quad \text{with } \bar{\phi}_{lin}(\xi) = \begin{cases} e^{i\xi} & \text{for } |\xi| < \pi p \\ 0 & \text{for } |\xi| > \pi p \end{cases} \quad (86)$$

Where the geometrical parameters  $H_R = (R_2 - R_1)/R_1$ ,  $H_\lambda = k(R_2 - R_1)$  and  $p$  quantify respectively the influence of axisymmetric terms (when  $H_R \rightarrow 0$  the domain is thin compared to its radius), the thickness of the magnetic gap compared to the reduced wavelength  $\tau/\pi$ , and the length of the inductor (in wavelengths).

The current problem can be solved using Fourier transforms along  $\xi$ , as suggested in [17] and [44], so that solutions of the form  $\hat{\alpha}_\kappa e^{i\kappa\xi}$  can be superposed, where  $\kappa$  is a continuously varying real wavelength and  $\hat{\alpha}_\kappa$  the complex amplitude of this mode. In the current case we will only use three modes, one at  $\kappa=1$  representing the solution of an infinite ALIP, and two others with complex wavenumbers  $\kappa_u$  and  $\kappa_d$  representing the end effect waves generated by the inlet and outlet of the inductor, which might be diffused upstream ( $\text{Im}(\kappa_u) < 0$ , so that the mode vanishes upstream) or convected downstream ( $\text{Im}(\kappa_d) > 0$ , so that the mode disappears downstream by joule dissipation). Those end effect modes are requested to verify system formed by (85) and (86) with zero source term  $J_{lin}$ , so they can be added to the infinite pump solution without destroying it far from the ends.

Therefore, we look for solutions in the form:

$$\begin{cases} \bar{\alpha} = \hat{\alpha}_{iu} e^{i\kappa_u(\xi + \pi p)} & \text{for } \xi < -\pi p \\ \bar{\alpha} = \hat{\alpha}_{od} e^{i\kappa_d(\xi - \pi p)} & \text{for } \xi > \pi p \\ \bar{\alpha} = \hat{\alpha}_{id} e^{i\kappa_d(\xi + \pi p)} + \hat{\alpha}_1 e^{i\xi} + \hat{\alpha}_{ou} e^{i\kappa_u(\xi - \pi p)} & \text{for } -\pi p < \xi < \pi p \end{cases} \quad (87)$$

With subscripts  $i$  and  $o$  for inlet and outlet respectively.

With the request that the induction problem (85) and (86) must be fulfilled in every subdomain, we get an ordinary differential problem with complex unknown  $\hat{\alpha}_\kappa(\eta)$  for each mode of wavelength  $\kappa$ , and we will connect the domains imposing continuity to  $\bar{\alpha}$  and  $\partial\bar{\alpha}/\partial\xi$  at each inductor end ( $\zeta=\pm\pi p$ ).

Consequently, the problem formed by (85) and (86) becomes:

$$\frac{d^2\hat{\alpha}_\kappa}{d\eta^2} + \left(\frac{H_R}{1+H_R\eta}\right)\frac{d\hat{\alpha}_\kappa}{d\eta} - \left(\frac{H_R}{1+H_R\eta}\right)^2\hat{\alpha}_\kappa = H_\lambda^2[\kappa^2 - iRm_B(1-\kappa q)]\hat{\alpha}_\kappa \quad (88)$$

$$\frac{d\hat{\alpha}_\kappa}{d\eta} + \left(\frac{H_R}{1+H_R\eta}\right)\hat{\alpha}_\kappa = \begin{cases} 0 & \text{at } \eta = 0 \\ 0 & \text{at } \eta = 1 \text{ for } \kappa = \kappa_u, \kappa_d \\ H_\lambda & \text{at } \eta = 1 \text{ for } \kappa = \kappa_u, \kappa_d \end{cases} \quad (89)$$

Looking for a non-zero solution for  $\kappa=\kappa_u$  or  $\kappa=\kappa_d$  (a singular value problem), it is required that  $\kappa^2 - iRm_B(1-\kappa q) = 0$ , which gives two solutions. Since  $\kappa_u$  has negative imaginary part, and with the complex square root defined as the square root with positive real part, we have:

$$\kappa_u = -i\frac{qRm_B}{2}\left(1 + \sqrt{1 - i\frac{4}{q^2Rm_B}}\right) \text{ and } \kappa_d = -i\frac{qRm_B}{2}\left(1 - \sqrt{1 - i\frac{4}{q^2Rm_B}}\right) \quad (90)$$

Here we note that for large values of  $q^2Rm_B$ , the upstream mode is damped along a short axial distance ( $1/qRm_B$ ) without oscillations because of the counterflow diffusion, whereas the downstream mode is a weakly damped travelling wave propagating at the fluid velocity  $q$ , since the current loops convected by the fluid cannot change rapidly.

The infinite pump solution of (88) can be written analytically using modified Bessel functions of first kind and second kind and the slip magnetic Reynolds number ( $Rms = (1-q)Rm_B$ ).

Under this form, the solution can be developed considering two assumptions:

1. The ALIP configuration is quasi-flat ( $H_R \rightarrow 0$ )
2. The channel is thin compared to the wavelength ( $H_\lambda \rightarrow 0$ )

These conditions together make reference to the thin channel assumption defined in previous chapter, where the channel height is small compared to the mean radius and to the wavelength ( $H_R \ll 1, H_\lambda \ll 1$ ).

## CHAPTER 3

Then we obtain that:

$$\hat{\alpha}_1 = \frac{H_\lambda \cosh(c_1 \eta)}{c_1 \sinh(c_1)} \text{ for } H_R \ll 1 \text{ and } \hat{\alpha}_1 = \frac{1}{H_\lambda(1-iRms)} + \frac{H_\lambda \eta^2}{2} \text{ for } H_R \ll 1, H_\lambda \ll 1 \quad (91)$$

With  $c_1 = H_\lambda \sqrt{1 - iRms}$ .

Notice that for thin channels, the distribution of  $\hat{\alpha}_1$  is approximately constant along  $\eta$ , but its variation with  $\eta$  is useful to calculate  $B_z$  and then verify the boundary condition.

However, the continuity of  $\bar{\alpha}$  and  $\partial \bar{\alpha} / \partial \xi$  cannot be exactly satisfied in the general case for any value of  $\eta$ , because the three modes do not have the same profile along  $\eta$ . Expression  $\bar{\alpha}(\xi, \eta) = \hat{\alpha}_1(\eta) \bar{f}(\xi)$  is indeed an approximation, but it becomes precise for the thin channel consideration, where all profiles become uniform. We will use such a formula in all cases because real ALIPs have indeed  $H_R \ll 1$  and their  $H_\lambda$  value remain in general lower than 1, i.e. in PEMDyn  $H_R = 0.44$  and  $H_\lambda = 0.46$ . Writing the continuity conditions without influence of the outlet on inlet we get:

$$\bar{f}(\xi) = \begin{cases} a_{iu} e^{i\kappa_u(\xi+\pi p)} & \text{for } \xi < -\pi p \\ a_{id} e^{i\kappa_d(\xi+\pi p)} + e^{i\xi} + a_{ou} e^{i\kappa_u(\xi-\pi p)} & \text{for } -\pi p < \xi < \pi p \\ a_{od} e^{i\kappa_d(\xi-\pi p)} & \text{for } \xi > \pi p \end{cases} \quad (92)$$

With:

$$\begin{cases} a_{iu} = (-1)^p \frac{1 - \kappa_d}{\kappa_u - \kappa_d} \\ a_{id} = (-1)^p \frac{1 - \kappa_u}{\kappa_u - \kappa_d} \end{cases}; \quad \begin{cases} a_{ou} = -a_{id} \\ a_{od} = -a_{id}(1 - e^{2i\pi\kappa_d}) \end{cases} \quad (93)$$

Finally, we can obtain the volumetric force density distribution from the current density ( $j_\varphi = \sigma(i\omega A_0 - U_z \partial A_0 / \partial z)$ ) and the radial component of the magnetic field. The axial component of the force has a mean part ( $F_{z \text{ avg}}$ ) and an oscillating part at the double of the supply frequency ( $\bar{\bar{F}}_{z \text{ DSF}}$ ), where double bar indicates a phasor for the DSF time fluctuation. Using the dimensionless solution, we extract:

$$f_{z \text{ avg}} = Rm_B \operatorname{Re} \left\{ \left( i\bar{\alpha} - q \frac{\partial \bar{\alpha}}{\partial \xi} \right) \frac{\partial \bar{\alpha}^*}{\partial \xi} \right\} \quad \text{and} \quad \bar{\bar{f}}_{z \text{ DSF}} = Rm_B \left( i\bar{\alpha} - q \frac{\partial \bar{\alpha}}{\partial \xi} \right) \frac{\partial \bar{\alpha}}{\partial \xi} \quad (94)$$

Where  $F_{z \text{ avg}} = F_{ref} f_{z \text{ avg}}$  and  $\bar{\bar{F}}_{z \text{ DSF}} = F_{ref} \bar{\bar{f}}_{z \text{ DSF}}$ , with  $F_{ref} = \frac{k\mu_0 J_{peak}^2}{2}$ .

We can remark that in the thin channel case, the force density will depend only on  $\xi$  and will be equilibrated by the pressure rise along the channel (and by friction forces which are typically one or two orders of magnitude lower). In other cases, the non-uniform distribution of the forces across the channel is not compatible with a developed velocity profile, and it

will make the velocity profile evolve towards an equilibrium profile described elsewhere for infinite pumps. Since we used a uniform velocity profile, we will only present results calculated with thin channel hypothesis.

Integrating the average force density  $F_{z,avg}$  over the channel length will give the pressure rise provided by the pump (neglecting friction) and integrating  $\bar{F}_{z,DSF}$  will give the DSF fluctuation of this pressure rise. The results presented below employ a numerical integration of the calculated values over the interval  $-p-1 < \xi/\pi < p+1$ , out of which the force density is considered negligible, with axial step of  $\delta\xi = \pi/25$ .

The model has been applied to a pump with  $p = 3$  pairs of poles and  $Rm_B = 8$ , and thus similar to PEMDyn. Figure 49 shows a typical travelling wave shape at moderate slip ( $1-q=20\%$ ), with the different modes contributing to  $f(\xi)$  (shown only for the real part). The upstream diffusion of each end effect is hardly visible since it affects a very short length, whereas the downstream convection affects the whole inductor and a large zone after it. The inlet wave (dark red curve), almost compensating the infinite pump solution (light blue curve) at inlet, propagates downstream with damping, but since it propagates at a different speed, it can be in phase before outlet. Therefore the module of the wave does not increase monotonically from inlet downwards, as shown in Figure 50, where it is plotted for several values of  $q$ . For lower  $q$ , the velocity difference between both waves is larger and the interference effect is stronger.

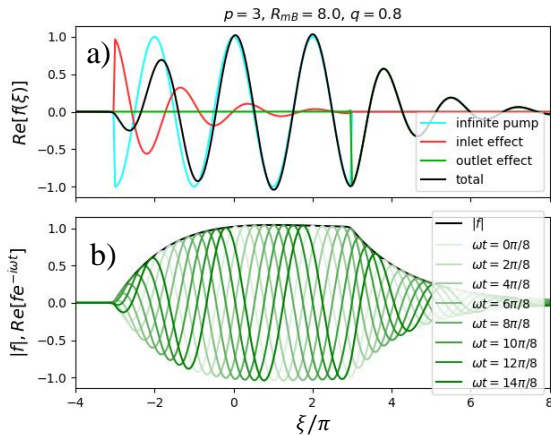


Figure 49: a) Modes added up to get the finite pump solution b) Resulting traveling wave

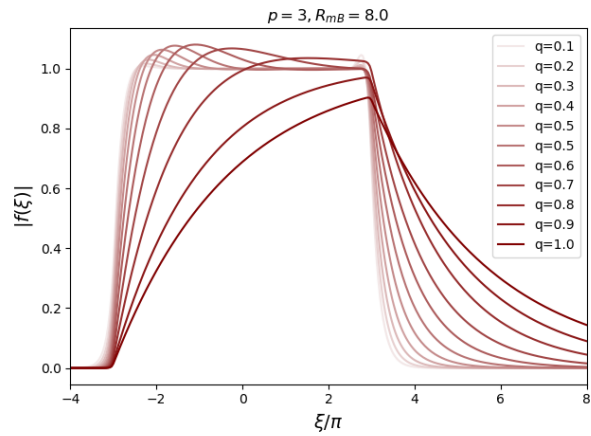


Figure 50: Module of the travelling wave for  $p=3, RmB=8$  and several values of  $q$

The axial force density distribution is presented in Figure 51 for a typical PEMDyn case ( $p = 3, Rm_B = 8$ ), and in Figure 52 for an hypothetical pump with 10 poles and higher magnetic Reynolds number ( $p = 5, Rm_B = 20$ ). This last figure clearly shows the interference effects making the module of the wave oscillate with  $\xi$ .

The inlet end effect is responsible for a negative force (directed upstream), on a zone that appears to be longer as the flowrate tends to synchronism. The electromagnetic problem seen from the fluid side is similar to transient diffusion into the channel of a suddenly applied AC field, whereas the fluid is convected downwards: the length of the inlet effect thus increases

with  $qRm_B$  (and not  $Rms$ ). It appears in our model that a zone with similar length would exist after the inductor end because of the convection of the electromagnetic field after the pump outlet, if the magnetic yokes were long enough. That zone would generate little net pressure but a large amount of DSF fluctuations, and thus its limitation due to the end of the yokes is certainly favorable.

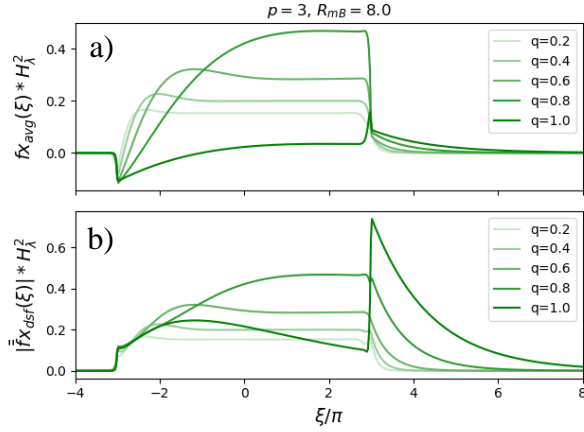


Figure 51: Force density along the pump  
Average b) DSF

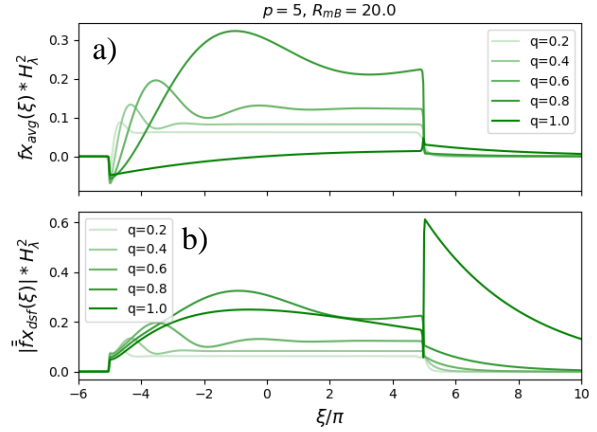


Figure 52: Force density along the pump  
Average b) DSF

Integrating the force distribution, we obtain the pressure difference provided by the pump and the fluctuation of this pressure difference at different values of  $q$  for constant supply current. Such curves are presented in Figure 53 for  $p = 3$  and several values of  $Rm_B$ . The dimensionless values plotted in that figure should be divided by  $H_\lambda^2$ , multiplied by  $F_{ref}$  and by  $l/k$  to get pressure differences in SI units. Notice that the DSF pressure fluctuation can be 0 even if the module of the fluctuating force phasor is constant along the pump (this is typically the case for the infinite pump solution), because the phase of this force evolves along  $\xi$  (the phasor is proportional to  $e^{2i\xi}$  in an infinite pump, integrating this complex function from  $-\pi$  to  $\pi$  gives 0). We can conclude that DSF fluctuation is due to end effects.

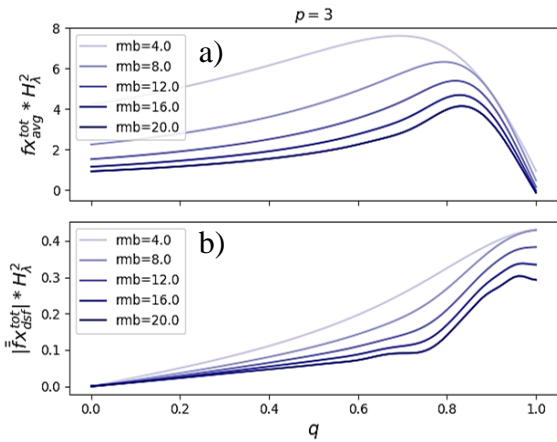


Figure 53: Pressure provided by the pump  
a function of flowrate at different  $Rm_B$  values  
for: a) Mean value b) DSF fluctuation

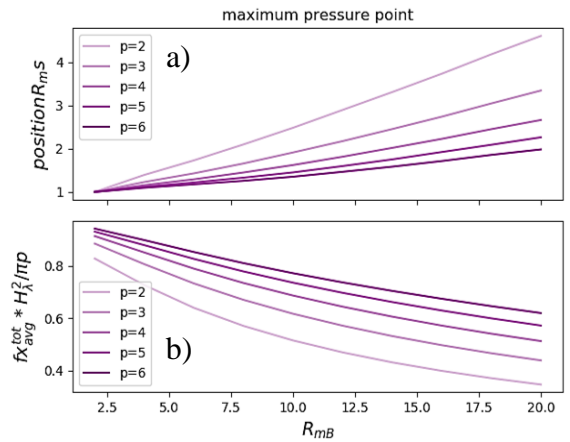


Figure 54: Maximum pressure point of an  
ALIP with  $p$  pairs of poles: a) Position  
b) Maximum value

## CHAPTER 3

Notice that an infinite pump with thin channel would give a maximum average force density at  $Rms = 1$ , where  $H_\lambda^2 f x_{avg} = 0.5$ , so that the total dimensionless force would be  $H_\lambda^2 f x_{avg}^{tot} = \pi p$  at the maximum point if we integrate over the finite length without end effects. The maximum of the performance curves such as the ones in *Figure 53a*) can be compared to those values, and this work can be repeated for other values of  $p$ . The results are presented in *Figure 54*, and shows that the maximum always occur at higher slip than  $Rms = 1$ , especially for a small number of poles where the end effects are more present. Because of the end effects, the maximum pressure provided by the pump is lower than expected from the infinite pump solution, especially if the number of pole pairs is small and especially for large values of  $Rm_B$ .

## 3.2. Stability analysis

### 3.2.1. Linear stability for the case of azimuthal perturbations

This section is the continuation of the study carried out by Linards Goldsteins [3] about the linear analysis of convective stability for azimuthal perturbations in an ALIP. In this subsection we study the non-axisymmetric perturbations of the fully coupled problem, and more precisely the perturbations of the thin channel infinite pump model. The stability study is developed up to the obtaining of amplification exponents for low frequency perturbations (compared to the travelling field scales), and not only stability thresholds as in previous studies. The complete theory is to be published soon.

Here we formulate the fully perturbed problem using induction equation in terms of magnetic field and Navier-Stokes equation. In dimensionless form (indicated with tilde  $\sim$ ) they read:

$$\tilde{\Delta}\tilde{\mathbf{B}} = Rm_B \left[ \frac{\partial \tilde{\mathbf{B}}}{\partial \tilde{t}} + (\tilde{\mathbf{u}} \cdot \tilde{\nabla})\tilde{\mathbf{B}} - (\tilde{\mathbf{B}} \cdot \tilde{\nabla})\tilde{\mathbf{u}} \right] \quad (95)$$

$$\tilde{\nabla} \cdot \tilde{\mathbf{B}} = 0 \quad (96)$$

$$\frac{\partial \tilde{\mathbf{u}}}{\partial \tilde{t}} + (\tilde{\mathbf{u}} \cdot \tilde{\nabla})\tilde{\mathbf{u}} = -\tilde{\nabla}\tilde{p} + \frac{1}{Re_{bis}}\tilde{\Delta}\tilde{\mathbf{u}} + \frac{N_{bis}}{Rm_B}\tilde{\mathbf{j}} \times \tilde{\mathbf{B}} \quad (97)$$

$$\tilde{\nabla} \cdot \tilde{\mathbf{u}} = 0 \quad (98)$$

Using dimensionless factors:

$$L_{ref} = \frac{1}{k}, \quad T_{ref} = \frac{1}{\omega_B}, \quad B_{ref} = k\mu_0 J_{peak}, \quad u_{ref} = U_B, \quad j_{ref} = J_{peak} \text{ and } p_{ref} = \rho_{Na} U_B^2.$$

Where  $Re_{bis} = U_B/(k\nu_{Na})$  and  $N_{bis} = \mu_0\sigma_{Na}B_{ref}^2L_{ref}/\rho_{Na}U_B$  with  $\nu_{Na}$  the fluid kinematic viscosity.

For the case of thin magnetic gap compared to the wavelength ( $H_\lambda \ll 1$ ) we assume that the perturbed fields of velocity  $\mathbf{u}$  and current density  $\mathbf{j}$  are contained in the  $\varphi$ - $z$  surface, which is almost plane in the thin channel approximation. However, because of azimuthal fluctuations of  $\mathbf{u}$  and  $\mathbf{j}$ , some pressure and electric potential variations could be needed to maintain to maintain those two fields divergence free. Fortunately, the electric potential can be eliminated using the induction equation for the magnetic perturbed field  $\mathbf{B}$  (calculating  $\mathbf{j}$  with its curl), and the pressure can be eliminated using the vorticity transport equation or taken into account using the continuity and Navier-Stokes equation.

Furthermore, we only study perturbations that are slowly varying compared to the electromagnetic scales (time period  $2\pi/\omega_B$  and axial period  $2\pi/k$ ), enabling to replace the t-derivatives and z-derivatives of electromagnetic terms by simple products by  $ik$  and  $i\omega_B$ , since phasor notation will be employed.

We consider a small perturbation hypothesis  $\tilde{\mathbf{u}} = \tilde{\mathbf{U}}_0 + \tilde{\mathbf{u}}'$ ,  $\tilde{p} = \tilde{P}_0 + \tilde{p}'$ ,  $\tilde{\mathbf{j}} = \tilde{\mathbf{J}}_0 + \tilde{\mathbf{j}}'$ , and the axisymmetric steady solution with a solid body approximation for the velocity profile:  $\tilde{\mathbf{U}}_0 = \tilde{U}_0 \mathbf{e}_z$ ,  $\tilde{\mathbf{V}}\tilde{P}_0 = (\partial\tilde{P}_0/\partial\tilde{z})\mathbf{e}_z$ ,  $\tilde{\mathbf{J}}_0 = \tilde{J}_{0\varphi}\mathbf{e}_\varphi$ ,  $\tilde{\mathbf{B}}_0 = \tilde{B}_{0r}\mathbf{e}_r + \tilde{B}_{0z}\mathbf{e}_z$ . For the fluid flow perturbation equation, the  $H_\lambda \ll 1$  assumption permits to neglect the radial component of velocity and assume that  $\varphi$  and  $z$  components are uniform along  $r$  (out of the boundary layers). Furthermore, this permits to average  $\varphi$  derivatives over the mean radius  $R_m$  as a thin channel approximation for  $r$ .

We can thus separate the equations (95), (97) and (98) into a non-perturbed problem verified by the infinite thin pump solution (base solution in sub-section 3.1.2.1), and a perturbed problem. Linearizing the system, the perturbed problem reads:

$$\tilde{\Delta}\tilde{\mathbf{b}}' = Rm_B \left[ \frac{\partial\tilde{\mathbf{b}}'}{\partial\tilde{t}} + (\tilde{\mathbf{U}}_0 \cdot \tilde{\nabla})\tilde{\mathbf{b}}' + (\tilde{\mathbf{u}}' \cdot \tilde{\nabla})\tilde{\mathbf{B}}_0 - (\tilde{\mathbf{B}}_0 \cdot \tilde{\nabla})\tilde{\mathbf{u}}' \right] \quad (99)$$

$$\frac{\partial\tilde{u}'_\varphi}{\partial\tilde{t}} + \tilde{U}_0 \frac{\partial\tilde{u}'_\varphi}{\partial\tilde{z}} = -\frac{1}{\tilde{R}_m} \frac{\partial\tilde{p}'}{\partial\varphi} + \frac{N_{bis}}{Rm_B} \tilde{f}'_\varphi - 2\lambda'_h |\tilde{U}_0| \tilde{u}'_\varphi \quad (100)$$

$$\frac{\partial\tilde{u}'_z}{\partial\tilde{t}} + \tilde{U}_0 \frac{\partial\tilde{u}'_z}{\partial\tilde{z}} = -\frac{\partial\tilde{p}'}{\partial\tilde{z}} + \frac{N_{bis}}{Rm_B} \tilde{f}'_z - 2\lambda'_h |\tilde{U}_0| \tilde{u}'_z \quad (101)$$

$$\frac{\partial\tilde{u}'_z}{\partial\tilde{z}} + \frac{1}{\tilde{R}_m} \frac{\partial\tilde{u}'_z}{\partial\tilde{\varphi}} = 0 \quad (102)$$

Where  $\lambda'_h = \lambda_h/(2d_h)$ , with  $\lambda_h$  the hydraulic friction coefficient, can be obtained from the Moody chart [45] from the hydraulic Reynolds number  $Re$  and the rugosity of the walls  $\varepsilon_h$ .

We will consider here that the inductor current remains unperturbed even with MHD fluctuations inside the pump (it is the case for a power supply at constant current, but not a constant voltage). Then the boundary conditions for perturbations are:

$$\begin{aligned} \text{At } \tilde{r} = \tilde{R}_2 &\rightarrow \frac{\partial\tilde{b}'_r}{\partial\tilde{r}} = 0, & \tilde{b}'_\varphi = 0, & \tilde{b}'_z = 0 \\ \text{At } \tilde{r} = \tilde{R}_1 &\rightarrow \frac{\partial\tilde{b}'_r}{\partial\tilde{r}} = 0, & \tilde{b}'_\varphi = 0, & \tilde{b}'_z = 0 \end{aligned} \quad (103)$$

Because of the fluid inertia, we look for perturbations of the fluid flow variables with axial variations at large scales  $\delta\varphi$ ,  $\delta z$  compared to the scale  $L_{ref}$  of the electromagnetic wave and time variations at long period  $\delta t$  compared to the electromagnetic period. These flow variations will make the electromagnetic variables vary at the same scales, while they locally remain traveling waves at the scale of the electromagnetic wave. Therefore, we will write  $\tilde{\mathbf{b}}' = Re\{\hat{\mathbf{b}}'_1 e^{i(x-t)}\}$ , with slowly varying phasors  $\hat{b}'_{r1}$ ,  $\hat{b}'_{\varphi 1}$  and  $\hat{b}'_{z1}$ , so that:

$$\frac{\partial \tilde{\mathbf{b}}'}{\partial \tilde{z}} = \text{Re}\{i\hat{\mathbf{b}}'_{\mathbf{1}}(\varphi, \tilde{z}, \tilde{t})e^{i(\tilde{z}-\tilde{t})}\} \text{ and } \frac{\partial \tilde{\mathbf{b}}'}{\partial \tilde{t}} = \text{Re}\{-i\hat{\mathbf{b}}'_{\mathbf{1}}(\varphi, \tilde{z}, \tilde{t})e^{i(\tilde{z}-\tilde{t})}\} \quad (104)$$

Suppressing  $\tilde{u}'_r$  and the derivatives of the other velocity perturbations (i.e. neglecting  $(\mathbf{B} \cdot \nabla)\mathbf{u}'$  compared to  $(\mathbf{u}' \cdot \nabla)\mathbf{B}$  which varies at smaller scale), we can get the electromagnetic perturbation equations written in terms of electromagnetic phasors. In addition, we obtain that the azimuthal component of magnetic field perturbation is formerly zero, since it obeys a convection-diffusion equation without source and it is imposed null at the boundaries.

Splitting  $\hat{\mathbf{b}}'_{r\mathbf{1}} = b'_{r\mathbf{1}R} + ib'_{r\mathbf{1}I}$  into real ( $R$ ) and imaginary ( $I$ ) parts (slowly varying with  $\tilde{z}$ ,  $\tilde{t}$ , and  $\varphi$  at the scale of the flow field perturbations), we can write the complex equation for  $\hat{\mathbf{b}}'_{r\mathbf{1}}$  as systems of two real equations. Introducing the base solution  $\hat{B}_{r\mathbf{1}} = \frac{Rms-i}{H_\lambda(Rms^2+1)}$ , we obtain:

$$\begin{cases} -b'_{r\mathbf{1}R} + \frac{1}{\tilde{R}_m^2} \frac{\partial^2 b'_{r\mathbf{1}R}}{\partial \varphi^2} - Rms b'_{r\mathbf{1}I} = \frac{Rm_B}{H_\lambda(1+Rms^2)} u'_x \\ -b'_{r\mathbf{1}I} + \frac{1}{\tilde{R}_m^2} \frac{\partial^2 b'_{r\mathbf{1}I}}{\partial \varphi^2} + Rms b'_{r\mathbf{1}R} = \frac{Rm_B Rms}{H_\lambda(1+Rms^2)} u'_x \end{cases} \quad (105)$$

Decomposing the perturbations in Fourier series along  $\varphi$  (because of periodicity) and Fourier integrals along  $\tilde{z}$  and  $\tilde{t}$ , we can treat separately each mode because of the linearity of our small perturbation equations. Furthermore, since the choice of the  $\varphi=0$  line is arbitrary, we will use a mode in cosine for the axial velocity perturbation:

$$\tilde{u}'_z = \cos(m\varphi) \text{Re}\{\hat{u}'_z e^{n\tilde{z}-\gamma\tilde{t}}\} \quad (106)$$

From (105) we deduce the same distribution for  $b'_{r\mathbf{1}R}$ ,  $b'_{r\mathbf{1}I}$ ,  $b'_{z\mathbf{1}R}$ ,  $b'_{z\mathbf{1}I}$ :

$$\begin{cases} b'_{z\mathbf{1}R} = \cos(m\varphi) \text{Re}\{\hat{b}'_{z\mathbf{1}R} e^{n\tilde{z}-\gamma\tilde{t}}\}, & b'_{r\mathbf{1}R} = \cos(2\pi m\varphi) \text{Re}\{\hat{b}'_{r\mathbf{1}R} e^{n\tilde{z}-\gamma\tilde{t}}\} \\ b'_{z\mathbf{1}I} = \cos(m\varphi) \text{Re}\{\hat{b}'_{z\mathbf{1}I} e^{n\tilde{z}-\gamma\tilde{t}}\}, & b'_{r\mathbf{1}I} = \cos(2\pi m\varphi) \text{Re}\{\hat{b}'_{r\mathbf{1}I} e^{n\tilde{z}-\gamma\tilde{t}}\} \end{cases} \quad (107)$$

Here  $m = 1, 2, \dots$  is the azimuthal mode number (number of wavelengths on the whole circumference) and  $n$  and  $\gamma$  are complex numbers, with imaginary parts  $n_I$  and  $\gamma_I$  being the dimensionless wavenumber and pulsation of the perturbation, and real parts  $n_R$  and  $\gamma_R$  characterizing respectively its amplification with time and damping along the flow direction  $z$ .

Our hypothesis of slowly varying perturbations means that we only consider perturbations with  $|n| \ll 1$  and  $|\gamma| \ll 1$ . The double hat variables in (106) and (107) are complex amplitudes, but not with the same significance as single hat phasors of the electromagnetic fields, and with derivation rules along  $z$  and  $t$  based on  $n$  and  $-\gamma$  in place of  $i$  and  $-i$ .

Using (107) and introducing  $m'=m/\tilde{R}_m$  and  $M=1+m'^2$ , the electromagnetic perturbation equations (105) can be solved to obtain:

$$\begin{cases} \hat{b}'_{r1R} = \frac{Rm_B(-M + Rms^2)}{H_m(1 + Rms^2)(M^2 + Rms^2)} \hat{u}'_z \\ \hat{b}'_{r1I} = \frac{Rm_B Rms(-1 - M)}{H_m(1 + Rms^2)(Rms^2 + M^2)} \hat{u}'_z \end{cases} \quad (108)$$

To calculate the perturbations of the dimensionless electromagnetic force  $\mathbf{f}=\mathbf{j}\times\mathbf{b}$  for the fluid flow model, we need the perturbation of the dimensionless current density. Calculating it from  $\mathbf{j}=\nabla\times\mathbf{b}$  gives the linearized fluctuation of the mean force  $f_{avg} = \text{Re}\{\hat{j}_1 \times \hat{b}_1^*\}/2$  as  $f'_{avg} = \text{Re}\{\hat{j}'_1 \times \hat{b}'_1^* + \hat{j}'_1 \times \hat{B}_1^*\}/2$  or, keeping only the significant terms,  $f'_z = -\frac{1}{2}\text{Re}\{\hat{j}'_{\varphi 1} \hat{b}'_{r1}^* + \hat{j}'_{\varphi 1} \hat{B}_{r1}^*\}$ , and  $f'_\varphi = \frac{1}{2}\text{Re}\{\hat{j}'_{1z} \hat{B}_{1r}^*\}$ . Introducing the base solution of subsection 3.1.2.1 (with the fluctuation phasors splitted into their real and imaginary parts) and introducing the perturbation mode (106) for the axial velocity, and the corresponding modes (107) for the magnetic field and current fluctuations, with expression (108) of the fluctuation of  $\tilde{b}'_r$ , we finally obtain the force fluctuation as a function of the velocity fluctuation:

$$\begin{cases} \hat{f}'_z = \frac{Rm_B(-M+Rms^2)}{2H_\lambda^2(1+Rms^2)(M^2+Rms^2)} \hat{u}'_z \\ \check{f}'_\varphi = \frac{m'Rm_B Rms}{2H_\lambda^2(1+Rms^2)(M^2+Rms^2)} \hat{u}'_z \end{cases} \quad (109)$$

Where the inverted hat over complex amplitudes stand for a sine dependence along  $\varphi$  in place of a cosine dependence.

In addition, using the perturbation mode for the axial velocity (106), the continuity equation (102) gives a relation between the fluctuation of azimuthal velocity and the axial velocity fluctuation:

$$\tilde{u}'_\varphi = \sin(2\pi m\varphi) \text{Re}\{\check{u}'_\varphi e^{n\tilde{z}-\gamma\tilde{t}}\} \quad (110)$$

With  $n\hat{u}'_z + m'\check{u}'_\varphi = 0$ .

Furthermore, from the momentum equations we know that the pressure fluctuation is proportional to  $\tilde{u}'_z$  (cosine mode) so that its  $z$ -derivative is a cosine mode and its  $\varphi$ -derivative a sine mode. Therefore  $\tilde{p}' = \cos(2\pi m\varphi) \text{Re}\{\hat{p}' e^{n\tilde{z}-\gamma\tilde{t}}\}$  and, reporting the force fluctuations (109) in the linearized momentum equations (100) and (101), we obtain:

$$\begin{cases} (n\tilde{U}_0 - \gamma)\hat{u}'_z = -n\hat{p}' + \frac{N_{bis}(-M+Rms^2)}{2H_\lambda^2(1+Rms^2)(M^2+Rms^2)}\hat{u}'_z - 2\lambda'_h|\tilde{U}_0|\hat{u}'_x \\ (n\tilde{U}_0 - \gamma)\check{u}'_\varphi = m'\hat{p}' + \frac{m'N_{bis}Rms^2}{2H_\lambda^2(1+Rms^2)(M^2+Rms^2)}\hat{u}'_z - \lambda'_h|\tilde{U}_0|\check{u}'_\varphi \end{cases} \quad (111)$$

Introducing the real coefficients  $\Phi = N_{bis}/[2H_\lambda^2(1+Rms^2)(M^2+Rms^2)]$  ( $\Phi > 0$ ),  $\Gamma = \gamma - n\tilde{U}_0$ ,  $\Lambda_h = \lambda'_h|\tilde{U}_0|$ , rearranging and adding the continuity (110) to close the system, we get:

$$\begin{bmatrix} (M - R_{ms}^2)\Phi + 2\Lambda_h - \Gamma & 0 & n \\ -m'Rms\Phi & \Lambda_h - \Gamma & -m' \\ n & m' & 0 \end{bmatrix} \cdot \begin{pmatrix} \hat{u}'_z \\ \check{u}'_\varphi \\ \hat{p}' \end{pmatrix} = \begin{pmatrix} 0 \\ 0 \\ 0 \end{pmatrix} \quad (112)$$

To have non-zero solutions of (112), we need that the determinant of this system is zero, what gives:

$$\begin{aligned} (m'^2 - n^2)(\gamma - \tilde{U}_0 n) &= \\ = (-m'^2 Rms^2 + m'^2(1 + m'^2) - m'^2 Rms n)\Phi + (2m'^2 - n^2)\Lambda_h \end{aligned} \quad (113)$$

This complex relation makes it possible to calculate two of the four reals  $n_R$ ,  $n_I$ ,  $\gamma_R$ ,  $\gamma_I$  (real and complex parts of  $n$  and  $\gamma$ ) from the two others. For example, we can choose a perturbation which is axially purely sinusoidal ( $n_R = 0$ ,  $0 < n_I \ll 1$ ) to have slowly varying perturbations compared to the electromagnetic wave and calculate its temporal evolution (pulsation  $\gamma_I$  and amplification  $\gamma_R$ ). Or we could look for a perturbation oscillating at pulsation  $\gamma_I$  with an amplitude invariant in time ( $\gamma_R = 0$ ) and calculate its wavenumber  $n_I$  and its amplification factor  $n_R$  along  $z$  (growing perturbation for  $n_R > 0$ , decreasing for  $n_R < 0$ ), but this would need to solve non-linear equations.

For  $n_R = 0$ , rearranging (113), we can calculate  $\gamma_R$  and  $\gamma_I$  from  $n_I$  considering  $n = in_I$ :

$$\begin{cases} \gamma_R = \frac{m'^2(1+m'^2-Rms^2)\Phi + (2m'^2+n_I^2)\Lambda_h}{m'^2+n_I^2} \\ \gamma_I = (\tilde{U}_0 - \frac{m'^2 Rms\Phi}{m'^2+n_I^2})n_I \end{cases} \quad (114)$$

The imaginary part of  $\gamma$  show that for moderate values of  $Rms\Phi$ , the perturbations that are sinusoidal in space are actually traveling waves, convected downstream at a velocity smaller than the fluid velocity  $\tilde{U}_0$ . The numerical applications show that this is the case for real pumps, i.e.  $Rms\Phi$  remains smaller than one, and the perturbation velocity remains equal to  $\tilde{U}_0$  minus some percents.

The formula for  $\gamma_R$  shows that the friction term ( $\Lambda_h$ ) is always stabilizing (positive contribution to  $\gamma_R$ ), whereas the MHD term ( $\Phi$ ) can be stabilizing at low  $Rms$  or destabilizing

at high  $Rms$ . Quantitatively, the modes purely sinusoidal in space are amplified in time if and only if  $\gamma_R < 0$ . Developing  $A_h$ ,  $\Phi$  and  $m'$ , and replacing  $\tilde{U}_0$  by  $1-Rms/Rm_B$ , this instability condition can be written:

$$\gamma_R < 0 \text{ with } n = in_I \Leftrightarrow$$

$$Rms^2 > 1 + \frac{m^2}{\tilde{R}_m^2} + \frac{\lambda_h H_\lambda^2}{N_{bis} \tilde{d}_h} (2 + n_I^2 \frac{\tilde{R}_m^2}{m^2}) |1 - \frac{Rms}{Rm_B}| (1 + Rms^2) (1 + \frac{m^2}{\tilde{R}_m^2} + Rms^2) \quad (115)$$

With  $\tilde{d}_h$  the non-dimensional hydraulic diameter.

Since  $\lambda_h$  and  $H_\lambda$  are small parameters, whereas all other parameters (including  $H_\lambda / \tilde{d}_h$ ) are of order 1, we can consider the last term  $(2+n_I^2/m^2)A_h/\Phi$  of the inequality as a small modification (due to friction) of the stability parameter that would be  $Rms > (1+m^2/\tilde{R}_m^2)^{1/2}$  without friction term. This is the "simplified criterion"<sup>1</sup> of [23], that shows that the first unstable mode is  $m=1$ , and that the  $Rms$  value for which it becomes unstable decreases when the mean dimensionless radius  $\tilde{R}_m$  increases or the  $m$  mode number decreases.

For a known  $Rms$  value above this simple criterion, this relation may be solved in  $n_I$ :

$$\gamma_R < 0 \text{ and } n = in_I \Leftrightarrow$$

$$n_I^2 \frac{\tilde{R}_m^2}{m^2} < \frac{Rms^2 - 1 + \frac{m^2}{\tilde{R}_m^2}}{\frac{\lambda_h H_\lambda^2}{N_{bis} H_h} |1 - \frac{Rms}{Rm_B}| (1 + Rms^2) (1 + \frac{m^2}{\tilde{R}_m^2} + Rms^2)} - 2 \quad (116)$$

Which shows that with friction ( $\lambda_h \neq 0$ ), and for a  $Rms$  value just above the simplified criterion (the large fraction should remain lower than 2), there exists a maximum value of  $n_I$  below which  $\gamma_R < 0$  (i.e. we are in a zone of conditional instability where the perturbations with a low spatial frequency are amplified). Furthermore, knowing that first term in the numerator of  $\gamma_R$  in (114) is dominant, this equation shows that the lower the wavenumber, the higher the amplification (even without friction). Since low wavenumbers  $n_I$  correspond to low pulsations  $\gamma_I$  (because the perturbation velocity is not far from  $\tilde{U}_0$ ), this explains why for an unstable working point, low frequency oscillations are observed and a stable asymmetry ( $n_I = 0$ ) may be installed.

For a given pump geometry (given values of  $H_\lambda$ ,  $\tilde{R}_m$ ,  $H_\lambda/\tilde{d}_h$ ), the stability diagram of the pump depends on the values of  $Rm_B$  and  $\lambda_h/N_{bis}$ , i.e. on the frequency and current of the power supply. Numerical applications were done for the Toshiba pump [6] and the PEMDyn pump

---

<sup>1</sup>The simplification was not evident in this paper, since the friction term was used to scale the other terms. With this scaling, their performance curve tends to infinity when the friction is negligible, and the intersection of their "instability curve" with this infinite performance curve give the simplified criterion.

(Table I in previous chapter), at their maximum frequency<sup>2</sup> and for a current corresponding to a maximum magnetic field  $B_{ref}/H_\lambda = 0.2$  T. Notice that frequency and current do not affect the simplified stability criterion, which gives a critical  $Rms$  value for mode  $m=1$  that only depends on the pump geometrical parameter  $\tilde{R}_m$ : this simple criterion (without friction) would give the first amplified mode when the slip increases ( $m=1, n_l=0$ ), at  $Rms = 1.02$  (i.e.  $\tilde{U}_0 = 0.84$ ) for the Toshiba pump and  $Rms = 1.27$  ( $\tilde{U}_0 = 0.89$ ) for the PEMDyn pump.

The real stability diagrams are plotted in Figure 55 for the Toshiba pump and Figure 56 for the PEMDyn pump, at their nominal working point. The simplified stability criterion has also been indicated on those figures using dashed lines. The first effect of friction is to slightly delay the instability threshold to higher slip values (smaller fluid velocities). Another effect is to stabilize high frequency modes, what is especially visible for mode 1 in the Toshiba pump. In that case, whatever the value of  $Rms$  the high frequency mode 1 fluctuations will never be amplified. However high frequency modes may appear for modes 2, 3, 4... if their respective stability threshold is exceeded.

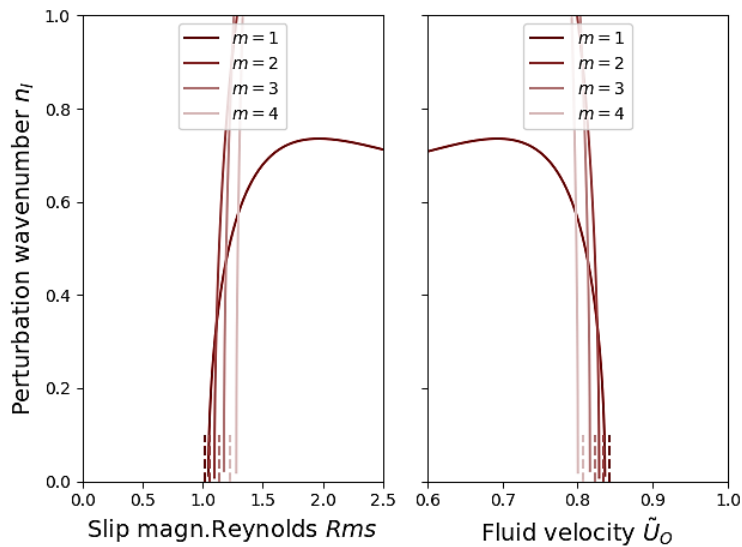


Figure 55: Stability diagram of the Toshiba pump for azimuthal perturbations (each mode is unstable below its curve)

<sup>2</sup>The conductivity of the fluid has been multiplied by  $d_h/d_m$  for those applications, which is a crude way to consider the difference of electric conductivities in the fluid channel and the magnetic gap.

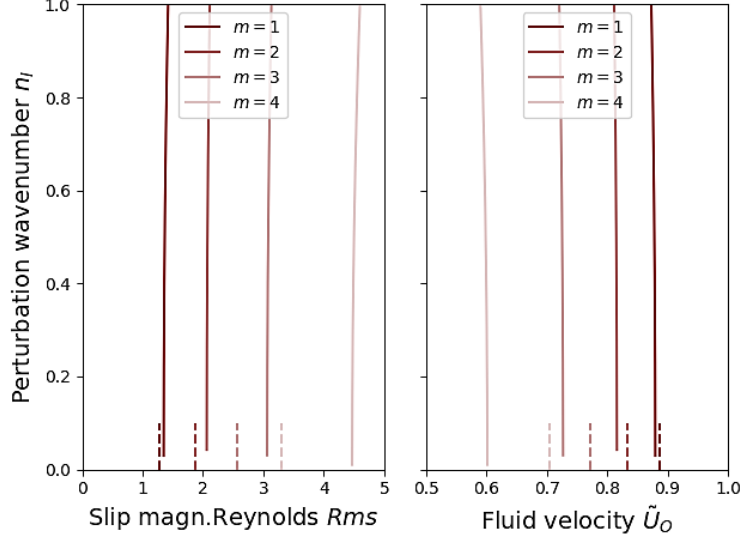


Figure 56: Stability diagram of the PEMDYN pump for azimuthal perturbations (each mode is unstable below its curve)

### 3.2.2. Linear stability for the case of radial perturbations

From the precedent study we know that azimuthal perturbations are keen on generating destabilization of the flow for certain working regimes. However, for the moment radial perturbations have not been identified as a potential cause for the onset of instability in ALIPs. The following discussion treats the linear analysis of marginal stability for radial perturbations, where, *marginal stability* makes reference to the estimation of possible perturbed solutions in the MHD system described. This corresponds to the first step to do regarding stability, and then if it is considered appropriate, the study might be extended with the convective analysis to better describe the behaviour of perturbation modes.

Considering a 2D axisymmetric perturbed system where  $\mathbf{A}$  and  $\mathbf{u}$  read:

$$\mathbf{A}_{total}(r, z, t) = \text{Re}(\hat{A}_\varphi(r, z, t)e^{i(kz - \omega_B t)})\mathbf{e}_\varphi = \text{Re}(A_\varphi)\mathbf{e}_\varphi \quad (117)$$

$$\hat{A}_\varphi(r, z, t) = \hat{A}_0(r) + \hat{\alpha}(r, z, t) \quad (118)$$

$$\mathbf{u} = \begin{pmatrix} 0 \\ 0 \\ U_0(r) \end{pmatrix} + \begin{pmatrix} u_r' \\ 0 \\ u_z' \end{pmatrix} = \begin{pmatrix} u_r \\ 0 \\ u_z \end{pmatrix} \quad (119)$$

We will use the curl of Navier-Stokes equations, i.e. the transport equation of vorticity, to eliminate the pressure field. Perturbed vorticity  $\boldsymbol{\omega}$  is obtained from  $\mathbf{u}$  as:

$$\boldsymbol{\omega} = \left( \frac{\partial u'_r}{\partial z} - \frac{\partial u'_z}{\partial r} - \frac{\partial U_0}{\partial r} \right) \mathbf{e}_\varphi = (\omega_0 + \omega_p) \mathbf{e}_\varphi \quad (120)$$

Where  $\omega_0 = -\frac{\partial U_0}{\partial r}$  and  $\omega_p = \frac{\partial u'_r}{\partial z} - \frac{\partial u'_z}{\partial r}$ .

Assuming that the complex amplitude  $\hat{A}_\varphi$  varies slowly with  $t$  and  $z$  (compared to the period and wavelength):

$$\frac{\partial \mathbf{A}_{total}}{\partial t} \approx \text{Re}(-i\omega_B \hat{A}_\varphi e^{i(kz - \omega_B t)}) \mathbf{e}_\varphi \quad (121)$$

$$\frac{\partial \mathbf{A}_{total}}{\partial z} \approx \text{Re}(ik \hat{A}_\varphi e^{i(kz - \omega_B t)}) \mathbf{e}_\varphi \quad (122)$$

Azimuthal component of vector potential equation becomes:

$$\frac{1}{r} \frac{\partial}{\partial r} \left( r \frac{\partial \hat{A}_\varphi}{\partial r} \right) - k^2 \hat{A}_\varphi - \frac{\hat{A}_\varphi}{r^2} = \mu_0 \sigma_{Na} \left[ i(u_z k - \omega_B) \hat{A}_\varphi - u_r \frac{1}{r} \frac{\partial (r \cdot \hat{A}_\varphi)}{\partial r} \right] \quad (123)$$

The continuity equation has only contributions from the perturbed flow:

$$\frac{\partial u'_z}{\partial z} = - \left( \frac{\partial u'_r}{\partial r} + \frac{u'_r}{r} \right) \quad (124)$$

In laminar flow, the vorticity equation reads:

$$\frac{\partial \boldsymbol{\omega}}{\partial t} + (\mathbf{u} \cdot \nabla) \boldsymbol{\omega} = \nu_{Na} \nabla^2 \boldsymbol{\omega} + \frac{1}{\rho_{Na}} \nabla \times \mathbf{F}_{mag} \quad (125)$$

For the case being it yields:

$$\frac{\partial \omega}{\partial t} + u_r \frac{\partial \omega}{\partial r} + u_z \frac{\partial \omega}{\partial z} = \nu \left[ \frac{1}{r} \frac{\partial}{\partial r} \left( r \frac{\partial \omega}{\partial r} \right) + \frac{\partial^2 \omega}{\partial z^2} - \frac{\omega}{r^2} \right] + \frac{1}{\rho_{Na}} \left[ \frac{\partial F_r}{\partial z} - \frac{\partial F_z}{\partial r} \right] \quad (126)$$

And electromagnetic force:

$$\mathbf{F}_{mag} = \mathbf{j} \times \mathbf{B} = \begin{bmatrix} j_0 B_z \\ 0 \\ -j_0 B_r \end{bmatrix} = \begin{bmatrix} F_r \\ 0 \\ F_z \end{bmatrix} \quad (127)$$

Owing to the importance of inertia effects, we assume that the velocity field cannot oscillate at the pulsation  $2\omega_B$  of electromagnetic forces [14], so that the liquid metal flow only reacts to their mean part:

$$\begin{aligned}\bar{F}_r &= \overline{Re(\hat{j}_0 e^{i(kz-\omega_B t)}) \cdot Re(\hat{B}_{z0} e^{i(kz-\omega_B t)})} \\ &= \frac{1}{4} \overline{(\hat{j}_0 e^{i(kz-\omega_B t)} + cc) \cdot (\hat{B}_{z0} e^{i(kz-\omega_B t)} + cc)} = \frac{1}{2} Re(\hat{j}_0 \hat{B}_{z0}^*)\end{aligned}\quad (128)$$

$$\begin{aligned}\bar{F}_z &= -\overline{Re(\hat{j}_0 e^{i(kz-\omega_B t)}) \cdot Re(\hat{B}_{r0} e^{i(kz-\omega_B t)})} \\ &= -\frac{1}{4} \overline{(\hat{j}_0 e^{i(kz-\omega_B t)} + cc) \cdot (\hat{B}_{r0} e^{i(kz-\omega_B t)} + cc)} = -\frac{1}{2} Re(\hat{j}_0 \hat{B}_{r0}^*)\end{aligned}\quad (129)$$

We express current and magnetic field in terms of vector potential:

$$\begin{aligned}\mathbf{j} &= \sigma \left( -\frac{\partial \mathbf{A}_{total}}{\partial t} + \mathbf{u} \times (\nabla \times \mathbf{A}_{total}) \right) \\ &= \sigma \left( i \omega_B \hat{A}_\varphi - i u_z k \hat{A}_\varphi + u_r \frac{1}{r} \frac{\partial (r \cdot \hat{A}_\varphi)}{\partial r} \right) e^{i(kz-\omega_B t)} \mathbf{e}_\phi\end{aligned}\quad (130)$$

$$\mathbf{B} = \nabla \times \mathbf{A}_{total} = \begin{bmatrix} -ik \hat{A}_\varphi e^{i(kz-\omega_B t)} \\ 0 \\ \frac{1}{r} \frac{\partial (r \cdot \hat{A}_\varphi)}{\partial r} e^{i(kz-\omega_B t)} \end{bmatrix} = \begin{bmatrix} B_r \\ 0 \\ B_z \end{bmatrix}\quad (131)$$

So both force components become:

$$\bar{F}_r = \frac{\sigma}{2} Re \left( i(\omega_B - u_z k) \hat{A}_\varphi \left( \frac{1}{r} \frac{\partial (r \cdot \hat{A}_\varphi^*)}{\partial r} \right) + u_r \left( \frac{1}{r} \frac{\partial (r \cdot \hat{A}_\varphi)}{\partial r} \right) \left( \frac{1}{r} \frac{\partial (r \cdot \hat{A}_\varphi^*)}{\partial r} \right) \right)\quad (132)$$

$$\bar{F}_z = \frac{\sigma}{2} Re \left( k(\omega_B - u_z k) |\hat{A}_\varphi|^2 - i k u_r \left( \frac{1}{r} \frac{\partial (r \cdot \hat{A}_\varphi)}{\partial r} \right) \hat{A}_\varphi^* \right)\quad (133)$$

With star superscript (\*) indicating a complex conjugate.

This reasoning puts in evidence that if we neglect the viscous diffusion of vorticity (which is valid outside the boundary layers), only irrotational electromagnetic forces allow the vorticity not to change along the trajectory, i.e.  $D\omega/dT = 0$ , which is necessary at the established flow  $U_0(r)$ . Therefore, the established base flow requires irrotational forces (deriving from a potential), and then compensated by a pressure gradient. Consequently, this "basic" case implies that the rotational forces will cause the profile to evolve (by the non-zero term  $D\omega/dT$ ) towards the basic profile or not.

## CHAPTER 3

This means for the basic flow solution that we can assume the fluid equation as a balance of uniform pressure gradient and axial electromagnetic force. This will be considered latter in following developments.

In order to simplify equations (123) and (126) we consider perturbations  $u'_r, u'_z, \hat{a}$  function of  $r$  only (as the base solution  $U_0, \hat{A}_0$ ). Thus, we study the stability of the perturbations of the basic solution for velocity profile and vector potential in section 3.1.2.2. For such a perturbation, only function of  $r$ , the continuity equation shows that there is no radial component of the velocity. The components of the electromagnetic force then verify:

$$\frac{\partial \overline{F_r}}{\partial z} = 0, \quad \frac{\partial \overline{F_z}}{\partial r} = \frac{\sigma}{2} \frac{\partial}{\partial r} \left( k(u_z k - \omega_B) |\hat{A}|^2 \right) \quad (134)$$

And the equations of induction and vorticity with neglected friction at walls read:

$$\frac{1}{r} \frac{\partial}{\partial r} \left( r \frac{\partial \hat{A}}{\partial r} \right) - k^2 \hat{A} - \frac{\hat{A}}{r^2} = \mu_0 \sigma [i(\omega_B - u_z k) \hat{A}] \quad (135)$$

$$\nu_{Na} \rho_{Na} \left[ \frac{1}{r} \frac{\partial}{\partial r} \left( r \frac{\partial \tilde{\omega}}{\partial r} \right) - \frac{\tilde{\omega}}{r^2} \right] = \frac{\sigma}{2} \frac{\partial}{\partial r} \left( k(u_z k - \omega_B) |\hat{A}|^2 \right) \quad (136)$$

In non-dimensional form, the system of equations becomes:

$$\left[ \frac{1}{r} \frac{\partial}{\partial r} \left( r \frac{\partial}{\partial r} \right) - \frac{1}{r^2} - 1 \right] \tilde{A} = i Rm_B (1 - \tilde{u}_z) \tilde{A} \quad (137)$$

$$\left[ \frac{1}{\tilde{r}} \frac{\partial}{\partial \tilde{r}} \left( \tilde{r} \frac{\partial \tilde{\omega}}{\partial \tilde{r}} \right) - \frac{\tilde{\omega}}{\tilde{r}^2} \right] = -\frac{1}{2} \left( \frac{1}{kd_h} \right)^2 Ha^2 \left( \frac{\partial}{\partial \tilde{r}} \left[ (1 - \tilde{u}_z) |\tilde{A}|^2 \right] \right) \quad (138)$$

Where  $kd_h$  is the ratio of the hydraulic diameter to the reference length  $\lambda/2\pi$ , where  $\lambda$  is the wavelength of the travelling magnetic field and  $Ha$  is the Hartmann number described in precedent chapter.

Linearized, equation (137) turns into:

$$\left[ \frac{1}{r} \frac{\partial}{\partial r} \left( r \frac{\partial}{\partial r} \right) - \frac{1}{r^2} - 1 - i Rm_B (1 - \tilde{U}_0) \right] \tilde{\alpha} = i Rm_B \tilde{u}_z' \tilde{A}_0 \quad (139)$$

If we express equation (138) in terms of velocities:

$$\left[ \frac{1}{\tilde{r}} \frac{\partial}{\partial \tilde{r}} \left( \tilde{r} \frac{\partial^2 \tilde{u}_z}{\partial \tilde{r}^2} \right) - \frac{1}{\tilde{r}^2} \frac{\partial \tilde{u}_z}{\partial \tilde{r}} \right] = -\frac{1}{2} \left( \frac{1}{kd_h} \right)^2 Ha^2 \left( \frac{\partial}{\partial \tilde{r}} \left[ (1 - \tilde{u}_z) |\tilde{A}|^2 \right] \right) \quad (140)$$

Which linearized becomes:

$$\begin{aligned} & \left[ \frac{1}{\tilde{r}} \frac{\partial}{\partial \tilde{r}} \left( \tilde{r} \frac{\partial^2 \tilde{w}'}{\partial \tilde{r}^2} \right) - \frac{1}{\tilde{r}^2} \frac{\partial \tilde{w}'}{\partial \tilde{r}} \right] = \\ & = \frac{1}{2} \left( \frac{1}{kd_h} \right)^2 Ha^2 \left( \frac{\partial}{\partial \tilde{r}} \left[ 2(1 - \tilde{U}_0) Re(\tilde{A}_0^* \tilde{\alpha}) - \tilde{u}_z' Re(\tilde{A}_0 \tilde{A}_0^*) \right] \right) \end{aligned} \quad (141)$$

The perturbed system to solve is formed by equations (139) and (141). We can appreciate that the steady state solution of  $\tilde{A}_0$  and  $\tilde{U}_0$  is needed in order to perform the stability analysis. Sections 4.3 and 4.4 explained in detail the obtaining of the stationary MHD base flow and magnetic field.

Now, it is possible to inject the obtained base MHD flow ( $\tilde{A}_0$  and  $\tilde{U}_0$ ) into our last system formed by (139) and (141). We look for small perturbations of the base velocity profile and magnetic potential verifying the linearized equations and boundary conditions, with particular attention to the case where there are non-zero solutions to this problem, meaning that we can add some small perturbation mode (the non-zero solution of our problem) to the base flow solution and this remains to be solution of the system. This corresponds to the so-called marginal stability threshold of our base solution:

$$\begin{cases} \tilde{A}_{Re} = \tilde{A}_{0Re}(r) + \tilde{\alpha}(r) \\ \tilde{A}_{Im} = \tilde{A}_{0Im}(r) + \tilde{\beta}(r) \end{cases} \text{ with } \begin{cases} \tilde{\alpha}(r) \ll |\tilde{A}_0| \\ \tilde{\beta}(r) \ll |\tilde{A}_0| \end{cases} \quad (142)$$

$$\tilde{\mathbf{u}} = \begin{pmatrix} 0 \\ 0 \\ \tilde{U}_0(r) \end{pmatrix} + \begin{pmatrix} 0 \\ 0 \\ \tilde{u}_z' \end{pmatrix} = \begin{pmatrix} 0 \\ 0 \\ \tilde{u}_z \end{pmatrix} \text{ with } w' \ll \tilde{U}_0 \quad (143)$$

Nevertheless, the system presented still remains quite complicate to solve. Regarding assumptions, it is congruent to use momentum conservation equation instead of vorticity equation (141), since axial component of velocity is the only to solve. The NS equation is also considered as a balance of electromagnetic force and gradient of pressure neglecting friction losses:

$$\sigma k^2 (U_B - u_z(r)) \frac{|A(r)|^2}{2} = \frac{dp}{dz} \quad (144)$$

Where we suppose that gradient of pressure is known since it is imposed by external circuit. Then, in a non-dimensional form this balance becomes:

$$Rm_B(1 - \tilde{u}_z) \frac{|\tilde{A}|^2}{2} = G \quad (145)$$

Or in another manner:

$$Rm_B(1 - \tilde{u}_z) = \frac{2G}{\tilde{A}\tilde{A}^*} \quad (146)$$

Injecting equation (146) into perturbed induction equation (137) we obtain:

$$\left[ \frac{1}{r} \frac{\partial}{\partial r} \left( r \frac{\partial}{\partial r} \right) - \frac{1}{r^2} \right] \tilde{A} = \left( 1 + i \frac{2G}{\tilde{A}\tilde{A}^*} \right) \tilde{A} \quad (147)$$

So, two equations from real and imaginary part of (147) come out:

$$\begin{cases} \frac{1}{r} \frac{\partial}{\partial r} \left( r \frac{\partial \tilde{A}_{Re}}{\partial r} \right) - \frac{\tilde{A}_{Re}}{r^2} = \tilde{A}_{Re} - \frac{2G}{\tilde{A}_{Re}^2 + \tilde{A}_{Im}^2} \tilde{A}_{Im} \\ \frac{1}{r} \frac{\partial}{\partial r} \left( r \frac{\partial \tilde{A}_{Im}}{\partial r} \right) - \frac{\tilde{A}_{Im}}{r^2} = \tilde{A}_{Im} + \frac{2G}{\tilde{A}_{Re}^2 + \tilde{A}_{Im}^2} \tilde{A}_{Re} \end{cases} \quad (148)$$

With perturbation (142) and linearizing:

$$\begin{cases} \frac{1}{r} \frac{\partial}{\partial r} \left( r \frac{\partial \tilde{\alpha}}{\partial r} \right) - \frac{\tilde{\alpha}}{r^2} = \tilde{\alpha} \left( 1 + 4G \frac{\tilde{A}_{0Re}\tilde{A}_{0Im}}{|\tilde{A}_0|^4} \right) + \tilde{\beta} \left( -2G \frac{\tilde{A}_{0Re}^2 - \tilde{A}_{0Im}^2}{|\tilde{A}_0|^4} \right) \\ \frac{1}{r} \frac{\partial}{\partial r} \left( r \frac{\partial \tilde{\beta}}{\partial r} \right) - \frac{\tilde{\beta}}{r^2} = \tilde{\alpha} \left( 2G \frac{\tilde{A}_{0Im}^2 - \tilde{A}_{0Re}^2}{|\tilde{A}_0|^4} \right) + \tilde{\beta} \left( 1 - 4G \frac{\tilde{A}_{0Re}\tilde{A}_{0Im}}{|\tilde{A}_0|^4} \right) \end{cases} \quad (149)$$

So, in a more condensed manner, we can express this in terms of four parameters (A, B, C and D) fully dependent on base MHD flow solution:

$$\begin{cases} \frac{\partial^2 \tilde{\alpha}}{\partial r^2} + \frac{1}{r} \frac{\partial \tilde{\alpha}}{\partial r} - \frac{\tilde{\alpha}}{r^2} = \tilde{\alpha}A + \tilde{\beta}B \\ \frac{\partial^2 \tilde{\beta}}{\partial r^2} + \frac{1}{r} \frac{\partial \tilde{\beta}}{\partial r} - \frac{\tilde{\beta}}{r^2} = \tilde{\alpha}C + \tilde{\beta}D \end{cases} \quad (150)$$

Where that the parameters verify  $B \equiv C$  and  $A + D \equiv 2$

A general form of perturbation verifying the system of equations for  $\tilde{\alpha}$  and  $\tilde{\beta}$  is chosen:

$$\begin{cases} \tilde{\alpha} = \text{Re}(\hat{\alpha}e^{sr}) \\ \tilde{\beta} = \text{Re}(\hat{\beta}e^{sr}) \end{cases} \quad (151)$$

Where  $s$  is the complex number  $s = s_r + is_i$ ,  $\hat{\alpha}$  and  $\hat{\beta}$  are the complex amplitudes of the perturbations of the real and imaginary parts of  $\tilde{A}$ . Notice that any perturbation can be expressed using such modes using a Fourier transform.

Injecting these expressions, the following system is obtained from (150):

$$\begin{cases} \left(s^2 + \frac{s}{\tilde{r}} - \frac{1}{\tilde{r}^2}\right) \hat{\alpha} = \hat{\alpha}A + \hat{\beta}B \\ \left(s^2 + \frac{s}{\tilde{r}} - \frac{1}{\tilde{r}^2}\right) \hat{\beta} = \hat{\alpha}B + \hat{\beta}D \end{cases} \quad (152)$$

Assuming that this system should have a non-zero solution  $(\hat{\alpha}, \hat{\beta})$ , we obtain the characteristic equation that will define the shape of the perturbation mode:

$$s^4 + \frac{2s^3}{\tilde{r}} - \left(\frac{2\tilde{r}^2 + 1}{\tilde{r}^2}\right)s^2 - \left(\frac{2\tilde{r}^2 + 2}{\tilde{r}^3}\right)s + \left(\frac{2\tilde{r}^2 + 1}{\tilde{r}^4}\right) = B^2 - AD \quad (153)$$

$$\text{Where } B^2 - AD = \frac{4G^2}{|\tilde{A}_0|^4} - 1$$

This last equation (153) gives as solution the complex exponent of vector potential perturbation. Obtaining of instability marginal threshold would consist on finding the global *Rms* regime proving the existence of this exponential form of perturbation. However, equation (152) is dependent on radius, so in order to obtain the global threshold of instability (and not dependent on  $r$ ) we have averaged it over the height of the channel:

$$\begin{aligned} s^4(\tilde{R}_2 - \tilde{R}_1) + 2s^3 \ln\left(\frac{\tilde{R}_2}{\tilde{R}_1}\right) + \left(\frac{1}{\tilde{R}_2} - \frac{1}{\tilde{R}_1} - 2(\tilde{R}_2 - \tilde{R}_1)\right)s^2 \\ + \left(\frac{1}{\tilde{R}_2^2} - \frac{1}{\tilde{R}_1^2} - 2\ln\left(\frac{\tilde{R}_2}{\tilde{R}_1}\right)\right)s - (\tilde{R}_2 - \tilde{R}_1) - 2\left(\frac{1}{\tilde{R}_2} - \frac{1}{\tilde{R}_1}\right) \\ - \frac{1}{3}\left(\frac{1}{\tilde{R}_2^3} - \frac{1}{\tilde{R}_1^3}\right) = \int_{\tilde{R}_1}^{\tilde{R}_2} \frac{4G^2}{|\tilde{A}_0|^4} d\tilde{r} \end{aligned} \quad (154)$$

Using our coupled solution (velocity profile + vector potential) computed in part 3.1.2.2 from equations (76) and (80), to calculate the right-hand side of equation (154), we can find the roots of this fourth degree equation for  $s$  using numerical methods. *Figure 57* shows the real and imaginary parts of the four possible values for the  $s$  exponent as a function of the global

$Rms$  of the MHD flow. These values are obtained using the parameters of *Table I* of previous chapter for the PEMDyn pump.

In *Figure 57* and *Figure 58* it can be noted that two of the roots are completely real (s1 and s4). For the other two roots (s2 and s3) *Figure 59A* shows that at  $Rms$  lower than 1.8 roots are completely real, and that for higher values of  $Rms$  they become complex, conjugate one to the other, with small negative real part. These roots must verify boundary conditions for  $\hat{\alpha}$  and  $\hat{\beta}$  imposed by the model:

$$\begin{cases} \frac{d\tilde{\alpha}}{d\tilde{r}} + \frac{\tilde{\alpha}}{\tilde{r}} = 0 & \text{at } \tilde{r} = \tilde{R}_1 \\ \frac{d\tilde{\alpha}}{d\tilde{r}} + \frac{\tilde{\alpha}}{\tilde{r}} = 0 & \text{at } \tilde{r} = \tilde{R}_2 \end{cases} \quad (155)$$

$$\begin{cases} \frac{d\tilde{\beta}}{d\tilde{r}} + \frac{\tilde{\beta}}{\tilde{r}} = 0 & \text{at } \tilde{r} = \tilde{R}_1 \\ \frac{d\tilde{\beta}}{d\tilde{r}} + \frac{\tilde{\beta}}{\tilde{r}} = 0 & \text{at } \tilde{r} = \tilde{R}_2 \end{cases} \quad (156)$$

This permits to identify permitted perturbations by the present problem. In other words, a criterion of existence of the perturbation (157) and (158) is obtained from boundary conditions (155) and (156).

$$\begin{cases} \left[ \text{Re} \left[ \left( s + \frac{1}{\tilde{R}_1} \right) e^{s\tilde{R}_1} \right] \hat{\alpha}_r - \text{Im} \left[ \left( s + \frac{1}{\tilde{R}_1} \right) e^{s\tilde{R}_1} \right] \hat{\alpha}_i = 0 \right. \\ \left. \left[ \text{Re} \left[ \left( s + \frac{1}{\tilde{R}_2} \right) e^{s\tilde{R}_2} \right] \hat{\alpha}_r - \text{Im} \left[ \left( s + \frac{1}{\tilde{R}_2} \right) e^{s\tilde{R}_2} \right] \hat{\alpha}_i = 0 \right. \end{cases} \quad (157)$$

$$\begin{cases} \left[ \text{Re} \left[ \left( s + \frac{1}{\tilde{R}_1} \right) e^{s\tilde{R}_1} \right] \hat{\beta}_r - \text{Im} \left[ \left( s + \frac{1}{\tilde{R}_1} \right) e^{s\tilde{R}_1} \right] \hat{\beta}_i = 0 \right. \\ \left. \left[ \text{Re} \left[ \left( s + \frac{1}{\tilde{R}_2} \right) e^{s\tilde{R}_2} \right] \hat{\beta}_r - \text{Im} \left[ \left( s + \frac{1}{\tilde{R}_2} \right) e^{s\tilde{R}_2} \right] \hat{\beta}_i = 0 \right. \end{cases} \quad (158)$$

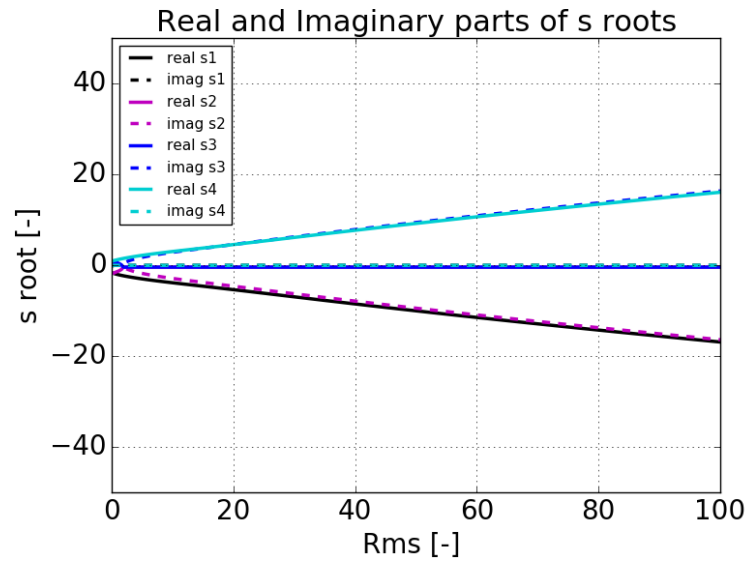


Figure 57: Comparison of the four Roots of perturbation exponent

We can express it more condensed as:

$$\begin{cases} Re[C_1] \hat{\alpha}_r - Im[C_1] \hat{\alpha}_i = 0 \\ Re[C_2] \hat{\alpha}_r - Im[C_2] \hat{\alpha}_i = 0 \end{cases} \quad (159)$$

With same system for  $\hat{\beta}$ .

Then, criterion for existence of the perturbation, also called marginal instability criterion, is:

$$Re(C_1)Im(C_2) - Re(C_2)Im(C_1) = 0 \quad (160)$$

This last equation (160) is plotted on zoom of *Figure 59B* and in *Figure 60* for each one of the four roots, named as criterion followed by the number of the root. The existence criterion for perturbation is fulfilled when it reaches zero.

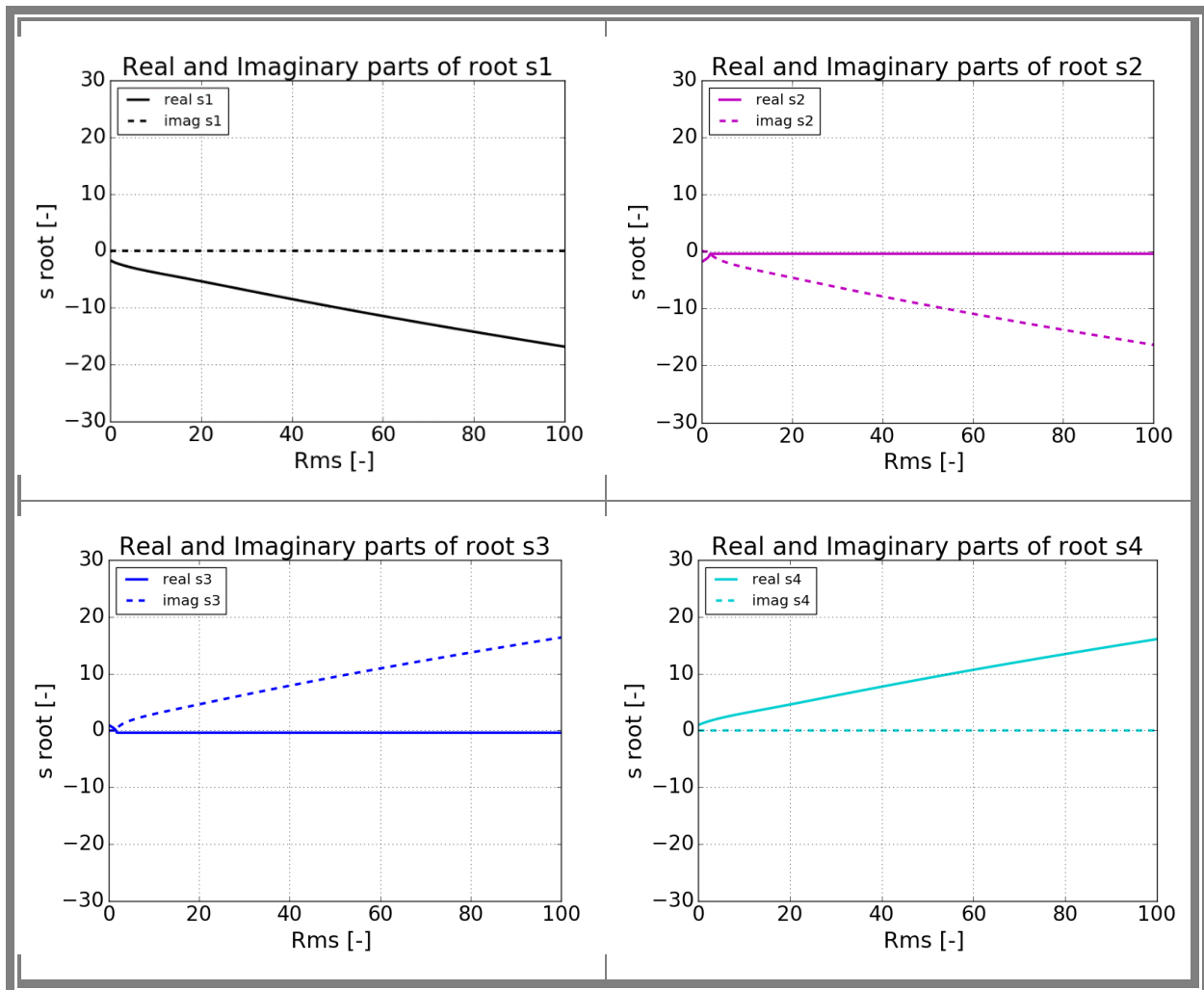


Figure 58 : Real and imaginary parts of roots of perturbation exponent

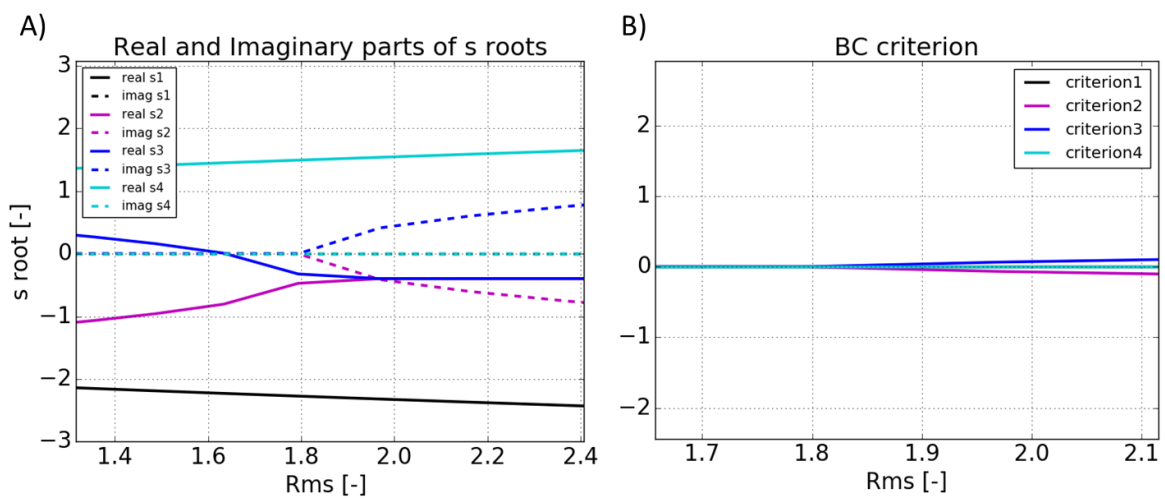
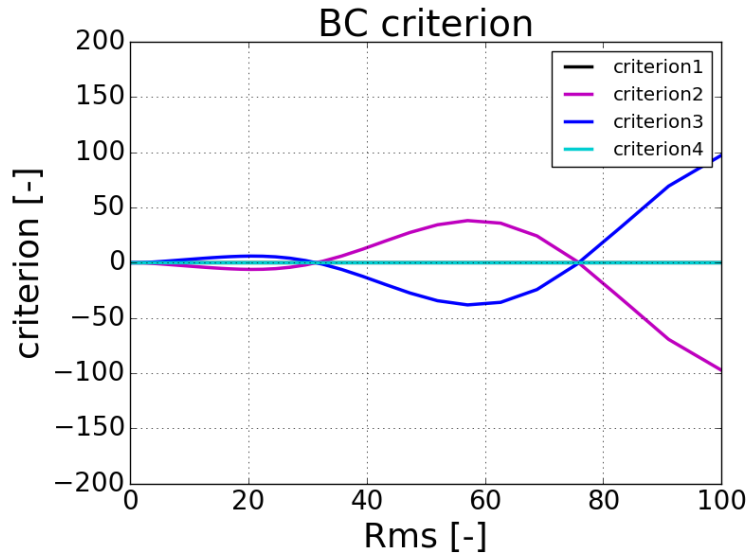


Figure 59: A) Zoom on Roots of perturbation exponent B) Zoom on Boundary condition criterion of marginal instability for higher values of Rms

It is important to note that, in order to avoid from having a trivial solution ( $\hat{\alpha}_r = 0$  and  $\hat{\alpha}_i = 0$ ), neither real nor imaginary parts of  $C_1$  and  $C_2$  must be equal to zero. Therefore, criterions 1 and 4 can be discarded for all regimes and criterions 2 and 3 for regimes with  $Rms$  lower than 1.8, since only real part is present there. As a result, we can conclude that the zoom of *Figure 59B* does not show a global  $Rms$  value for which marginal stability criterion is attained.

However, looking at higher values of  $Rms$ , we see on *Figure 60* that criterion is reached several times at precise values of  $Rms$  for both criterions 2 and 3. As a matter of fact, the first threshold is reached at  $Rms$  around 30, which is indeed quite large compared to normal regimes of an EMIP.



*Figure 60: Boundary condition criterion of marginal instability for higher values of  $Rms$*

In conclusion, marginal instability threshold is obtained for big values of global  $Rms$ , which a priori, are not reached in an EMIP since for a supply frequency of 20 Hz and PEMDyn dimensions, maximum  $Rms$  expected is 11.23 at sodium velocity equal to zero.

### 3.2.3. Energetic stability analysis

The last method explored here to study the stability of the MHD flow in an ALIP is the energetic approach. As it was presented in bibliographic study, this method provides complementary results to the linear stability thresholds since it permits to consider all kind of perturbations, including all sizes.

For the current problem, we examine a liquid metal flow delimited by two parallel planes on the  $z$  axis, at heights  $H$  and 0 respectively. On the upper plane, a sheet of alternative current density is applied and at the bottom perfect ferromagnetic condition is considered. Here, we can describe a stationary state for velocity and magnetic field in the form:

$$\mathbf{U}_0 = \begin{cases} U_0(r) \\ 0 \\ 0 \end{cases} \quad \text{and} \quad \mathbf{B}_0 = \begin{cases} B_{r0}(r, z, t) \\ 0 \\ B_{z0}(r, z, t) \end{cases} \quad (161)$$

In order to study the energetic stability of the MHD flow, we must analyze its behavior regarding any kind of disturbance:

$$\mathbf{U} = \mathbf{U}_0 + \mathbf{u}'(r, \phi, z, t) \quad (162)$$

$$\mathbf{B} = \mathbf{B}_0 + \mathbf{b}'(r, \phi, z, t) \quad (163)$$

So the perturbed state system of equations with boundary conditions becomes:

$$\begin{aligned} \frac{\partial \mathbf{u}'}{\partial t} + (\mathbf{U}_0 \cdot \nabla) \mathbf{u}' + (\mathbf{u}' \cdot \nabla) \mathbf{u}' + (\mathbf{u}' \cdot \nabla) \mathbf{u}' = \\ = -\nabla p + \nu_{Na} \Delta \mathbf{u}' + \frac{1}{\mu_0 \rho_{Na}} [(\mathbf{B}_0 \cdot \nabla) \mathbf{b}' + (\mathbf{b}' \cdot \nabla) \mathbf{B}_0 + (\mathbf{b}' \cdot \nabla) \mathbf{b}'] \end{aligned} \quad (164)$$

$$\nabla \cdot \mathbf{u}' = 0 \quad (165)$$

$$\frac{\partial \mathbf{b}'}{\partial t} + (\mathbf{U}_0 \cdot \nabla) \mathbf{b}' + (\mathbf{u}' \cdot \nabla) \mathbf{B}_0 + (\mathbf{u}' \cdot \nabla) \mathbf{b}' = \eta \Delta \mathbf{b}' + (\mathbf{B}_0 \cdot \nabla) \mathbf{u}' + (\mathbf{b}' \cdot \nabla) \mathbf{U}_0 + (\mathbf{b}' \cdot \nabla) \mathbf{u}' \quad (166)$$

$$\nabla \cdot \mathbf{b}' = 0 \quad (167)$$

$$\text{BC} : \begin{cases} \mathbf{u}' = 0 \text{ at } r = H \text{ and } z = 0 \\ b'_r = b'_z = \partial_r b'_r = 0 \text{ at } r = H \text{ and } z = 0 \end{cases} \quad (168)$$

With  $\eta = 1/\mu_0 \sigma_{Na}$ .

We must point out that periodicity of solution is considered on  $\phi$  and  $z$ .

Now, temporal evolution equations for kinetic and magnetic energy are obtained multiplying equations (164) and (166) by velocity and magnetic field disturbances respectively and integrating them over the volume of the domain. They read:

$$\begin{aligned} \frac{\partial}{\partial t} \int \left( \frac{\mathbf{u}'^2}{2} \right) dV + \int \mathbf{u}' \cdot (\nabla \mathbf{U}_0) \cdot \mathbf{u}' dV = \\ = \int \left\{ -\nu |\nabla \mathbf{u}'|^2 + \frac{1}{\rho_{Na} \mu_0} [\mathbf{B}_0 \cdot (\nabla \mathbf{b}') \cdot \mathbf{U}_0 + \mathbf{b}' \cdot (\nabla \mathbf{B}_0) \cdot \mathbf{u}' + \mathbf{b}' \cdot (\nabla \mathbf{b}') \cdot \mathbf{u}'] \right\} dV \end{aligned} \quad (169)$$

$$\frac{\partial}{\partial t} \int \left( \frac{\mathbf{b}'^2}{2} \right) dV + \int \mathbf{b}' \cdot (\nabla \mathbf{U}_0) \cdot \mathbf{b}' dV = \quad (170)$$

$$= \int \{-\eta |\nabla \mathbf{b}'|^2 + [\mathbf{B}_0 \cdot (\nabla \mathbf{u}') \cdot \mathbf{b}' + \mathbf{b}' \cdot (\nabla U_0) \cdot \mathbf{b}' + \mathbf{b}' \cdot (\nabla \mathbf{u}') \cdot \mathbf{b}']\} dV$$

Notice that terms at the borders get zero by periodicity on  $\varphi$  and  $z$  and by boundary conditions on  $r$ .

From those equations, we can write the evolution of the total energy under the form:

$$\begin{aligned} \frac{d\xi}{dt} = & \frac{\partial}{\partial t} \int \left( \frac{\mathbf{u}'^2}{2} \right) dV + \frac{\partial}{\partial t} \int \left( \frac{\mathbf{b}'^2}{2\rho\mu_0} \right) dV = \\ & \int -\mathbf{u}' \cdot (\nabla V) \mathbf{u}' + \frac{1}{\rho\mu_0} [\mathbf{b}' \cdot (\nabla \mathbf{B}_0) \cdot \mathbf{u}' - \mathbf{u}' \cdot (\nabla \mathbf{B}_0) \cdot \mathbf{b}' + \mathbf{b}' \cdot (\nabla U_0) \cdot \mathbf{b}'] - \\ & - \frac{\eta}{\rho_{Na}\mu_0} |\nabla \mathbf{b}'|^2 - \nu |\nabla \mathbf{u}'|^2 dV \end{aligned} \quad (171)$$

Or splitted in different terms:

$$\frac{d\xi}{dt} = \int \left\{ \overset{1)}{\mathbf{u}' \cdot (\nabla U_0) \mathbf{u}'} + \frac{1}{\rho_{Na}\mu_0} \overset{2)}{[\mathbf{b}' \cdot (\nabla \mathbf{B}_0) \mathbf{u}']} - \overset{3)}{\mathbf{u}' \cdot (\nabla \mathbf{B}_0) \mathbf{b}'} + \overset{4)}{\mathbf{b}' \cdot (\nabla U_0) \mathbf{b}'} - \overset{5)}{\nu_{Na} |\nabla \mathbf{u}'|^2} - \overset{6)}{\frac{\eta}{\rho_{Na}\mu_0} |\nabla \mathbf{b}'|^2} \right\} dV \quad (172)$$

Energy evolution in time can be also seen as a functional dependent on velocity and magnetic field disturbances:

$$\frac{d\xi}{dt} = H\{\mathbf{u}', \mathbf{b}'\} \quad (173)$$

The approach to be followed is based on the obtaining of the space of parameter for our system ( $J_{peak}, \eta, \nu \dots$ ) such that  $H\{\mathbf{u}', \mathbf{b}'\} = 0$  for all velocity and magnetic fields satisfying the boundary conditions and that make  $\nabla \cdot \mathbf{u}' = 0$  and  $\nabla \cdot \mathbf{b}' = 0$ . In other words, we seek for the biggest region of the space of parameters ( $J_0, \eta, \nu \dots$ ) fulfilling  $H\{\mathbf{u}', \mathbf{b}'\} < 0$ . As a result, all disturbances decrease over the time regardless of their initial amplitude. This locus is named energetic stability region.

For the current case, we have focused on the estimate approach, which consists of considering simple approximations for each one of the terms in equation (171) from the knowledge of the problem, such as the basic flow solution or information about the disturbance input. Nevertheless, the tricky point using this method lies on paying attention to keep these estimates realistic.

This result can then be improved using variational techniques, which permits to obtain the optimal disturbance using Euler-Lagrange equation. Unfortunately, in this research we have decided to leave this question open for latter studies.

The goal is to obtain the energy threshold for which any disturbance inserted is damped by the system. For this, we use penalizing estimates of the terms of increase/decrease of energy. That is, the approach consists in maximizing the terms in red 1 to 4 in equation (172), which can potentially increase energy of the system and minimizing the energy dissipation terms in blue 5 and 6. In such a way, we seek to obtain the threshold from which the system concerning the introduction of a disturbance makes positive the variation of energy of the system for the most hostile situation that can occur for a specific regime.

Following this logic, we maximize terms 1 to 4:

1)

$$\begin{aligned} \left| \iiint \mathbf{u}'(\nabla \mathbf{U}_0) \mathbf{u}' dV \right| &\leq \iiint |u'_i| |\partial_i U_{0j}| |u'_j| dV \\ &\leq \sum_{i,j} \text{Max}_{vol} |\partial_i U_{0j}| \iiint |u'_i| |u'_j| dV \\ &\leq \|\nabla \mathbf{U}_0\|_\infty \cdot 3 \cdot \iiint |\mathbf{u}'|^2 dV \end{aligned}$$

2)

$$\begin{aligned} \frac{1}{\rho_{Na}\mu_0} \left| \iiint \mathbf{b}'(\nabla \mathbf{B}_0) \mathbf{u}' dV \right| &\leq \frac{\|\nabla \mathbf{B}_0\|_\infty}{\sqrt{\rho_{Na}\mu_0}} \iiint \left[ \frac{|\mathbf{b}'|^2}{2\rho_{Na}\mu_0} + \frac{|\mathbf{u}'|^2}{2} \right] dV \\ &\leq \frac{\|\nabla \mathbf{B}_0\|_\infty}{\sqrt{\rho_{Na}\mu_0}} \cdot 3\xi \end{aligned}$$

3)

$$\begin{aligned} \frac{1}{\rho_{Na}\mu_0} \left| \iiint \mathbf{u}'(\nabla \mathbf{B}_0) \mathbf{b}' dV \right| &\leq \frac{\|\nabla \mathbf{B}_0\|_\infty}{\sqrt{\rho_{Na}\mu_0}} \iiint \left[ \frac{|\mathbf{u}'|^2}{2} + \frac{|\mathbf{b}'|^2}{2\rho_{Na}\mu_0} \right] dV \\ &\leq \frac{\|\nabla \mathbf{B}_0\|_\infty}{\sqrt{\rho_{Na}\mu_0}} \cdot 3\xi \end{aligned}$$

4)

$$\begin{aligned} \frac{1}{\rho_{Na}\mu_0} \left| \iiint \mathbf{b}'(\nabla \mathbf{U}_0) \mathbf{b}' dV \right| &\leq \frac{1}{\rho\mu_0} \iiint |b'_i| |\partial_i U_{0j}| |b'_j| dV \\ &\leq \|\nabla \mathbf{U}_0\|_\infty \cdot 3 \cdot \iiint \frac{|\mathbf{b}'|^2}{\rho_{Na}\mu_0} dV \end{aligned}$$

So, expression (172) becomes:

$$\frac{d\xi}{dt} \leq \left[ 6\|\nabla\mathbf{U}_0\|_\infty + 6\frac{\|\nabla\mathbf{B}_0\|_\infty}{\sqrt{\rho_{Na}\mu_0}} \right] \cdot \xi - \iiint \left[ \frac{\eta}{\rho_{Na}\mu_0} |\nabla\mathbf{b}'|^2 - \nu_{Na} |\nabla\mathbf{u}'|^2 \right] dV \quad (174)$$

Now, we look for the estimates minimizing quadratic gradients of disturbances. The Poincare's inequality makes it possible to estimate these terms for disturbances bounded at extremes.

This reads:

*« Let  $f(z)$  be a smooth function which vanishes at the frontier. Then, it can be decomposed using Fourier series:*

$$f(z) = \sum_{n=1}^{\infty} a_n \sin\left(n\pi \frac{z}{H}\right)$$

$$f(0) = f(H) = 0$$

*Such that:*

$$\int_{z=0}^H f^2(z) dz = \sum_{n=1}^{\infty} \sum_{p=1}^{\infty} a_n a_p \int_{z=0}^H \sin\left(n\pi \frac{z}{H}\right) \sin\left(p\pi \frac{z}{H}\right) dz = \sum_{n=1}^{\infty} \frac{H}{2} a_n^2$$

*Where:*

$$f'(z) = \sum_{n=1}^{\infty} \frac{n\pi}{H} a_n \cos\left(n\pi \frac{z}{H}\right)$$

$$\int_{z=0}^H (f'(z))^2 dz = \sum_{n=1}^{\infty} \left(\frac{n\pi}{H}\right)^2 a_n^2 \frac{H}{2}$$

*Then, for  $n=1$ :*

$$\int_{z=0}^H (f'(z))^2 dz \geq \left(\frac{\pi}{H}\right)^2 \sum_{n=1}^{\infty} \frac{H}{2} a_n^2$$

*So, there exists a minimal wavenumber such that for all function  $f$  it makes:*

$$\int_{z=0}^H (f'(z))^2 dz \geq \left(\frac{\pi}{H}\right)^2 \int_{z=0}^H f^2(z) dz . \quad \gg$$

In the case of the velocity perturbation, it is logical to guess that it vanishes at the walls of the channel. On the other hand, in the case of the magnetic field disturbance one cannot assure this hypothesis, since the perfect ferromagnetic condition is imposed at the lower edge.

As mentioned above, it is necessary to know information pertaining to disturbances in order to attribute realistic estimates to diffusive terms. It is from the work on the linear stability analysis of an ALIP [23] [3] that we use the hypothesis of a convective azimuthal disturbance for both, the velocity and the magnetic field.

So, perturbations are considered in the form:

$$\mathbf{u}' = \mathbf{u}'(\varphi, z, t) = \left[ \sum_k \sum_m \delta \mathbf{u}_{km} \cos(m\varphi) \cos\left(\frac{k\pi}{L}z\right) \right] e^{st} \quad (175)$$

$$\mathbf{b}' = \mathbf{b}'(\varphi, z, t) = \left[ \sum_k \sum_m \delta \mathbf{b}'_{km} \cos(m\varphi) \cos\left(\frac{k\pi}{L}z\right) \right] e^{st} \quad (176)$$

Then, we can obtain the expression for quadratic modulus of velocity perturbation:

$$\begin{aligned} & \iint |\mathbf{u}'^2| d\varphi dz \\ &= \int_{\varphi=0}^{2\pi} \int_{z=0}^H \sum_k \sum_m \sum_{k'} \sum_{m'} \delta \mathbf{u}_{km} \delta \mathbf{u}'_{k'm'} \cos(m\varphi) \cos(m'\varphi) \cos\left(\frac{k\pi}{L}z\right) \cos(m\varphi) \cos\left(\frac{k\pi}{L}z\right) \cos\left(\frac{k'\pi}{L}z\right) d\varphi dz \\ &= \sum_k \sum_m \frac{2\pi L}{4} |\delta \mathbf{u}'_{km}|^2 \end{aligned}$$

5)

$$\begin{aligned} \int_{\varphi=0}^{2\pi} \int_{z=0}^H |\nabla \mathbf{u}'|^2 d\varphi dz &= \sum_k \sum_m \frac{2\pi L}{4} \frac{m^2}{r^2} |\delta \mathbf{u}_{km}|^2 + \sum_k \sum_m \frac{2\pi L}{4} \left(\frac{k\pi}{L}\right)^2 |\delta \mathbf{u}_{km}|^2 \\ &= \sum_k \sum_m \frac{2\pi L}{4} |\delta \mathbf{u}_{km}|^2 \left[ \frac{m^2}{r^2} + \left(\frac{k\pi}{L}\right)^2 \right] \end{aligned}$$

This resumes the same structure as the Poincare's inequality, a minimal wave number that multiplies the function.

$$\iint |\nabla \mathbf{u}'|^2 d\varphi dz \geq \text{Min} \left[ \frac{1}{R^2}, \left(\frac{\pi}{L}\right)^2 \right] \iint |\mathbf{u}'^2| d\varphi dz \quad (177)$$

And in analogous way, for the magnetic field disturbance we obtain:

6)

$$\iint |\nabla \mathbf{b}'|^2 d\varphi dz \geq \text{Min} \left[ \frac{1}{R^2}, \left( \frac{\pi}{L} \right)^2 \right] \iint |\mathbf{b}'|^2 d\varphi dz$$

Adding the two terms in the equation, we find that 5 and 6 consider themselves as:

$$\iiint \frac{\eta}{\rho_{Na}\mu_0} |\nabla \mathbf{b}'|^2 - v_{Na} |\nabla \mathbf{u}'|^2 r dr d\varphi dz \leq \text{Min}[v_{Na}, \eta] \cdot \text{Min} \left[ \frac{1}{R^2}, \left( \frac{\pi}{L} \right)^2 \right] \cdot \xi \quad (178)$$

Finally we can estimate equation (172) in the form:

$$\frac{d\xi}{dt} \leq \left[ 6\|\nabla \mathbf{U}_0\|_\infty + 6\frac{\|\nabla \mathbf{B}_0\|_\infty}{\sqrt{\rho\mu_0}} \right] \cdot \xi - \text{Min}[v_{Na}, \eta] \cdot \text{Min} \left[ \frac{1}{R^2}, \left( \frac{\pi}{L} \right)^2 \right] \cdot \xi \quad (179)$$

We note that the temporal derivative of energy in the system can be expressed as:

$$\frac{d\xi}{dt} \leq \gamma \cdot \xi \quad (180)$$

As a result, energy evolution is actually exponential, with parameter  $\gamma$  dependent on problem conditions, such as the basic flow solution and physical properties and dimensions of the system. Therefore, the energetic threshold corresponds to the limit of basic flow regime which makes coefficient  $\gamma$  equal to zero.

It is important to highlight that the two first terms in equation (179) correspond to the maximal spatial derivative for the basic solution of velocity and magnetic field respectively, which can be obtained from solution in sub-section 3.1.2.2. However, in this previous development, velocity boundary layer was not calculated since friction forces were neglected.

We know from previous dissertations about the subject that our case of study presents regimes with high interaction parameter and Hartmann number, and thus, we can consider without any problem that velocity profile is similar to that of a Hartmann flow. With this last assumption the first term in equation (179) would be the radial derivative of the Hartmann layer, since this is much more important than the radial dependency of bulk velocity. Therefore, we should not be obtaining the stability threshold for azimuthal perturbations, but the same as in the Hartmann layer case, which is indeed out of scope of our research.

Another issue to point out is that we have assumed a specific form of perturbation that permitted us to apply Poincare's inequality. In contrast to other energetic studies, we remark that in order to preserve the global character of the method disturbances must be as general as possible.

## CHAPTER 3

Consequently, this development should not be seen as a reliable method to obtain the stability threshold, but as a qualitative examination of the physical mechanisms that should produce or delay instabilities in ALIPs.

## 4. NUMERICAL DEVELOPMENTS

This chapter aims to discuss about numerical simulations of an ALIP, where the flow of an electrically conducting fluid is coupled to an oscillating electromagnetic field. Here, fully-coupled MHD calculations are carried out using “EPM-INDUC” module for ANSYS Fluent® commercial code, which has been originally developed by the EPM group (Electromagnetic Processing of Materials) of the SIMaP Laboratory in Grenoble, France. This has provided a powerful tool to Fluent for electromagnetic and MHD simulations, and in our particular case it has enabled to clarify some hints left behind in previous analytical investigations.

### 4.1. Methodology of MHD simulation of ALIPs

#### 4.1.1. Presentation of the EPM-INDUC code

The EPM-INDUC code solves Maxwell’s equations with the “quasi-steady” hypothesis of electromagnetism [46], so as to simplify the MHD system. This implies that any description of electromagnetic propagation at the speed of light is neglected, since it is supposed instantaneous. In these conditions equations read:

$$\nabla \times \mathbf{E} = -\frac{\partial \mathbf{B}}{\partial t} \quad (181)$$

$$\nabla \times \frac{\mathbf{B}}{\mu_0} = \sigma(\mathbf{E} + \mathbf{u} \times \mathbf{B}) \quad (182)$$

$$\nabla \cdot \mathbf{B} = 0 \quad (183)$$

$$\nabla \cdot (\sigma \mathbf{E}) = -\nabla \cdot (\sigma \mathbf{u} \times \mathbf{B}) \quad (184)$$

These equations are written for electrically conductive materials or not, that is to say that they remain valid for  $\sigma = 0$ . This allows to use the same equations throughout all the domain.

Nevertheless, Maxwell's equations are first-order differential equations, and then they are not adequate for direct numerical treatment, because they include 8 scalar partial differential equations for only 6 unknown scalar fields. Therefore, a rigorous derivation of a second order  $\mathbf{A}$ - $V$  formulation is employed, where  $\mathbf{A}$  is the magnetic vector potential and  $V$  the electric scalar potential. Inspired on [47], we retain that the general Maxwell problem is well posed if it is associated to boundary conditions of "perfect electrical conductor" and / or "perfect ferromagnetic conductor". Switching to the  $\mathbf{A}$ - $V$  formulation with the coulomb gauge  $\nabla \cdot \mathbf{A} = 0$ , the problem is equivalent to a second-order differential problem, in the form of Laplace operator containing other additional boundary conditions:

$$\Delta \mathbf{A} = \mu_0 \sigma \left[ -\nabla V - \frac{\partial \mathbf{A}}{\partial t} + \mathbf{u} \times (\nabla \times \mathbf{A}) \right] \text{ in } \Omega \quad (185)$$

$$\nabla \cdot (-\sigma \nabla V) = \nabla \cdot \sigma \frac{\partial \mathbf{A}}{\partial t} - \sigma \mathbf{u} \times (\nabla \times \mathbf{A}) \text{ in } \Omega \quad (186)$$

And perfect electric and magnetic boundary conditions read:

$$\left\{ \begin{array}{l} \partial A_n / \partial n = (k_1 + k_2) A_n \\ A_{t_1} = 0 \\ A_{t_2} = 0 \\ V = C^{ste} \end{array} \right. \text{ on } \Gamma_e \quad (187)$$

$$\left\{ \begin{array}{l} A_n = 0 \\ \partial A_{t_1} / \partial n = k_1 A_{t_1} \\ \partial A_{t_2} / \partial n = k_2 A_{t_2} \\ \partial V / \partial n = 0 \end{array} \right. \text{ on } \Gamma_m \quad (188)$$

Where  $\Gamma_e$  is the union of perfect electric boundaries (ideal conductors) and symmetry planes parallel to  $\mathbf{B}$ ,  $\Gamma_m$  is the union of perfect magnetic boundaries (perfect magnetic yokes) and symmetry planes perpendicular to  $\mathbf{B}$ . At boundaries the index  $n$  represents the normal direction at a boundary, and  $t_1, t_2$  are tangential coordinates directed along the main curvature axes of the surface, where the curvatures are respectively  $k_1$  and  $k_2$ .

This formulation, when combined with boundary conditions cited above, contains implicitly the Coulomb gauge ( $\nabla \cdot \mathbf{A} = 0$ ), without any penalty technique. This condition is necessary to ensure the uniqueness of the solution and also to produce a  $V$  potential, which corresponds to the voltage that can be measured with a voltmeter.

As it was mentioned previously, conservation of current densities ( $\nabla \cdot \mathbf{j} = 0$ ) is included in transport equations above. Here, the conservative character of currents is guaranteed by electric potential in an analogous manner as pressure field in fluid equations is adjusted in order to ensure continuity ( $\nabla \cdot \mathbf{v} = 0$ ). Furthermore, each component of induced electric current in the fluid constitutes a source term in Poisson equations for vector potential components, which are solved separately ones to the others. In fact, the only link among them is electric potential and boundary conditions.

Another issue to remark is that, since electromagnetic equations are linear (magnetic saturation is neglected), all the electromagnetic fields can be written in harmonic form with their (pre-conditioned) complex amplitude:

$$G(\mathbf{r}, t) = \text{Re}(\sqrt{2} \hat{G}_{rms}(\mathbf{r}) \cdot e^{i\omega t}) \text{ for scalar fields } (V \dots) \quad (189)$$

$$\mathbf{G}(\mathbf{r}, t) = \text{Re}(\sqrt{2} \hat{\mathbf{G}}_{rms}(\mathbf{r}) \cdot e^{i\omega t}) \text{ for vector fields } (\mathbf{A}, \mathbf{B}, \mathbf{j}, \mathbf{E} \dots) \quad (190)$$

Where, the complex  $\hat{\mathbf{G}}_{rms}$  (or "phasor") has a module equal to the root mean square amplitude over a period, of the sine function  $G(t)$  at point  $\mathbf{r}$  and an argument equal to its phase lag versus a fixed reference, for example the current or voltage of an electric supply. Additionally, using RMS amplitudes have the advantage to enable a simple transition towards continuous currents by setting  $\omega=0$ .

With this formalism, the induction equation (185) becomes:

$$\begin{aligned} & \text{Re}[\sqrt{2}e^{i\omega t}(-\Delta\hat{\mathbf{A}}_{rms})] = \\ & = \text{Re}\left[\sqrt{2}e^{i\omega t}\mu_0\sigma\left(-\nabla\hat{V} - i\omega\hat{\mathbf{A}}_{rms} + \mathbf{u} \times (\nabla \times \hat{\mathbf{A}}_{rms})\right)\right] \text{ in } \Omega \end{aligned} \quad (191)$$

Since both sides of this time dependent real equation are harmonic functions of time, it is equivalent to the equality of phasors (steady complex equation). Proceeding in the same manner with the current conservation equation (186), we give rise to 8 scalar diffusion equations to be solved with boundary conditions described above, using the numerical discretization process available in Fluent, based on the finite-volume method.

For the interest of the reader, all scalar equations in Cartesian and cylindrical coordinates and the bases for coding yoke boundary condition (perfect ferromagnetic) in 2D and 3D are detailed in Annex II: EPM-INDUC code structure.

In bibliography, we found that Asada et al. [39] had already adopted this approach for 3D simulations. These considerations permit to transform a linear transient problem into stationary when simulation does not seek for the description of time-dependent velocity field  $\mathbf{u}$ . As a result, convergence times are significantly decreased and analysis is more affordable and easier to post-treat, since simulation result files are not in time evolution form and thus they are much smaller in size. However, this kind of approach neglects flow fluctuations produced by the electromagnetic forces, which is a product of harmonic functions and contains a part at double of the supply frequency (DSF).

In a flow model coupled to an harmonic electromagnetic model, only the mean part over a period of electromagnetic force is considered, and thus DSF pulsations cannot be simulated. For this reason, in latter results we will always consider that DSF forces are high enough in terms of frequency to be unable to modify the fluid velocity (because of the fluid inertia) and thus unable to produce MHD instabilities (which are LF pulsations).

Once electromagnetic scalars have been estimated, the code calculates the current density and mean part of electromagnetic force, since it is averaged over a period in the case of oscillating electromagnetic fields. This last is implemented as source term into the Reynolds-Averaged Navier-Stokes (RANS) equations available on Fluent and velocity is solved for the specified turbulent model. Finally, velocity influence on magnetic field is taken into account including currents induced by the fluid velocity in order to readjust electromagnetic variables.

The iterative procedure described here is said to be a strong coupling schema, since both directions of coupling between electromagnetic and hydraulic variables are taken into account. This is illustrated in *Figure 61*.

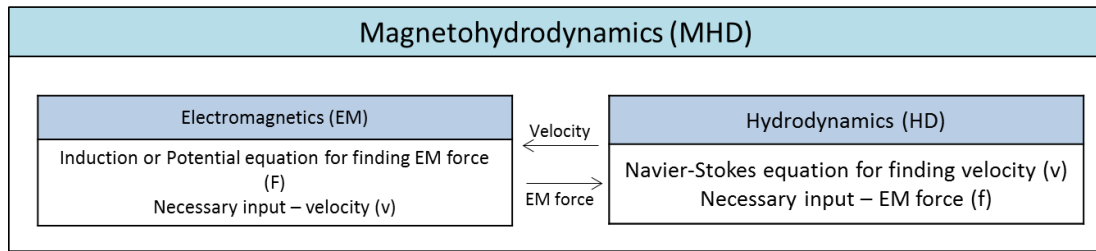


*Figure 61: Strong coupling schema using EPM-INDUC code.*

At user’s level, simulations have been carried out using the module interface, developed in Scheme language. This makes more accessible to launch simulations because first contact with the structure of code sources might result quite confusing.

Adding an induction instance is the normal way to activate the module (shown in *Figure 62*), and it can be used several times to add new instances, in the case we want to superpose several magnetic fields. This performs numerous initializations and settings, for example hooking the correct functions as source terms in the equations, which has to be done for every cell zone in the domain. Therefore, activating the module (i.e. adding an instance) can only be performed when a mesh has been read (else, an error message is issued).

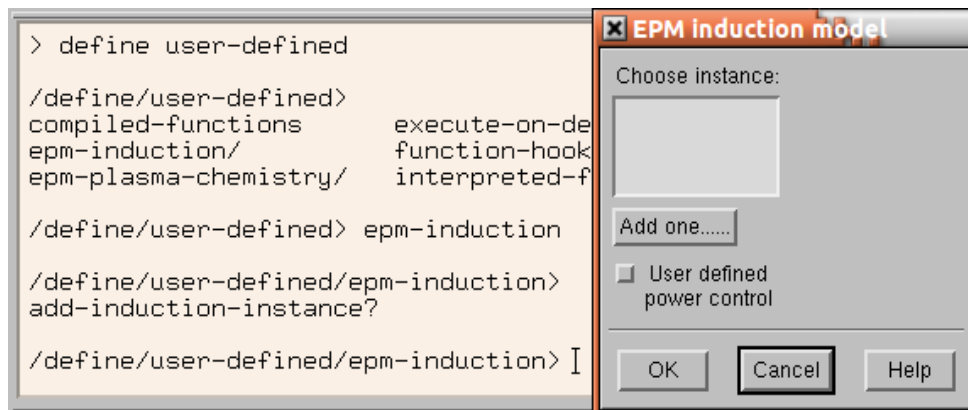


*Figure 62: EPM-INDUC submenu & panel : Activation of the module*

After activation of an instance, several new controls, devoted to the settings of physical methods and values, will be available in the menu. Following submenu in *Figure 63* will be at user’s disposal:

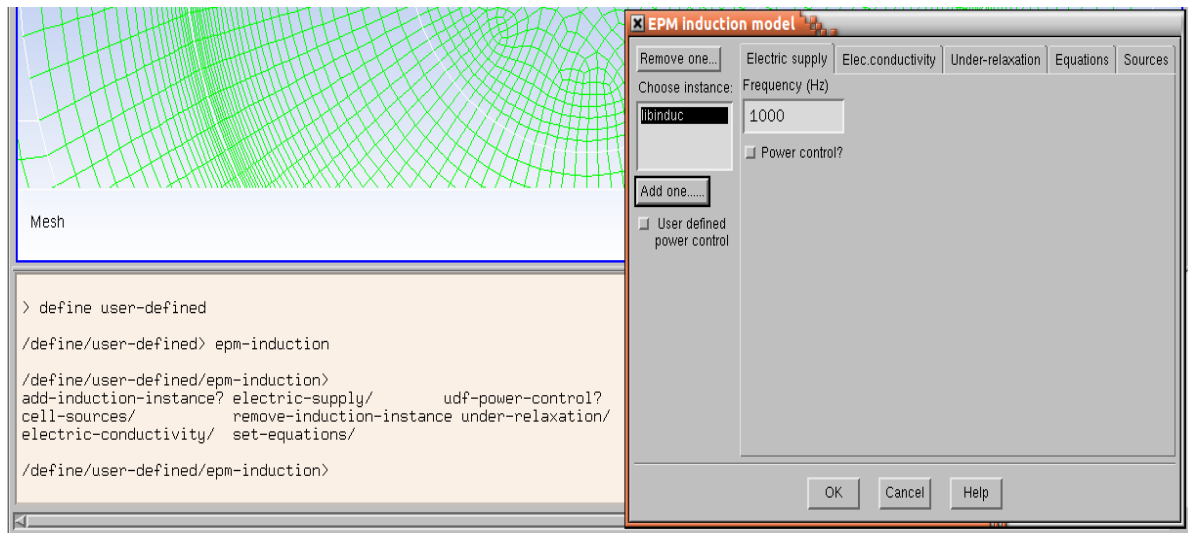


Figure 63: EPM-INDUC submenu and panel after activation of one instance

First, we notice in equations (185) and (186) that two new properties, linked to diffusivity terms, must be specified: magnetic permeability and electrical conductivity. When the EPM-INDUC module is loaded, electrical conductivity is activated in Fluent and can be modified using the standard interface for materials properties, together with the magnetic permeability which has to remain equal to the magnetic permeability of vacuum.

Then, we choose from the menu to enable or disable a subset of electromagnetic equations. For example, there is the specific option “Az only” for axisymmetric cases.

Additionally, electric supply must be specified, so the different zones of the domain are identified either as a source (input of current) or either as a charge. In the case of sources zones, we can impose the total current, the current density, or the voltage per turn in each coil for a specified supply frequency. For travelling field problems there should be either several coil zones with phase difference between their currents or a current density distribution function patched to the desired zone.

Finally, as for every transport equation used in Fluent, under-relaxation factors can be applied to electromagnetic equations in order to improve convergence if it is required.

#### 4.1.2. Description of the pump in the model

In order to validate the good performance of the code and compare numerical results with first data obtained from PEMDyn experimental loop (i.e. flow rate and developed pressure for different regimes), we have developed a simplified 2D axisymmetric model inspired in PEMDyn geometry. Based on analytical developments we can appreciate that if we consider azimuthal symmetry, the electromagnetic problem is reduced to only the azimuthal component of vector potential. This is translated in the code into a problem with only two scalars to solve (real and imaginary parts of  $\hat{A}_\phi$ ).

This consideration is acceptable for one first approach to the subject about the general performance of an ALIP, leaving aside consideration of azimuthal dependency of velocity and magnetic field, linked to the study of MHD instabilities.

In the model geometry shown in *Figure 64*, 36 coils are defined, in which the distribution of current density represents the three-phase electric supply (6 coils per phase). The sodium channel is the only domain where NS equation is solved. The inner and outer stainless-steel tubes are conducting but not ferromagnetic, and two “air” zones neither conducting nor ferromagnetic are described to model the damping of magnetic field far from the inductor.

However, upper and lower ferromagnetic cores are not defined in the model. We consider the effect of guiding and confining effect of the magnetic yoke with perfect magnetic boundary condition (188) on the edges of zones in contact with outer and inner ferromagnetic boundaries and thus, without magnetic permeability jump in our equations.

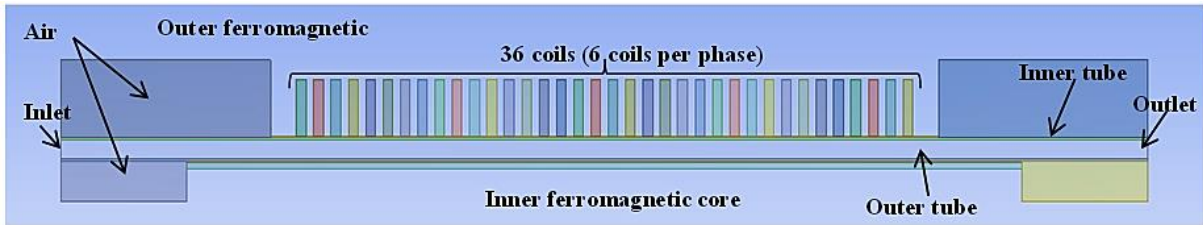


*Figure 64: Axisymmetric discrete coils model geometry*

In the current model, four materials are taken into account: Copper for the coils, steel for the rest of the pump, argon for the air domains, and liquid sodium.

*Table VIII: Material properties used in simulations at  $T_{Na} = 350\text{ C}$ .*

Sodium	Copper	Steel	Argon
$\rho = 868.8\text{ kg/m}^3$	$\rho = 8978\text{ kg/m}^3$	$\rho = 8030\text{ kg/m}^3$	$\rho = 1.6228\text{ kg/m}^3$
$\mu = 0.000307\text{ Pa s}$	$\mu = 9\text{ }10^5\text{ Pa s}$	$\mu = 5.8\text{ }10^7\text{ Pa s}$	$\mu = 0\text{ Pa s}$
$\sigma = 5.1\text{ }10^6\text{ S/m}$	$\sigma = 5.8\text{ }10^7\text{ S/m}$	$\sigma = 9\text{ }10^5\text{ S/m}$	$\sigma = 0\text{ S/m}$

Here, we must point out that sodium properties are adapted in simulations depending on working conditions. In one hand, if the aim is to simulate operation of an ALIP in the secondary loop of a SFR, then fluid temperature is close to  $350^\circ\text{C}$ , and thus conditions in *Table VIII* are used. On the other hand, sodium temperature in PEMDyn experiment is much lower, around  $170^\circ\text{C}$ . This implies different properties of sodium in *Table IX*, in particular higher electrical conductivity of sodium that must be taken into account in simulations. Following obtained results will always specify simulation conditions to the reader.

Table IX: Material properties used in simulations at  $T_{Na} = 170$  C.

Sodium	Copper	Steel	Argon
$\rho = 910.6 \text{ kg/m}^3$	$\rho = 8978 \text{ kg/m}^3$	$\rho = 8030 \text{ kg/m}^3$	$\rho = 1.6228 \text{ kg/m}^3$
$\mu = 0.004943 \text{ Pa s}$	$\mu = 9 \cdot 10^5 \text{ Pa s}$	$\mu = 5.8 \cdot 10^7 \text{ Pa s}$	$\mu = 0 \text{ Pa s}$
$\sigma = 8.1 \cdot 10^6 \text{ S/m}$	$\sigma = 5.8 \cdot 10^7 \text{ S/m}$	$\sigma = 9 \cdot 10^5 \text{ S/m}$	$\sigma = 0 \text{ S/m}$

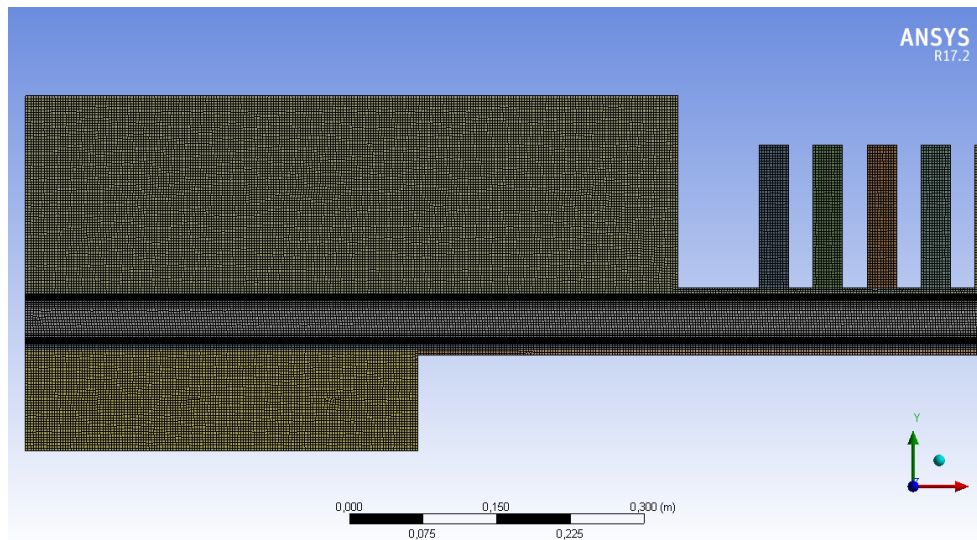
Geometrical parameters used are shown in Table X. They have been chosen close to those of PEMDyn and thus to those of the analytical solving, in order to permit the comparison.

Table X: Geometrical parameters of discrete coils model

$R_1$	Internal radius of channel	0.10955 [m]
$R_2$	External radius of channel	0.15738 [m]
$R_m$	Mean radius of channel	0.13346 [m]
$d_h$	Hydraulic gap	0.04783 [m]
$d_m$	Magnetic gap	0.06015 [m]
$L_{inductor}$	Length of inductor	1.98 [m]
$L_{channel}$	Length of the channel	3.449 [m]
$2\tau$	Pole length	0.66 [m]

For the geometry presented, a multi-zone method was used with structured mesh. This option permitted to precisely control the thickness of the cells near the walls, with a smooth increase towards the core flow. On the one hand, from a CFD point of view, a wall dimensionless thickness  $y^+$  of 1 is needed in the boundary layer (no wall function is used). This parameter is defined as  $y^+ = Uy/\nu$ , with  $U$  the sodium velocity outside the boundary layer,  $y$  the characteristic length (in this case, the thickness of the first cell) and  $\nu$  the dynamic viscosity of sodium. It results that the first layer thickness should be of 5  $\mu\text{m}$ . On the other hand, from an electromagnetic point of view, this size is sufficient to describe the velocity profile, similar to that of a Hartmann flow for cases close to synchronism, for an estimated magnetic field of 0.5 T.

The generated mesh is shown in Figure 65. It has a total of 190165 cells with maximal size of element of 2.75 mm, which is indeed a good compromise of mesh weigh for having a good description of phenomena and relatively small computational time of solving (around 20 min per simulation).



*Figure 65: Mesh used for 2D axisymmetric discrete coils model.*

Once the mesh is loaded, it is necessary to specify the general settings for the calculation. For 2D simulations we set axisymmetric and stationary calculation in the frequency domain with following boundary conditions:

1. At the boundaries representing the contact with a yoke we have applied perfect ferromagnetic condition.
2. At the inlet of the channel we apply a “mass-flow inlet” condition, which permits to impose a fixed mean velocity (in terms of mass flow with known inlet surface and fixed sodium density) with a velocity profile selected by the user. For considering this last, we had launched a previous simulation without electric supply where the developed velocity profile obtained was exported and then inserted as input of coupled simulations. The turbulent quantities are also imposed as a profile coming from this previous simulation at the synchronism velocity.
3. At the outlet, null pressure is imposed. This means that averaged inlet pressure can be interpreted as the opposite of the pressure gain provided by the EMIP, and thus during simulation we can also monitor it.

About solver settings, we have selected a pressure-based solver for incompressible flow, the “SIMPLEC” pressure-velocity coupling, and Green-Gauss cell based gradient evaluation. Discretization of the convective terms is done with the second order upwind scheme for hydrodynamic variables, “PRESTO!” discretisation of pressure, and first order upwind for the electromagnetic ones, but since the transport equations included by EMP-INDUC module do not have convection terms, this last choice does not influence the precision which remains second order for the diffusion terms.

As it was previously said in bibliography, we have adopted a classical 2 equations turbulence model  $k-\omega$  SST with default settings, and thus with no special consideration for MHD turbulence. This combines the original  $k-\omega$  model near walls, which is able to calculate the boundary layer, and the  $k-\varepsilon$  away from walls. The eddy viscosity formulation is modified to account for the transport effects of the main turbulent shear stress [48].

Finally, calculation feedback allowed to fix convergence criteria, so we defined adequate dimensionless residuals of  $10^{-3}$  for all equations except the induction equations which have residuals of  $10^{-5}$ . It is often difficult to have the continuity residual drop to its converged value ( $10^{-3}$ ), since in Fluent it is scaled differently from the rest of residuals, based on the largest absolute value of the continuity residual in the first five iterations, instead of a physical measure of the total flux across each cell. *Figure 66* shows an example of the residual evolution during the convergence process.

However, it is important to also use monitors to judge convergence, and not only the residuals. The residuals are good for telling how the model is behaving, as a guide to evaluate the calculation process, but it is not sufficient, checking own physical criteria during solving is needed, because each model is unique. For example, in our model equilibrium of forces (EM force and pressure gradient) has been monitored regarding the fluctuation of averaged pressure at inlet and flowrate at outlet. The fact that they remain constant over iterations is a good indicator that simulation has reached the solution.

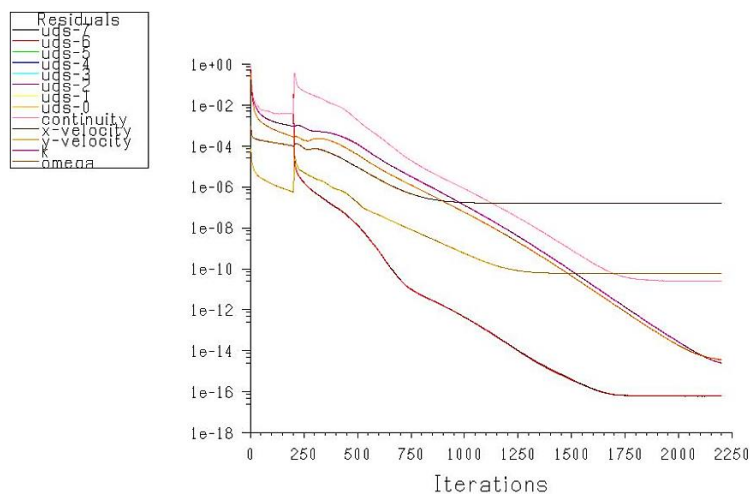


*Figure 66 : Example of residuals in 2D axisymmetric simulations with discrete coils*

### 4.1.3. Validation of EPM-INDUC code

Before carrying out coupled MHD cases, the module has been validated for purely electromagnetic simulations. For this aim, we compared EPM-INDUC results with an analogous electromagnetic model carried out using the commercial code COMSOL Multiphysics®.

COMSOL model is purely electromagnetic and considers no electric conducting fluid in the channel. For the case of INDUC, we changed electric conductivity to zero for sodium in

channel to avoid MHD coupling. In both models we have considered an input of phase RMS current of 45.6 A and 10 Hz of frequency, in order to compare them thereafter to experimental measurements in PEMDyn in chapter 5.

The calculated distributions of the radial and axial components of the magnetic field at the mean radius of the channel are presented in *Figure 67* and *Figure 68* respectively. Slight differences between the COMSOL and INDUC models remain, due to the fact that geometries are not exactly the same. For the case of INDUC model geometry is quite simpler i.e. we do not consider the ferromagnetic yoke in the geometry.

However, results are very close, and we can consider convenient the geometry choice for EPM-INDUC model. Therefore, we concluded that the simulations carried out with the EPM-INDUC module are valid.

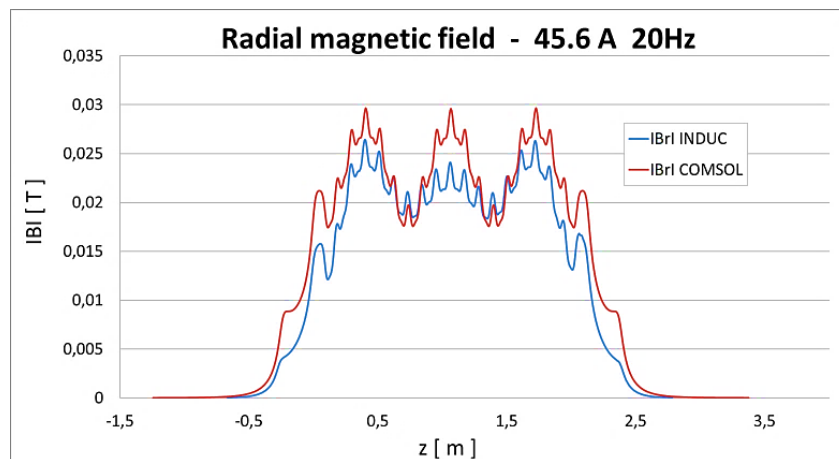


*Figure 67: Radial magnetic field component comparison*

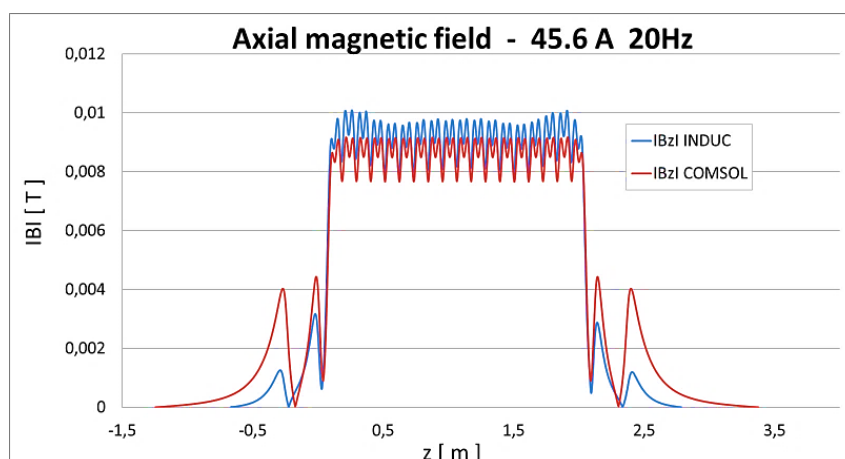


*Figure 68: Axial magnetic field component comparison*

## 4.2. 2D axisymmetric models

### 4.2.1. MHD coupling with the discrete-coils model

In this subsection we focus on the study of numerical results obtained with the 2D axisymmetric discrete-coils model presented above, with two key objectives: First, the analysis of electric supply influence on performance curves. Secondly, the understanding of physical phenomena governing the behaviour of the flow and magnetic field for different regimes of the performance curve.

In first place, a set of simulations has been launched for different intensities and frequencies of electric supply for PEMDyn conditions in order to later enable comparison with experimental data. Performance points of the curve are obtained varying inlet velocity of sodium ( $Rms$ ) from synchronism to lower values (and therefore higher  $Rms$  values).

Evaluating the influence of intensity in *Figure 69*, we notice the increase of developed pressure with electrical current. This is not surprising, since axial electromagnetic force is directly proportional to the square of external supply current.

In terms of  $Rms$ , *Figure 70* shows similar relation with intensity. The only extra information that we can extract from it is that the maximum of the curve is not placed at  $Rms$  equal to one, as it was the case of the analytical solution in subsection 3.3.2, but around  $Rms = 1.8$ . We also see a slight difference comparing curves maximums among them, though we consider that they are negligible to reach any meaningful conclusion.

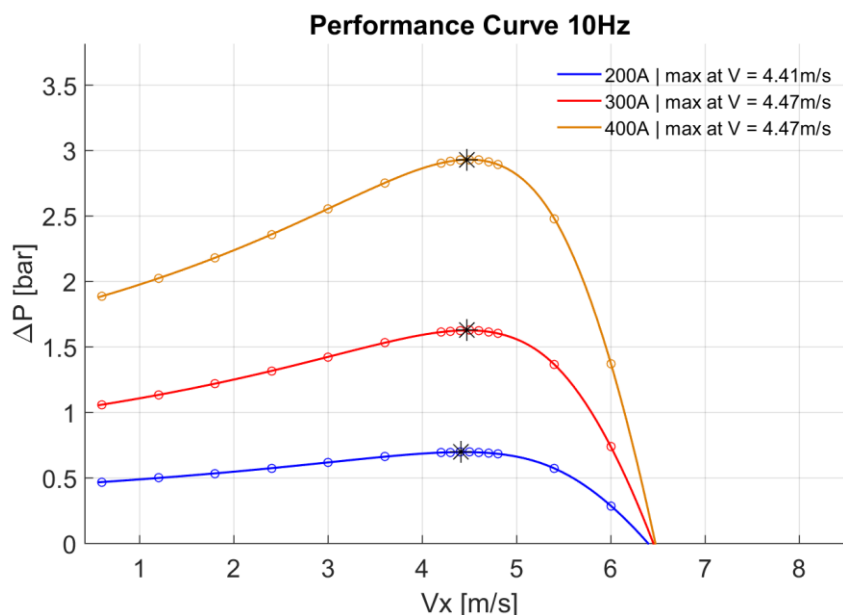


*Figure 69: Performance curves in terms of axial velocity of sodium at different intensity supplies*

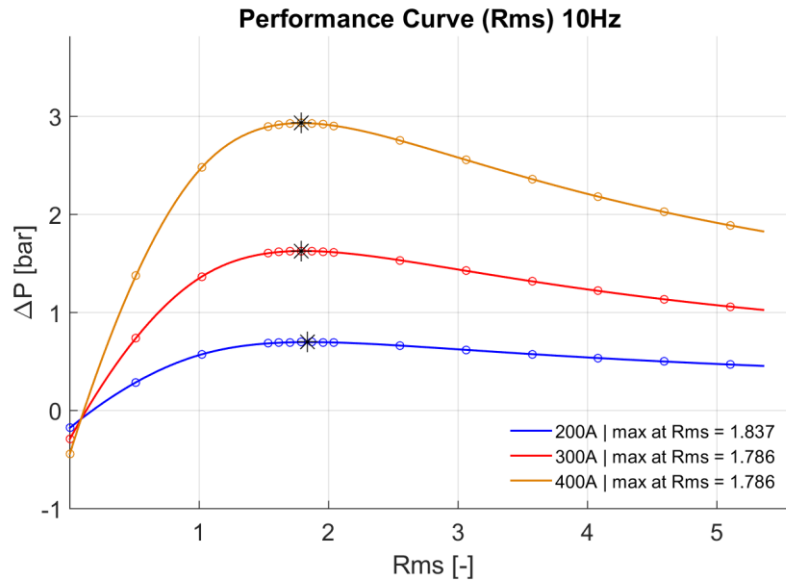


Figure 70: Performance curves in terms of Rms at different intensity supplies

Analyzing the impact of frequency, in Figure 73 a displacement of performance curves in the velocity domain is appreciated. This was expected since the maximum velocity expected in an EMIP is fixed by the synchronism velocity, which depends directly on the supply frequency.

Additionally, Figure 72 proves that numerical simulations do not confirm the infinite pump theory, which expects that frequency would not affect the maximum pressure position measured by its Rms. Here, we confirm not only that maximum is not reached at Rms = 1, but also that it is shifted to higher Rms numbers with the increase of frequency.

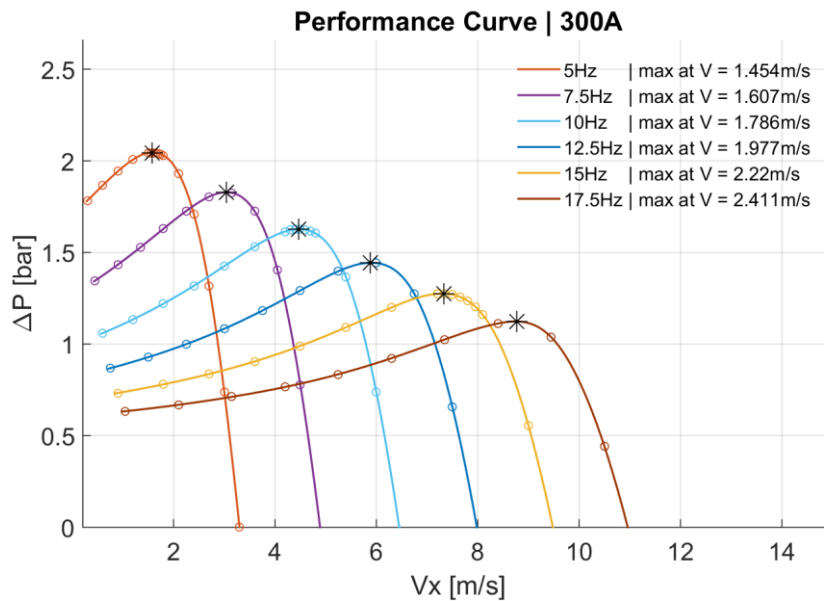


Figure 71: Performance curves in terms of axial velocity of sodium at different frequency supplies

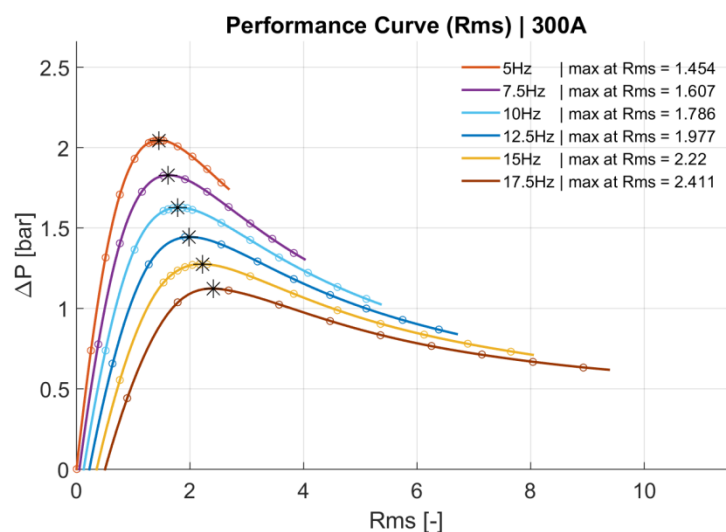


Figure 72: Performance curves in terms of Rms at different supply frequencies

It is stated in literature that the change of slope in performance curve determines the transition from stable to stalled regimes. If we have a look into numerical results obtained, we find a significant discrepancy with theory that estimates the stalling threshold at  $Rms = 1$ , and thus too conservative in comparison with numerical results presented.

In order to clarify the potential causes for the delay of the stalling appearance, we have first identified several effects in this model with discrete inductor that could have an impact on the performance curve. The three following factors are listed:

1. End effects caused by the finite length of the inductor.
2. Discrete coils definition, more realistic than continuous inductor with sinusoidal source of current.
3. Joule losses in materials, and less developed pressure as a consequence.

This reasoning is the starting point for the characterisation of the stalling threshold in a real EMIP configuration. In order to characterize the impact of these three factors cited above, several 2D-axisymmetric models with different levels of detail have been built and studied.

For this aim, it is reasonable to begin with the direct comparison of the discrete coils model with analytical results in section 3.1.2.2, so this time calculation was carried out imposing an electric supply of 300 A and 20 Hz and properties in *Table VIII* for several fluid velocities.

Looking at the obtained performance curve on *Figure 73*, it is appreciated that the maximum of developed pressure (marked as a yellow star) is less important (1.2541 bars) than in the analytical case in section 3.1.2.2 (4.34 bars), and that it is placed at a higher  $Rms$  (2.1). However, even if quantitative results are not the same for both models, they are qualitatively correct since the same physical phenomena are observed in both of them.

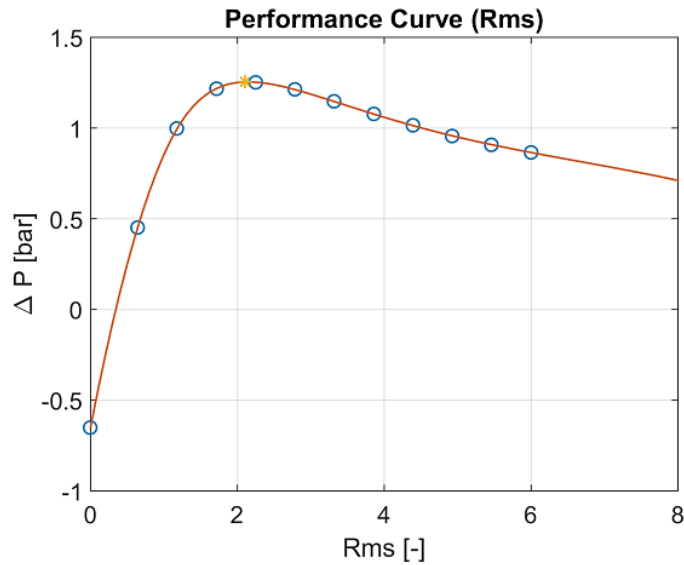


Figure 73: Performance curve of the discrete coils model

Contours in Figure 74 show the magnetic field lines going through the sodium channel. Comparing both figures, a) and b) it is appreciated that less radial magnetic field component penetrates through the channel for the case of  $Rms = 3.8543$  (stalled case). So, it is seen the same expulsion phenomenon with the increment of  $Rms$  than for the analytical solving.

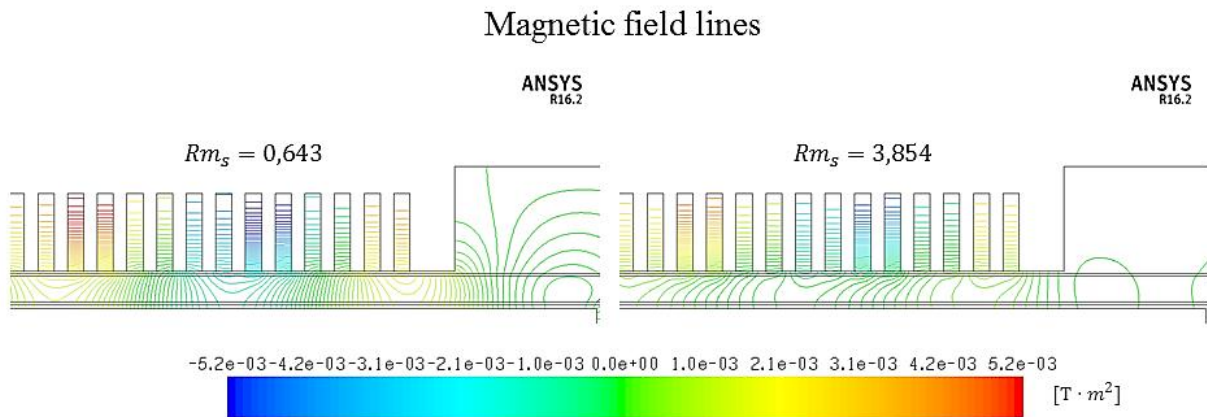


Figure 74: Magnetic field lines of the discrete coils model – a) Stable  $Rms = 0.64328$   
 b) Stalled  $Rms = 3.8543$

Looking at the velocity profiles in Figure 75, we can appreciate that with increasing  $Rms$ , the velocity tends to be higher at the bottom of the channel than at the top. In order appreciate this easier, velocities in profiles in Figure 75 have been divided by their mean value. This phenomenon can also be seen in the analytical case

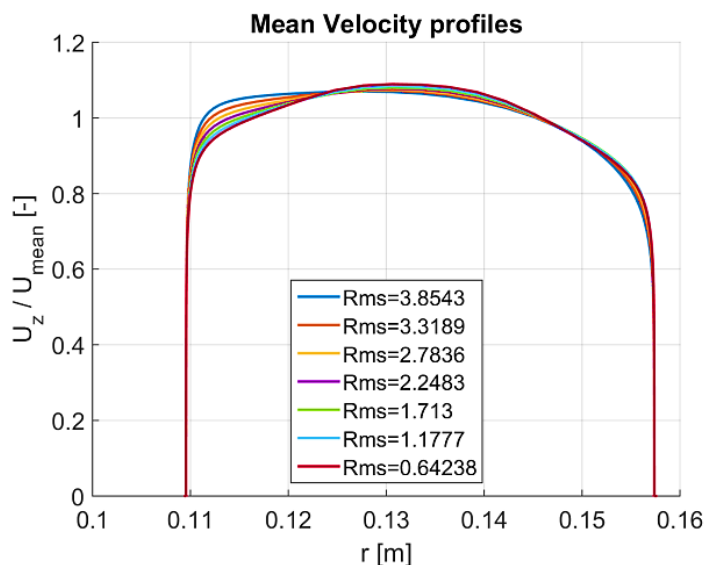


Figure 75: Mean velocity profiles of the discrete coils model at middle channel length

#### 4.2.2. Axisymmetric sheet-of-current inductor model

The geometry used in this case is closer to the one presented in the theoretical study. The series of coils are substituted by a continuous inductor in the axial direction, where a sinusoidal distribution will be imposed for the density of current perpendicular to the plane. This is modelled on Fluent as a thin layer of current above the sodium channel of 0.2 mm of width.

Also, geometry is simplified in comparison to coils model, since tubes are not described (magnetic gap  $d_m$  and hydraulic gap  $d_h$  are both of 47.83 mm), and thus magnetic field disturbance by the penetration into the steel walls is neglected. Furthermore, it is important to note that for a given supply current the magnetic field would be greater for a reduced magnetic gap and also effective values of  $Rm_B$  and  $Rms$  would increase due to the lack of correction factor  $d_h/d_m$ .

However, the main difference between analytical and numerical sheet-of-current inductor model is that inductor is finite and centered in the pump. This allows the analysis of inlet and outlet phenomena. Figure 76 shows the geometry and main boundary conditions of the model.

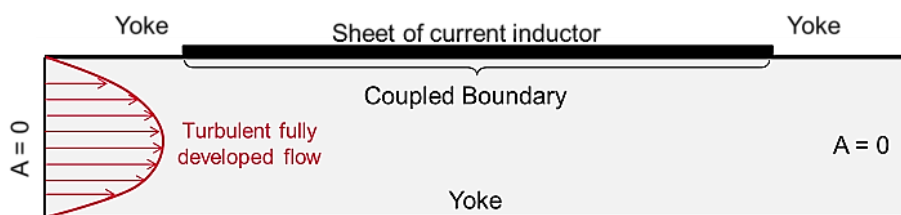
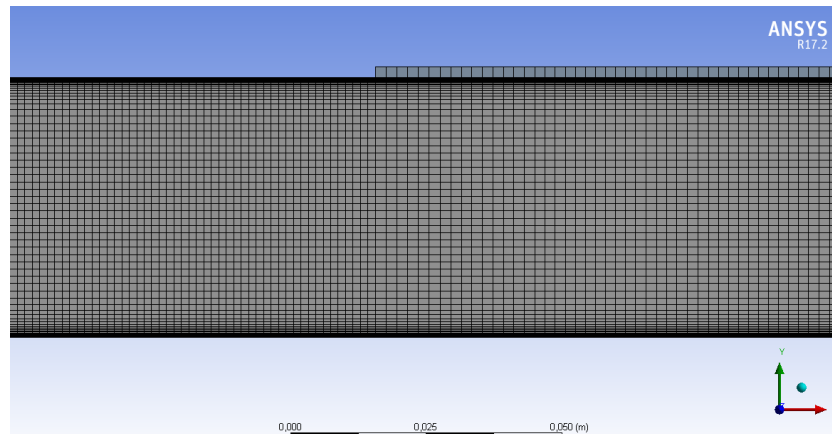


Figure 76: Schema of sheet model geometry and BC

About mesh (*Figure 77*), it has been built using similar inflation and maximal size of element as the previous case. The only difference implemented is that the inductor sheet has been meshed using only one layer of elements. This consideration with the simplification of geometry permits to interestingly reduce the size of mesh to 178731 elements.



*Figure 77: Mesh of sheet model*

The case is also solved for an electric supply of 300 A and 20 Hz. Peak linear density current  $j_{peak}$  is estimated the same manner as in theoretical case. The sinusoidal current distribution is applied to the sheet of current using two user's defined functions (for real and imaginary components), which are patched to the density current source terms at the inductor layer zone after initialization.

Otherwise, boundary conditions are similar to the previous discrete coils model, including perfect ferromagnetic conditions at the upper and lower parts of the domain, turbulent fully developed flow profile with imposed velocity at inlet and null pressure at outlet. Solving options are also chosen similar to those of previous case, with the only particularity of a slight under-relaxation of 0.99 for real and imaginary parts of vector potential perpendicular to the plane. This last feature permitted to stabilize calculation, since variation of electromagnetic force from one iteration to the following one was limited.

Looking at obtained results, we remark that even if this model is designed with characteristics close to the theoretical one (continuous inductor and no tubes), performance curve in *Figure 78* is still much closer to the numerical model with discrete coils, since we obtain a similar shift of the maximum of developed pressure (marked as a yellow star). This time it is of 2.541 bars and it is placed at  $Rms = 1.9$ . Once again, the conclusion is that analytical model is not representative enough of reality.

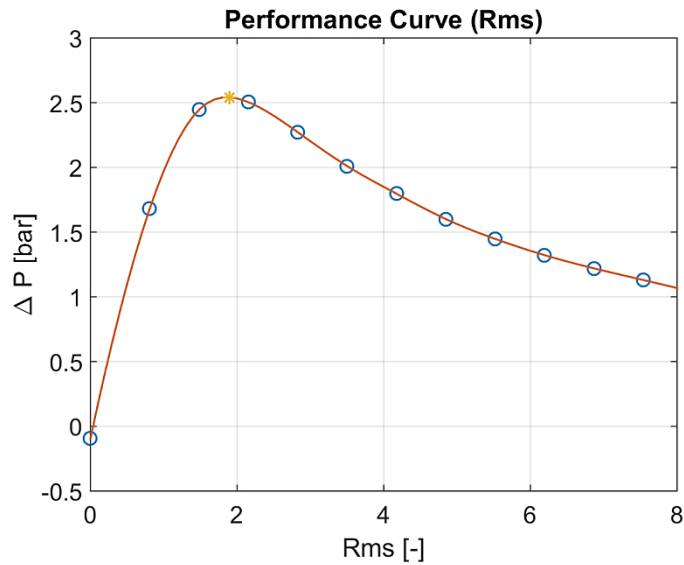


Figure 78: Performance curve of the sheet inductor model

Magnetic field behavior in this simplified model (Figure 79) is the same as in coils model (Figure 74). It is clear that high  $Rms$  regimes provide low penetration of the magnetic field.

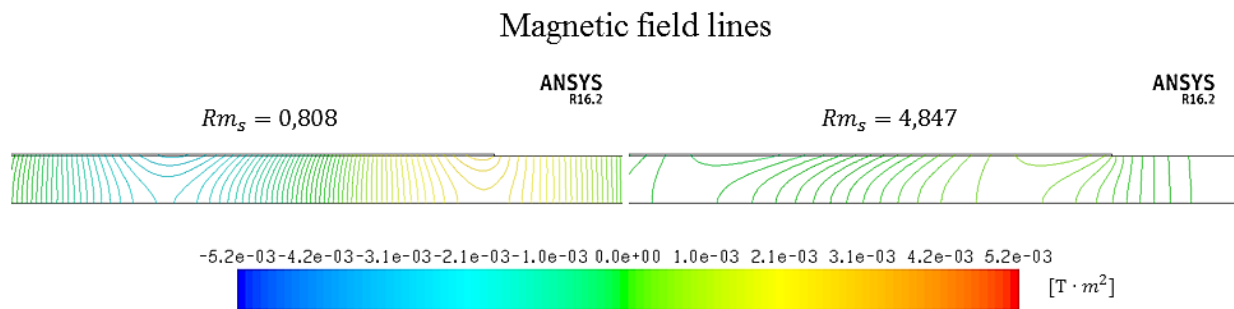


Figure 79: Magnetic field lines of the sheet inductor model – a) Stable  $Rms = 0.80784$   
 b) Stalled  $Rms = 4.84704$

Furthermore, velocity profiles are very close between both cases. There is only the small difference that, in sheet-of-current inductor model, obtained velocity profiles (Figure 80) are slightly flatter. This should be caused by the fact of considering simplified geometry with smaller magnetic gap  $d_m$  than discrete coils model.

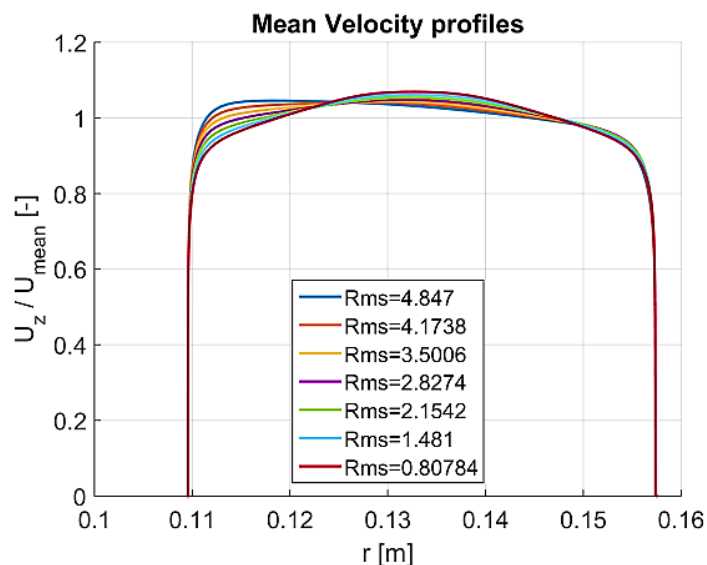


Figure 80: Mean velocity profiles of the sheet model at middle channel length

### 4.2.3. Axisymmetric periodic model

Finally, a periodic 2D axisymmetric model has been developed to validate our approach with the analytical solution. In this model, periodic condition is imposed in the inlet and outlet of the channel for velocity and vector potential, and the inductor is defined as a continuous sheet-of-current inductor all along the channel with periodic condition applied at the borders. In other words, this model permits the evaluation of the infinite inductor case, and therefore its target is to find out why precedent numerical models have their pressure maximums placed relatively far from the analytical solution position at  $Rms = 1$ . Geometry and conditions are detailed in *Figure 81* and parameters and mesh employed are the chosen similarly than for the case of the sheet-of current inductor model.

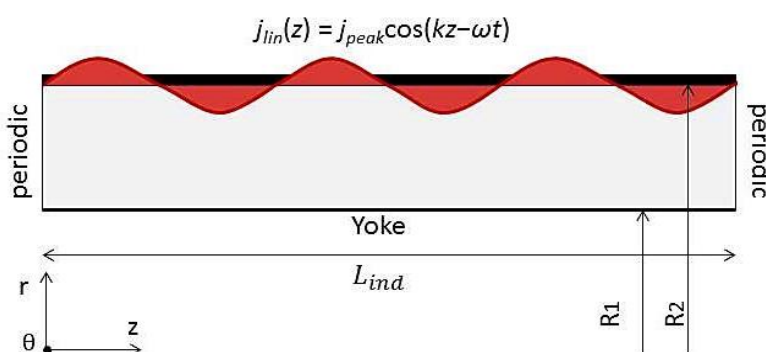


Figure 81: Periodic model with infinite inductor

Calculations are also solved for an electric supply of 300 A and 20 Hz. In this case peak linear density current  $j_{peak}$  is estimated the same manner as for the analytic case. Therefore, this model also permits to identify other factors which could have an impact on developed

pressure apart from the finite length inductor effect through direct comparison to experimental.

Before analyzing results, we should remark that convergence in this case was difficult to achieve because, even if theoretically this is the easiest case to solve, periodic conditions in Fluent are quite delicate to pose. This is because applying periodicity implies that both inlet and outlet are at the same pressure conditions, so the solver must obtain the pressure drop using a correction factor which is updated based on the difference between the imposed mass flow rate and the actual one. Unfortunately, this process usually implies divergence problems, so relaxation factor of 0.01 had to be used in following simulations.

*Figure 82* shows the performance curve of the periodic model, where the maximum of developed pressure (marked as a yellow star) is of 4.1522 bars and is placed at a *Rms* of 1.1. We can extract as conclusion that this model is more similar to the analytical case than to the other two numerical cases presented before, since the maximum of pressure is placed very close to  $Rms = 1$ , as theory estimates, and values of developed pressure are similar.

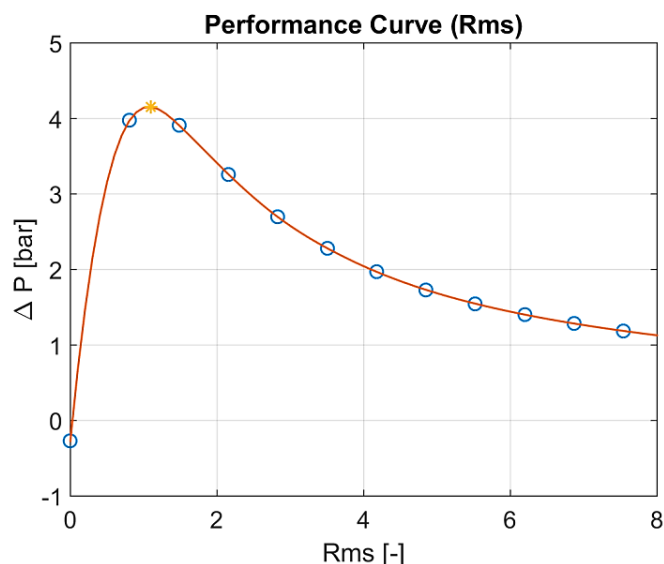


*Figure 82: Performance curve of the periodic model*

In this *Figure 83* we can appreciate that the difference between models in terms of developed pressure is minor (around 2% of the maximum in average). This makes sense with the fact that in analytical model viscous losses are not considered, which should be of an order of magnitude of 5% of total axial electromagnetic force induced in the channel. This comparison also permits to validate the satisfactory performance of the EPM-INDUC code for coupled cases and verifies that considering a standard two-equation turbulence model instead of a specific model for MHD turbulence is a good approach for the current case.

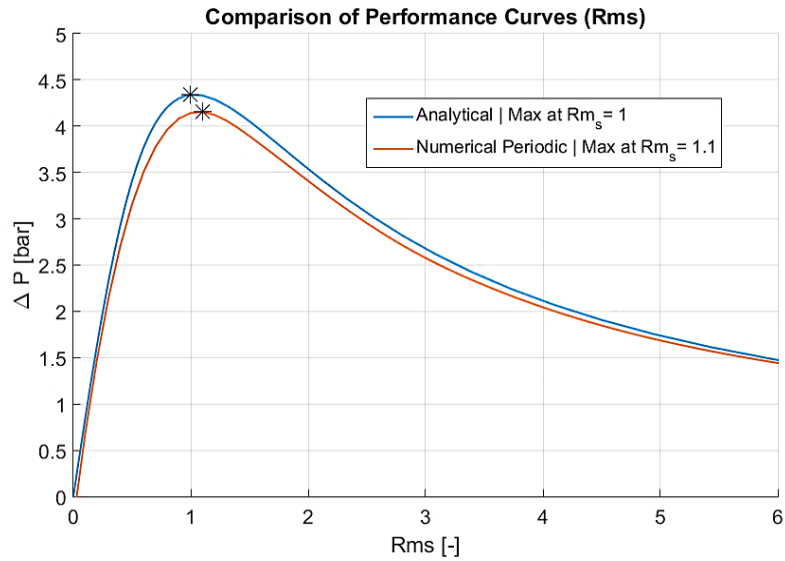


Figure 83: Comparison of performance curves of analytical and periodic model

Magnetic field lines shown in Figure 84 put again in evidence the expulsion of the magnetic field at high  $Rms$ . However, the difference to the rest of 2D models is the periodicity of magnetic lines in the inlet and the outlet, and of course no evidence of end-effects is found.

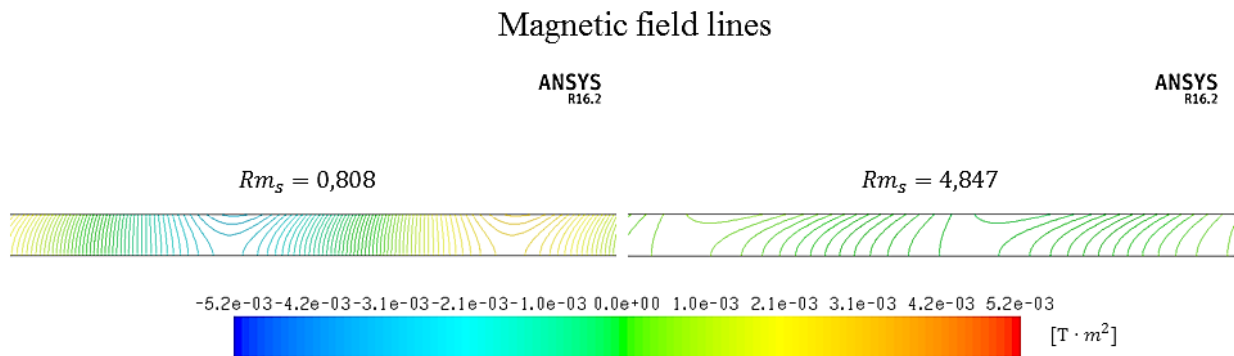


Figure 84: Magnetic field lines of the periodic model – a) Stable  $Rms = 0.80784$  b) Stalled  $Rms = 4.84704$

Figure 85 shows that at low  $Rms$  regimes velocity profiles are flatter compared to those in Figure 80. This should be a consequence of the infinite character of the inductor, since this would permit to reach a well-balanced velocity profile, and then closer to the one found analytically. We also find that at high  $Rms$  velocity profiles are accelerated at the lower part of the channel, as it was observed in all precedent models.

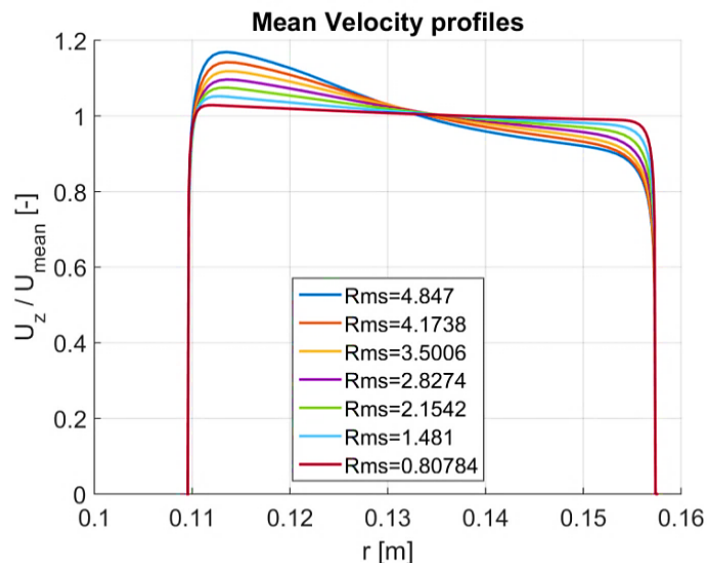


Figure 85: Mean velocity profiles of the periodic model at middle channel length

#### 4.2.4. Comparison of 2D models

In this section, several models have been treated with the interest of giving an estimation of the stalling threshold in terms of the Global Slip Reynolds Magnetic number ( $Rms$ ). Figure 86 gives the comparison of performance curves obtained using the different presented models: analytical, numerical with discrete inductor and numerical with continuous sheet-of-current inductor.

We can extract the following conclusions:

1. Analytical model manages to describe main physical effects due to the MHD coupling in an EMP. However, theory lacks precision, since the maximum of pressure is quite high ( $\Delta P = 4.338$  bars) with respect to results obtained numerically with discrete coils model, and more importantly because the estimate of stalling at  $Rms = 1$  remains quite conservative.
2. The periodic numerical model modelling an infinite sheet of current model gives results very close to those of the analytic case since the maximum of pressure is  $\Delta P_{\max} = 4.152$  bars and is placed at  $Rms = 1.1$ . It confirms that the numerical model is able to describe quantitatively the theoretical stall phenomenon.
3. The numerical model with a finite sheet-of-current inductor model has been built as a compromise between analytical and numerical discrete coils model, but results are closer to the second one ( $\Delta P_{\max} = 2.541$  bars at  $Rms = 1.9$ ). This gives a hint about the effect of inductor extremities (end effects) which are present in this model but not in the previous ones.

4. Comparing the previous model (with a finite sheet of current), to the model with discrete coils, we can see that the value of the maximum pressure changes (mainly because the magnetic gap has changed), but the position of the maximum pressure point is almost unchanged. Since this point is the limit of stable operation of the pump, those two last models are equivalent to study the pump stability limits.

Thus, this study confirms from a numerical point of view that the main reason for the offset of the maximum of pressure in the discrete-coils and sheet-of-current models is due to the impact of end-effects caused by a finite inductor.

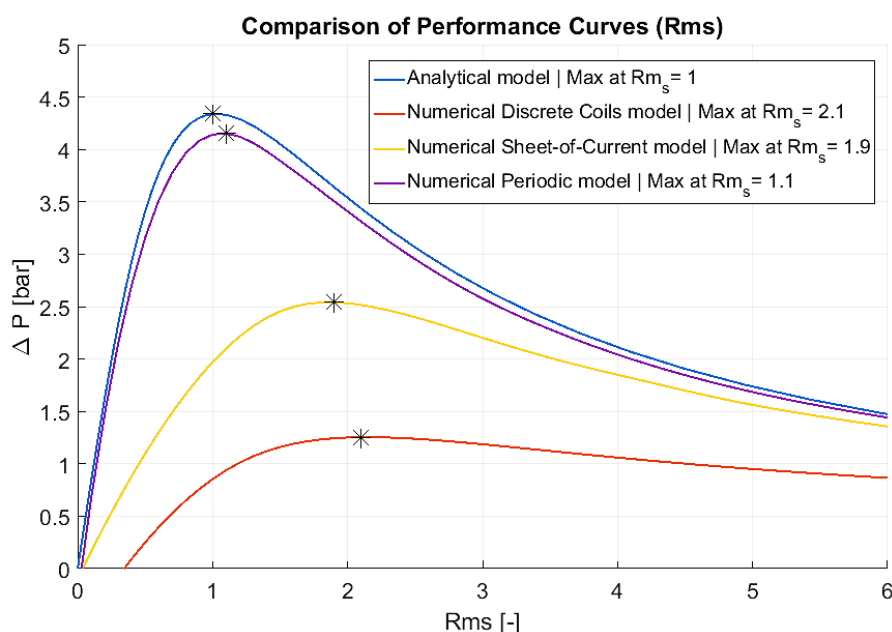
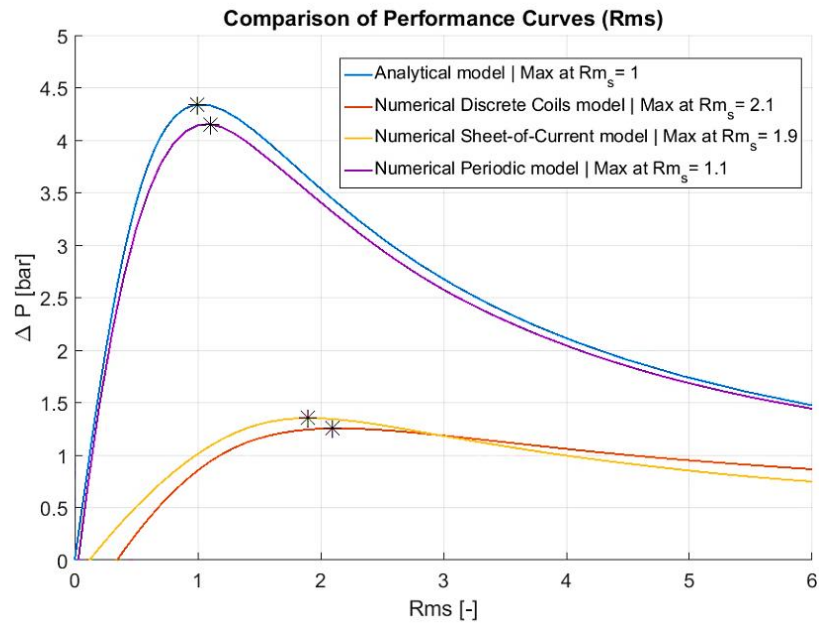


Figure 86: Comparison of Performance curves and stalling thresholds for the different 2D models and the analytical solution

Consequently, the simplified sheet-of-current inductor model gathers most of the phenomena found in the original 2D axisymmetric model with discrete coils. This includes the flattening of velocity profiles at stable regimes and the acceleration at the bottom of channel for stalled regimes (all of the simulations carried out present geometries with curved channel), the end-effects and the expulsion of the magnetic field, responsible for the loss of developed pressure.

Finally, the geometry-simplified model results a good compromise to describe the phenomenology of the stalling appearance in an EMP. Furthermore, thanks to the small weight of the mesh, this model is an interesting option for the development of the 3D model. This last would make possible to analyse the impact of the azimuthal dependency on the stability of an EMIP and compare it to the theoretical instability threshold of Gailitis and Lielausis [23].

However, we also remark in *Figure 86* that developed pressure using the sheet-of current model is greater than in the case of discrete coils model, since magnetic field losses are higher using a geometry closer to reality. In order to obtain the same order of magnitude of applied magnetic field in both models we have considered a correction factor of 0.75 to the peak linear density of current ( $j_{peak} = 65454$  A/m). *Figure 87* hereby verifies that this approach permits a better comparison between both models.



*Figure 87: Impact of factor correction in Sheet-of-current model*

### 4.3. 3D models

#### 4.3.1. Development and first results

Last 2D model comparison suggested that the sheet-of-current inductor model is a good compromise between the mesh size and the quality of results compared to the discrete coils model. Therefore, the 3D model has been built using this consideration.

The geometry used is shown in *Figure 88* is formed by two concentric annular cylinders, the inner describing the annular channel with liquid sodium flow and the outer describing the inductor as a thin (0.2 mm) sheet for current along the pump. In this region, the distribution of linear current density is applied around the azimuth with the help of an external user's defined program. In order to describe the finite character of the inductor, the distribution is chosen with finite length ( $L_{ind}$ ) and it is centered in the channel.

Dimensions of the channel are the same as for the 2D model (PEMDyn values), and as it is observed in *Figure 88*, the flow is established over the axial direction imposing velocity at inlet and null pressure at outlet.

As well as in previous 2D numerical models, perfect ferromagnetic boundary condition is applied to consider the magnetic field confining effect of yokes at both internal and external annular boundaries. However, formulation in EPM-INDUC of this boundary condition for 3D cases is not evident.

About mesh (*Figure 89*), here we have considered bigger axial size of elements (10 mm) compared to sheet-of-current case (2 mm). A study to see if the solution is grid-dependent was previously carried out in 2D model and concluded that the impact is minimal (2.42% of impact on performance curve for increasing one order of magnitude). Furthermore, inflation applied close to walls was limited to first layer size of 0.2 mm (instead of 5  $\mu\text{m}$ ). This means that description of velocity profile is more approximate than in previous cases, which presented similar profile to a Hartmann flow when conditions were close to synchronism. However, impact on overall performance is very slight, since in our case of study currents are not concentrated close to walls (as in the case of flat EMIPs), but they close over the azimuth. Hence, boundary layers are indeed inactive and less important to study rigorously than in other MHD flows.

The most significant difference compared to 2D simulations is that hereby we need to solve for the whole 8 scalars problem, since there is no axisymmetry simplification. The solving was first carried out stationary, with similar method settings than in 2D simulations. However, stronger under-relaxation factors were needed in this case, particularly for electric potential and axial component of vector potential scalars (0.1), which wasn't indeed very problematic since they play a minor role in governing physics. The rest of variables were also under-relaxed using a factor of 0.95.

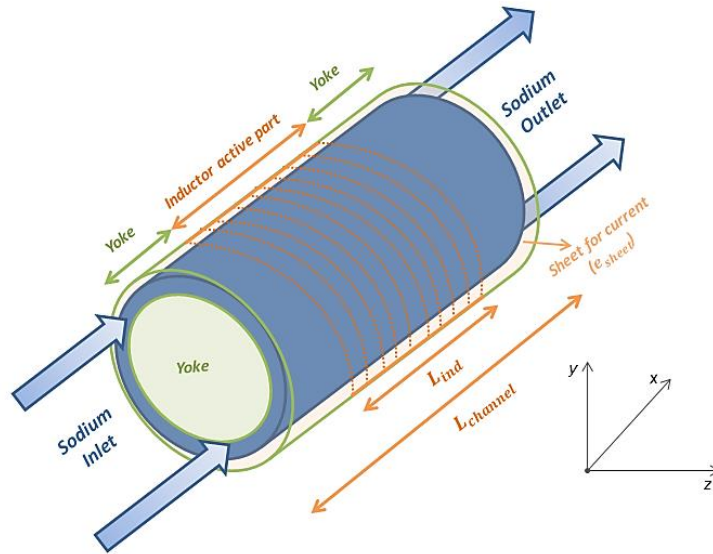


Figure 88 : Geometry and conditions of the 3D model

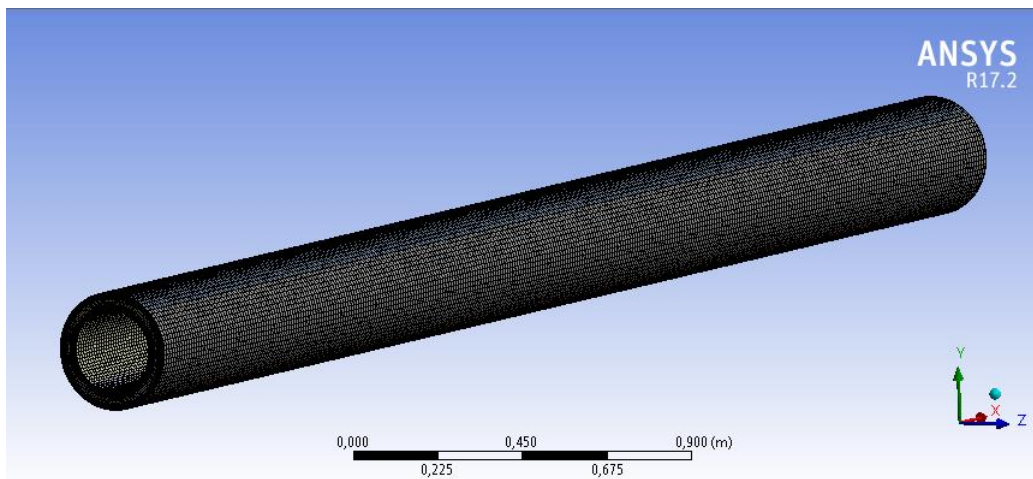


Figure 89 : Mesh of the 3D model

The performance curve of the 3D model for the same parameters of sheet-of-current axisymmetric model is shown in *Figure 90*. Here, the electric supply is also for a frequency of 20Hz and a linear density current of 87300 A/m, which, similarly to the other models with a sheet-of-current inductor, is corrected by a factor of 0.75 (65454 A/m).

The maximum of developed pressure (marked as a yellow star) is of 1.3924 bars and is placed at  $Rms$  of 1.9. As expected, this model gives a performance curve quasi identical to that of the 2D sheet-of-current inductor model in *Figure 78*, since maximums are located at the same of  $Rms$  and their values are very close ( $\Delta P = 1.3524$  bars in the 2D model).

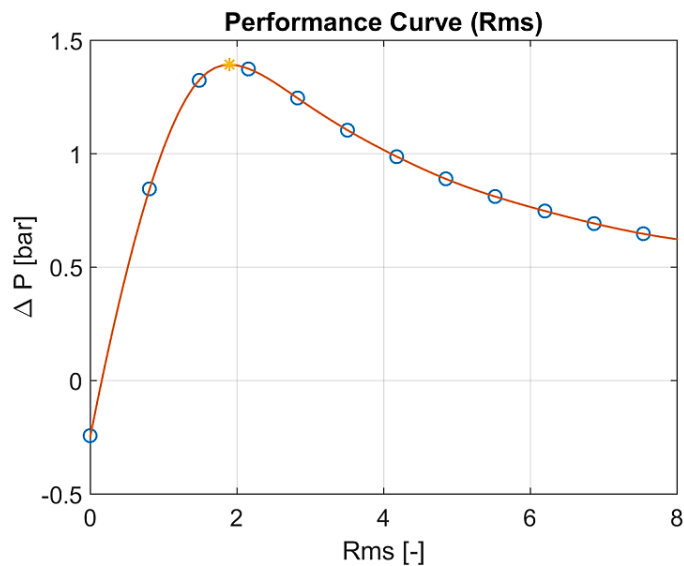


Figure 90 : Performance curve of the 3D model

Examining results at synchronism, radial and axial components of magnetic field and axial velocities are shown in *Figure 91* and *Figure 92* respectively. They are plotted at three radial positions corresponding to an external position close to the inductor ( $r = 0.156$  m), the middle of the channel ( $r = 0.133$  m) and an inner position close to the magnetic yoke ( $r = 0.11$  m).

In *Figure 91*, we can appreciate that the radial component is more important at the inner part of the channel, and on the contrary, the axial component is greater at the external part, being close to zero close to the yoke. The increase of the radial component towards the core is simply an effect of curvature (the magnetic gap is not thin compared to its radius), since a purely radial field would verify  $R_2 \cdot B_r(R_2) = R_1 \cdot B_r(R_1)$  to fulfill the conservation of magnetic flux. The distribution of the axial component is strongly influenced by the two perfect magnetic boundaries, which impose  $B_z = 0$  at  $r = R_1$  and  $B_z = \mu_0 J_{peak}$  at  $r = R_2$ .

Also, it can be seen that the radial component is shifted towards the outlet in comparison to the axial component, which is centered in the channel. This is an effect of the convection of the magnetic field by the velocity of the fluid, which is in conformity with the theory of end effects (the effect of each extremity of the inductor is mainly a weakly damped wave travelling almost at the fluid velocity downstream). The end effects are mainly visible on the radial component, which is less constrained than the axial one (Neumann conditions for the radial component, Dirichlet condition for the axial component).

*Figure 92* shows that there aren't heterogeneities of velocities over the azimuth at synchronism. Also, the evolution of the boundary layer over the length of the pump for the inner and external surfaces can be appreciated because of the influence of the inductor.

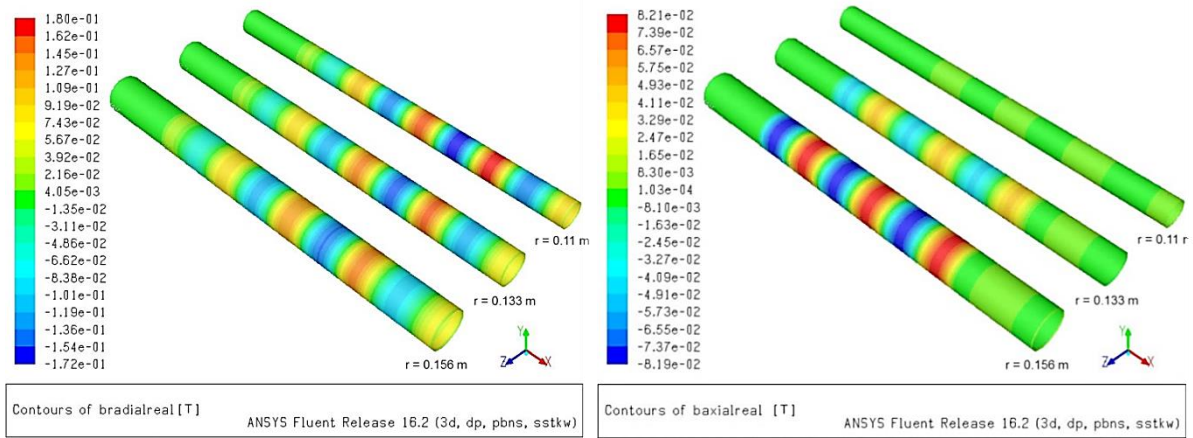


Figure 91 : Radial and axial components of magnetic field at three radial positions at synchronism

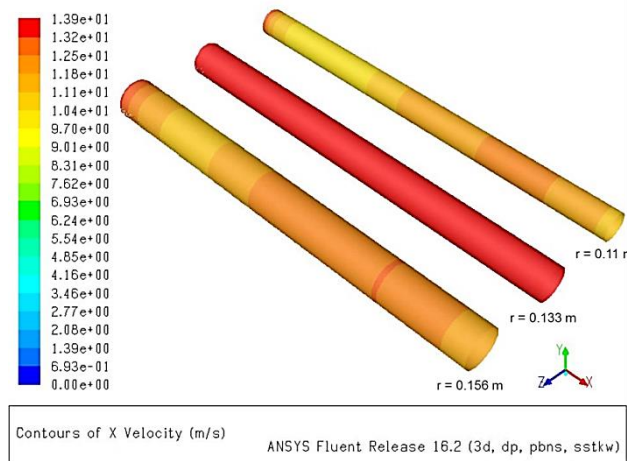


Figure 92 : Axial component of velocity at three radial positions at synchronism

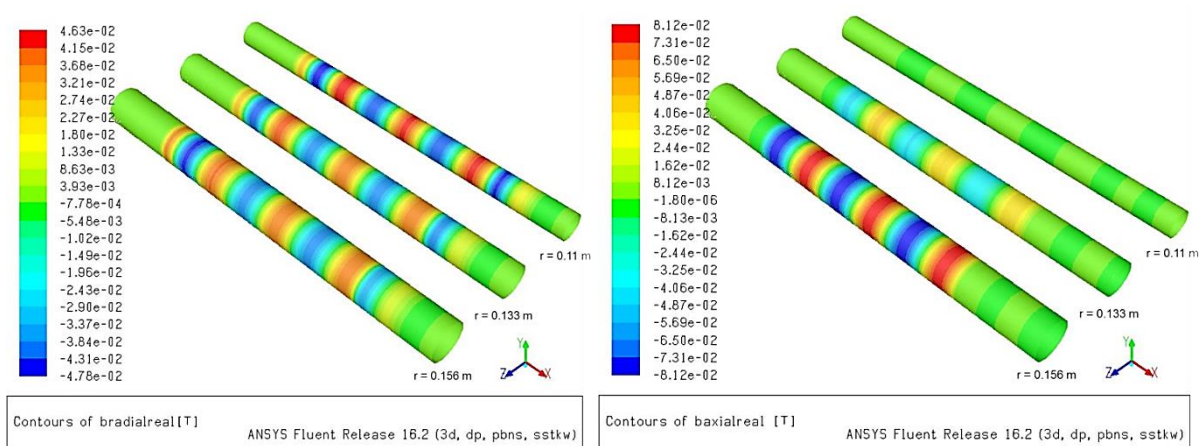


Figure 93 : Radial and axial components of magnetic field at three radial positions at  $Rms = 4.8484$

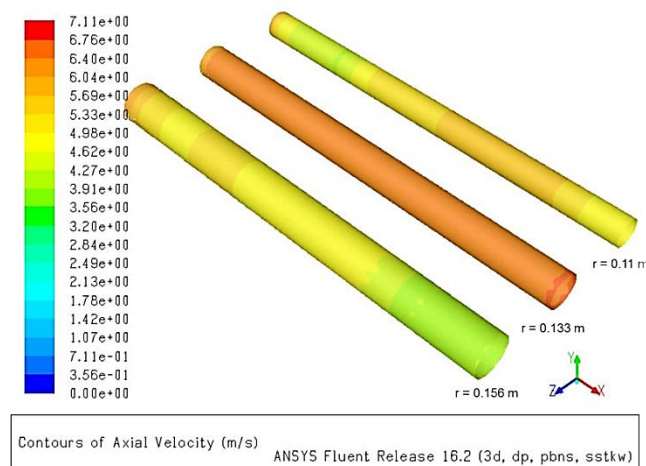


Figure 94 : Axial component of velocity at three radial positions at  $Rms = 4.8484$

Looking at *Figure 93* and *Figure 94* we can compare precedent results to a stalled case at  $Rms = 4.8484$ . *Figure 93* shows the same behavior for magnetic field components than *Figure 91* ; Radial magnetic field is greater at the inner part of the channel, where axial component is close to zero. However, contrary to synchronism results, in this stalled regime radial component of magnetic field is less important (by a factor of 2) than the axial component. This is due to the phenomenon of magnetic field expulsion out of the channel at high  $Rms$ . In addition, here the effect of the inductor extremities (end effects) is less convected downstream (the radial component is more centered in the pump) because the fluid velocity is almost twice lower than at synchronism. Inside the inductor, the travelling wave near the core has a phase lag compared to the travelling wave near the inductor, what can be interpreted as a convection of magnetic field, driven by the difference of velocities between the travelling wave and the sodium.

About axial velocity in *Figure 94*, we see the same tendency as for the case at synchronism. We can neither appreciate any disequilibrium of velocity over the azimuth, even if the performance point is supposed to be unstable, as it is predicted by Gailitis [23]. Nevertheless, as it was seen in 2D models for stalled regimes, inner part of the channel is faster than the extern.

It is among our foreseen perspectives to pursue with the development of this 3D model. Specifically, we evaluate the impact of a velocity perturbation over the azimuth at the inlet of the channel. This provides information about the evolution of the disequilibrium along the pump for different  $Rms$  regimes of operation.

As a summary of all models presented here, *Figure 95* shows the different performance curves obtained. As it was expected, we see that performance curves of the 2D sheet-of-current inductor model and of the 3D model are very similar, and also close to results of the 2D discrete coils model. In conclusion, it can be affirmed that the 3D model is representative of MHD performance of an ALIP.

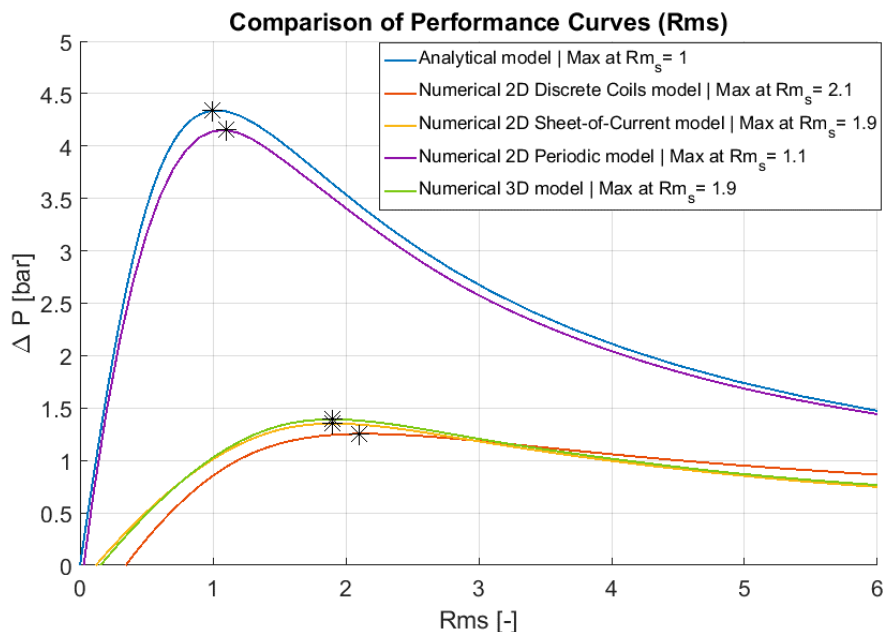


Figure 95 : Comparison of performance curves and stalling thresholds for the different 2D and 3D models and the analytical solution

### 4.3.2. Stationary analysis of perturbations

Once we have verified that the solution furnished by the 3D model is coherent with behaviour expected at each regime, the same case can be used to analyse stability from different points of view. Looking at the literature, we observe that there are two main phenomena linked to MHD instability in ALIPs: inhomogeneity of velocity and magnetic field over the azimuth and low frequency (LF) pulsations of the fluid.

The first one of those has been studied first theoretically by Gailitis et al. [23]. In their work the marginal instability threshold was obtained in terms of developed pressure for a certain  $m$  mode perturbation, where the ALIP could develop stationary velocity disequilibrium with the azimuthal mode distribution. Though, results furnished by the study remain quite conservative, since end effects are not considered.

In addition, from a numerical point of view Asada et al. [39] investigated about the impact of an azimuthal disequilibrium of velocity at inlet considering an azimuthally non-uniform velocity distribution in first mode form and with amplitude of 30% of mean velocity in the channel.

It is in the aim of pursuing previous works on the subject that we have decided to analyse more in detail the obtained azimuthal velocity distributions in previous 3D model. However, Figure 95 shows that inhomogeneity does not seem to appear at high values of  $Rms$ . In fact, velocities all the long of the pump are close to mean value in both stable and unstable cases.

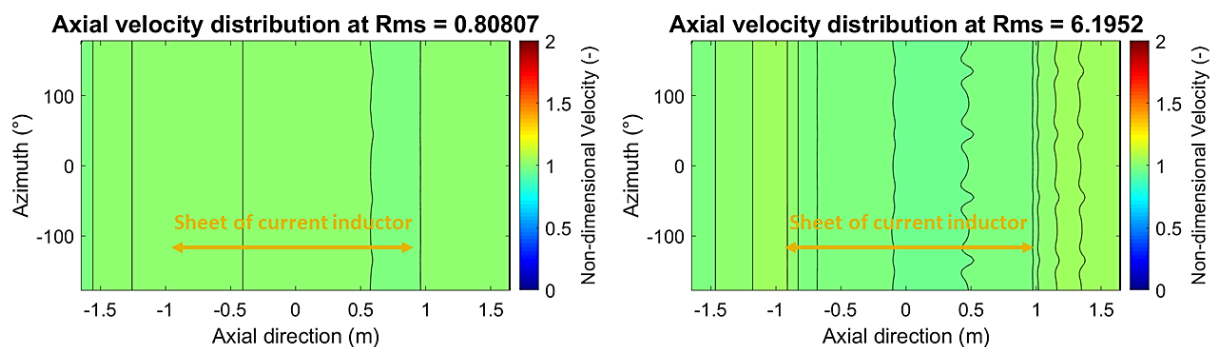


Figure 96: Contours of velocity distributions with homogenous distribution at inlet for stable (left) and unstable (right) regimes

Nevertheless, it is too optimistic to consider a perfect homogeneous velocity distribution at the inlet. For instance, in the case of PEMDyn loop, geometry was not optimized during design and an important velocity disturbance over the azimuth is attended at the inlet of the ALIP.

In order to characterize the velocity distribution at inlet, experiments were carried out by the CEA at CERG laboratory in Grenoble, France. Tests were done in water, that has a kinetic viscosity at  $37^\circ$  equivalent to the sodium one at  $110^\circ$ , using a Plexiglas mock-up facility with similar geometry to that of the PEMDyn loop (Figure 97).

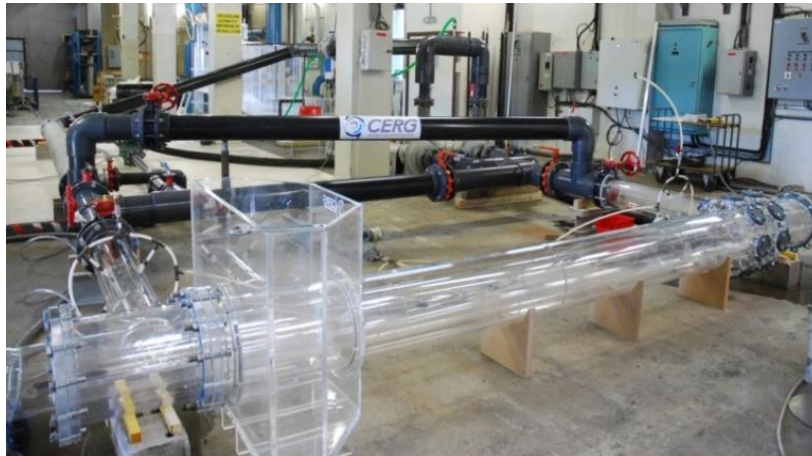


Figure 97: CERG mock-up for characterisation of PEMDyn velocity distribution

Velocity distribution in Figure 98 was obtained via Particle Image Velocimetry (PIV) measurements at the inlet of the ALIP active zone. Experiment confirmed that inlet perturbation amplitude was around 30% of mean velocity and with azimuthal shape similar to a first mode (velocity proportional to the cosine of the azimuth angle), corresponding to  $m = 1$  in our theoretical study in subsection 3.2.1.

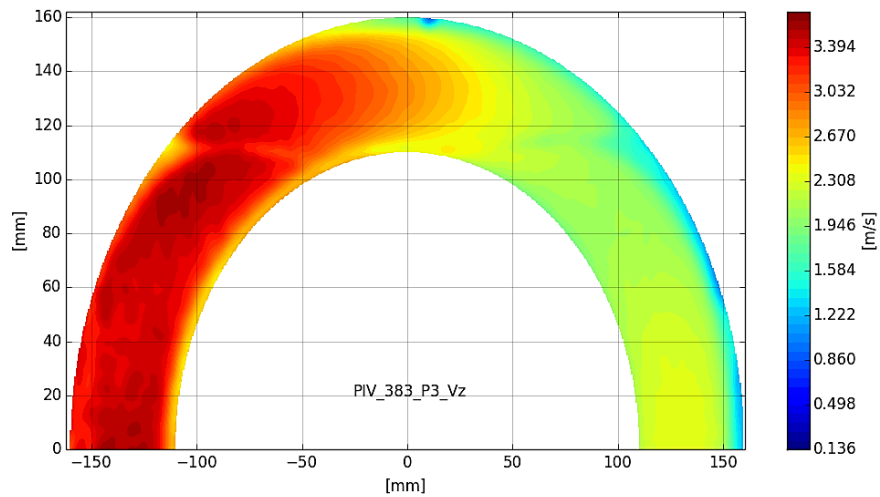


Figure 98: PIV measurements of inlet velocity perturbation

Solutions to avoid this maldistribution were proposed by the CEA. One of the best welcomed ideas was the implementation of a homogenisation grate able to damp out the perturbation. Two different designs were tested in the facility, one with homogeneous grid (CERG grate) and other with optimized grid considering PIV measurements (CEA grate). The implementation of grates in the mock-up is shown in *Figure 99A*.

We can appreciate in *Figure 99B* that CEA grate manages to reduce perturbation to 15% and that its form is now close to a mode  $m = 3$  (in fact, this mode was also present in the original distribution without grate). On the contrary CERG grate is not retained as potential solution to velocity disequilibrium since in some zones deviation from mean velocity is even greater than in the original case, reaching values around 50%.

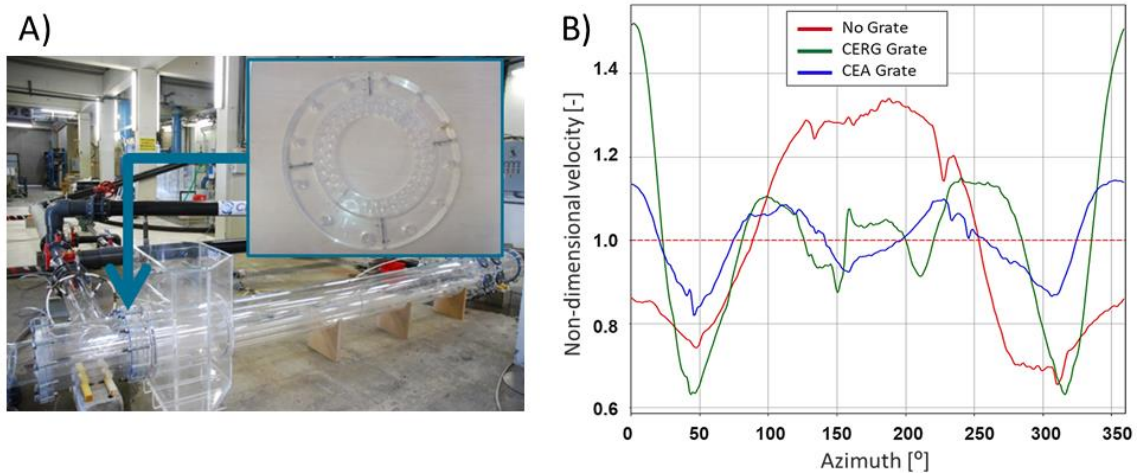
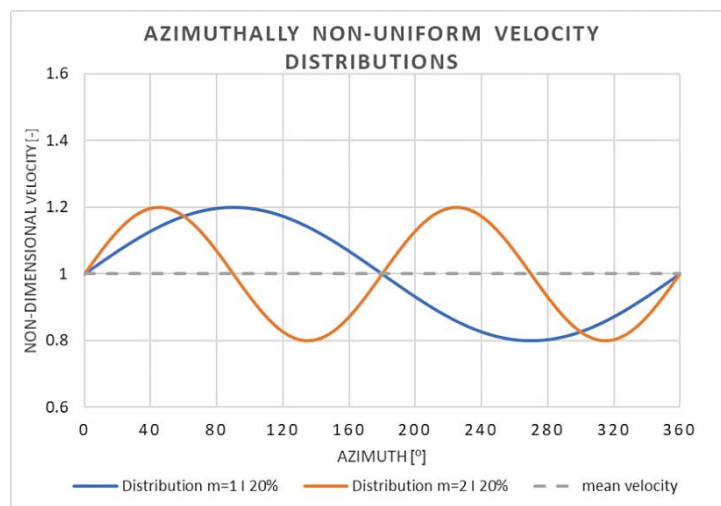


Figure 99: A) Implementation of grate in the CERG facility  
 B) PIV measurements of azimuthal distributions at inlet using different grates

This global state of art has encouraged a stationary study to characterize the impact of different velocity distributions at the inlet of the PEM using the 3D model presented above.

For this aim, a program able to calculate different azimuthal distributions of velocity has been constructed. Setting the mode index and amplitude of perturbation in terms of percentage of mean inlet velocity, the source file is compiled into a library which is directly manipulated by Fluent and implemented at the inlet boundary condition as the velocity profile for the mass flow rate chosen by the user. Otherwise, same mesh and global settings presented in the 3D model description are set.

First, we have analysed the impact of the mode index. Simulations for the full set of points of performance curves presented previously have been launched for inlet perturbations with first and second mode shapes and 20% of amplitude. These are represented graphically in *Figure 100*.



*Figure 100: Azimuthal distributions used in simulations to study the impact of modes*

*Figure 101* shows that the implementation of those perturbations doesn't have a significant influence on performance curves, since the shift of pressure maximums is minor with respect to homogeneous velocity distribution ( $m = 0$ ) and the developed pressure decreases slightly with the input of a non-homogeneous velocity distribution. Therefore, we concluded that both tested modes haven't significant importance in the global performance of the ALIP.

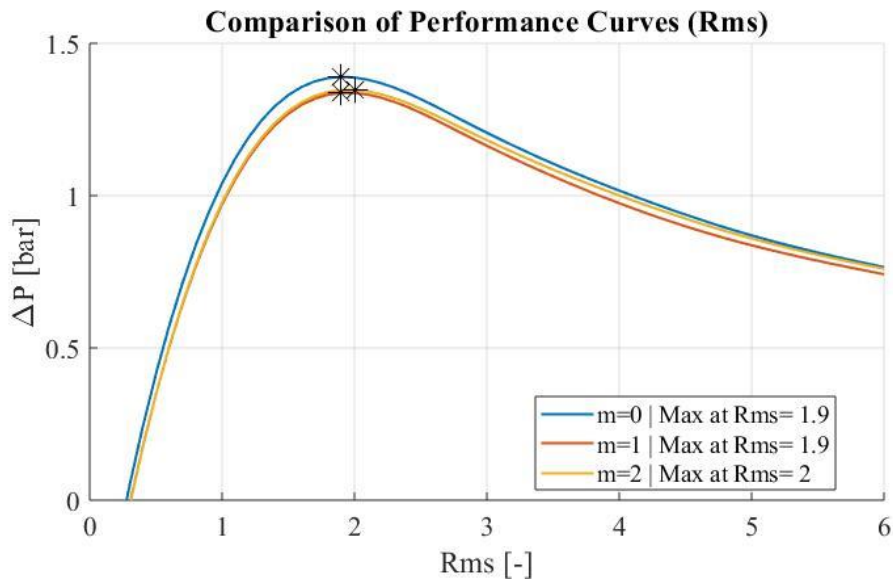


Figure 101: Impact of disturbance mode in performance curve.

However, analysing the development of perturbation in terms of the inhomogeneity of mean velocity<sup>3</sup> along the pump, we notice that every performance point has different behaviour in comparison to the others. Figure 102 and Figure 103 put in evidence that it exists a certain threshold for each mode at which disturbance amplitude starts to grow along the channel.

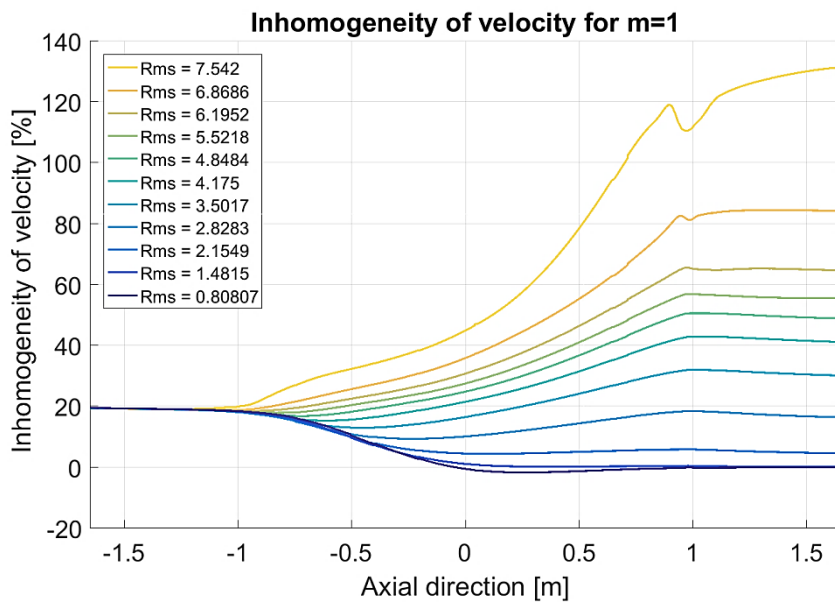


Figure 102: Inhomogeneity of velocity along the ALIP for mode 1 with 20% inlet amplitud

<sup>3</sup> Here we have defined the inhomogeneity of velocity as half the difference of maximum and minimum values divided by the mean inlet velocity.

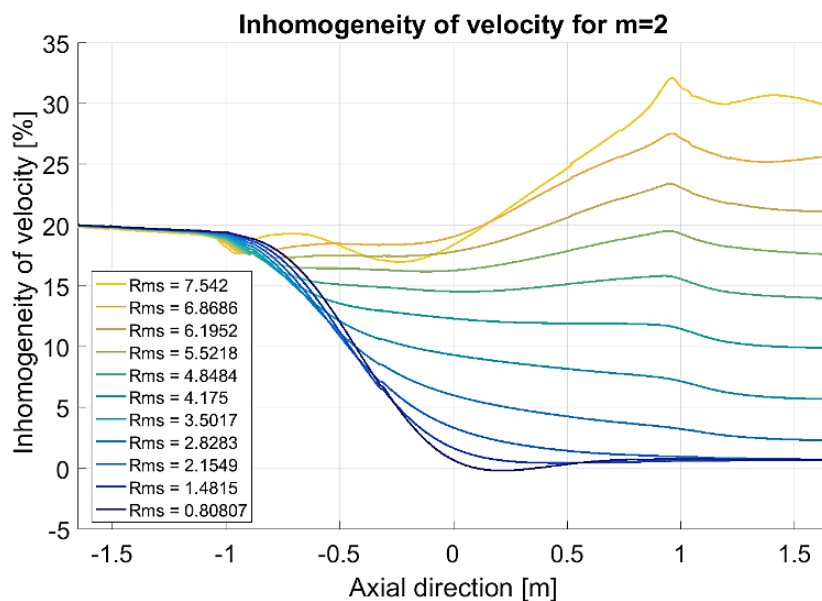


Figure 103: Inhomogeneity of velocity along the ALIP for mode 2 with 20% inlet amplitude

The first perturbation mode in *Figure 102* is damped out for *Rms* values below 2.8, while in the case of second perturbation mode (*Figure 103*) this happens until *Rms* values around 5.5. This demonstrates that simulations present the same tendency than theory, which states that the instability threshold for lower mode indices is smaller.

Furthermore, we appreciate that for the same *Rms* regime the growth of perturbation varies significantly, since for the same disturbance amplitude at *Rms* of 7.5 the first mode case would present outlet azimuthal maldistribution of 120%, besides the second mode perturbation would only grow up to 30%.

As a consequence, we can highlight the interest for the implementation of the CEA grate described before. Not only would this decrease the amplitude of perturbation, but also would enable a higher mode distribution at inlet, and therefore disturbance growth along the pump would be less important.

From another point of view, we can also analyse the contour plots of the magnetic field and axial velocity in the azimuth-axial direction plane at the middle of the channel. Here, in order to better describe velocity and magnetic field behaviour at the outlet of the ALIP, simulations were carried out using longer geometry. Instead of one wavelength before and after the sheet of current inductor, calculations were done doubling both at inlet and outlet.

From *Figure 104* to *Figure 111* show axial velocity and radial magnetic field module distributions at a stable performance point (*Rms* = 1.4815) and an unstable point (*Rms* = 6.1952) for first and second mode perturbations at inlet.

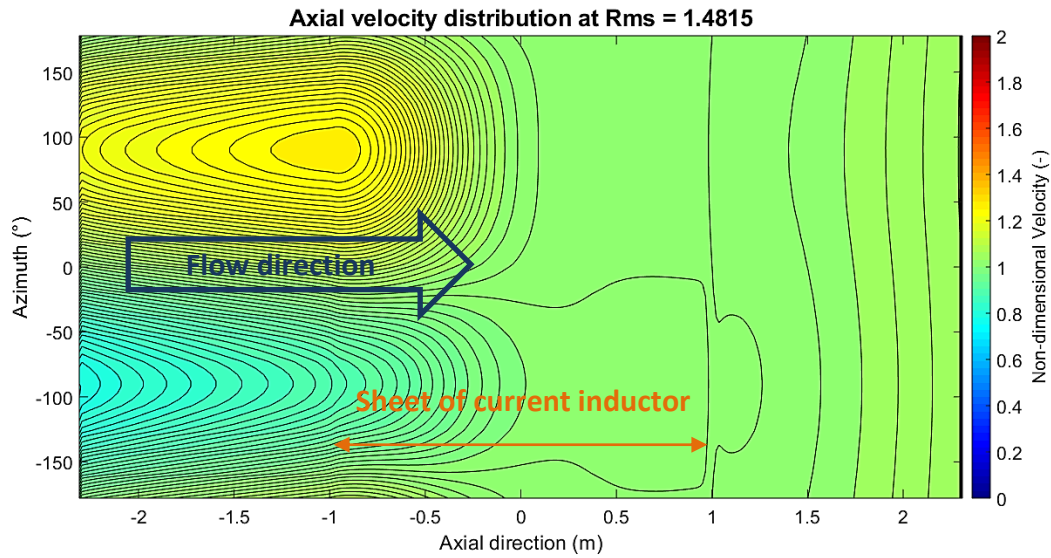


Figure 104: Contours of axial velocity distribution with inlet perturbation  $m=1$  at stable regime  $Rms = 1.4815$

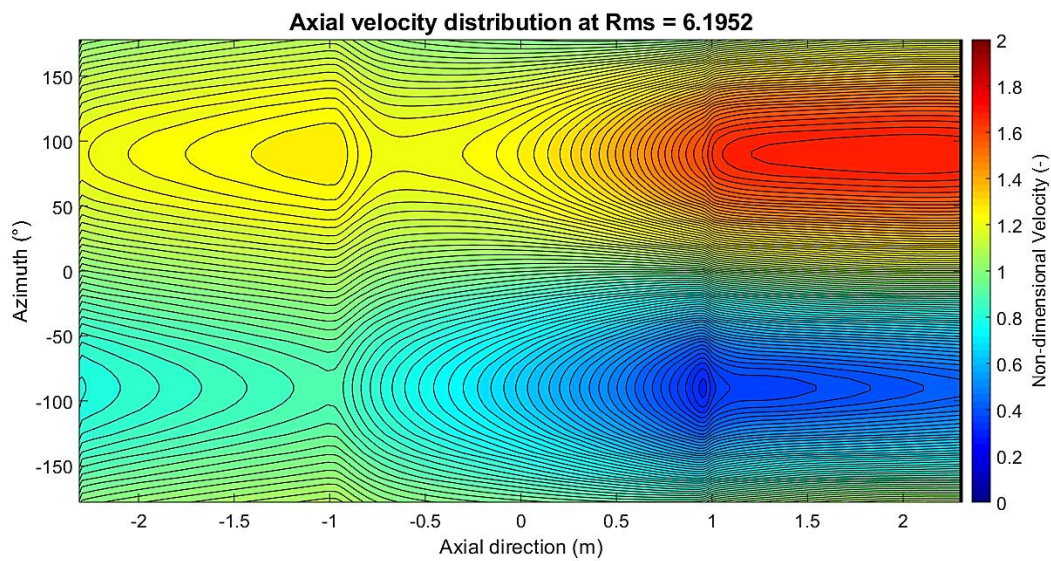


Figure 105: Contours of axial velocity distribution with inlet perturbation  $m=1$  at unstable regime  $Rms = 6.1952$

Results reveal that at  $Rms$  around 1.5 outlet velocity distribution is homogeneous, while for the unstable case at  $Rms$  around 6.2 the inlet perturbation increases along the pump. It is seen that end effects have an important role in this growth, especially at the outlet of the inductor.

Another important conclusion to extract is that the mode is conserved along the pump. This means that perturbation does not change its form along the ALIP, so maximums and minimums of velocity at inlet should be found at the same azimuth at outlet.

## CHAPTER 4

Peak values of azimuthal velocity are obtained around 0.04 % of the mean axial velocity for the stable case and of 0.1 % for the unstable one. We conclude that they are negligible in comparison to axial velocity.

Looking at radial magnetic field module in *Figure 106* and *Figure 107*, we observe similar behaviour than in velocity contours. Mode 1 is not very significant in the stable case while for the unstable one we observe that it is importantly increased at the outlet of the inductor.

Plots of axial magnetic field module are not shown here because they don't add further information to the study, since in both cases homogenous distributions are found.

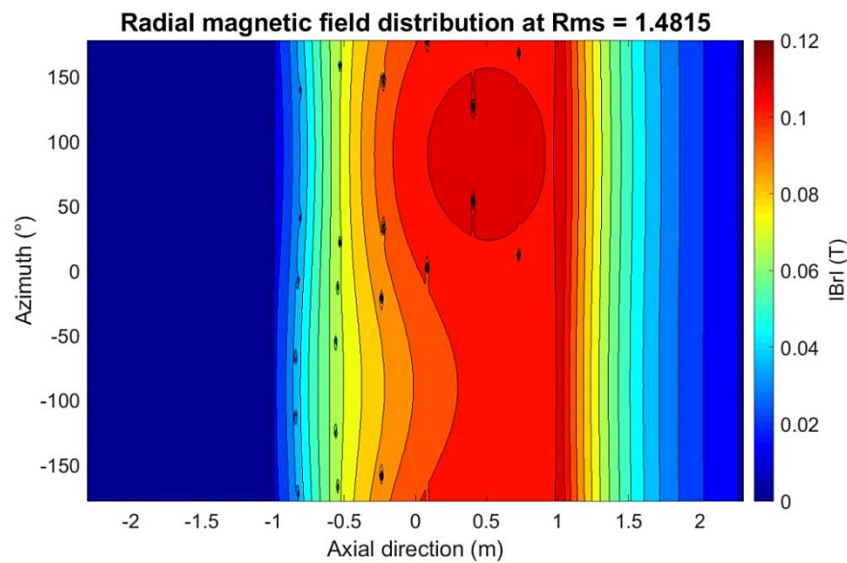


*Figure 106: Contours of radial magnetic field module distribution with inlet perturbation  $m=1$  at stable regime  $Rms = 1.4815$*

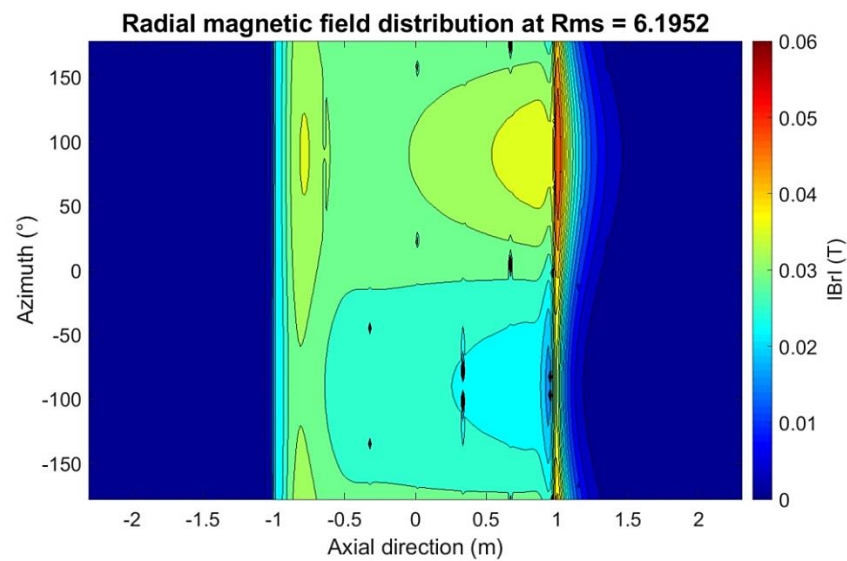


*Figure 107: Contours of radial magnetic field module distribution with inlet perturbation  $m=1$  at unstable regime  $Rms = 6.1952$*

Analysing contours for mode 2, we obtain that perturbations have lower growth along the ALIP for the same regimes than the previous calculations using mode 1. In particular, the axial velocity distributions shown in *Figure 109* and

*Figure 110* show a similar behaviour to the first mode perturbation, but with smoother amplification at outlet. In addition, azimuthal velocities were also evaluated in this case, where peak value was around 0.02 % for the stable case and 0.04% for the unstable one. Once again we can conclude that they are insignificant in comparison to axial values.

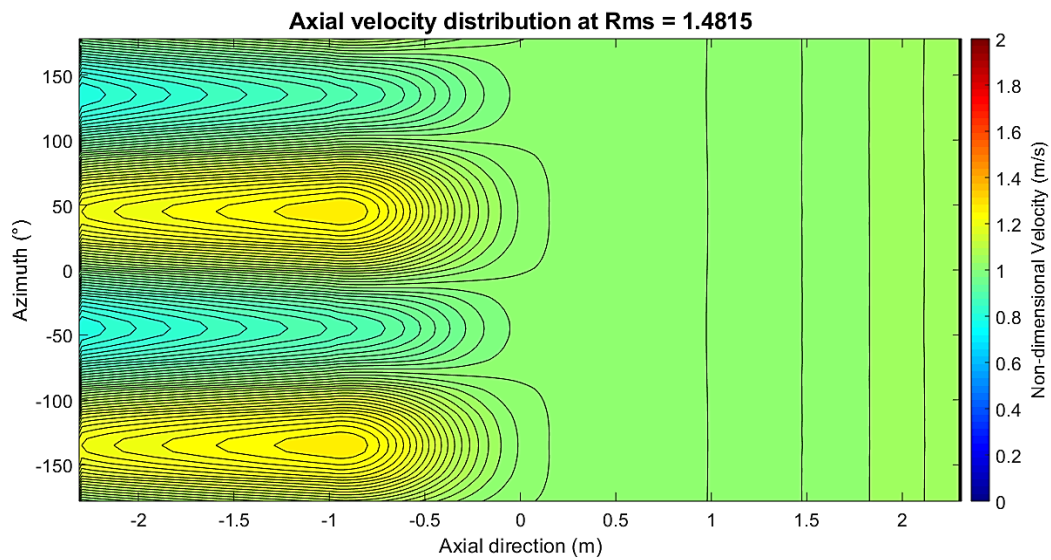


*Figure 108: Contours of axial velocity distribution with inlet perturbation  $m=2$  at stable regime  $Rms = 1.4815$*

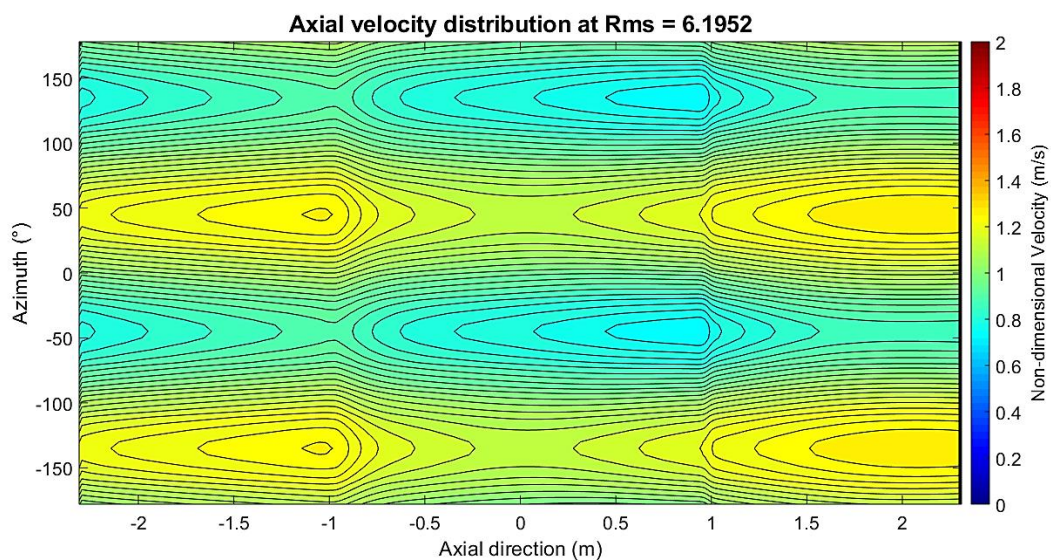


*Figure 109: Contours of radial magnetic field module distribution with inlet perturbation  $m=2$  at unstable regime  $Rms = 6.1952$*

Radial magnetic field results for the mode 2 in *Figure 110* and *Figure 111* are also coherent with previous case solution. Second mode is slightly visible in the stable regime, while at higher *Rms* regime we find a stronger relative amplitude of mode 2 at the outlet of the ALIP, somehow shaded by the importance of the outlet effect in that regime, that drives the maximum value of the colour map.

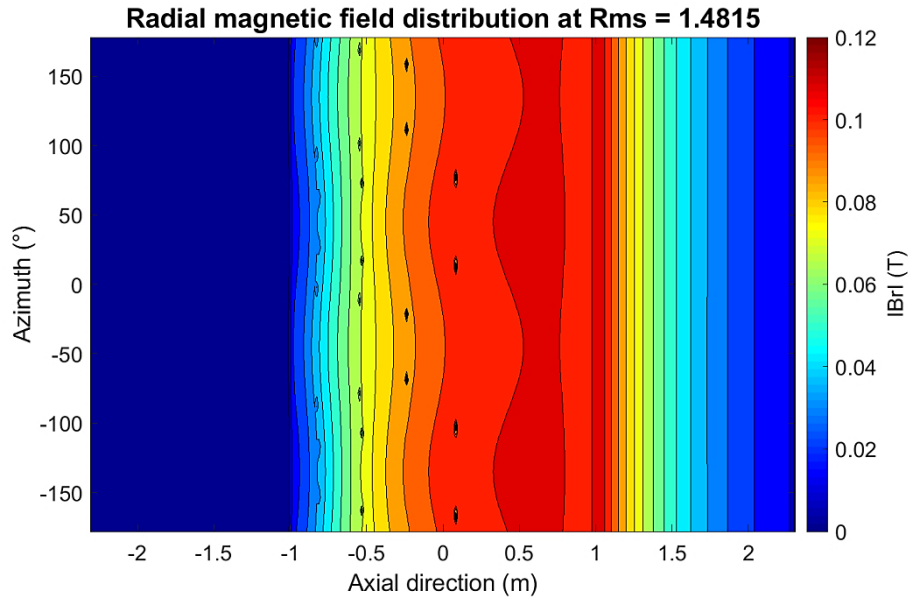


*Figure 110: Contours of radial magnetic field module distribution with inlet perturbation  $m=2$  at stable regime  $Rms = 1.4815$*

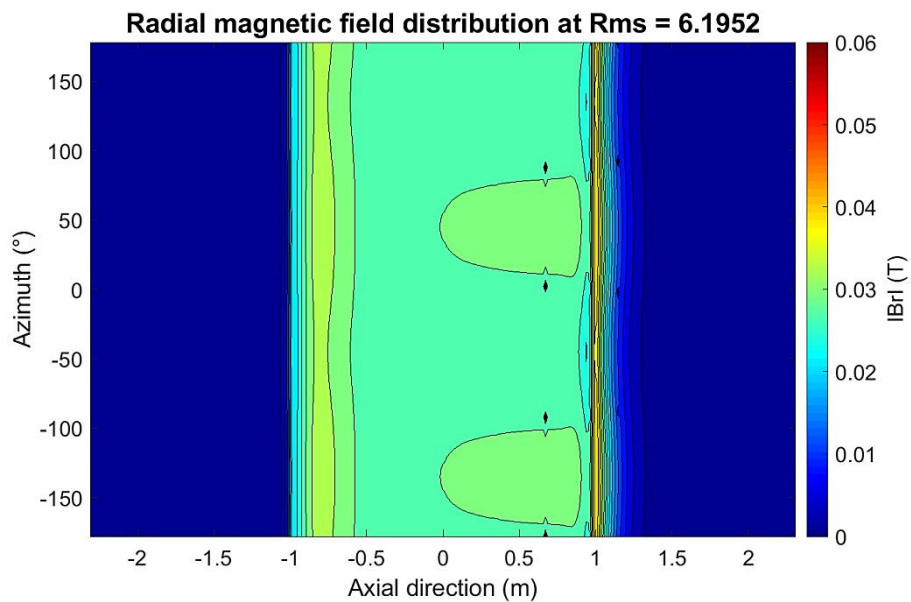


*Figure 111: Contours of radial magnetic field module distribution with inlet perturbation  $m=2$  at unstable regime  $Rms = 6.1952$*

Once the impact of the disturbance shape has been rigourously studied, the following question to answer is how the ALIP reacts to different amplitudes of perturbations.

For this aim we have consider inlet velocity distribution with first mode shape for three different amplitudes (10%, 20% and 30%) using the same model and settings presented in sub-section 4.3.1.

The comparison of obatined performace curves (*Figure 112*) puts in evidence that there is a slight impact on developed pressure with the size of perturbations. In addition, maximums are placed at same *Rms* value (1.9), so we expect inhomogeneity growth to start at the same *Rms* threshold for different disturbance amplitudes, only if the mode number remains the same.

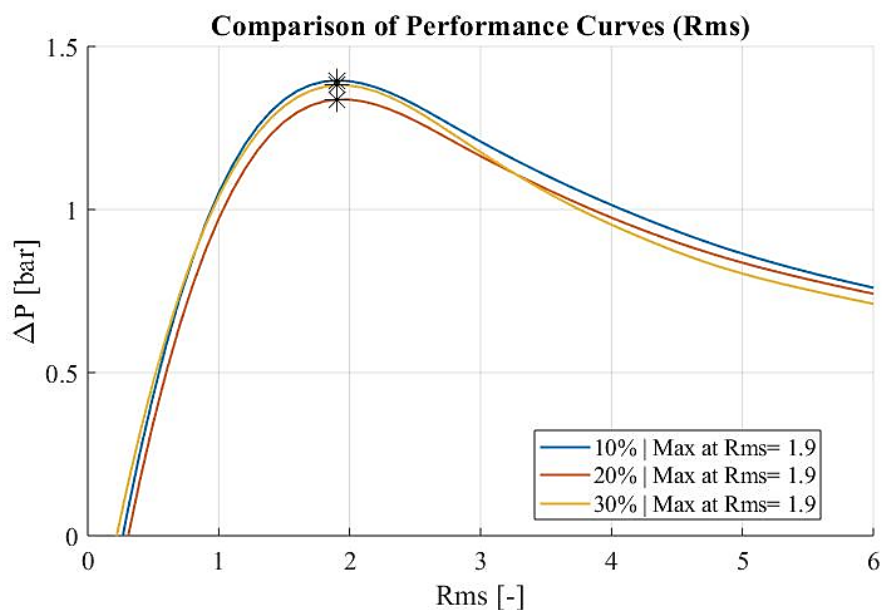


*Figure 112: Impact of disturbance amplitude in performance curve.*

*Figure 113* and *Figure 114* analyse the development of the first perturbation mode for 10% and 30% amplitudes respectively. Behaviour is similar to that found for the 20% perturbation (*Figure 102*), as the threshold for the growth of disturbance is the same in the three cases with *Rms* value of 2.8. However, we can remark that a higher inhomogeneity at the inlet implies bigger disturbance at the outlet, since at same regime we find greater outlet disequilibrium in the case of 30% amplitude.

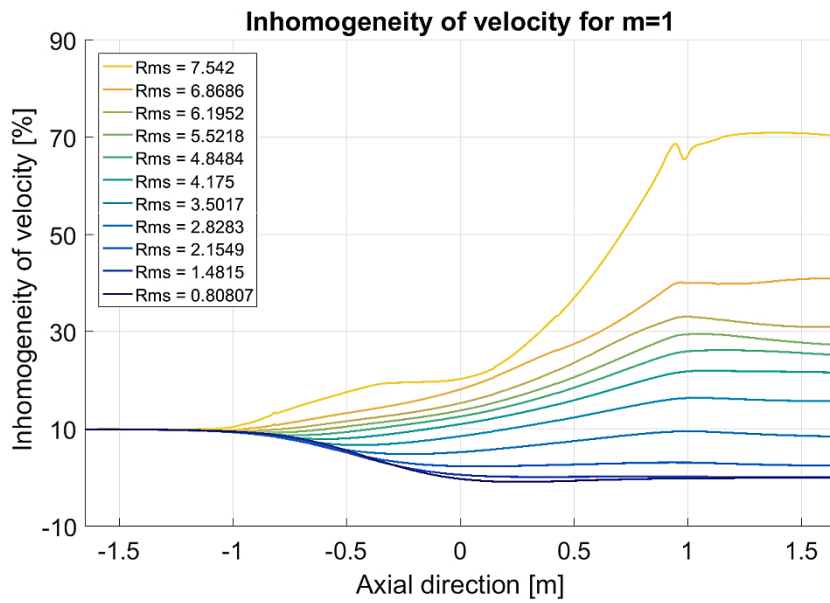


Figure 113: Inhomogeneity of velocity along the ALIP for mode 1 with 10% inlet amplitude

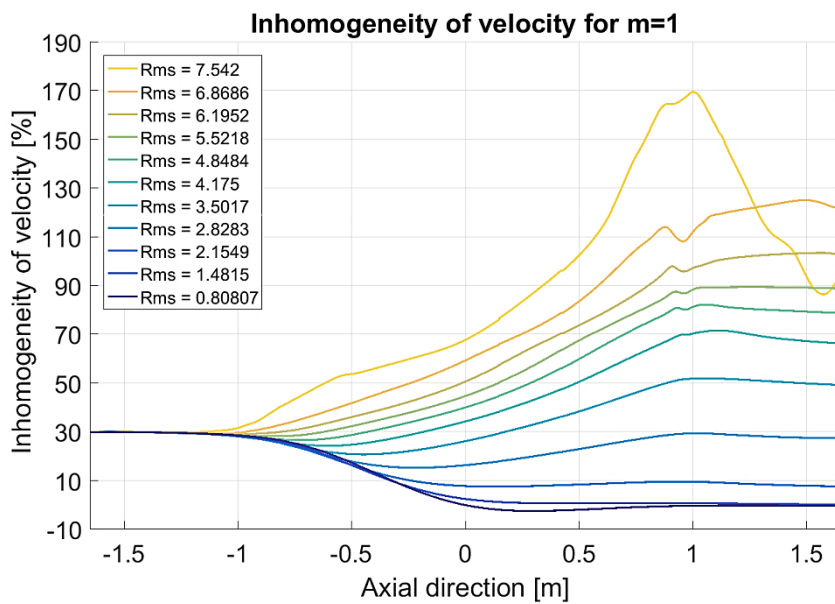


Figure 114: Inhomogeneity of velocity along the ALIP for mode 1 with 30% inlet amplitude

As a conclusion of the whole stationary analysis carried out, *Figure 115* express perturbation growth rates estimated along the active part of the pump<sup>4</sup> as a function of the *Rms* regime for each one of the cases considered above. Here positive values of the growth rate imply the amplification of the inserted perturbation at the given regime, so we would consider that zero value would be the threshold for the increase of inhomogeneity in the flow.

We can clearly see that perturbations with the same first mode shape has same amplification threshold at *Rms* of 2.8, while for the second mode we find that the limit is around *Rms* of 5.5.

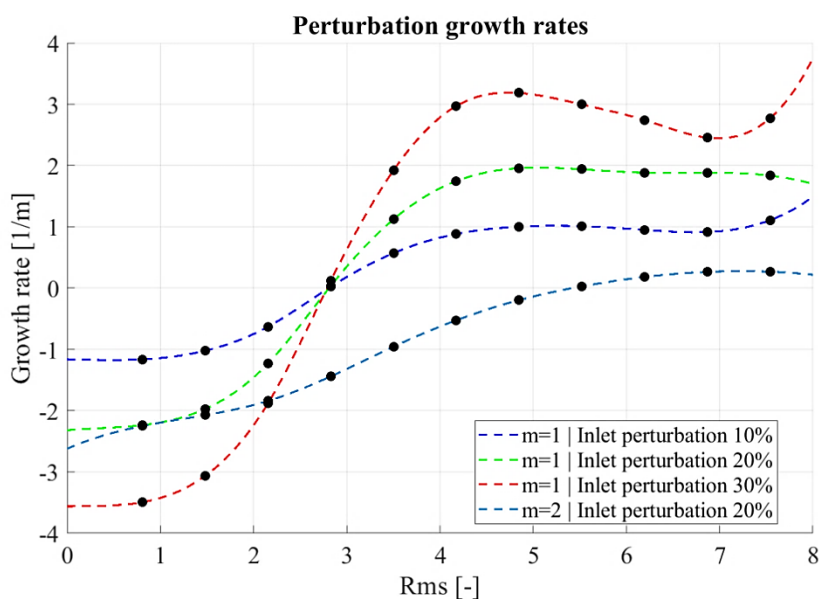


Figure 115: Perturbation growth rates

### 4.3.3. Transient analysis of perturbations

In this part, we present unsteady simulations that were run to seek the low frequency (LF) fluctuations obtained experimentally on PEMDYN and in earlier studies as well [24]. As it appears in our literature review (chapter 2), those LF fluctuations have always been related to the azimuthal instability of the pump and we want to further study this relation.

However, it was already highlighted that the simulation of double supply pulsations is out of scope of the code skills. Hereafter we would consider that if supply frequency is high enough, DSP frequencies would not interfere with low frequencies pulses, caused by MHD instability.

The transient model has been built using similar settings than in previous simulations for an electric supply of 20 Hz and 300A and properties of sodium at 350°C.

<sup>4</sup> Growth rates are estimated as the difference of velocity inhomogeneity at the inlet and outlet of the inductor divided by the length of the inductor.

## CHAPTER 4

However, in general terms, if a numerical model has a stationary solution (maybe unstable, but found with appropriate iterative scheme that doesn't mimic a time evolution), it can take long time to start to fluctuate when the model is switched to a time accurate simulation. Most often, the fact of considering a white noise perturbation in the time dependant simulation helps to fasten the process since this would excite all possible frequencies of the system.

Using the same program than previously to impose a non-axisymmetric inlet velocity distribution over the azimuth, we have implemented a random component varying with the calculation time, with a mean value and fluctuation amplitude specified by the user. For the current study we have considered a first mode perturbation of 20% in average, with an additional random fluctuation of 20% around this average value, so that the mode 1 amplitude varies from 0 to 40% of the mean velocity at inlet.

It is important to note that convergence times were important, since for good signal treatment small time-steps were required (0.01 s, which means that our white noise perturbation spectrum goes up to 50Hz, where it will be largely damped by the fluid inertia as the DSF fluctuations that we do not simulate). In addition, unstable cases might present recirculation of the flow, so for better convergence we estimated 100 iterations per time-step, which is quite conservative indeed). Therefore, even if geometry was importantly simplified and mesh was relatively light in terms of elements, calculation could last up to 2 weeks for a total simulation time of 50 s. Further reduction in the calculation time will be possible using a coarser mesh in the boundary layer zone and maybe specific MHD law of the wall, at the expense of validations and sensibility studies which were not included in this work.

Similarly to previous studies, here we have considered two simulations: a stable performance point ( $Rms = 1.5$ ) and an unstable one ( $Rms = 6.2$ ). Both simulations have been launched for a total simulation time of 17 s.

Results in the following page (*Figure 116* and *Figure 117*) show the time evolution of minimal and maximal inlet and outlet velocities for both cases. First of all we notice that at inlet velocity points are a sort of "cloud" of random points where the maximum velocity varies from the mean velocity to +20%, while the minimum velocity disequilibrium varies at the same time from 0 to 20% (the inlet perturbations are symmetrical since they follow the shape of mode 1)..

The outlet fluctuations, sampled at the same azimuthal positions than the inlet ones, are represented by solid line curves with long fluctuation periods on *Figure 116* and *Figure 117*. As in previous cases, stable case would tend to damp out disturbance at inlet (at  $Rms = 1.5$  outlet perturbation is of  $\pm 3.8\%$ ), while for the unstable case the inhomogeneity grows (at  $Rms = 6.2$  outlet perturbation goes up to  $\pm 53\%$ ).

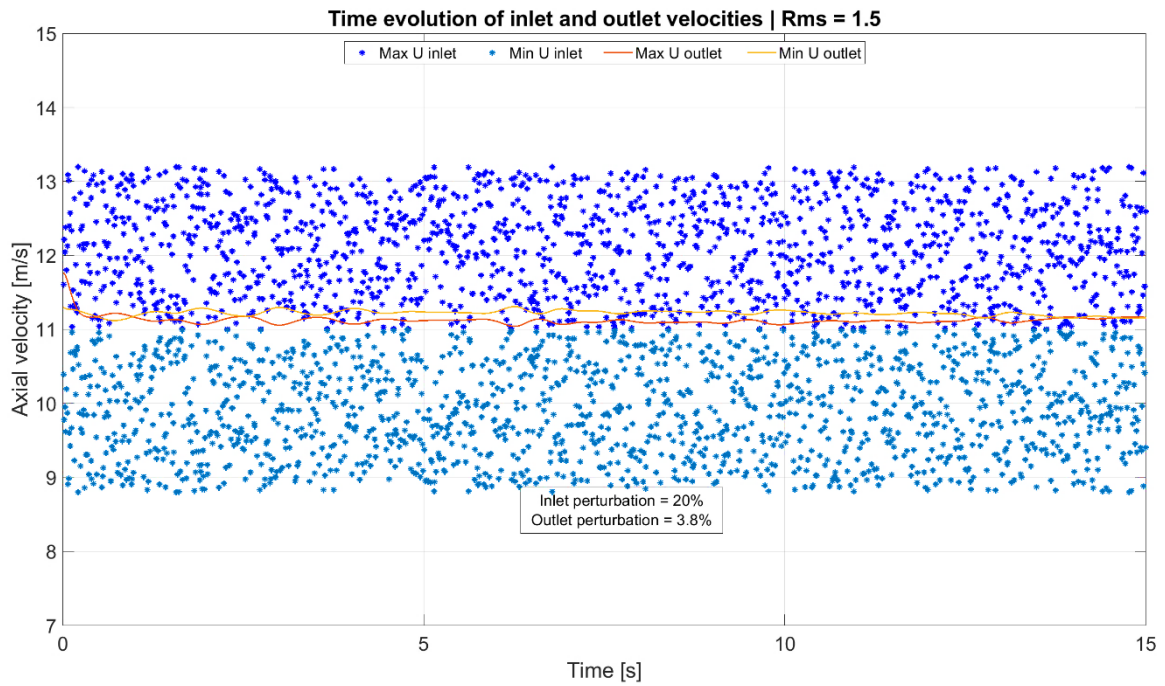


Figure 116: Time evolution of maximum and minimum inlet and outlet velocities at stable performance ( $Rms = 1.5$ )

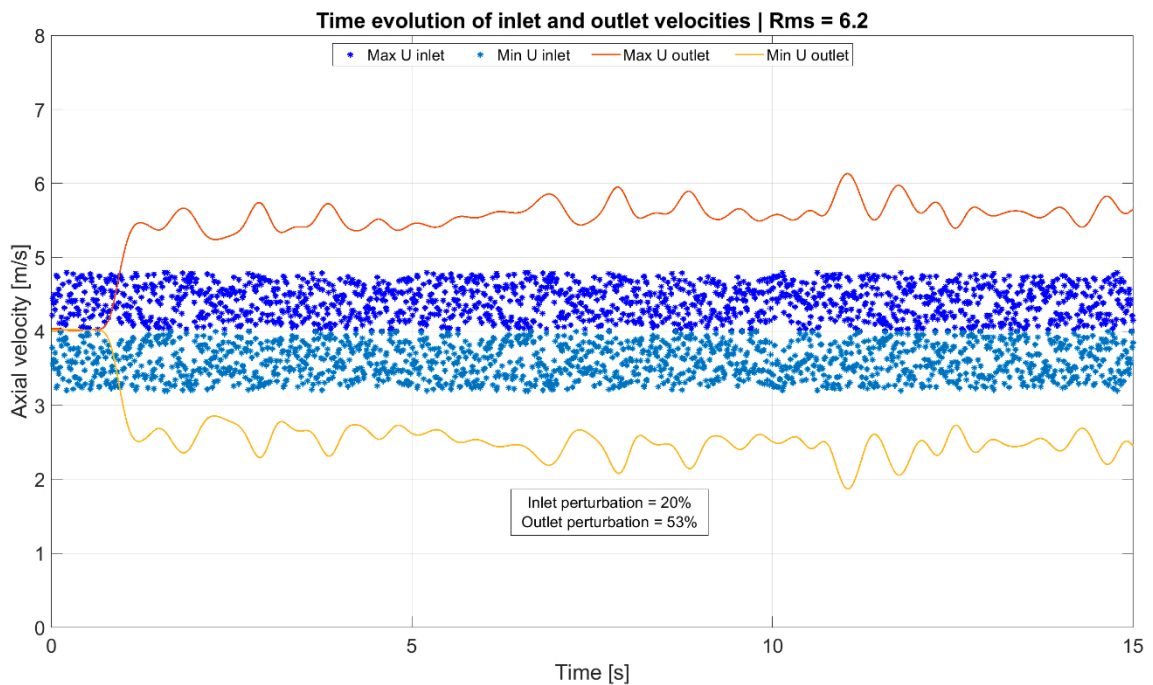


Figure 117: Time evolution of maximum and minimum inlet and outlet velocities at unstable performance ( $Rms = 6.2$ )

## CHAPTER 4

Analysing frequency spectrums we have applied power spectral density (*PSD*) to inlet and outlet velocity signals with HighPass Matlab designed filter applied for frequencies up to 0.2 Hz.

It is observed for the low slip case ( *Figure 118*) that at inlet, white noise disturbance excites all frequencies, so a continuous spectrum all along the band is obtained. However, at outlet pulsations are insignificant.

On the contrary, the unstable case presents strong low frequency fluctuations at the outlet, much stronger than the inlet fluctuations in the same band. Notice that the white noise pulsations injected in the unstable case appear smaller than the inlet fluctuations in the stable case, as they are  $\pm 20\%$  of a mean velocity that is lower than for the stable simulation.

We can conclude that the presented approach of transient MHD simulation of an ALIP shows same physical behavior than the one obtained in experimental researches on the subject. This confirms that EPM-INDUC code is able to simulate quantitatively the spectrum of MHD instabilities, and that it can be used in future studies to better understand the origin of these fluctuations and analyse the effect of different operating parameters on such phenomena.

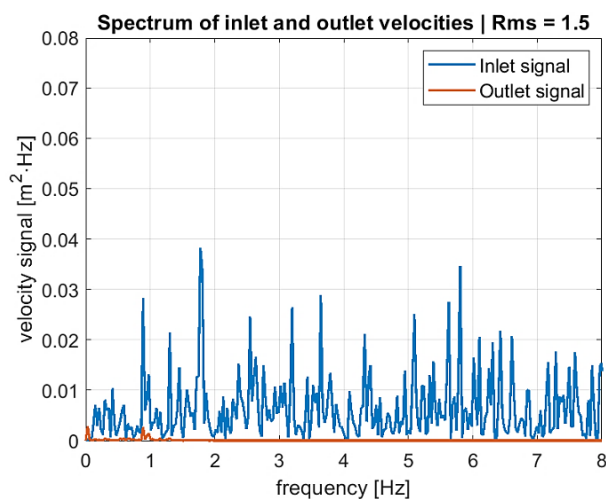


*Figure 118: Spectral Power Density of inlet and outlet velocities at stable performance*

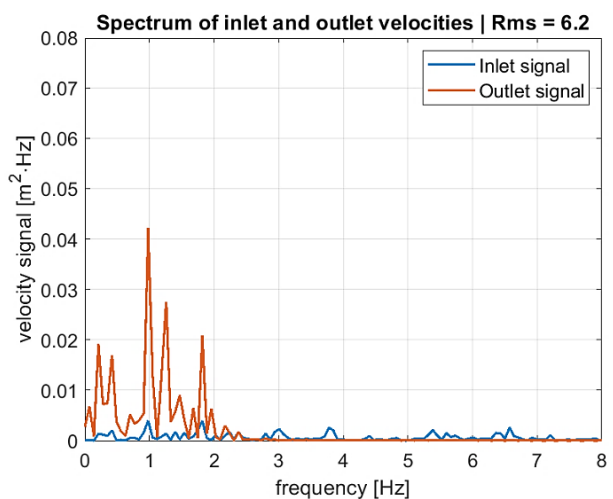


*Figure 119: Spectral Power Density of inlet and outlet velocities at unstable performance*

## 5. EXPERIMENTAL DEVELOPMENTS

Thanks to the exploitation of the PEMDyn experimental facility in CEA Cadarache, we could extract a large amount of relevant data that allow the characterization of several effects studied in previous sections. It should be noted that the operation of the loop was completely carried out by a team from LETS Laboratory (CEA Cadarache) specialized in sodium technology. The contribution of this PhD work in the current investigation concerns the choice of the different conditions for the loop operation and for the use of specific instrumentation. Afterwards, we proceeded to the data post-processing and physical analysis for the interpretation of results.

This chapter begins with an overall vision of the experimental facility with its principle components, instrumentation and operation limits. Secondly, a review of most relevant experimental campaigns carried out are explained including *modus operandi* and expectations. Each of them is accompanied with the approaches adopted for post-processing, presentation of results and main conclusions extracted.

### 5.1. PEMDyn experimental loop setup and equipment

The PEMDyn facility comprises the test circuit as main compound, placed at approximately 2.8m height from the ground, and all the utilities required to manage a sodium facility (storage tank, purification system, Argon circuit, power supply, command control, etc.). These are located below the test circuit and are supported using a metallic structure.

In order to give a more exhaustive vision of the whole experimental loop, following paragraphs detail the 5 main units that make up the facility (*Figure 120*). There are:

- **UF1: Sodium auxiliary circuit** [425°C – 1,5 bars absolute – 1 m<sup>3</sup> of Na]

Sodium auxiliary circuit manages the sodium level inside the test circuit. It contains a sodium storage tank, a small EMIP and a set of valves and piping equipped with their heating systems and instrumentation.

- **UF2: Sodium purification system** [425°C – 1,5 bars absolute – 220 l of sodium]

The purification unit ensures the quality of the sodium used in the test circuit. It consists of a cold trap for purification of the sodium, a plugging indicator that controls the quality of sodium and a set of three valves and pipes equipped with their heating systems and instrumentation.

- **UF3: Test circuit unit** [425 ° C, 10 bars absolute, 520 l Na] (*Figure 122*):

The high discharge test ALIP is comprised in this circuit, which can operate with a maximum power of 325 kW. Here, the performance of the pump is piloted with the closing / opening of a ball valve, which regulates and adjusts the pressure loss of the circuit.

## CHAPTER 5

The cooling of the external part of the EMP is carried out by eight heat exchangers using organic oil compatible with sodium placed on the 8 yokes in order to cool the inductor. Furthermore, three other heat exchangers are employed for cooling the sodium of the test circuit, and thus evacuate the heat from Joule losses. Between heat exchangers 1 and 2 a FLEXIM double beam ultrasonic (US) flowmeter FLUXUS F704 model is located.

In order to maintain sodium liquid, temperature above around  $100^{\circ}\text{C}$  must be ensured, so the pipes are heated with electrical windings around them and covered using specific insulation. Consequently, during operation the temperature of the pipes and components is always maintained higher than the melting temperature of the sodium.

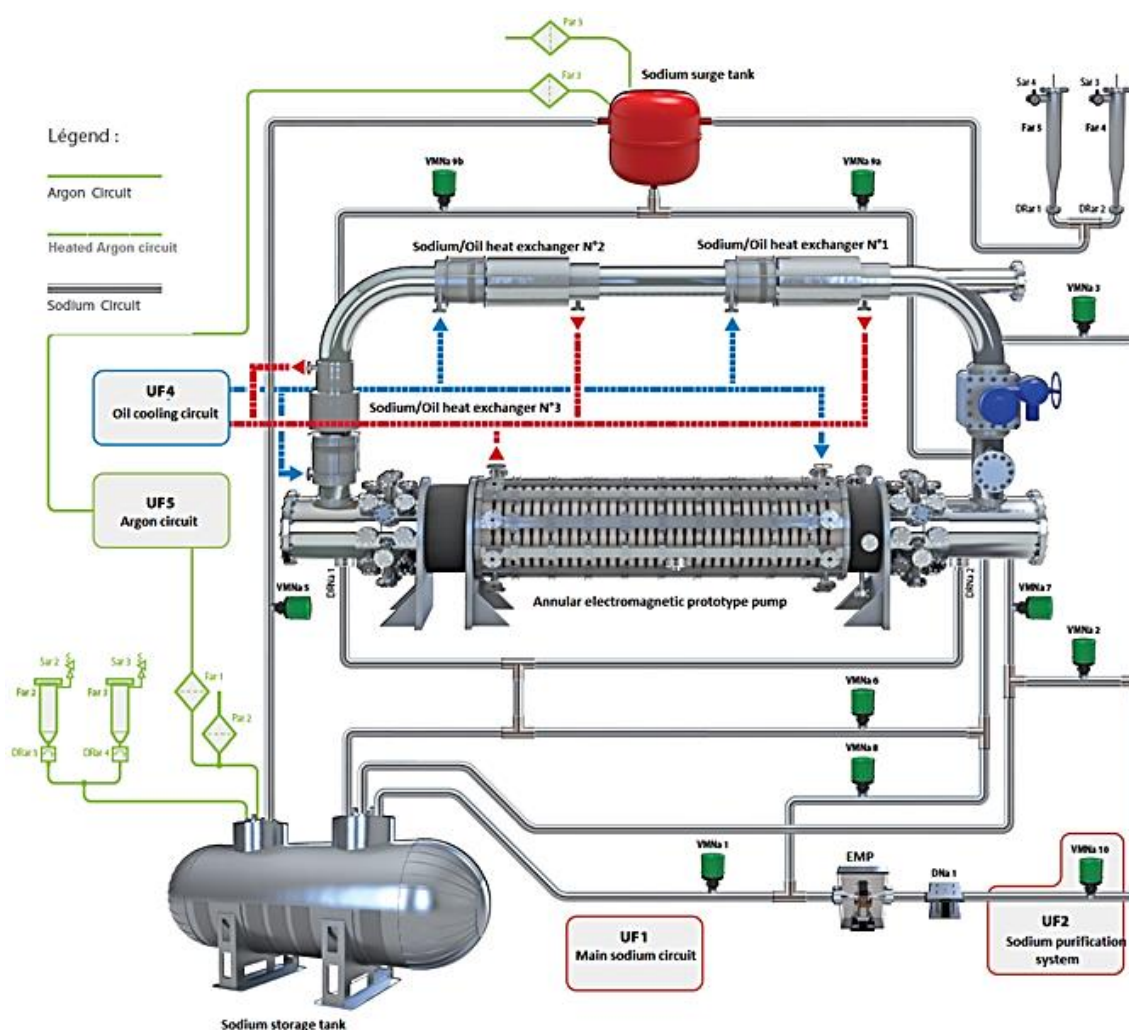


Figure 120: Hydraulic view of the overall sodium circuit

An expansion tank is also provided at the highest point of the loop for pressurizing the system. Its aim is to maintain the inert gaz (argon) in contact with sodium and to control sodium level fluctuations due to thermal dilatations. Pressurization also permits to avoid cavitation

## CHAPTER 5

phenomena and to reduce gas retention in the flow, and thus avoid measurements problems, particularly from the US flowmeter.

For security reasons, they are provided sodium leakage detection systems, placed on the various pipes and components and thermal insulation for all hot parts of the circuit. In fact, the entire circuit is inclined with an angle of 5% (in cold conditions) to ensure a gravity drain of the sodium inside the loop, so that the lowest point is located at one side of the EMP, and the expansion tank at the highest point.

In addition, several flanges are disposed at the inlet and outlet of the ALIP for specific measuring sensors and a pipe test section is reserved for the validation of instrumentation.

- **UF4: Cooling system** [Max.  $T^{\circ}=200^{\circ}\text{C}$  – Max.  $Q=55\text{ m}^3/\text{h}$  –  $P=365\text{ kW}$  –  $P_s=10\text{ bar}$ ]

The cooling unit evacuates the power injected through the pump using organic oil. It is divided into the oil circuit with the pumps, heat exchangers (oil / cold water), valves and pipes, the secondary cooling circuit (cold water) placed outside the building and electrical connection batch.

- **UF5: argon circuit** [5 bars absolute, ambient temperature]

This circuit is implemented in order to avoid chemical contact between air (oxygen) and sodium. It includes the main panoply for argon distribution, several filters and sodium vapor traps and passive protection. This last preserves from overpressure.

The electrical supply is furnished by a drive that operates in power inverter mode to provide a balanced three-phase network at a frequency that can vary between 5 and 25 Hz and delivering a current of about 500A (RMS).

The principle of this power supply is as follows: the TG-BT01 supplies a transformer 400VAC / 690VAC with three-phase power of 500 kVA. The latter feeds an inverter of 1000 kW of power that permits to vary frequency and voltage. At the output of the inverter 2 low-pass sine filters ensure the required quality of current. Three transformers raise the tension (primary 690 V AC / secondary 1300 V AC) to the level required to feed the ALIP. This three-phase supply network powers the inductor of the ALIP which consists of 3 sets of 12 coils (electrically in series with a star assembly) which are placed side by side along the length of the pump. This entire configuration is illustrated in *Figure 121*.

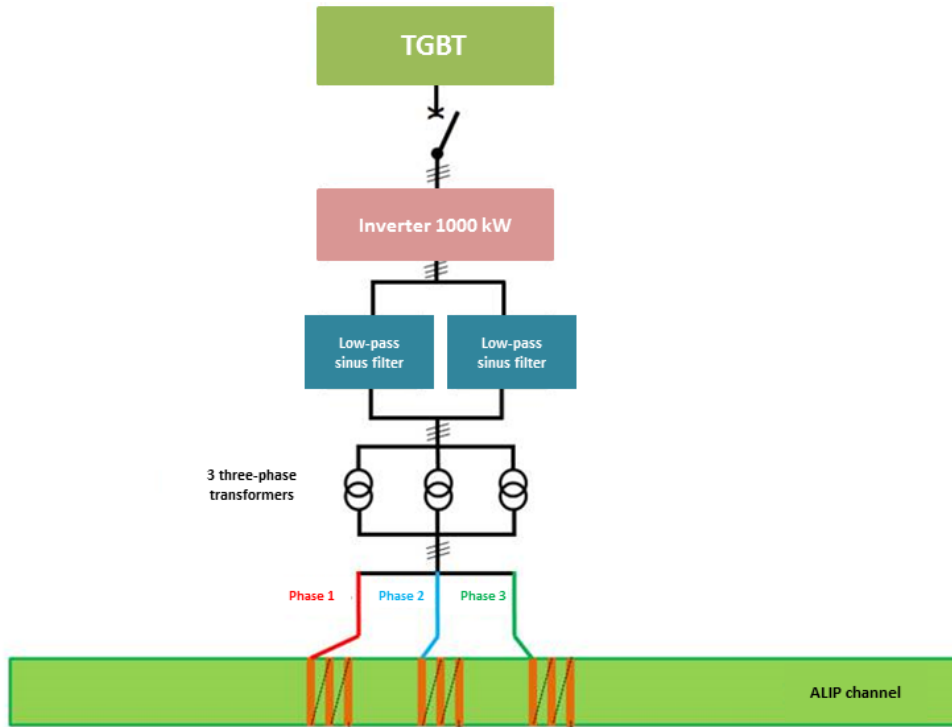


Figure 121 : Electric supply schema

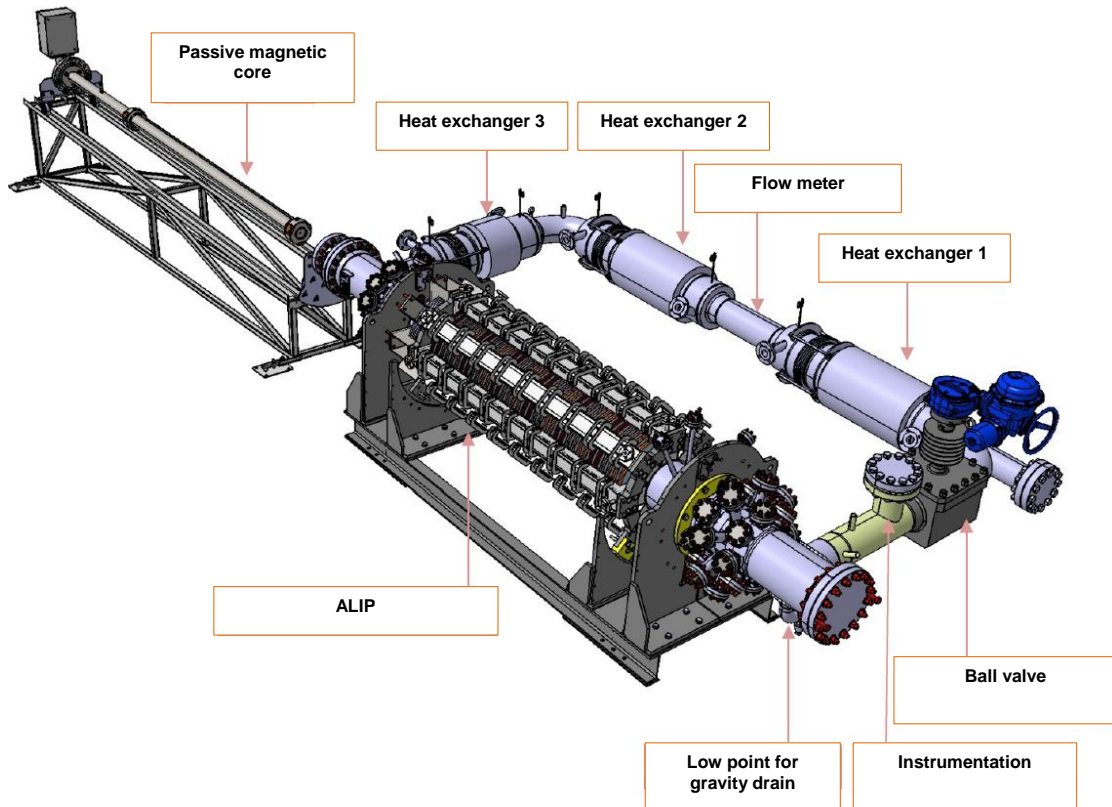


Figure 122 : Overview of the test circuit

## CHAPTER 5

*Figure 122* shows more in detail the test circuit previously described whose main component is the experimental ALIP. This consists of:

1. An annular pumping channel confined by two stainless steel walls, where at ends a set of taps and flanges for the instrumentation are disposed
2. An external inductor formed by 36 coils embedded in 8 ferromagnetic yokes
3. A ferromagnetic core permitting to close the magnetic field lines.

Both the yokes and the core form a magnetic circuit encouraging radial component of magnetic field in the channel. Nevertheless, another feasible configuration of ALIP would be changing the inner ferromagnetic core for a second inductor. This last is interesting for the study of MHD stabilization effects, so the CEA foresees to pursue investigations with the replacement of the inner core for a second active inductor. Commissioning of this configuration is scheduled for 2019.

For its maximum electrical power supply (325 kW), the ALIP is expected to operate with a maximum flow rate of 1500 m<sup>3</sup>/h and developed pressure of 5 bars. During operation, sodium circulates at a temperature between 115°C and 270° C according to the manufacturer's specifications. However, for safety provisions, maximum temperature permitted of organic oil in heat exchangers is of 200°C, and thus automatic sodium emptying is programmed at 210°C. Furthermore, furnisher's specifications remark that for the correct behavior of US flowmeter maximum sodium temperature must be limited to 225°.

Moreover, The EMP can work in both directions making vary the electric supply, however for all results presented in the current study it was fixed clockwise.

Internal CEA document [49] details all specifications of operation protocols for sodium circuit preparation for start-up and filling. Here, as summary, we only list main operating conditions of PEMD<sub>dyn</sub> ALIP:

- Sodium flow rate: 0-1500 m<sup>3</sup>/h,
- Sodium inlet temperature: 115-200°C
- Maximum temperature of the structure and pipes: 500°C,
- Electric supply power: 0-325 kW,
- Supply frequency: 5-25 Hz,
- Voltage per phase: 0-619 V,
- Phase current: 0-550 A

As mentioned before, PEMD<sub>dyn</sub> is equipped with a set of measuring devices for characterizing physical behavior of different performance regimes. Among others, they permit to record sodium flow rate, static pressure, local velocity, dynamic pressure, magnetic field, temperatures and vibration signals. The following paragraph details the location of different measuring sensor that are employed for the chacterization of phenomena.

## CHAPTER 5

The pump has three rows of eight flanges at the inlet and outlet, i.e. 48 slots. The inlet flange rows are numbered from 1 to 3 and those at outlet from 4 to 6. Each flange corresponds to a immersion sleeve (protective sleeve) that can accommodate a sensor. Currently 18 flanges are occupied:

- 2 Static pressure sensors (at inlet and outlet) which acquire the developed pressure by the ALIP.
- 6 Dynamic pressure sensors (3 at inlet , 3 at outlet) that record dynamic pressure variations.
- 6 Hall effect magnetic field distortion sensors (1 at inlet and 5 at outlet) for local velocity measurements.
- 2 Magnetic field sensors (at inlet and outlet) measuring the axial component
- 4 Empty immersion sleeve for complementary velocity or magnetic field instrumentation

In addition, a flowmeter located in the opposite part of the loop is used to measure the total sodium flow through the pump, and vibration sensors have been implemented along the loop in order to check pulsations level in structures during pump operation.

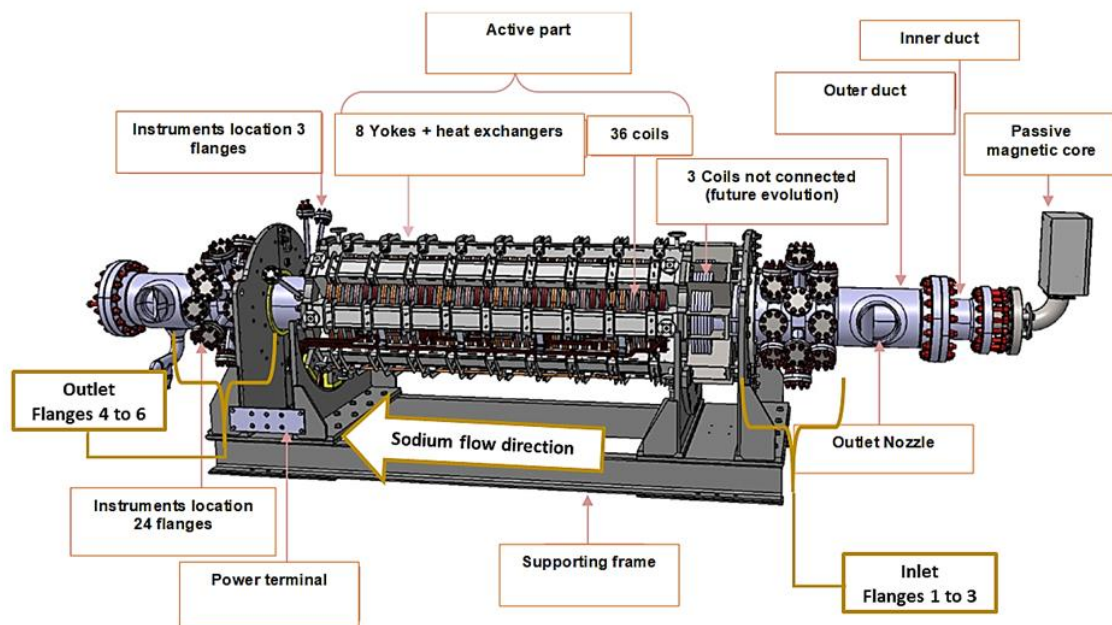


*Figure 123: ALIP configuration with instrumentation*

This disposition leaves 30 free flanges. However, to avoid sodium leakage, the flanges in lower positions are not used. Furthermore, one side of the pump is difficult to access and therefore positioning of the instrumentation on this side is not foreseen.

As previously mentioned, the flanges are arranged in three rows at inlet and outlet and disposed around the azimuth. The second row is shifted one sixteenth of a turn relative to the first flange,

which allows distributing all the sensors around sixteen different azimuths. The location of each of the sensors presented above is shown in *Figure 123*.

For the better comprehension of following results presented, a synthesis of main sensors exploited must be given. This includes US flowmeter, static pressure, dynamic pressure and local velocity sensors.

- US Flowmeter

It consists of a double beam ultrasonic flowmeter from *FLEXIM* society model FLUXUS F704. Four ultrasounds probes are set up on the sodium pipe opposite to the ALIP. The distance between the sensors is determined by the electronics according to the input data (diameter of piping, pipe thickness, pipe material and fluid properties).

For flow measurement, one ultrasonic pulse is emitted in the flow direction and another in the opposite direction, so that the sensors alternately serve as transmitters and receivers of US signals. Being shorted the transit time of the emitted signal in the direction of flow, sodium velocity can be calculated from the difference  $\Delta t$  of the transit times measured for both signals. Knowing the pipe section, the flowrate is then estimated.

As previously said, maximum temperature for correct measurements is fixed at 225°C. Precision is of 1.2% of acquisition  $\pm 0.01\text{m/s}$ .

- Static pressure sensors

Two pressure sensors are installed for the measurement of sodium pressure in the test circuit. They are placed upstream and downstream of the EPM on the flanges provided for the instrumentation to quantify the pressure difference developed by the pump.

The sensors obtain the difference between the sodium pressure in the circuit and the atmospheric pressure by piezo resistive measurement using a Wheatstone bridge in the range of 0 to 10 relative bars.

A calibration procedure is always carried out at the beginning and the end of the exploitation of the loop, so we can consider eventual offsets.

In this case, maximum temperature permitted is of 600°C and precision is of 1.2%.

- Dynamic pressure sensors

Eight sets of dynamic pressure measurement developed by *Prescamex* society have been installed at the inlet and outlet of the pumping channel at different azimuthal positions.

Each set of dynamic pressure measurement consists of a dynamic pressure probe, a thermocouple, a cooling fin system and a charge converter.

The probes are manufactured by *Columbia Research Laboratories* (model 934-M8) and are acoustic sensors built to operate in sodium environments for high frequency signals between 2 Hz and 6 kHz. The measurement is carried out by membrane deformation in contact with the sodium. This membrane displaces a thin metal rod that is connected to an airtight strain gauge. Afterwards, the analog signals of mechanical stresses on the gauge are converted into an electrical signal, which is translated into pressure unities with conversion factor.

*Figure 125* shows the specifications card of probe number 1.

During the operation of the facility, the acquisition and recording of the dynamic pressure sensor measurements are done at a frequency of 1613 Hz, where an algorithm is employed for monitoring the signal. Then, VASCO software enables real-time spectral analysis by FFT post-treatment.

Furthermore, the strain gauge and instrumentation are outside the pump so that if the seal leaks, the integrity of the sensor is not affected. The sensors have little influence on the dynamics of the flow, so the impact in the pressure field can be neglected. They can operate until maximum 200°C and 10 bars and sensitivity of 600 mV/psi.

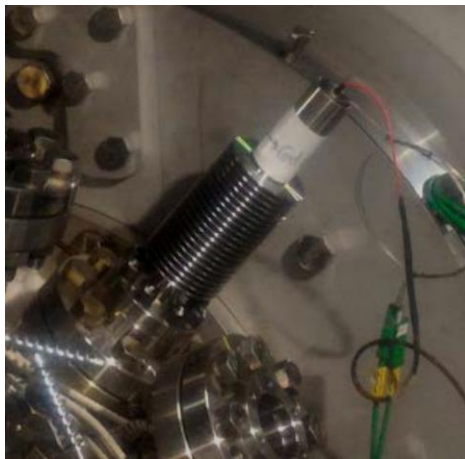


Figure 124: Dynamic pressure sensor in PEMDyn loop

Columbia Research Laboratories, Inc.		Pressure Transducer Calibration Card	
For: <u>GIACINTEC</u>	Order Number: <u>VP0/15/08311</u>		
Model: <u>934-M8</u>	Date of Calibration: <u>11-9-15</u>		
Serial Number: <u>1472</u>	Pressure Range: <u>-</u> psi to <u>1100</u> psi		
<b>Voltage Sensitivity:</b>	Temperature of Calibration: <u>72</u> °F		
So = <u>-</u> pk mv/pk-psi Open Circuit	Temperature Range: <u>100</u> °F to <u>900</u> °F		
S = <u>-</u> pk mv/pk-psi with <u>-</u> pF Load	Mounting: <u>1.125-12</u>		
<u>-</u> rms mv/pk-psi with <u>-</u> pF Load	Housing: <u>INCONAL</u>		
<b>Charge Sensitivity:</b>	Weight: <u>-</u> gm Crystal Cap. <u>690</u> pF		
Sq = <u>59.2</u> pk pcmb/ pk-psi	Cable Capacity: <u>-</u> pF Length		
Range: <u>2</u> Hz to <u>6</u> kHz	Calibrated By: <u>M. SHIELDS</u>		
07-2012		Form No. 348	
+ w/MODEL: 5814-10 S/N 011			
SYSTEM SENS - 600 mV/PSI			

Figure 125: Dynamic pressure sensor specifications

- Hall effect magnetic field distortion sensors for local velocity (ENS sensors)

Six local velocity sensors are located in the facility. The probes have been developed for PEMDyn by the *Ecole Normale Supérieure de Lyon (ENS)* and installed at the CEA Cadarache in September 2017. They operate by Hall effect, where the principle is as follows: When the conductive fluid flows into the ALIP channel, it induces a local distortion of the magnetic field generated by the inductor. This magnetic field difference is linear with the fluid velocity, so that the velocity probes output an electrical signal proportional to the field distortion with fixed acquisition frequency of 300 Hz.

Each probe consists of a measuring head with 8 piezoelectric sensors, 3 thermocouples and compressed air specific cooling. Four of these probes (placed at the outlet of the ALIP) have a permanent magnet in the center of the measuring heads. Thanks to this small magnet, the 4 sensors placed close to the fluid (A1, C1, A2, C2) capture the total distortion of magnetic field by the fluid. The other 4 more distant sensors (B1, D1, B2, D2) detect principally the magnetic field delivered by the ALIP inductor, slightly influenced by the sodium flow. Meanwhile, the two other probes without magnet are employed for reference measurements. Each pair of sensors equipped with a magnet can measure one components of local velocity, axial or azimuthal depending on orientation. *Figure 126* shows the schema of the probe's architecture.

Using adequate calibration, local sodium velocity can be obtained from the time average of the difference of close to fluid sensor signals and the distant detector signals. In latter developments, the denomination of *sensor signal* would make reference to this time averaged subtraction.

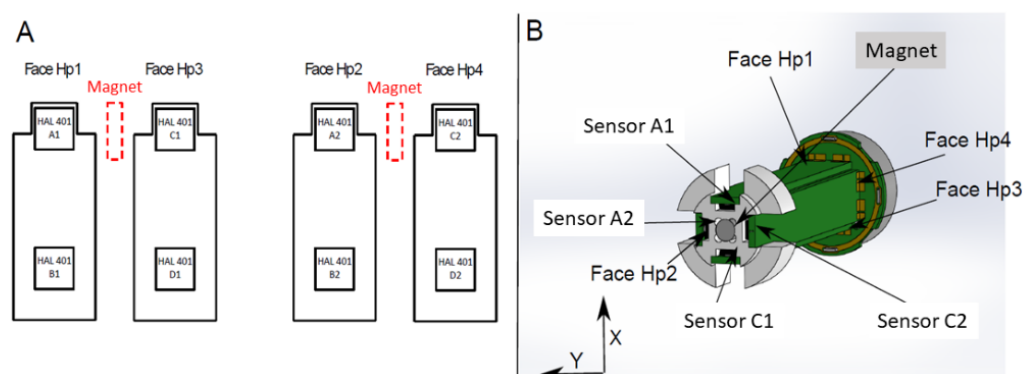


Figure 126: Architecture of ENS sensors

Measuring heads are cooled with a constant compressed air flow rate of 40 l/min for a pressure of 2 bars. It is important to note that high instrumentation temperatures might lead to calibration problems, since temperatures of 40 °C and over have a non-negligible effect on the relation of the magnetic field distortion with the output signal. The compressed air flow thus must avoid important temperature drifts of the sensors in order to guarantee reliable velocity measurements.

The instrumentation heads are placed close to the working fluid but without direct contact with sodium, since they are placed at the immersion sleeves at inlet and outlet. This disposition prevents the sensor from sodium corrosion. The locations of sensors in PEMDYN loop are shown in Figure 127.

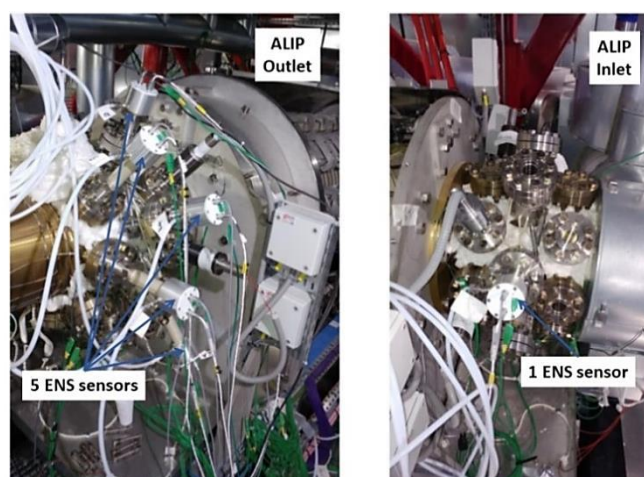


Figure 127: ENS Hall effect sensor location in PEMDYN loop

Unlike the rest of sensors presented previously, the ENS Hall effect sensors are still in prototype state, so analysis of its behavior and calibration is required for its use. In later sections the procedure adopted is explained in detail.

## 5.2. Experimental campaigns

Different protocols have been applied in order to characterize different performance features in the PEMDyn loop. Following subsections treat the four main ideas explored during the experimental exploitation:

1. Magnetic field measurements when loop was empty of sodium for validation of numerical codes.
2. Pressure developed by the ALIP at different operation regimes and comparison with solution obtained using EPM-INDUC simulation code.
3. Calibration of Hall effect magnetic field distortion sensors (ENS sensors) regarding the impact of different factors on measurements for the obtention of local velocity experimental values.
4. Characterization of stable and unstable behaviours related to bibliographic researches through dynamic pressure sensors and ENS sensors acquisitions.

### 5.2.1. Magnetic field measurement without sodium

Magnetic field measurements were carried out when the loop was empty of sodium using Hall Effect sensors. The 3 components of the magnetic field (radial, azimuthal and axial) were measured inside the ALIP channel on the whole length of the pumping duct (about 2.5 m) every 5 mm on 11 azimuthal positions and on 3 different radial positions inside the duct (outer, middle and inner). Disposition of sensors is shown in the schemas of *Figure 128*.

Measurements have been performed with a stick equipped with 9 Hall-effect sensors in order to measure the 3 components of the field (radial, axial and azimuthal). During the magnetic field measurement, the pump has been operated at low power in order to avoid overheating due to the lack of self-cooling by the sodium flow.

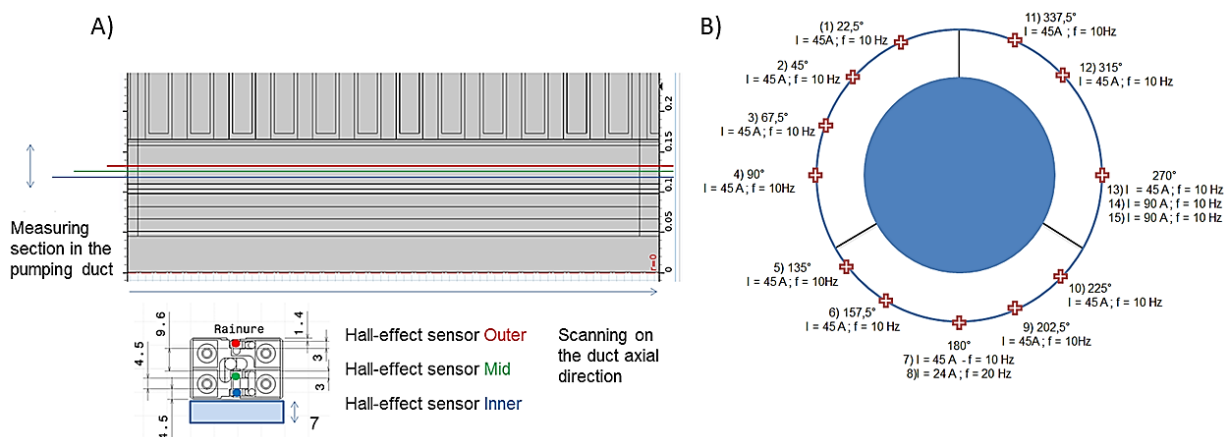


Figure 128: A) Hall-effect sensors radial localizations along the pump duct B) Diagram of magnetic field measurement azimuthal localizations

Conditions used for this aim were the following:

- Intensity of current: from 50 A to 100 A
- Frequency: from 5 Hz to 10 Hz
- Electric voltage: from 50 V to 100 V
- Induction heating of the pumping duct:  $<5.5$  kW
- test loop maximum temperature  $\approx 120^{\circ}\text{C}$
- Magnetic flux density in the pumping duct: 1 to 80 mT

Measurements obtained are documented in CEA internal report [49] and conference article [50]. There it was noticed that differences over the azimuth were slight and that azimuthal component was much weaker compared to the rest.

Nevertheless, the aim of this section is to show validity of electromagnetic description of numerical simulations. Two simulation tools have been used to compare with experimental data: COMSOL commercial code and EPM-INDUC code, previously presented in the numerical chapter. Both of the models employed present 2D-axisymmetric description.

COMSOL model performs purely electromagnetic simulation considering the channel empty with detailed geometry similar to that of the PEMDyn pump. On the other hand, in EPM-INDUC model we uncoupled EM solving from CFD solving setting the sodium material electrical conductivity to zero in the channel. Furthermore, geometry is much simpler than in previous case, i.e. ferromagnetic yokes are considered perfect and not described in the model.

Both simulations have been carried out to be compared with experimental acquisition in PEMDyn facility with electric supply of three-phase current of 45.6 A and 10 Hz of frequency.

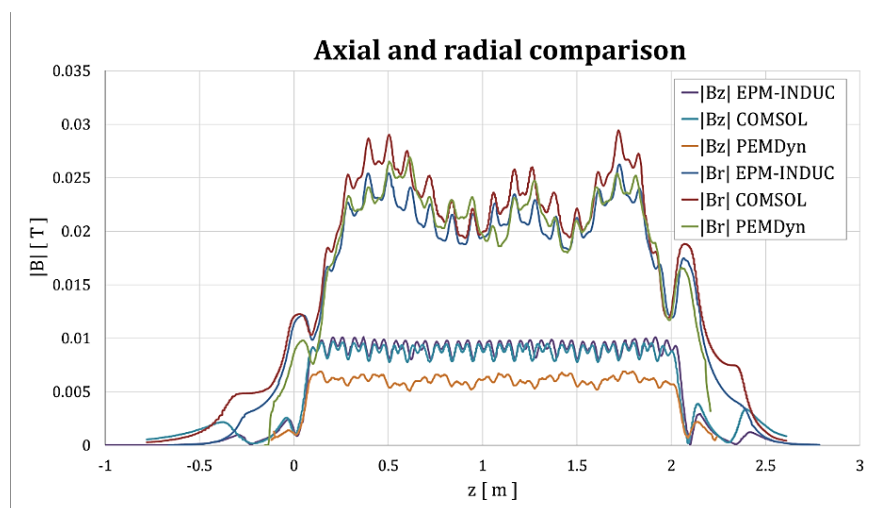


Figure 129: Comparison of radial and axial components of the magnetic field

Figure 129 shows that both radial and axial components of the experimental magnetic field are consistent with solutions obtained using COMSOL and INDUC models. Slight differences in values are due to the fact that geometries are not exactly the same. However, even if INDUC

model uses simpler geometry, results are very close to each other, so we can consider convenient the geometry choice for the magnetic field description.

We can conclude that both models (COMSOL and EPM-INDUC) give good estimations compared to experimental results for empty channel magnetic field measurements.

### **5.2.2. Experimental performance curves and comparison to numerical simulations**

Acquisitions with the loop filled with sodium were carried out for three supply frequencies (5 Hz, 10 Hz and 15 Hz) and three phase RMS intensities (200 A, 300 A and 400 A) at five different opening valve positions (22% 33% 44% 56% and 100%), in order to provide different performance points data. Sodium temperature was maintained at 170 °C and recordings were done during 30 seconds per performance point.

The procedure applied was the following:

- 1) The valve opening is set at 100%
- 2) Supply is set at 5 Hz and 200 A
- 3) Signals are recorded for 2 minutes. Flow rate and developed pressure are noted at each performance point.
- 4) Intensity is increased up to 400 A by increments of 100 A. The recording is repeated decreasing intensity until 200 A.
- 5) Frequency is changed and the whole procedure is repeated.
- 6) Valve opening is closed to the following position and the whole procedure is repeated.

Furthermore, before the filling of the loop, sensor offset measurements are recorded in the absence of sodium. Subsequently, for frequencies 5Hz, 7.5Hz, 10Hz, 12.5Hz; 15Hz; 17.5Hz; 20Hz and intensities 200A, 300A, 400A for 30 seconds of acquisition of speed signals, dynamic pressure sensors and temperature signals. At the end of the measurement campaign, once the ALIP is emptied this process is done again.

This process was carried out 3 times in order to have enough data to contrast results. Therefore, 75 acquisitions per repetition (225 acquisitions in total) were stocked during the experimental campaign.

In fact, the quantity of stored data was enormous considering the number of sensors recording signals (ENS sensors, dynamic pressure sensors, thermocouples, etc), and thus sorting the information for a correct post-treatment was imperative to extract valuable information.

First, we tackled with the comparison of experimental curves to numerical simulations using EPM-INDUC 2D axisymmetric model described in subsection 4.2.1.

*Figure 130* shows the comparison of experimental developed pressure–flow rate points obtained during the campaign to simulations at 5 Hz for different supply intensities. During

the exploitation we could notice that this power supply frequency was the one furnishing more points at both sides of the maximum pressure for the chosen valve openings, so this should be the more representative for describing the behaviour of both stable and unstable regimes.

In addition, we can observe that comparison is quite good, since experimental points are close to the interpolation done with numerical solutions with all pressure maximums around  $Rms$  of 1.45.

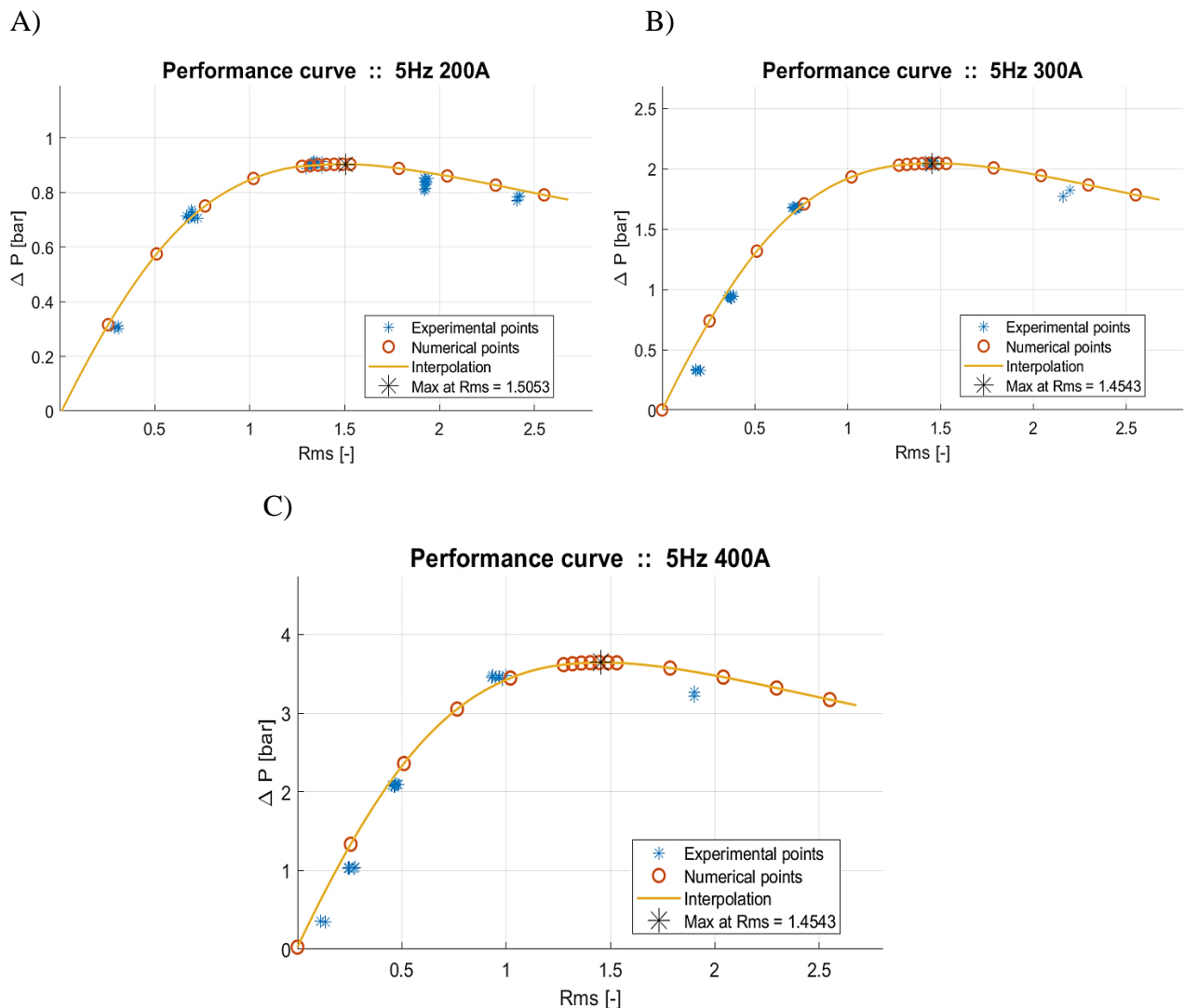


Figure 130: Comparison of experimental performance points to numerical simulations at 5 Hz for A) 200 A B) 300 A C) 400A

Looking now at other supply frequencies in Figure 131, we also obtain a good correlation to numerical interpolation. However, as commented before, with the increase of frequency for the defined valve openings most of performance points are placed at the unstable domain, and we have fewer points at low  $Rms$  to compare.

It is also important to note that, as in previous sections pressure maximums are shifted with the supply frequency, and then we would expect instability phenomena to appear at higher values of  $Rms$ .

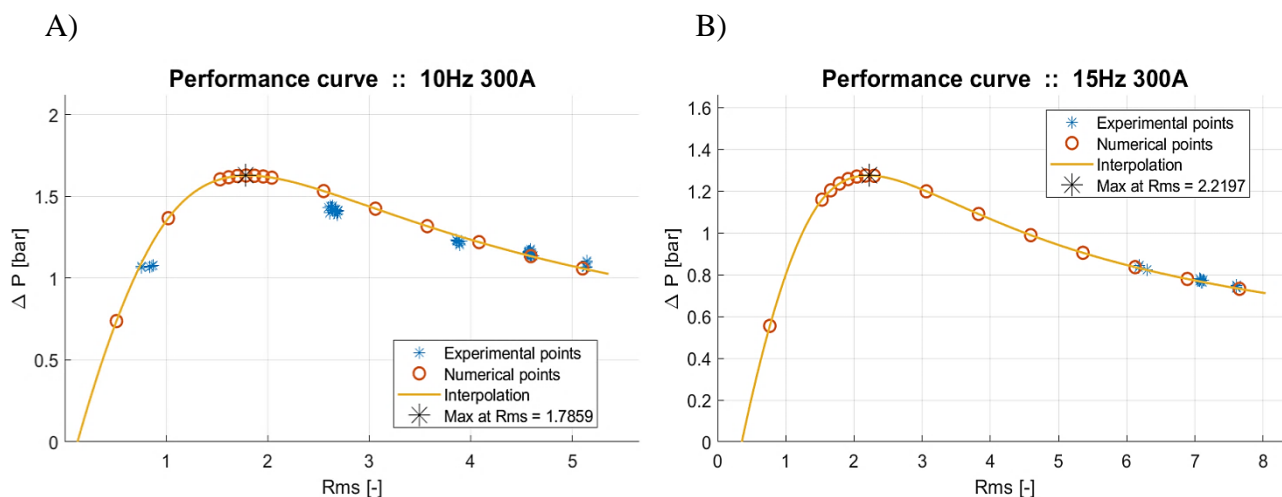


Figure 131: Comparison of experimental performance points to numerical simulations at 300 A for A) 10 Hz B) 15 Hz

### 5.2.3. ENS Sensor calibration

The objective of the signal analysis of magnetic field distortion probes was to highlight the inhomogeneity of the velocity field during unstable regimes. For this, it was necessary to calibrate the sensors, in order to be able to interpret signals and characterize their reliability.

During all the experiments we used the sensors containing the permanent magnet, numbered 1 to 4. They were located at the outlet of the ALIP at different azimuths and axial positions, as shows *Figure 132*.

The sensors measure two signals, one for the magnetic field distortion due to the axial velocity and the other due to the azimuthal velocity. However our procedures aimed at calibrating the axial component using the flowmeter measurement. In future developments it could be needed to permute position of sensors in order to also calibrate the other pair of probes.

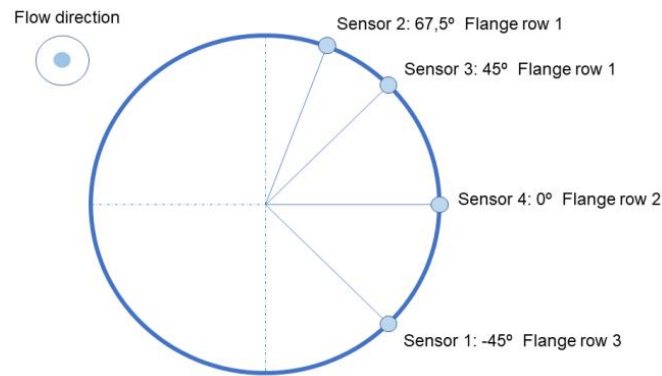


Figure 132: Cross-section of ENS sensor locations at outlet

The difficulty of those measurements lies in the fact that this technology hadn't been used before in such kind of loop as PEMDyn. They served in real conditions for the first time during the experimental campaign in Mach 2018, so it was necessary to study the impact of the different variables on the output signals: fluid temperature, frequency, voltage, instrumentation temperature, etc. The protocols were those detailed in L. Goldsteins' report on sensor calibration [51], and they were constructed in order to check the following assumptions:

- A1. The sodium temperature has a negligible impact on the measurements of the probes.
- A2. The instrumentation temperature also does not induce significant drift of the probe measurements.
- A3. The pump power supply does not influence the measurement offsets.

To verify the first hypothesis (A1.), on the 15th March 2018 we have driven a protocol in order to observe the dependency of the probes signals and the sodium temperature.

Here, we registered all sensors signals (from 1 to 4) and sodium thermocouples measurements of ENS sensors with fully open valve at 5 Hz and 400 A. The aim was to stay at constant flowrate (around 450 m<sup>3</sup>/h), and then at stable regime for presented conditions, so that we can make the assumption that at the outlet of the ALIP velocity distribution is homogenous.

The methodology was based on increasing sodium temperature in multiple steps from 120°C to 180°C for heating sequence with and inversely for the cooling sequence. Coolers of the PEMDYN loop were regulated in such way to ensure change of temperature not faster than 1°C/min.

The idea was to maintain practically same temperature per step (+/- 1°C) during the test. Data acquisition was performed during 20 seconds with loop running and flowrate around  $Q = 450$  m<sup>3</sup>/h. In Figure 133 the heating procedure of the experiment is illustrated.

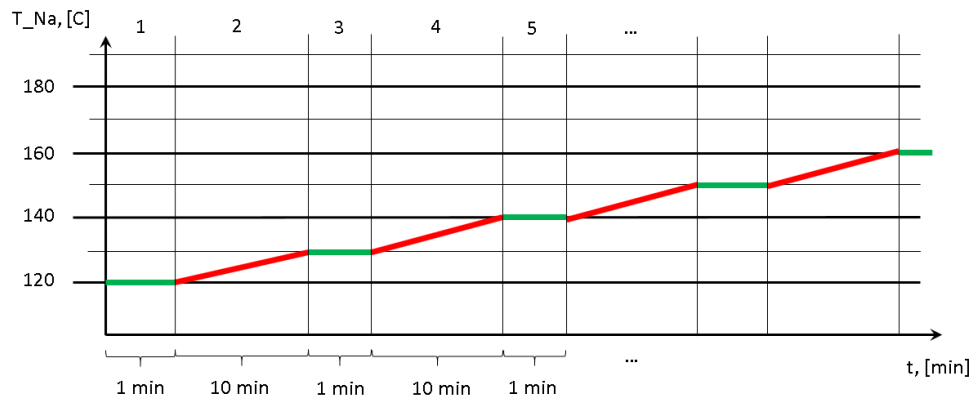


Figure 133: Scheme of operation during experiment with heating

As a result, in Figure 134 the time averaged signals for each sensor during last 20 seconds of recording are analysed as a function of sodium temperature. The purple curves represent the linear regression of the 14<sup>th</sup> March 2018 measurements for temperatures between 130°C and 180°C only for heating procedure. The one in green corresponds to the measurements of the 15<sup>th</sup> March, for both heating and cooling procedures. We observe that measurements present linear dependency with temperature, but there is an important gap in mean signals values between different days' recordings for most of the sensors.

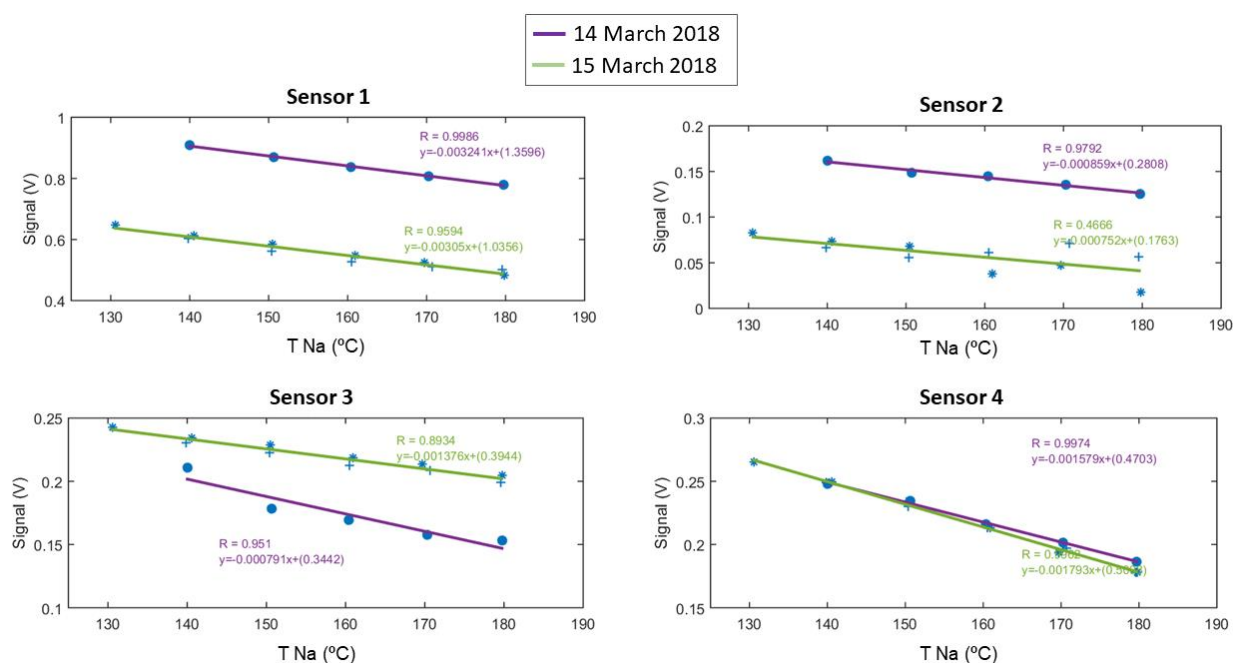


Figure 134: Probe signal dependency on sodium temperature

Analyzing the instrumentation temperature in Figure 135, we notice that a problem with the air-cooling system happened during 14<sup>th</sup> March recording, since recorded probe temperatures were significantly higher. Sensibility of the different sensors to high temperatures might be diverse,

but anyway the impact is not negligible, so probes temperatures might be monitored during operation and maintained at the same value up to 35°C. Therefore, we can conclude that the second hypothesis (A2.) doesn't apply and then 14<sup>th</sup> March measurements can be disqualified.

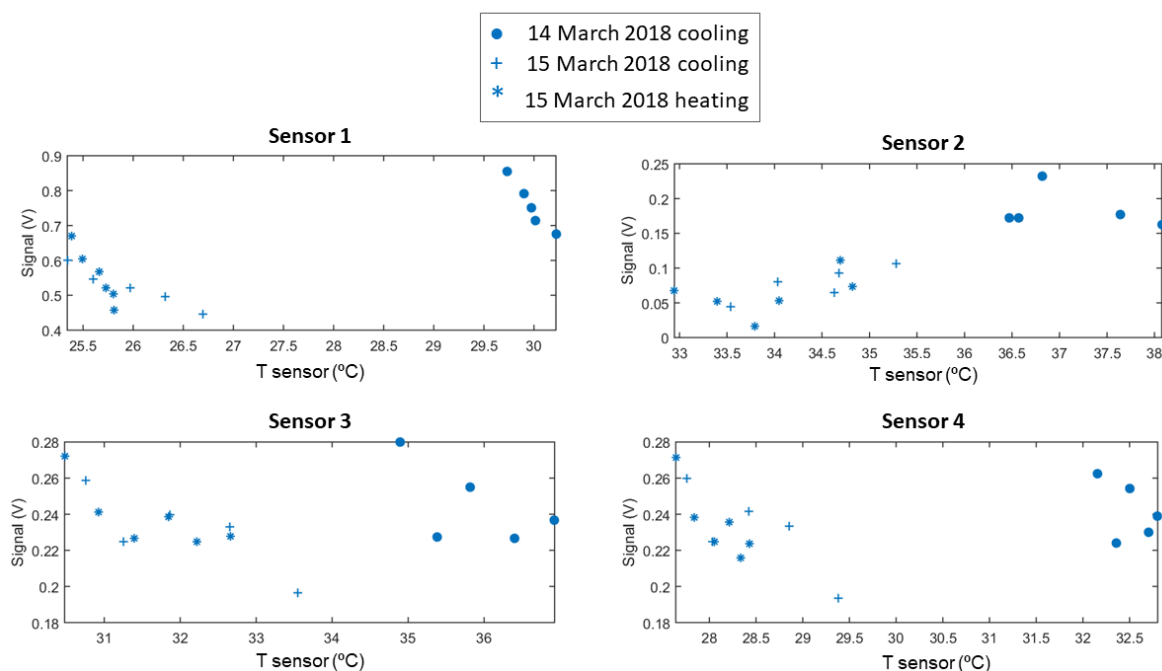


Figure 135: Probe signal dependency on instrumentation temperature

Now analyzing the sodium temperature dependency on 15<sup>th</sup> March measurements, we observe that a variation of 1°C induces a deviation of 0.00174 V in average. Knowing that throughout the campaign, the measurements vary between 160 °C and 165 °C, the variations are therefore in the worst case at 0.0087 V, which corresponds to less than 10% of the value of the weakest signals. It is therefore justified to accept the first hypothesis (A1.) that the influence of the fluid temperature is minimal over the restricted temperature range applied (160-165°C).

For the third hypothesis, sodium empty loop measurements were made for different ALIP supplies in terms of frequency and phase intensity. Few measurements have been made, but the results support the hypothesis A3, the influence of intensity and frequency is negligible in the operation range considered.

With all this information we are able to describe the relation of time averaged signal with flow rate. Using recorded data from campaign described in sub-section 5.2.2 at stable operation ( $Rms$  lower than 1.5) and adequate instrumentation temperature (bellow 35°C), we have plotted the linear regressions of time averaged signals over the last 20 seconds for the three repetitions and for the totality of data. This analysis permits to define a constitutive law for each sensor linking the acquired averaged signal to the measurement of flow rate with a linear relation. This reads:

$$\bar{S}_k = \alpha_k Q + \beta_k$$

With  $k$  the sensor number.

Figure 136 shows the linear regression model applied for outlet sensors calibration. First, linear regressions obtained from the three repetitions and the whole set of points are plotted in blue points. From these a mean regression curve is obtained as tendency (line in red), and using a weighted regression model we have obtained a better relation for all repetitions (line in green) with a 99% confidence interval (dotted green line) for each sensor. This last definition will be used latter for the post-treatment of results for the estimation of the uncertainty threshold.

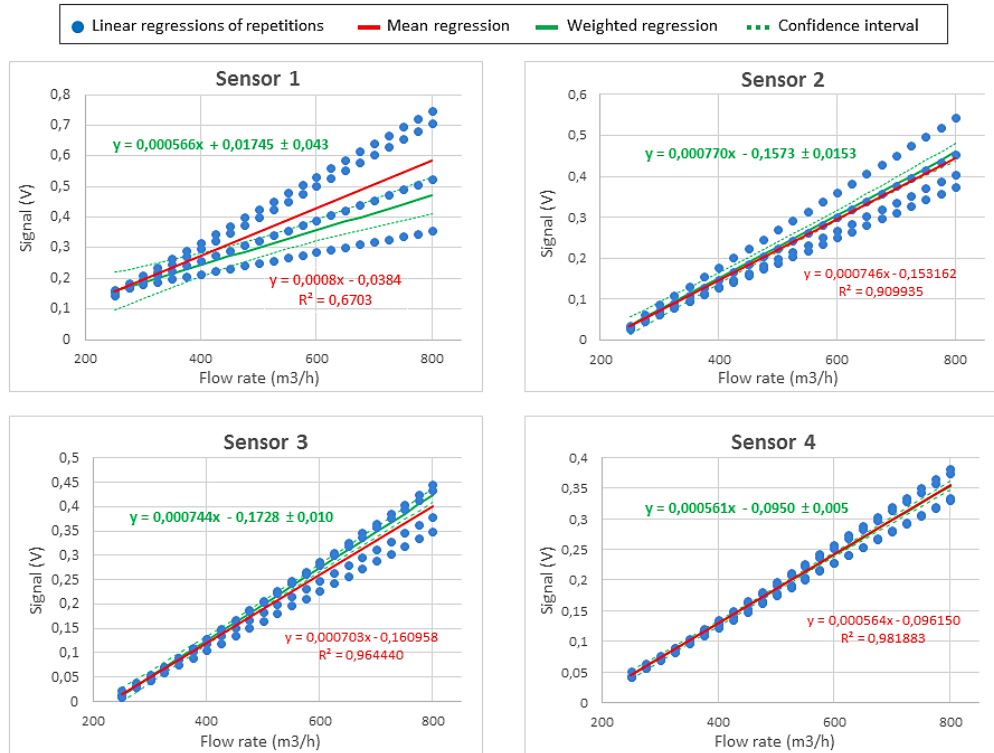


Figure 136: Linear regression curves for sensors calibration

Table XI: Weighted regression parameters for sensors calibration

	Sensor 1	Sensor 2	Sensor 3	Sensor 4
$\alpha_k$	0.000566	0.00077	0.000744	0.000561
$\beta_k$	0.01745	-0.1573	-0.1728	-0.095
$\pm 99\%$ Confidence interval	0.043	0.0153	0.01	0.005

Now we have obtained the calibration curves (parameters in Table XI) for each sensor we should be able to describe physical phenomena at different working regimes using the instrumentation available in the loop.

### 5.2.4. MHD instability characterization

Once again, we base our reasoning on bibliographic researches. The loss of developed pressure at high values of  $Rms$  was already characterized in previous section 5.2.2, and thus, it lacks the observation of two other main phenomena historically linked to MHD instability in ALIPs. They are the low frequency (LF) pulsation appearance and the azimuthal velocity inhomogeneity. For this aim we will post-process data recorded during the performance curve campaign by dynamic pressure sensors and Hall Effect magnetic field distortion (ENS) sensors respectively.

#### 1. Dynamic pressure sensor post-treatment

For the analysis of fluid pulsations in the loop, dynamic pressure sensor signals have been treated in the frequency domain in order to characterize present pulsations at different working regimes. We have exploited data recorded during the performance curve experimental campaign by the 6-sensor disposition (sensors 1 - 3 at outlet and 4 - 6 at inlet at different azimuths and flanges) presented in *Figure 137*.

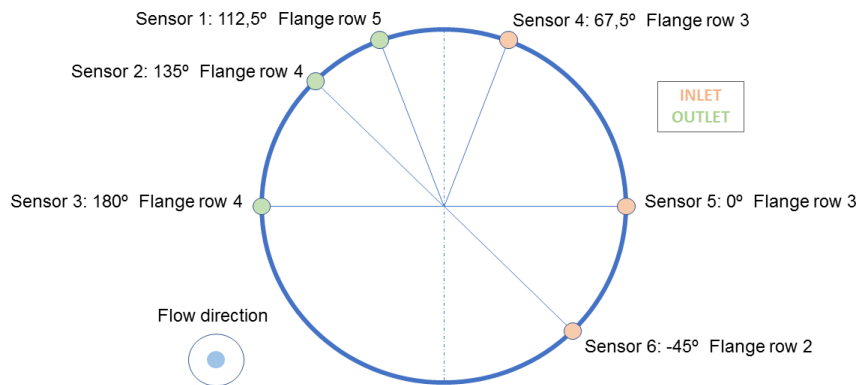


*Figure 137: Cross-section of dynamic pressure sensor locations*

Due to the big amount of acquired data, we have only selected at maximum three performance points per set of supply frequency and phase intensity in order to study the behaviour of stable ( $Rms < 1$ ), transition ( $Rms \sim 1.5$ ) and unstable performances ( $Rms > 2$ ).

First, sensors signals have been post-treated using the *Power Spectral Density* (PSD), a mathematical tool close to the *Fast Fourier Transform* (FFT) defined by the relation:

$$PSD(f) = \frac{1}{T} |FFT(S(t))|^2$$

With  $f$  the frequency,  $T$  the recording period and  $S$  the signal to post-treat.

## CHAPTER 5

The PSD has the advantage to show how the power of a signal is distributed over the frequency domain, and it is real whereas FFT is complex, so interpretation of the result is easier. Furthermore, this tool presents the following property:

$$\int_{f_{min}}^{f_{max}} PSD(f)df = Var(S(t))$$

Where  $Var(S(t))$  is the variance of the temporal signal (energy of the fluctuation), with  $f_{max}$  and  $f_{min}$  the maximum and minimal sample frequencies respectively, and  $PSD(f)$  is its power spectral density (distribution of the energy among frequencies).

This puts in evidence that the variance of the temporal signal is equal to the integral of the PSD over the frequency domain.

In order to study the energetic distribution of pulsations at high frequency (HF) and low frequency (LF) intervals we have built following definitions:

$$\%Var_{LF} = \frac{\int_{f_{min}}^{f_{supply}} PSD(f)df}{Var(S(t))} \times 100 \quad \text{and} \quad \%Var_{HF} = \frac{\int_{f_{supply}}^{f_{max}} PSD(f)df}{Var(S(t))} \times 100$$

With  $f_{supply}$  the electric supply frequency.

This enables to quantify rapidly the frequency pulsation distribution at different *Rms* values, and then to qualify the transition from stable to unstable domains.

Since recordings were quite long (2 min), we have applied a signal processing consisting in cutting into 5 samples and averaging their spectra in order to reduce the dispersion of the curves in the frequency domain.

Following *Table XII* describes the LF and HF distribution for different working regimes and also confirms that the energy of the fluctuations is conserved during the spectral treatment.

*Table XII: Analysis of frequency distributions for different experimental working regimes*

<i>Rms</i> (-)	$\%Var_{HF}$	$\%Var_{LF}$	$\int_{f_{min}}^{f_{max}} PSD(S(f))df$ [ $bar^2$ ]	$Var(S(t))$ [ $bar^2$ ]
2,40	6,70%	93,30%	0,000261 bar	0,000302
1,33	43,43%	56,57%	0,000242	0,000246
0,30	98,83%	1,17%	0,000414	0,000414
2,19	14,63%	85,37%	0,000786	0,001111
1,45	63,75%	36,25%	0,000557	0,000560
0,72	88,38%	11,62%	0,001338	0,001346
1,90	47,29%	52,71%	0,001615	0,001655

<i>Rms</i> (-)	$\%Var_{HF}$	$\%Var_{LF}$	$\int_{f_{min}}^{f_{max}} PSD(S(f))df [bar^2]$	$Var(S(t)) [bar^2]$
0,93	96,18%	3,82%	0,003825	0,003828
0,10	99,58%	0,42%	0,005323	0,005325
5,31	1,62%	98,38%	0,000047	0,000050
5,14	5,70%	94,30%	0,000165	0,000167
2,60	38,83%	61,17%	0,000651	0,000652
0,82	95,50%	4,50%	0,001689	0,001689
4,98	9,07%	90,93%	0,000737	0,000742
0,78	82,00%	18,00%	0,002405	0,002407
7,90	1,09%	98,91%	0,000156	0,000163
7,60	5,04%	94,96%	0,000289	0,000291
7,27	19,47%	80,53%	0,000351	0,000351

The following figures present in detail some obtained power spectrums. *Figure 138*, *Figure 139* and *Figure 140* show the behaviour of stable, transition and unstable regimes respectively for an electric supply of 5 Hz and 300 A.

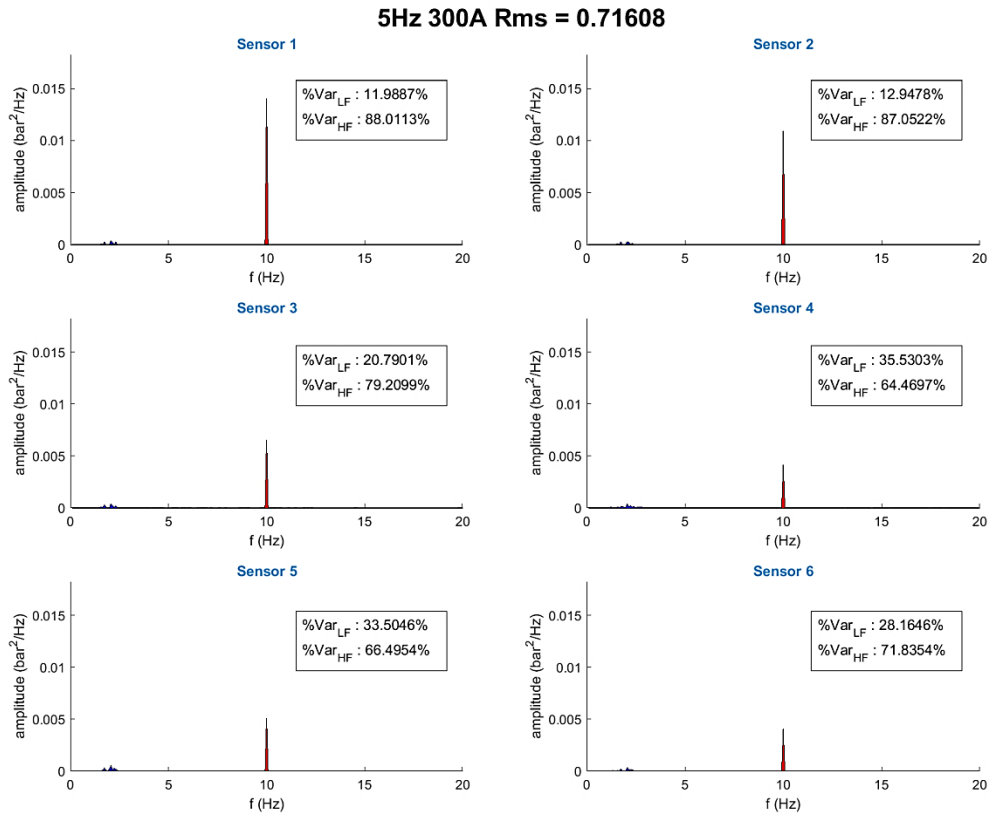


*Figure 138: Power spectral density of dynamic pressure signals at stable regime*

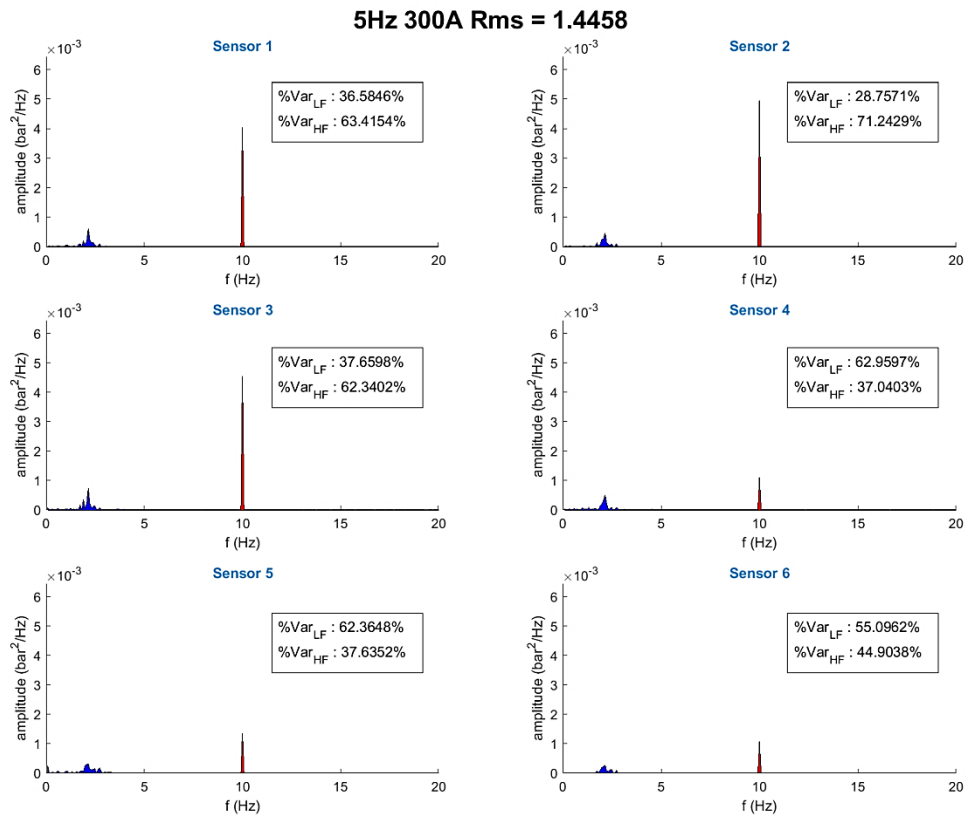


Figure 139: Power spectral density of dynamic pressure signals at transition regime

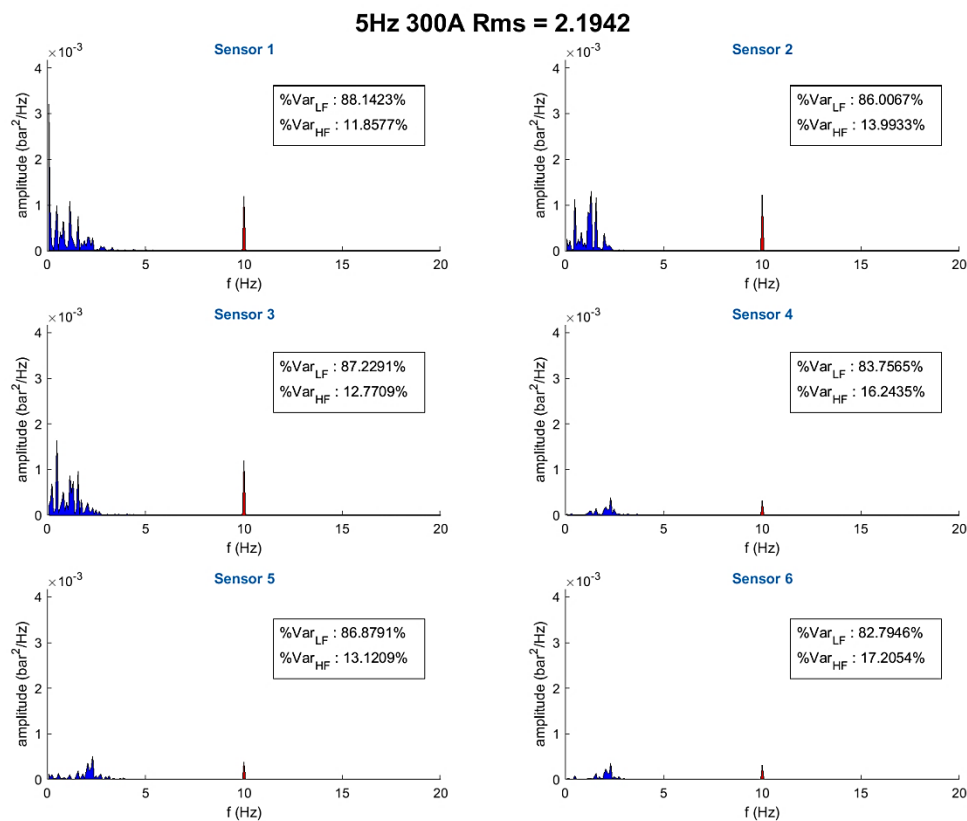


Figure 140: Power spectral density of dynamic pressure signals at unstable regime

We can extract as conclusion that spectrums verify that double frequency peak is more important in the cases with low  $Rms$  values, and that the increment of  $Rms$  makes MHD instability appear in the form of low frequency pulsations with order of magnitude of frequencies around the Hertz. Furthermore, we can note that pulsations are more important for sensors 1-3 at outlet than for sensors 4-6 at inlet.

In order to offer a complementary physical interpretation of acquisitions we have introduced two other parameters:

$$\frac{\sigma_{LF}}{\Delta P} [\%] = \frac{\sqrt{\int_{f_{min}}^{f_{supply}} PSD(f)df}}{\Delta P} \times 100 \quad \text{and} \quad \frac{\sigma_{HF}}{\Delta P} [\%] = \frac{\sqrt{\int_{f_{supply}}^{f_{max}} PSD(f)df}}{\Delta P} \times 100$$

These indicators link the pressure concentrated into a band of frequencies to the ALIP developed pressure with a non-dimensional relation permitting to compare among different experimental regimes.

In *Figure 141* we can note that for high  $Rms$  the distribution of the low frequencies is significant compared to that of the high frequencies, whereas for the low  $Rms$  the double supply frequency peak is much more important. This confirms that the higher the  $Rms$ , the more the pulsations amplitudes are concentrated towards the low frequencies. Finally, we note that the tilt of the two curves is around  $Rms = 2.5$ , however as we could remark previously in performance curves analysis, this threshold is a priori dependent on the supply frequency, since pressure maximums positions differ.

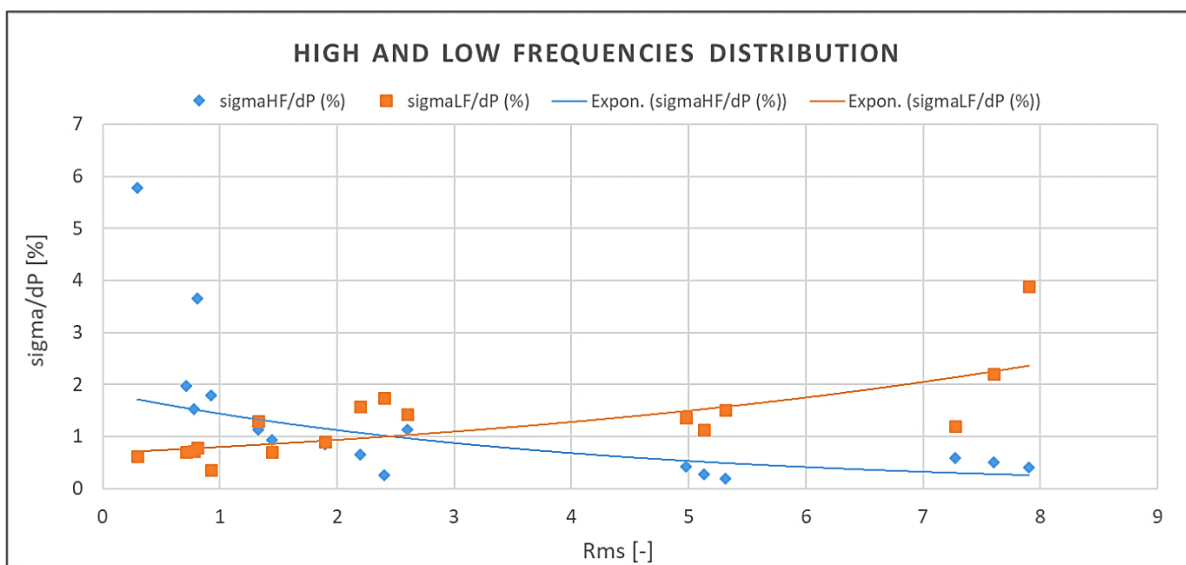


*Figure 141: High frequency and Low frequency distributions as a function of Rms*

## 2. ENS sensor post-treatment

Once calibration was adjusted, ENS sensor acquisitions were post-treated for different power supply parameters and opening valve positions. As in previous dynamic pressure analysis, we have constructed different indicators in order to make physical correlations of phenomena occurring at different working regimes.

As it was also documented in bibliography, inhomogeneity is a clear characteristic of MHD instability in an ALIP. This translates that velocity would not be uniform over the azimuth at the outlet of the inductor. In order to verify this hypothesis we have defined the following parameter:

$$Deviation_k[\%] = \frac{|u_{ENS_k} - U_Q|}{u_Q} \times 100$$

This defines the non-dimensional deviation of the local velocity at a given azimuth for a sensor  $k$  with respect to the mean velocity measured by the flowmeter in terms of percentage.

Analysing this parameter as a function of  $Rms$  we obtain the following azimuthal distributions in Figure 142, Figure 143 and Figure 144 for a supply of 5 Hz and different phase intensities (200 A, 300 A and 400 A respectively). It is important to note that all of the data presented take into account the 99% interval of confidence defined previously in the calibration subsection.

We can notice that in all the cases presented the deviation from mass flow rate increases with the  $Rms$ , and that for the stable cases and even transition regimes the difference from measured velocity by the flowmeter is weak, especially for regimes close to synchronism.

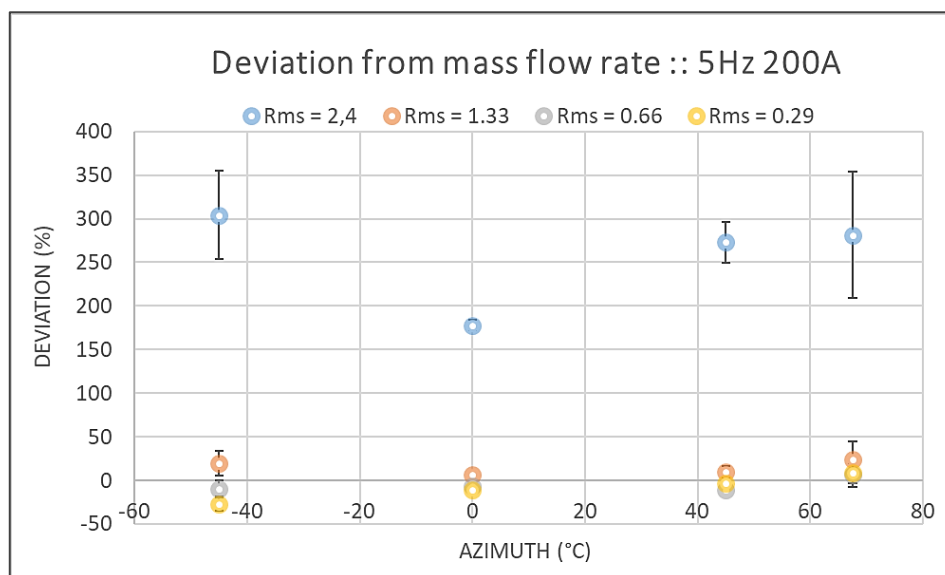


Figure 142: Azimuthal distribution of velocity deviation at 5Hz and 200A for different  $Rms$  regimes

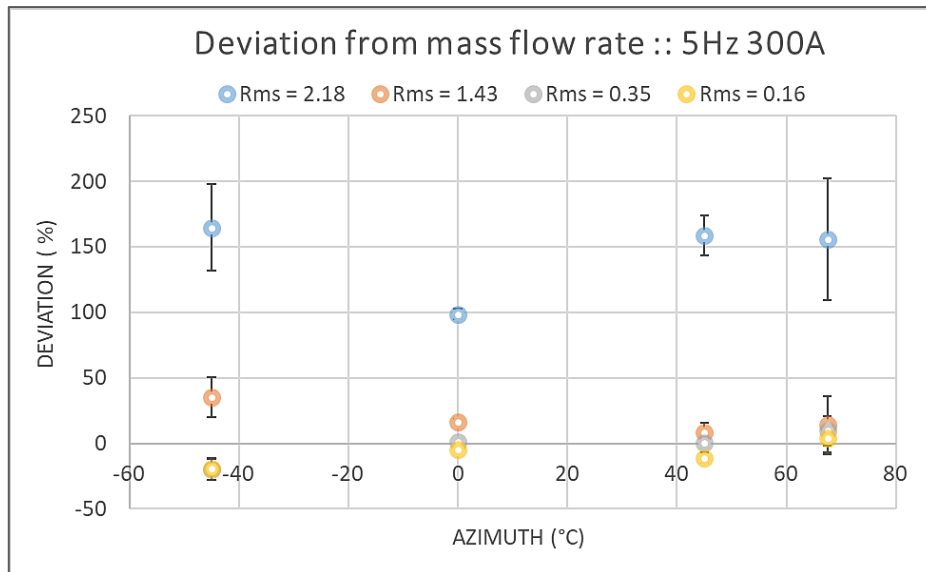


Figure 143: Azimuthal distribution of velocity deviation at 5Hz and 300A for different Rms regimes

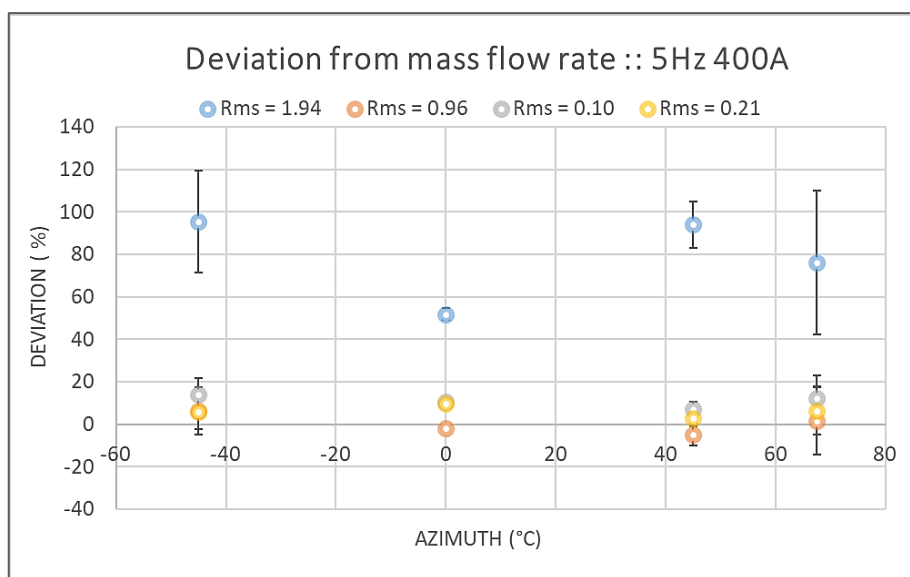


Figure 144: Azimuthal distribution of velocity deviation at 5Hz and 200A for different Rms regimes

In order to give a global vision of azimuthal velocity homogeneity a last indicator is evaluated. Here we define the homogeneity factor as the average of mass flow rate deviations for the 4 sensors ( $N_{sensors} = 4$ ). This reads:

$$Homogeneity [\%] = \sum_{i=1}^{N_{sensors}} \frac{Deviation_i}{N_{sensors}}$$

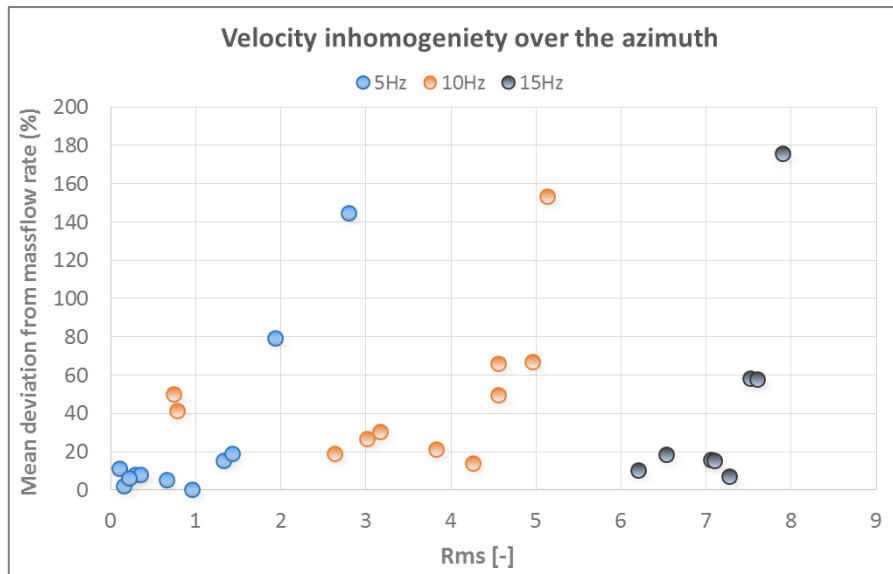


Figure 145: Homogeneity factor as a function of  $Rms$  for different electric supplies

Figure 145 might point out that there is a general tendency for the increase of velocity inhomogeneity with the  $Rms$ . However, we can remark that there is a kind of dependency on the electric supply, i.e. 15 Hz inhomogeneity at  $Rms$  of 6 is lower than for the 10 Hz case with  $Rms$  of 5. This last should be related to the fact that the stability threshold is also dependent on the interaction parameter ( $N$ ) and then on the relation between supply current intensity and frequency. Therefore, the MHD instability effects could be delayed with the increment of supply frequency.

## 6. CONCLUSIONS AND PERSPECTIVES

The present thesis contributes to predict the behaviour of high discharge annular electromagnetic pumps in the framework of the CEA R&D program. Three main complementary approaches are addressed in **Chapters 3 to 5** respectively: analytical, numerical and experimental investigations. This global vision of the problem has been introduced through a complete phenomenological and bibliographic study, presented in **Chapter 2** that presents previous researches on MHD phenomena in ALIPs using the three directions mentioned. Then, as in a treasure-hunting, the direction of the current study was gradually established as hints were found in literature, trying to innovate and support previous works in this vast and complex research domain.

We could present conclusions of this work as determined previously, in three different blocks with correlations among them.

First, **Chapter 3 in analytical investigations** aimed to describe MHD different behaviours in the performance of an ALIP using a theoretical approach. This consisted of two distinct blocks, one based on general phenomenology description using different level hypothesis and other on the study of MHD flow stability.

The phenomenological investigation had put the accent on three main topics: The study of the magnetic field created by a discrete coils inductor, the description of the base coupled MHD flow solution with and without uniform bulk velocity profile over radius, and the finite length inductor end effects impact on performance.

Then, section 3.1 meant to study the impact of different theoretical assumptions in models. Principally we can conclude that:

1. The fact of considering a detailed inductor with discrete slots increases importantly the complexity of the system of equations without giving much extra information (weak fluctuation over the length of RMS radial and axial magnetic field components in *Figure 39* compared to its mean value). The simplification in models of using a layer of current inductor with axial sinusoidal distribution results a good compromise.
2. The study of the stationary MHD coupled solution in an ALIP shows that a base flow can be established as the equilibrium of time-averaged axial electromagnetic force and pressure gradient, with negligible friction at walls. Furthermore, the validity of the use of a “piston flow” solution is analysed. Here, it would depend on application that we might have the possibility of introducing a thin channel approximation, and then a uniform velocity profile, or not. For example, in the study of the stability of the axisymmetric system it is important to keep the whole base flow solution with radial velocity profile (*Figure 45*).
3. The analysis of the perturbation created by finite length of the inductor puts in evidence that end effects cannot be explained using a purely electromagnetic

approach, since the travelling wave numbers of disturbance modes depend on the slip velocity. Their impact on performance depends on the machine configuration (high effect for a small number of poles) and directly on the  $Rm_B$ : the maximum developed pressure is higher and reached at lower  $Rms$  for low values of  $Rm_B$ . Moreover, DSF pulsations are a direct consequence of end effects, increasing for high  $Rms$  regimes. However, the end effects remains to be studied without the thin channel assumption, and with real velocity profiles.

Based on these models, in section 3.2 we studied stability in ALIPs from different points of view and using various methods (linear and non-linear). We paid special attention to the posing of hypothesis and we hope also to clarify the assumptions applied in the different analysis steps, which are indeed not always evident to follow. The three analyses performed concluded with following remarks respectively:

1. The linear stability analysis for azimuthal perturbations was built from Gailitis et al. [23], but instead of presenting a marginal study, here we obtain amplification factors for different excitation modes, and not only stability thresholds. This analysis puts in evidence that low wavenumber (and then low pulsations) disturbances present higher amplification, and then is coherent with the observation of LF pulsations and installed asymmetry in unstable regimes. The obtained thresholds are not far from those obtained in [23], but far from experiments, what could be a direct consequence of considering once again an infinite inductor approximation. The following developments should consider end effects in order to give more realistic estimates. In addition, the study of mode  $m = 0$  with flowrate fluctuations is among foreseen perspectives for the study of pump-circuit coupling stability.
2. The linear stability analysis for radial perturbations employs a 2D axisymmetric geometry where the base solution obtained in subsection is required. Compared to the previous study, here we have only applied a marginal stability analysis giving the threshold in terms of  $Rms$  above which a radial perturbation could exist. The value obtained was sufficiently high ( $Rms$  around 30) to exclude (at least from a theoretical point of view) the presence of important radial disturbances in an ALIP.
3. The energetic approach presented in this work did not give much information about the impact of finite length perturbations in ALIPs performance, since the problem was reduced to the study of the boundary layer gradients, and then result should be similar to that obtained in the energetic stability study of Hartmann layers [28]. Then, further application of energetic methods to ALIP stability remains an open research subject.

Next, **Chapter 4 in numerical investigations** starts with the presentation of EPM-INDUC code on Fluent for fully coupled MHD simulations. A validation follows, through comparison to a similar model with the commercial code COMSOL for a 2D axisymmetric model of an ALIP with finite-length discrete inductor and without fluid. Simulations coupled with fluid flow were then carried out with 2D axisymmetric steady models, then with a 3D model in steady and unsteady mode:

1. Using 2D axisymmetric models with different complexity, we evaluated from a numerical point of view i) the impact of a continuous inductor and ii) the impact of end effects. The simplest numerical model is closed to theory as expected. The other performance curves were coherent with the end effect theoretical analysis, since maximum developed pressures were shifted to higher values of  $Rms$  for the numerical models that include those end effects. Finally, we concluded that the model with intermediate complexity, (continuous inductor of finite length) gave acceptable results compared to the most representative model (describing individual coils), in particular the pressure maximums are placed at similar values of  $Rms$ . Then, this intermediate model was extended to 3D in order to save calculation time while still representing correctly the performance curve.
2. Inspired by the azimuthal perturbation analysis, we evaluated using 3D steady calculations the impact of different mode number perturbations, and also the impact of the size of the perturbation, since this last could not be analysed using linear methods. The inlet perturbations imposed in the calculations were deduced from existing PIV measurements on a water model of the pump. This analysis puts in evidence that for high  $Rms$  regimes the ALIP would amplify an inlet stationary velocity maldistribution, so that important axial velocity perturbations would be found at outlet. The study results could be summed up with *Figure 115*, expressing the perturbation growth rates for the different simulations performed (modes  $m=1$  or  $2$ ). Comparing to growth rates estimated from analytical studies remains to be done, and will quantify the impact of finite-length configurations on stability.
3. Transient calculations were inspired by Araseki et al. [24] [38] studies on MHD instability characterization by LF pulsations measurements. In this work we present two transient simulations (one at high  $Rms$  and one at low  $Rms$ ) with an inlet azimuthal velocity distribution perturbed by mode 1 with an amplitude varying randomly around a mean value of 20%. The results indicate the presence of LF pulsations with values around the Hertz for the high  $Rms$  regime simulation ( $Rms = 6.2$ ) with still an important mean velocity inhomogeneity at outlet of 53 %, whereas the low  $Rms$  simulation ( $Rms = 1.5$ ) presented negligible velocity fluctuations at outlet and a low mean inhomogeneity of 3.8 %. This study thus demonstrates that it is possible to simulate MHD instabilities with 3D fully coupled transient model, maintaining reasonable calculation times (around a week). Because of time constraints it was not possible to correctly post-treat other calculations in this work. However, it is foreseen to continue transient simulations in order to cover more situations and input conditions, especially for studying the impact of variable hydraulic loads in time.

Finally, **Chapter 5 in experimental investigations** consists of the post-treatment and physical analysis of acquired data in PEMDyn loop at CEA Cadarache. An overall vision of the experimental facility is given with the description of principle measuring technologies. Then, three main aspects were treated: i) comparison of numerical 2D axisymmetric model to

experimental magnetic field and performance curves, ii) calibration of local velocity (ENS) sensors and iii) characterization of MHD instability through experimental data.

1. Magnetic field measurements carried out with sodium-empty loop were compared to purely electromagnetic simulations using COMSOL and EPM-INDUC simulation codes, concluding to the validity of those codes. Then, coupled simulation were also compared favourably to developed pressure and flowmeter measurements at different operation conditions. Here, it would have been interesting to consider uncertainties for the flowmeter measurement, but this remains to be done with modifications on the equipment to access to raw acquisitions.
2. The calibration of ENS sensors of local sodium velocity measurement through magnetic field distortion was carried out and finally gave linear correlations of output signals with measured flow rate. Considering the multiple parameters influencing the measurement (sodium and probe temperatures, electric supply ...), this process should be repeated in order to verify our hypothesis and acquired data. Also, the probes aimed at measuring the azimuthal velocity were not used. They should be calibrated with probe positions permuted  $90^\circ$ .
3. The characterization of MHD instability was done using dynamic pressure and local velocity measurements. Once again, we draw our inspiration from experimental studies such as [24], which shows LF pulsations at high *Rms* regimes, and [27] which shows the increase of azimuthal velocity unbalance with *Rms*. Analysing acquisitions recorded at different supplies and valve positions, we found that for high *Rms* low frequency pressure fluctuations becomes more important than the high frequency ones. However, in order to obtain a stability threshold we should analyse measurements at intermediate supply frequencies, and so to perform this same analysis using more acquisitions. Using the velocity ENS sensors, we obtained that the velocity disequilibrium at outlet tends to increase with the *Rms* value, that MHD instability effects could be delayed with the rise of supply frequency. However, once again the current analysis should be enlarged with a bigger amount of data and other positions of sensors i.e. replace some probes at inlet to characterize perturbation amplification, and better distribute the probes among azimuthal directions.

Further experimental campaigns will also consist of the measurements of the radial magnetic field component when the second inductor without electric supply (with installed magnetic field measurement coils) will replace the present inner ferromagnetic yoke. This would permit to obtain full maps of the radial magnetic field component at different performance points and to directly compare with the 3D magnetic field distribution obtained by our 3D numerical model. We would also like to mention the interest of measuring flowrate fluctuations for the characterization of hydraulic circuit response. This would support analytical and numerical investigations on a future coupling pump-circuit transient study.

Finally, a broad infrastructure consisting of several analytical, numerical and experimental tools has been developed in the framework of this PhD study and made it possible to better know the static phenomena in an ALIP and its Magnetohydrodynamic instabilities. Those instabilities are characterized in shape and frequency, and we know that they don't grow indefinitely but just amplify the azimuthal inhomogeneities from inlet to outlet. The role of the flowrate fluctuations, connected to the circuit behaviour, remain to be studied.

Several points were raised to improve our analytical, numerical or experimental methods, and the author would like to express that hope that presented progresses will be helpful in future researches on the MHD phenomena and stability analysis on ALIPs.

## BIBLIOGRAPHY

- [1] “<https://www.atomicheritage.org/history/french-nuclear-program>,” 14 February 2017. [Online]. [Accessed August 2018].
- [2] J. A. SHERCLIFF, "A textbook of Magnetohydrodynamics," Oxford: Pergamon Press, 1965.
- [3] L. GOLDSTEINS, “Experimental and numerical analysis of behaviour of electromagnetic annular linear induction pump,” PhD Grenoble Alpes, 2015.
- [4] P. A. DAVIDSON, "An introduction to Magnetohydrodynamics," Cambridge: Cambridge University Press, 2001.
- [5] R. MOREAU, "Magnetohydrodynamics," St. Martin d'Hères, France: Kluwer Academic Publishers, 1990.
- [6] H. OTA et al., "Development of 160 m<sup>3</sup>/min Large Capacity Sodium-Immersed Self-Cooled Electromagnetic Pump," *Journal of Nuclear Science and Technology*, vol. 41, pp. 511-523, 2004.
- [7] S. VITRY, “Note Technique du Programme d'essais cartes de performance,” CEA/DEN/CAD/DTN/STCP/LCIT, CEA CADARACHE, 2016.
- [8] M. DUMONT, Y. FAUTRELLE, C. ROMAN, “Calcul de dimensionnement pompes ALIP-PEMDyn,” Laboratoire SIMAP - Grenoble, 2011.
- [9] J. KWAK and H. R. KIM, “Design and preliminary test of an annular linear induction electromagnetic pump for a sodium-cooled fast reactor thermal hydraulic experiment,” *Journal of Nuclear Science and Technology*, vol. 54, no. 12, 2017.
- [10] H. R. KIM and J. S. KWAK, “MHD design analysis of an annular linear induction electromagnetic pump for SFR thermal hydraulic experimental loop,” *Annals of Nuclear Energy*, vol. 92, no. 127-135, 2016.
- [11] R. S. BAKER and M. J. TESSIER, “Handbook of Electromagnetic Pump Technology,” New York: Elsevier.
- [12] L. LÉBOUCHER and D. VILLANI, “Slot design of optimized electromagnetic pump,” *IEEE Transactions of Magnetics*, vol. 29, no. 6, pp. 2953-2955, 1993.

- [13] K. UENO , R. ISHII and S. MORIOKA, "Two-dimensional channel flow of liquid metal in the presence of progressing alternating transverse magnetic field," *Fluid Dynamics Research* 6, vol. 53, no. 64, p. 12, 1990.
- [14] K. UENO, "Inertia effect in two-dimensional MHD channel flow under a travelling sine wave magnetic field," *Phys. Fluids A: Fluid Dynamics* 3, vol. 31, no. 07, p. 11, 1991.
- [15] J. J. VALDMANIS et al., "On theory of longitudinal finite length effect in linear induction magnetohydrodynamic machine," *Magnetohydrodynamics*, pp. 101 - 106, 1966.
- [16] H. ARASEKI et al., "Double - supply - frequency pressure pulsation in annular linear induction pump. Part I: Measurement and numerical analysis," *Nuclear Engineering and Design*, pp. 85 - 100, 2000.
- [17] H. R. KIM, "The theoretical approach for viscose and end effects on a MHD pump for sodium circulation," *Annals of Nuclear Energy*, no. 62, pp. 103 - 108, 2013.
- [18] I. R. KIRILLOV, "Londitodal end effects in cylindrical induction MHD machines," *Magnetohydrodynamics*, no. 2, pp. 109 - 116, 1972.
- [19] F. WERKHOFF, "Finite - length effects and stability of electromagnetic pumps," *Experimental theral and fluid science*, no. 4, pp. 166 - 170, 1991.
- [20] Y. D. M. M. F. S. LETOUT, "Pompes électromagnétiques à induction – analyse de la pompe ASTRID - Projet ASTRID SIMAP-CEA Cadarache," Grenoble, 2012.
- [21] J. P. LE FRERE, "Pompage des métaux liquides," *Techniques de l'Ingénieur*, no. article B4330, 2018.
- [22] S. H. STROGATZ, "Nonlinear Dynamics and Chaos," Perseus Books, 1994.
- [23] A. GAILITIS et al., "Instability of homogeneous velocity distribution in an induction-type MHD machine," *Magnetohydrodynamics*, no. 1, pp. 87 - 101, 1975.
- [24] H. ARASEKI et al., "Magnetohydrodynamic instability in annular linear induction pump. Part I. Experiment and numerical analysis," *Nuclear Engineering and Design*, pp. 29 - 50, 2004.
- [25] D. JOSEPH, "Stability of Fluid Motions I," Springer-Verlag, 1976.
- [26] I. R. KIRILLOV et al., "Local characteristics of a Cylindrical induction pump for

Rms  $> 1$ ," *Magnetohydrodynamics*, no. 2, pp. 95 - 102, 1987.

- [27] I. R. KIRILLOV et al., "Experimental investigation of flow non-uniformity in a cylindrical linear induction pump," *Magnetohydrodynamics*, no. 2, pp. 107-113, 1980.
- [28] R. J. LINGWOOD and T. ALBOUSSIÈRE, "On the stability of the Hartmann layer," *Physics of Fluids*, vol. 11, no. 2058, 1999.
- [29] P. MORESCO and T. ALBOUSSIÈRE, "Experimental study of the instability of the Hartmann layer," *Journal of Fluid Mechanics*, vol. 504, pp. 167-181, 2004.
- [30] S. CARMI and D. P. LALAS, "Universal stability of hydromagnetic flows," *Journal of Fluid Mechanics*, vol. 43, no. 4, pp. 711-719, 1970.
- [31] O. WIDLUND, S. ZAHRAI and F. H. BARK, "Development of a Reynolds stress closure for modeling of homogeneous MHD turbulence," *Physics of Fluids 10*, vol. 19, no. 87, 1998.
- [32] O. WIDLUND, S. ZAHRAI and F. H. BARK, "Structure information in rapid distortion analysis and one-point modeling of axisymmetric magnetohydrodynamic turbulence," *Physics of Fluids 12*, vol. 26, no. 09, 2000.
- [33] J. SOMMERIA and R. MOREAU, "Why, how and when, MHD turbulence becomes two-dimensional," *J. Fluid Mechanics*, vol. 118, no. 507, p. 11, 1982.
- [34] E. HAMLINGTON and W. J. A. DAHM, "Reynolds stress closure for nonequilibrium effects in turbulent flows," *Physics of Fluids 20*, vol. 115, no. 101, 2008.
- [35] C. GISSINGER, P. RODRIGUEZ IMAZIO and S. FAUVE, "Instability in electromagnetically driven flows Part I," *Physics of Fluids*, vol. 28, no. 034101, 2016.
- [36] P. RODRIGUEZ IMAZIO and C. GISSINGER, "Instability in electromagnetically driven flows Part II," *Physics of Fluids*, vol. 28, no. 034102, 2016.
- [37] G. RODRIGUEZ et al., "Development of experimental facility platform in support of the ASTRID program," *Intl. Conf on FAST REACTOR AND RELATED FUEL CYCLES*, 2013.
- [38] H. ARASEKI et al., "Magnetohydrodynamic instability in annular linear induction pump. Part II. Suppression of instability by phase shift," *Nuclear Engineering and Design*, pp. 965 - 974, 2006.

- [39] T. ASADA, R. AIZAWA, T. SUZUKI, Y. FUJISHIMA and E. HOASHI, “3D MHD simulation of pressure drop and fluctuation in electromagnetic pump flow,” *Mechanical engineering journal*, vol. 2, no. 5, 2015.
- [40] H. ARASEKI et al., "Double - supply - frequency pressure pulsation in annular linear induction pump. Part II: Reduction of pulsation by linear winding grading at both stator ends," *Nuclear Engineering and Design*, pp. 397 - 406, 2000.
- [41] D. L. TURCOTTE and J. M. LYONS, “A periodic boundary-layer flow in magnetohydrodynamics,” *Journal of Fluid Mechanics*, vol. 13, no. 04, pp. 519-528, 1962.
- [42] Y. DELANNOY and E. MARTIN LOPEZ, “The velocity profile in annular linear electromagnetic pumps,” *International Journal of Applied Electromagnetics and Mechanics* , 2018.
- [43] Y. DELANNOY, E. MARTIN LOPEZ and F. BENOIT, “Convective end effects in annular linear induction pumps,” in *EPM2018*, Hyogo, Japan, 2018.
- [44] M. POLOUJADOFF, B. MOREL and A. BOLOPION, “Simultaneous Consideration of Finite Length and Finite Width of Linear Induction Motors,” *IEEE Transactions on Power Apparatus and Systems* , no. 99, pp. 1172-1180, 1980.
- [45] F. WHITE, "Fluid mechanics," 4th edition, Mc Graw Hill, 1998.
- [46] E. PURCELL and D. J. MORIN, "Electricity and Magnetism," New York, USA: Cambridge University Press, 2013.
- [47] B. N. JIANG, "The Least-Squares Finite Element Method," Springer, 1998.
- [48] F. MENTER, “Two-Equation Eddy-Viscosity Turbulence,” *AIAA Journal*, vol. 32, no. 8, p. 1598–1605, 1994.
- [49] L. AYRAULT, F. BENOIT, D. CAMBET and F. DECHELETTE, “PEMDYN Commissioning report - CEA Internal report,” Cadarache, 2016.
- [50] S. VITRY, L. GOLDSTEINS, C. BISCARRAT, F. BENOIT, S. MADELEINE, F. DECHELETTE and O. GASTALDI, “Experimental and numerical analysis of magnetic field spatial measurements inside an electromagnetic pump channel duct,” in *PAMIR*, Cagliari, Italy, 2016.
- [51] L. GOLDSTEINS, “Experimental program of calibration and tests of ENS velocity sensors (14.03.2018 – 16.03.2018),” Internal report CEA, Cadarache, 2018.

- [52] S. CHADRASEKHAR, "Hydrodynamic and hydromagnetic stability," Oxford: Clarendon Press, 1961.
- [53] P. G. DRAZDIN, "Introduction to hydrodynamic stability," Cambridge: Cambridge University Press, 2002.
- [54] F. CHARRU, "Instabilités hydrodynamiques," CNRS EDITIONS , 2017.

## Annex I: Study of stability and available analytical methods

As it was mentioned in Chapter 2, it is not so simple to address the resolution of nonlinear differential equations. In order to become familiar with the formulation of the stability problem, the bases of the linear method of normal modes are presented here, which is indeed a solid and widely developed mathematical tool based on linear algebra. On the other hand, there is not a consolidated method for nonlinear analysis, but two methodologies are identified in bibliography to take up the challenge. They are respectively the weakly nonlinear and the energetic approach.

### Linear Stability method

To begin with linear analysis, first an initial flow that represents the stationary state of the system, named *basic flow solution* must be defined. We assume that the different physical variables describing the flow are altered by infinitesimal disturbances so that, in the partial differential systems, the products of two or more disturbances can be neglected. Furthermore, the non-disturbed terms vanish because the basic flow was a solution. In other words, we keep only the linear terms and the system can be expressed in matrix form. This type of method corresponds to a linearization of the system of equations that can be applied only when perturbations are infinitesimal [52].

The definition of a stable system requires that the amplitude of any perturbation input is damped out by the system. In practice, since the flow is bounded, all perturbations can be expressed in the general form of a superposition of countable infinity normal modes, which permits to examine their stability separately.

For example, for a basic case of a stationary flow confined between two parallel plates, where the physical variables are only functions of the coordinate  $z$  normal to the planes, one analyses any two-dimensional perturbation in terms of periodic wave with the following amplitude:

$$A(r, y, z, t) = \int_{-\infty}^{\infty} \int_{-\infty}^{\infty} dk_x dk_y A_k(z, t) \exp[i(k_x x + k_y y)] \quad (192)$$

Where the wave number of the perturbation  $A_k(z, t)$  is:

$$k = \sqrt{k_x^2 + k_y^2} \quad (193)$$

As soon as the system is linear, we can know the impact of a general disturbance taking all the wave numbers and thus find out which ones make the system unstable.

In problems with cylindrical geometry, a general disturbance can be expressed as follows:

$$A(r, z, \varphi, t) = \sum_{m=-\infty}^{+\infty} \int_{-\infty}^{\infty} A_{m,k}(r, t) \exp[i(kz - m\varphi)] dk \quad (194)$$

Where  $z$  is the component along the axis of symmetry,  $r$  is the distance to the axis and  $\varphi$  the azimuthal angle. In this example, stability is analysed in terms of normal modes defined by integers  $m$  and  $k$ .

It should be emphasized that the linear formulation of the system enables to study the stability of the system excited by any kind of disturbance that can be decomposed into the chosen eigenvectors of the differential operators. That is to say, we do not consider the appearance of other non-normal excitation modes resulting from non-linear interactions. In order to look at these effects we would have to take weakly non-linear method approach.

In the expression of the amplitude of the perturbation, the temporal dependence can be expressed as:

$$A(r, t) = \int A_k(r, t) dk \quad (195)$$

$$A_k(r, t) = A_k(r) e^{p_k t}$$

Where  $p_k$  is a constant for each mode  $k$  which can be decomposed in complex form:

$$p_k = p_k^{(r)} + p_k^{(i)} \quad (196)$$

A system can only be considered stable if it is stable with respect to all possible disturbances that may occur. That is, any disturbance must be damped ( $p_k^{(r)} < 0$ ). From a more general point of view, the real part of  $p_k$  in the exponential manages the growth or temporal decay of the perturbation amplitude. When it is zero the disturbance can only fluctuate with the frequency  $p_k^{(i)}$ .

This concept introduces the need to define a stability-to-instability limit in the space of possible base flow solutions, defined by the set of parameters  $(X_1, \dots, X_n)$  controlling the system. The states of marginal (or neutral) stability of the system, thus meet the condition:

$$p_k^{(r)}(X_1, \dots, X_n) = 0 \quad (197)$$

When a particular characteristic parameter of the system is modified until reaching a critical value, a transition from one stable state to another unstable is obtained. Marginal stability states are classified into two types depending on how this transition is accomplished:

1. Amplitudes grow aperiodically ( $p_k^{(i)} = 0$ ).

2. Amplitudes grow by oscillations of increasing amplitude with the characteristic frequency  $p_k^{(i)}$ .

With this classification of marginal states it is assumed that the system is dissipative. In the conservative non-dissipative case, the situation is different knowing that, for a stable state, any perturbation can trigger non-damped oscillations of characteristic frequencies.

Once a general form of perturbation has been introduced into the linearized system of equations (momentum and induction equation for the MHD case), an expression is obtained showing the evolution of a single "generic" normal mode. This is the *dispersion relation* [53] for infinitesimal disturbances which highlights the fact that the pulsation and the wave vector of a normal mode cannot be arbitrary, since they are related to each other. On the other hand, this relation does not involve the amplitude of the perturbation, which remains undetermined because of the linear and homogeneous character of the equation.

The linear method of normal modes gives a first estimate of the modes that can make the flow unstable according to the working regime. However, the rather restrictive assumption of the infinitesimal sizes of the disturbances leaves open the question of the impact of a finite disturbance to the stable operation of the pump. Therefore, other analytical tools are tested to consider the impact of non-linear effects.

### **Weakly non-linear method**

The previous linear method showed how an infinitesimal perturbation in a basic flow could be expressed as a superposition of eigenmodes in the form:

$$u'(\mathbf{r}, t) = \frac{1}{2} (A(t)f(\mathbf{r}) + A^*(t)f^*(\mathbf{r})), \quad (198)$$

Where  $f(\mathbf{r})$  defines the spatial structure of the mode and  $A(t)$  its temporal evolution, with star superscript (\*) indicating a complex conjugate

It demonstrated in chaos theory [22] that a dissipative system in a uniform, stationary state can become unstable when a control parameter exceeds a critical value or bifurcation parameter. Therefore, this type of study makes possible to establish a stability criterion and to identify the most amplified unstable mode. Unfortunately this approach is limited to disturbances of infinitesimal amplitudes, for which the effect of non-linearity of the problem is negligible. Above this threshold, some small perturbations will grow exponentially so that they don't remain small and the system exits its linear domain. A non-linear stability study may predict what happens beyond the initial exponential growth when the non-linear effects become significant, that is, we would consider a system where the amplitude of the perturbations is just large enough for the nonlinear terms to become relevant.

Nevertheless, in the case of the non-linear study, the methodology to solve the system is not established, as in the case of normal modes, based on linear algebra. Various approaches have

been developed, each one dedicated to a type of non-linearity. The weakly nonlinear approach [53] is one of the most widespread approaches because of its rather general character among perturbative methods.

In the linear theory for a stationary basic flow with velocity  $U$ , we consider a perturbation which makes  $u = U + u'$  in the linearized NS equation for a perturbation  $u'$ , which is expressed in the form of the sum of normal modes  $u' = \epsilon [A(t)\hat{u} + A^*(t)\hat{u}^*]$ , for a certain parameter  $\epsilon$  which causes the complex amplitude  $A(t) = A_0 e^{st}$  to be in the order of unity for moderate values of time  $t$ .

It is from this reasoning that the Soviet physicist Lev Landau (1944) contributed to the developed of the weakly non-linear approach. The initial idea is to remark that, in the context of linear stability, the differential equation of the amplitude  $A(t)$  is an eigenvalue problem in the form:

$$\frac{dA}{dt} = \sigma A \quad (199)$$

Where  $\sigma$  is the temporal growth rate.

Using weakly nonlinear permits the study of the dynamics of the system with small nonlinearities, when a control parameter is close to the linear instability threshold, in which case this also means that there are only few unstable modes.

For small amplitudes equation (199) can be seen as Taylor's growth rate growth  $dA/dt$  in amplitude powers, truncated to first order. A natural way of including non-linearity is to complete this equation with higher order terms (quadratic first in  $A^2, A^*A, A^{*2}$  then cubic in  $A^3, A^{*2}A, A^*A^2$  and so on for higher orders).

The analysis of the symmetries of the problem is important in this kind of approach since it allows in general excluding a large number of these terms. For example, in the case that the problem is invariant to the translation of time ( $t \rightarrow t + t_0$ ), if  $A \sim e^{i\sigma t}$  is solution of the equation, any function translated of a phase  $\phi$ ,  $A \sim e^{i\sigma t + \phi}$ , must also be solution. The equation of the amplitude must then be invariant by the rotations in the complex plane ( $A \rightarrow Ae^{i\phi}$ ). The lowest degree term to satisfy this condition is  $|A|^2 A$ , and the equation for the order of development three is:

$$\frac{dA}{dt} = \sigma A - \kappa |A|^2 A \quad (200)$$

This is the Landau amplitude equation which involves the Landau coefficient  $\kappa$ , a priori complex like  $\sigma$  and  $A$ . This parameter must be evaluated case by case because it depends on the terms responsible for the non-linearity of the equation to solve. In classical hydrodynamics, the non-linearity comes from the adjective term of the acceleration, but it can also proceed from the boundary conditions of the system or a coupling between thermal or dynamic phenomena. The latter constitutes the nonlinearity that we seek to evaluate for a

system with magnetohydrodynamic coupling. The general methodology for obtaining the Landau parameter consists in seeking the solution of the problem as a development in amplitude powers [54].

For the case of a classical hydrodynamic system, we make the approximation to consider only the evolution of the most unstable mode ignoring the rest when flow conditions are not far from the unstable threshold. Then, only a single unstable mode or a thin band of unstable modes in the form of wave packets is considered. The Navier-Stokes equation thus has a non-linear quadratic form because the non-linear convective part of the perturbation ( $u' \cdot \nabla u'$ ), which generates terms proportional to  $|A|^2$ , and therefore of order  $\epsilon^2$ .

In the beginning, these terms grow exponentially with  $A$  and gradually they will generate a cascade of non-linear interactions between them and the normal mode. From some orders, normally quadratic, there is a resonance interaction with the normal mode which affects the amplification ratio of the perturbation. This method permits indeed to identify if a system has either fast or slow dynamics.

It should be emphasized that one of the main effects of weakly nonlinearity will be to have altered the exponential rate of growth of the unstable linear mode, i.e. the exponential part in the expression of the convective analysis of the disturbance. Though, its spatial character will not be affected, in other words the disturbance will maintain the same form.

It is possible to write the cascade of nonlinear interactions in a more complete way by considering a plane wave  $u' = \epsilon [A(t)e^{i\alpha x} \hat{u}(y, z) + A^*(t)e^{-i\alpha x} \hat{u}^*(y, z)]$  as a normal mode. Thus, because of the non-linear interactions, the different harmonics (the first  $e^{\pm 2i\alpha x}$ , the second  $e^{\pm 3i\alpha x}$ , etc.) will also contribute to the fundamental mode and will affect the average flow. The implicit translational symmetry of the flow is therefore the cause of the non-linearity, and main effects will be triggered with the cubic order terms in  $\epsilon$  ( $|A|^2 A e^{i\alpha x}$ ,  $|A|^2 A^* e^{-i\alpha x}$  and  $A^3 e^{3i\alpha x}$ ,  $A^{*3} e^{-3i\alpha x}$ ) rather than quadratic ( $|A|^2$  and  $A^2 e^{2i\alpha x}$ ,  $A^{*2} e^{-2i\alpha x}$ ).

Therefore, the pair of modes that interact resonantly with the fundamental mode will either reinforce or moderate its amplification ratio. In particular, this last type of interaction should saturate the linear instability and then balance the fundamental mode, which will then become a non-linear stationary wave. It is because of this mechanism that weakly non-linear modes of small amplitude can attenuate the growth of the fundamental mode.

In the case of a magnetohydrodynamic system the application of this method is much more complex than for the previous case, since we need to apply the method to both coupled differential equations. The procedure to be followed has not yet been defined for the present case but a priori it will be a good start to consider the following points:

1. Identification of precursor terms of non-linearity for the coupled system of equations.
2. Comparison of the stationary problem for basic flow solution to the perturbed system.
3. Estimation of the impact of neglected phenomena with the linear approach.
4. Evaluation of the importance of nonlinear effects in the coupled Navier-Stokes equations with respect to the induction equation.

As mentioned before, there are different ways of building the weakly nonlinear equations, since procedure is not unique, and neither is the result. However, only one way of studying the problem will actually yield equations to correctly model observations. This is the main reason why it is difficult to tackle with weakly nonlinear theory. The key is to already have an idea, ahead of time, of the types of dynamics we need to end up with (based on experiments, or numerical simulations), and use this information to find the way to deal with the problem. This is the reason why analytical developments have focused on the four last points in order to identify nonlinear phenomena and give qualitative information for the research on MHD instabilities in ALIPs.

### **Energetic method**

So far, we have evaluated two methods needing hypothesis about the size of the perturbation. This last assumption makes that stability conditions given by these methods still remain rather weak, because they can say nothing about the stability of finite amplitude perturbations. In fact, to consider the finite amplitude of disturbances we shall analyze the fully-nonlinear problem. This is the framework where the energetic stability method comes into play.

The method was mainly developed and applied to hydrodynamic stability in the 1960's by Daniel D. Joseph [25] using calculus of variations techniques. It is based on the evaluation of physical phenomena in the energy budget of the disturbance of a general basic flow. For this aim, a functional defining the evolution in time of the total energy of perturbation over the domain flow is derived. Classical hydrodynamic analyses take the total kinetic energy of the perturbation  $u'$  in tensor notation as:

$$\frac{d\varepsilon}{dt} = \frac{\partial}{\partial t} \int \left( \frac{1}{2} u_i'^2 \right) dV \quad (201)$$

Thus, the energetic method stems from a derivative problem related to the equation that governs the evolution of the energy of the perturbation. Examining the energy equation derived from dimensionless Navier-Stokes equations it yields:

$$\begin{aligned} & \frac{\partial}{\partial t} \left( \frac{1}{2} u_i'^2 \right) = \\ & - \frac{\partial}{\partial x_j} \left( \frac{1}{2} u_i'^2 U_j \right) + D_{ij} (-u_i' u_j') - \frac{\partial}{\partial x_j} (-u_i'^2 u_j') - \frac{\partial (p' u_i')}{\partial x_j} + R^{-1} \left[ \frac{\partial}{\partial x_j} \left( u_i' \frac{\partial u_i'}{\partial x_j} \right) - \left( \frac{\partial u_i'}{\partial x_j} \right)^2 \right] \end{aligned} \quad (202)$$

Where  $U_j$  is the basic solution of the flow,  $D_{ij}$  the rate -of-strain tensor of the basic flow and  $R$  the Reynolds number.

If we evaluate in order every one of the six terms of equation (202), it follows that each of them represents:

1. The rate of increase of the kinetic energy density
2. The convection of the perturbation kinetic energy by the basic flow
3. The transference of energy from the basic flow to the perturbation
4. The convection of the perturbation kinetic energy by the perturbation velocity
5. The rate of working of the perturbation of pressure
6. The dissipation of energy by viscosity

Integrating energy equation over the domain of flow, expression (202) becomes:

$$\frac{d\varepsilon}{dt} = \int \left[ D_{ij}(-u'_i u'_j) - R^{-1} \left( \frac{\partial u'_i}{\partial x_j} \right)^2 \right] dV \quad (203)$$

The fundamental idea of the method is to show that if  $R$  is sufficiently small, lower than a critical value  $R_C$ , then the viscous dissipation is large enough to ensure that:

$$\int \left[ D_{ij}(-u'_i u'_j) - R^{-1} \left( \frac{\partial u'_i}{\partial x_j} \right)^2 \right] dV < 0 \quad (204)$$

$$\text{and then } \frac{d\varepsilon}{dt} < 0$$

In fact, the critical value  $R_C$  refers to the energetic stability threshold  $v_\varepsilon$ , which separates disturbances whose energy may increase initially from those whose energy must decay monotonically. Its value is bounded by the ratio of perturbation convection by the basic flow to viscous dissipation in the system such that:

$$\frac{1}{R_C} = \sup_{\mathbf{u}'} \left[ - \frac{\int [D_{ij}(-u'_i u'_j)] dV}{\int \left[ \left( \frac{\partial u'_i}{\partial x_j} \right)^2 \right] dV} \right] \quad (205)$$

This last expression reveals the sufficient condition for stability to perturbations of all magnitudes to be damped by the system if  $R < R_C$  is accomplished.

One of the procedures to deal with this problem comes from the fact that these integrals can be approximated using estimations of terms using known information of the flow, such as the basic solution or a general perturbation form solution of the system. In this way, we can proceed to use penalizing estimates of the terms of increase/decrease of perturbation energy. That is, the approach consists in maximizing the energy production terms and minimizing the energy dissipation terms in order to obtain the threshold from which the variation of energy of the system with the introduction of a disturbance is positive for the most hostile situation that can occur in the specified case. Thus, we can conclude that the threshold obtained via the energetic method can be viewed as a lower bound for stability.

## Annex II: EPM-INDUC code structure

### Module equations

Electromagnetic equations in EPM-INDUC are coded splitting vectors into their scalar coordinates in the Cartesian referential (i.e.  $x$ ,  $y$  and  $z$  indices) and complex numbers into their real and imaginary parts (i.e.  $R$  and  $I$  indices). Then, the system is formed by 8 diffusive equations for the vector potential and electric potential real and imaginary components which refer to each one of the *user's defined scalars* (UDS) variables on Fluent to be solved by the code. They read respectively:

$$\nabla \cdot (-\sigma \nabla V_R) = \nabla \cdot (-\sigma \mathbf{u} \times \mathbf{B}_R - \omega \sigma \mathbf{A}_I) \quad (206)$$

$$\nabla \cdot (-\nabla A_{xR}) = \mu_0 j_{xR} \quad (207)$$

$$\nabla \cdot (-\nabla A_{yR}) = \mu_0 j_{yR} \quad (208)$$

$$\nabla \cdot (-\nabla A_{zR}) = \mu_0 j_{zR} \quad (209)$$

$$\nabla \cdot (-\sigma \nabla V_I) = \nabla \cdot (-\sigma \mathbf{u} \times \mathbf{B}_I + \omega \sigma \mathbf{A}_R) \quad (210)$$

$$\nabla \cdot (-\nabla A_{xI}) = \mu_0 j_{xI} \quad (211)$$

$$\nabla \cdot (-\nabla A_{yI}) = \mu_0 j_{yI} \quad (212)$$

$$\nabla \cdot (-\nabla A_{zI}) = \mu_0 j_{zI} \quad (213)$$

For the case in cylindrical coordinates (i.e.  $x$ ,  $r$  and  $\varphi$  indices), complementary terms must be added to previous vector potential equations because of the expression of Laplace operator in cylindrical reference. For axisymmetric cases ( $\partial/\partial\varphi = 0$ ), they give:

$$\nabla \cdot (-\sigma \nabla V_R) = \nabla \cdot (-\sigma \mathbf{u} \times \mathbf{B}_R - \omega \sigma \mathbf{A}_I) \quad (214)$$

$$\nabla \cdot (-\nabla A_{xR}) = \mu_0 j_{xR} \quad (215)$$

$$\nabla \cdot (-\nabla A_{rR}) = \mu_0 j_{rR} - \frac{A_{rR}}{r^2} \quad (216)$$

$$\nabla \cdot (-\nabla A_{\varphi R}) = \mu_0 j_{\varphi R} - \frac{A_{\varphi R}}{r^2} \quad (217)$$

$$\nabla \cdot (-\sigma \nabla V_I) = \nabla \cdot (-\sigma \mathbf{u} \times \mathbf{B}_I + \omega \sigma \mathbf{A}_R) \quad (218)$$

$$\nabla \cdot (-\nabla A_{xI}) = \mu_0 j_{xI} \quad (219)$$

$$\nabla \cdot (-\nabla A_{rI}) = \mu_0 j_{rI} - \frac{A_{rI}}{r^2} \quad (220)$$

$$\nabla \cdot (-\nabla A_{\phi I}) = \mu_0 j_{\phi I} - \frac{A_{\phi I}}{r^2} \quad (221)$$

The linearity of equations for the electric potential permits to dissociate electric currents depending on their origin in electrokinetic (source of current with potentials  $V_s$  and  $A_s$ ) or electrodynamic (Foucault currents). The electrokinetic part corresponds to the imposed difference of potential (boundary condition  $\Gamma_e$ ) or to the imposed density of current (boundary condition  $\Gamma_j$ ) without considering the induction terms linked to  $\mathbf{A}$ . The electrodynamic part is defined in the code from the fully solution as  $V_f = V - V_s$  and  $j_f = j - j_s$ . Using these source currents, the total current expression gives:

$$\mathbf{j} = \sigma(-\nabla V_f + \mathbf{u} \times \mathbf{B} - i\omega \mathbf{A}) + \mathbf{j}_s \quad (222)$$

After obtaining the UDS variables at the start of each iteration (i.e. segregative solver procedure such as Fluent), additional fields  $\mathbf{j}$  and  $\mathbf{B}$  are calculated by the induction module and stocked as *user's defined memories* (UDM) on Fluent. These variables would permit the coupling with CFD calculation.

The same approach as for the potentials is employed, so variables are calculated separately in scalar components and real and imaginary parts.

$$j_{xR} = \sigma(-\partial V_R / \partial x + u_y B_{zR} - u_z B_{yR} + \omega A_{xI}) + j_{sxR} \quad (223)$$

$$j_{yR} = \sigma(-\partial V_R / \partial y + u_z B_{xR} - u_x B_{zR} + \omega A_{yI}) + j_{syR} \quad (224)$$

$$j_{zR} = \sigma(-\partial V_R / \partial z + u_x B_{yR} - u_y B_{xR} + \omega A_{zI}) + j_{szR} \quad (225)$$

$$j_{xI} = \sigma(-\partial V_I / \partial x + u_y B_{zI} - u_z B_{yI} - \omega A_{xR}) + j_{sxI} \quad (226)$$

$$j_{yI} = \sigma(-\partial V_I / \partial y + u_z B_{xI} - u_x B_{zI} - \omega A_{yR}) + j_{syI} \quad (227)$$

$$j_{zI} = \sigma(-\partial V_I / \partial z + u_x B_{yI} - u_y B_{xI} - \omega A_{zR}) + j_{szI} \quad (228)$$

$$B_{xR} = \partial A_{zR} / \partial y - \partial A_{yR} / \partial z \quad (229)$$

$$B_{yR} = \partial A_{xR} / \partial z - \partial A_{zR} / \partial x \quad (230)$$

$$B_{zR} = \partial A_{yR} / \partial x - \partial A_{xR} / \partial y \quad (231)$$

$$B_{xI} = \partial A_{zI} / \partial y - \partial A_{yI} / \partial z \quad (232)$$

$$B_{yI} = \partial A_{xI} / \partial z - \partial A_{zI} / \partial x \quad (233)$$

$$B_{zI} = \partial A_{yI}/\partial x - \partial A_{xI}/\partial y \quad (234)$$

Considering the contribution of the curl in cylindrical coordinates, magnetic field components give:

$$B_{xR} = \partial A_{\varphi R}/\partial r + A_{\varphi R}/r - [\partial A_{rR}/r\partial\varphi] \quad (235)$$

$$B_{rR} = [\partial A_{xR}/r\partial\varphi] - \partial A_{\varphi R}/\partial x \quad (236)$$

$$B_{\varphi R} = \partial A_{rR}/\partial x - \partial A_{xR}/\partial r \quad (237)$$

$$B_{xI} = \partial A_{\varphi I}/\partial r + A_{\varphi I}/r - [\partial A_{rI}/r\partial\varphi] \quad (238)$$

$$B_{rI} = [\partial A_{xI}/r\partial\varphi] - \partial A_{\varphi I}/\partial x \quad (239)$$

$$B_{\varphi I} = \partial A_{rI}/\partial x - \partial A_{xI}/\partial r \quad (240)$$

And for the axisymmetric case with  $\partial/\partial\varphi = 0$  and  $\vec{A} = (0, 0, A_\varphi)$  :

$$B_{xR} = \partial A_{\varphi R}/\partial r + A_{\varphi R}/r \quad (241)$$

$$B_{rR} = -\partial A_{\varphi R}/\partial x \quad (242)$$

$$B_{\varphi R} = 0 \quad (243)$$

$$B_{xI} = \partial A_{\varphi I}/\partial r + A_{\varphi I}/r \quad (244)$$

$$B_{rI} = -\partial A_{\varphi I}/\partial x \quad (245)$$

$$B_{\varphi I} = 0 \quad (246)$$

This last corresponds to the 2D axisymmetric model of an ALIP.

Furthermore, the divergence of the vector potential is also calculated by the code in order to check that the Gauge condition is verified.

From these last variables we obtain the terms responsible for the coupling with fluid mechanics (density of electromagnetic force  $f$ ) and thermal physics (density of dissipated thermal power  $\psi$ ). They read:

$$\mathbf{f}(t) = \mathbf{j}(t) \times \mathbf{B}(t) \rightarrow \bar{\mathbf{f}} = \mathbf{j}_R \times \mathbf{B}_R + \mathbf{j}_I \times \mathbf{B}_I \quad (247)$$

$$\psi(t) = \frac{\mathbf{j}(t) \cdot \mathbf{j}(t)}{\sigma} \rightarrow \bar{\psi} = (\mathbf{j}_R \cdot \mathbf{j}_R + \mathbf{j}_I \cdot \mathbf{j}_I) / \sigma \quad (248)$$

The fields  $\mathbf{f}$  and  $\psi$  are not harmonic, but the product of harmonic functions. They are composed by a mean part over a period (previous expressions (247) and (248)) and a fluctuating part at the double of the supply frequency ( $2\omega$ ), which is not considered by the code. However, the frequency associated to  $\mathbf{f}$  and  $\psi$  fluctuations might be high enough to neglect the respective fluid answer.

### Boundary conditions

Boundary conditions for the real or imaginary part of the electric potential are either of Dirichlet type ( $V=V_{s0}$  for  $\Gamma_e$ : perfect conductors or symmetry planes  $//\mathbf{B}$ , with fixed voltage), or Neumann type ( $\partial V/\partial n=0$  for  $\Gamma_m$ : perfect yokes or symmetry planes  $\perp\mathbf{B}$ , with  $\partial V/\partial n=-j_n-i\omega A_n$  and for  $\Gamma_j$ : perfect conductors or symmetry planes  $//\mathbf{B}$ , with fixed currents). On  $\Gamma_j$  we need to extrapolate the vector potential (known from last iteration) up to the boundary, to project it along the normal to the boundary, in order to calculate the flux of  $V$  to be imposed. This is not difficult in a segregative code such as Fluent.

For the vector potential, boundary conditions apply to the normal part or to the tangential part, and not to components in the axes  $x,y,z$  or  $x,r,\varphi$ . We use mixed boundary conditions written in an explicit form, obtained after having looked among the 3 axes (or 2 in 2D), the one which is nearer from the normal to the surface (i.e. the index  $k$  which maximize  $|\mathbf{e}_k \cdot \mathbf{n}|$ , or which maximize  $|n_k|$ ). We'll call  $j_1$  and  $j_2$  the two other indices, in an order that makes  $(k,j_1,j_2)$  be direct coordinates, i.e. an odd permutation of  $x,y,z$  (or  $x,r,\varphi$ ). With such coordinates  $n_k$  is never 0 and we can write:

$$\mathbf{A} \cdot \mathbf{n} = \sum_{j=1,3} A_j n_j \Rightarrow A_k = \frac{\mathbf{A} \cdot \mathbf{n} - A_{j_1} n_{j_1} - A_{j_2} n_{j_2}}{n_k} \quad (249)$$

$$\begin{aligned} \mathbf{A} \times \mathbf{n}_j &= \sum_{k,l=1,3} \varepsilon_{jkl} A_k n_l \\ \Rightarrow \begin{cases} \mathbf{A} \times \mathbf{n}_{j_1} = A_{j_2} n_k - A_k n_{j_2} \\ \mathbf{A} \times \mathbf{n}_{j_2} = A_k n_{j_1} - A_{j_1} n_k \end{cases} &\Rightarrow \begin{cases} A_{j_2} = \frac{A_k n_{j_1} + A_k n_{j_2}}{n_k} \\ A_{j_1} = \frac{-A_k n_{j_2} - A_k n_{j_1}}{n_k} \end{cases} \end{aligned} \quad (250)$$

The idea is then to apply to the  $k^{th}$  component (almost normal to the surface) a condition deduced from the one on  $A_n$ , using the derivatives of the other components at the previous iteration; and to apply to components  $j_1$  and  $j_2$ , almost tangential, some boundary conditions deduced from the one on  $\mathbf{A}_t$  (using  $\mathbf{A} \times \mathbf{n} = \mathbf{A}_t \times \mathbf{n}$ ), using the values of other components at the previous iteration.

Projecting that way the conditions on  $\mathbf{A}$ , and adjoining the  $V$  condition on each type of boundary condition (i.e.  $\Gamma_e$ ,  $\Gamma_m$  and  $\Gamma_j$ ), we obtain following expressions with index  $r$  for the real part and  $i$  for the imaginary part:

$$\text{On } \Gamma_e : \quad \frac{\partial A_{kR}}{\partial n} = -\frac{n_{j1}}{n_k} \frac{\partial A_{j1R}}{\partial n} - \frac{n_{j2}}{n_k} \frac{\partial A_{j2R}}{\partial n} \quad \frac{\partial A_{kI}}{\partial n} = -\frac{n_{j1}}{n_k} \frac{\partial A_{j1I}}{\partial n} - \frac{n_{j2}}{n_k} \frac{\partial A_{j2I}}{\partial n}$$

$$\left\{ \begin{array}{l} A_{j1R} = (n_{j1}/n_k) A_{kR} \\ A_{j2R} = (n_{j2}/n_k) A_{kR} \\ V_R = V_{s0R} \end{array} \right. \quad \text{and} \quad \left\{ \begin{array}{l} A_{j1I} = (n_{j1}/n_k) A_{kI} \\ A_{j2I} = (n_{j2}/n_k) A_{kI} \\ V_I = V_{s0I} \end{array} \right. \quad (251)$$

$$\text{On } \Gamma_m : \quad \frac{\partial A_{kR}}{\partial n} = -\frac{n_{j1}}{n_k} A_{j1R} - \frac{n_{j2}}{n_k} A_{j2R} \quad \frac{\partial A_{kI}}{\partial n} = -\frac{n_{j1}}{n_k} A_{j1I} - \frac{n_{j2}}{n_k} A_{j2I}$$

$$\left\{ \begin{array}{l} \frac{\partial A_{j1R}}{\partial n} = \left(\frac{n_{j1}}{n_k}\right) \left(\frac{\partial A_{kR}}{\partial n}\right) \\ \frac{\partial A_{j2R}}{\partial n} = \left(\frac{n_{j2}}{n_k}\right) \left(\frac{\partial A_{kR}}{\partial n}\right) \\ \partial V_R / \partial n = 0 \end{array} \right. \quad \text{and} \quad \left\{ \begin{array}{l} \frac{\partial A_{j1I}}{\partial n} = \left(\frac{n_{j1}}{n_k}\right) \left(\frac{\partial A_{kI}}{\partial n}\right) \\ \frac{\partial A_{j2I}}{\partial n} = \left(\frac{n_{j2}}{n_k}\right) \left(\frac{\partial A_{kI}}{\partial n}\right) \\ \partial V_I / \partial n = 0 \end{array} \right. \quad (252)$$

$$\text{On } \Gamma_j : \quad \frac{\partial A_{kR}}{\partial n} = -\frac{n_{j1}}{n_k} \frac{\partial A_{j1R}}{\partial n} - \frac{n_{j2}}{n_k} \frac{\partial A_{j2R}}{\partial n} \quad \frac{\partial A_{kI}}{\partial n} = -\frac{n_{j1}}{n_k} \frac{\partial A_{j1I}}{\partial n} - \frac{n_{j2}}{n_k} \frac{\partial A_{j2I}}{\partial n}$$

$$\left\{ \begin{array}{l} A_{j1r} = \left(\frac{n_{j1}}{n_k}\right) A_{kr} \\ A_{j2r} = \left(\frac{n_{j2}}{n_k}\right) A_{kr} \\ \frac{\partial V_r}{\partial n} = j_{nr} \end{array} \right. \quad \text{and} \quad \left\{ \begin{array}{l} A_{j1I} = \left(\frac{n_{j1}}{n_k}\right) A_{kI} \\ A_{j2I} = \left(\frac{n_{j2}}{n_k}\right) A_{kI} \\ \frac{\partial V_I}{\partial n} = j_{nI} \end{array} \right. \quad (253)$$

With  $j_{nR} = j_{n0R} + \omega(A_{ki}n_k + A_{j1i}n_{j1} + A_{j2i}n_{j2})$  and  $j_{nI} = j_{n0I} - \omega(A_{kr}n_k + A_{j1r}n_{j1} + A_{j2r}n_{j2})$ .

To implement those boundary conditions, we use in the right-hand side the latest known values of  $\mathbf{A}$  or its derivatives at the boundary. The left-hand side is the real boundary condition as seen from the solver (Neumann or Dirichlet depending of the type of boundary). Because in Fluent, one can only choose the type of boundary for a whole zone (and not face by face, locally), we suppose that the boundaries are separated into pieces where the ‘‘almost normal’’ coordinate is always the same. That supposes for example to cut the boundary of a sphere into six pieces (that can be grouped by two).